NORTHWESTERN UNIVERSITY

Materials by Design: A Combined Computational and Experimental Approach to Thermoelectrics

A DISSERTATION

SUBMITTED TO THE GRADUATE SCHOOL

IN PARTIAL FULFILLMENT OF THE REQUIREMENTS

for the degree

DOCTOR OF PHILOSOPHY

Field of Materials Science and Engineering

By

Samuel A. Miller

EVANSTON, ILLINOIS

December 2018

ABSTRACT

Materials by Design: A Combined Computational and Experimental Approach to Thermoelectrics

Samuel A. Miller

In the United States and around the world, the growing energy demands and climate concerns necessitate renewable and efficient energy production. Thermoelectric materials could be one small part of this larger picture movement, but their high cost and low efficiency must be improved to realize commercial use. To decrease the time to application of new compounds, computations which provide predictions of material properties may guide the discovery and investigation of novel thermoelectric materials. For these models to be useful for high-throughput screening of numerous compounds across a varied phase space, they must be accurate enough to provide trustworthy predictions and inexpensive enough to be suitable for large and diverse groups of compounds.

This work focused on the development of empirical models for predicting material properties relevant to thermoelectric applications as well as the use of these models to guide experimental investigation of interesting compounds. A semi-empirical model was

constructed by fitting physics-based equations to experimental properties using inexpensive inputs. By utilizing inputs which are readily accessible from known structural data and basic first-principles calculations, this model is capable of being implemented for high-throughput predictions without limitations on the complexity or number of compounds considered. Since we begin with analytical expressions for these properties and utilize a small number of fitting parameters, rationalization of the effects and outputs is straightforward. This model was refined by adding additional data to the learning set, introducing a structural parameter, and statistical fitting, thereby increasing the accuracy.

SnO, GeSe and $ZrTe_5$ are three layered compounds which were investigated for their thermoelectric performance. While all exhibit high potential based on predictions using the semi-empirical model, realization of this potential through optimization proved difficult. Individually, each compound poses a unique challenge; collectively, they demonstrate that chasing high potential alone is not recommended. Rather the possibility of realizing the optimum performance must be acknowledged. If we are to use predictions from models to guide experiments, we must predict dopability in addition to thermoelectric potential.

Dopability estimates are accomplished through statistical and machine learning on experimental carrier concentration data gathered from the literature. Predictions using this model are accurate to approximately one order of magnitude and the drivers of dopability are rationalized and compared to previous efforts due to the simplicity of the model. The combination of these two models, one for optimum performance and the other for dopability, demonstrates the effectiveness of building prediction engines from empirical data to allow human learning and guide further experimental and computational work.

Acknowledgements

I would like to express my deepest gratitude to those who have advised me throughout my time as a graduate student at Northwestern University. To Prof. Scott Barnett, who willingly accepted me into his group under less than ideal circumstances. You were always willing to provide suggestions and guidance along the way. To Prof. Jeff Snyder, who provided an environment to learn and grow as a scientist, including laboratory facilities, training in the field of thermoelectrics, a group which inspired new and interesting discussions and research, and advice whenever it was needed. To Prof. Eric Toberer, who even from afar, mentored me throughout my PhD, stimulating new and bigger ideas to investigate and take ownership of. And to Prof. Tom Mason, who continued to meet with me and remained interested in my work. I would also like to thank Prof. Chris Wolverton for agreeing to be a member of my committee and offer suggestions and advice.

This work was made possible by National Science Foundation DMREF grants and a GRFP fellowship. I'm grateful for all of the collaborators who have provided samples, made measurements, or assisted with computational data and modeling, most notably Prashun Gorai.

I am grateful for the friendship and support of those I met while at Northwestern, without them I would not be here today. My classmates and friends provided the support network and study groups to make it through classes. Original Mason group members Arpun Nagaraja, Alex Dolgonos, Patrick Duffy, Stephanie Moffitt helped start me with

laboratory work and got me out of the office/lab for lunches, not to mention friendship after graduating. Snyder group members Umut Aydemir, Stephen Kang, and Saneyuki Ohno taught me solid state chemistry, instrument usage and upkeep, data interpretation and analysis, and much else for which I am eternally grateful (and I enjoyed the soccer too!). Other Snyder group memebers (Ian Witting, Max Dylla, Max Wood, Riley Hanus, Kazuki Imasato, Shashwat Anand, and others) have assisted me with modeling, instruments, and data analysis. Thank you to Ha-Kyung Kwon, Karen DeRocher, and Shawn Chen for meals, movies, games, and friendship. And finally, to the Lifesavers Lunch Bunch, Fernando Castro, Matt Peters, and Nick Sather for more support and great times than can be listed here.

I would like to thank my family, soon-to-be in-laws, and friends for their love and support these past (more than) five years, and for being interested in and trying to understand my research. In particular, thank you to my parents for the nurturing environment and always pushing me to be my best, to Hannah for setting an example to which I should aspire, and to Jared for his knowledgable assistance and patience with statistics that was so helpful. Finally, thank you to my fiancée Katie for her love and continuous support, for countless adventures, meals, and experiences. Without you, this process would have been joyless and insurmountable.

Table of Contents

List of Tables

List of Figures

CHAPTER 1

Introduction

1.1. Fundamentals of Thermoelectrics

As the global population continues to grow and develop, energy use will rise in lockstep. A significant fraction of the energy used today comes from non-renewable sources, thereby necessitating technological solutions to solve society's energy dilemma. To diminish dependence on fossil fuels, energy consumption must be reduced by broadening energy resources to include more renewable sources or by more efficiently converting non-renewable sources to usable energy. Due to the large fraction of energy consumed that is lost as waste heat, upwards of 50%, there is opportunity to significantly alter the global energy landscape by capturing just a small fraction of this wasted energy.[1] Thermoelectric (TE) generators are one possible solution to this issue, converting waste heat to useful electricity.

The Seebeck effect is a phenomenon where two parallel, dissimilar metals or semiconductors placed in a temperature gradient produce a voltage. This was originally discovered by Johann Cristoph Seebeck in 1820.[2] Thermoelectric materials can also be used in reverse, as Peltier discovered in 1834 that the application of an electric current induces a temperature gradient.[3] To realize the benefit of these effects in a useful device, a thermoelectric generator must be constructed. These are made out of alternating TE 'legs' made of p- and n-type materials that are thermally in parallel and electrically in series

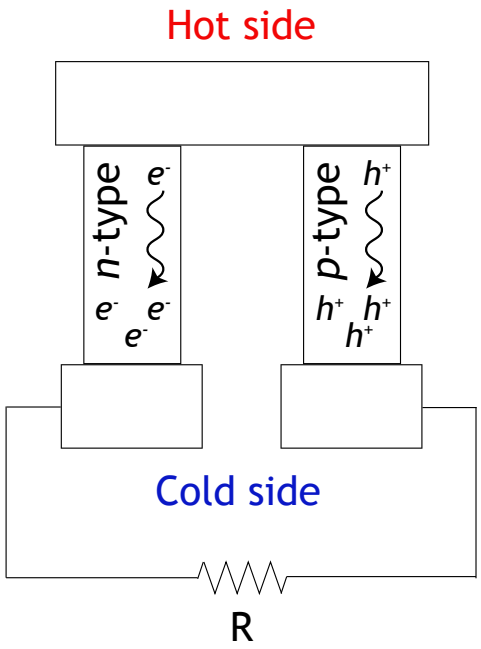

Figure 1.1. Schematic of thermoelectric generator with n- and p-type legs. Carriers move from the hot side to cold side, generating a voltage.

(Fig. 1.1). By placing dozens of these legs in a module, a reasonable amount of power can be generated in the presence of a temperature gradient.

The charge carriers in these conducting materials (holes and electrons for p- and n-type, respectively) can be envisioned as a gas of charged particles, such that the temperature difference causes the carriers to flow from the hot end to the cold side. To maintain equilibrium, the chemical diffusive force is balanced by an electric field, thus a temperature gradient leads to a voltage. The Seebeck coefficient can therefore be written as the ratio of the measured voltage across a sample subject to a temperature difference (α=-$\frac{dV}{dT}$).[4] While this effect is utilized in thermocouples, the voltage is much smaller than is useful for thermoelectrics.[5] The thermoelectric efficiency is then given by the figure-of-merit, zT=$\frac{\alpha^2\sigma T}{\kappa}$, where the electrical conducvity (σ) is in the inverse of the resistivity (ρ)

and κ is the total thermal conductivity.[6,7] The total thermal conductivity is given as the sum of individual contributions; in thermoelectrics we are primarily concerned with the electronic (κ_e) and lattice (κ_L) contributions to the total thermal conductivity, assuming there is no bipolar effect (κ_{BP}).[8]

The device level figure-of-merit, ZT_{avg}, accounts for both the n- and p-type materials and geometry of the individual legs. This device efficiency is governed by the Carnot efficiency.[9–14] Currently, state-of-the-art thermoelectric material zT is near unity, leading to device level efficiency on the order of $\sim$12%.[1] But compared to other energy sources, both sustainable and non-renewable, the efficiency is still quite low. If the average zT could be enhanced to between 2 and 4, this would make thermoelectrics competetive with alternatives, opening the market to applications including waste heat recovery in automotobiles and power generation as well as refrigeration.[1,15]

A significant advantage of thermoelectric generators is that they are solid-state devices and therefore have no moving parts. This makes them vibration-free and reliable for long term use in situations where the power supply can not be interrupted. Thermoelectrics are therefore the best option for some niche applications such as remote weather stations and missions in space where the solar flux is insufficient.[16] Furthermore, TEs are sustainable as they do not emit greenhouse gases when used for power generation and do not use ozone-depleting or greenhouse gases for cooling. The main disadvantage in all situations is that thermoelectric devices are less efficient than traditional power sources. Much of the cost-ineffectiveness of TE generators is due to the critical bottleneck of heat exchangers. But for broad commercial viability to be realized, the underlying material zT must be improved.[17] This can be achieved either by improving the performance of already discovered TE

materials or by discovering new compounds with desirable thermoelectric properties. The various challenges and strategies for both optimizing performance and discovering new materials are discussed in the following sections.

1.2. Strategies for Optimization of Known Materials

To understand the challenge in realizing high efficiency thermoelectrics we must revisit the equation for the figure-of-merit. In order to increase zT, the thermal conductivity and electrical resistivity should be minimized as these are both parasitic losses. Since ρ decreases with increasing carrier concentration (n), one might consider this the simplest way to increase efficiency. However, there is an interplay between all of the properties of which zT is composed, as seen in Fig. 1.2. Even though the electrical conductivity increases with increasing carrier concentration, the total thermal conductivity also increases due to the corresponding increase in κ_e, and the Seebeck coefficient decreases. Therefore, the performance of each compound can be optimized at a given n, usually in the range of 10^{19} to 10^{20} cm^{-3}, leading thermoelectrics to commonly be referred to as heavily doped semiconductors.

To quantify the shape and height of the zT *vs* n curve we use an effective mass model, which is a useful tool in determining the "potential" of an investigated material as a thermoelectric.[18] In this model, the states near the band edge are responsible for the electronic transport properties and typically are well described by an effective mass. For most band conductors, the dispersion can, to first order, be considered parabolic. Collecting measureable properties and transforming them to this metric that characterizes band structure is a useful tool since the effective mass is a slowly changing function. It is

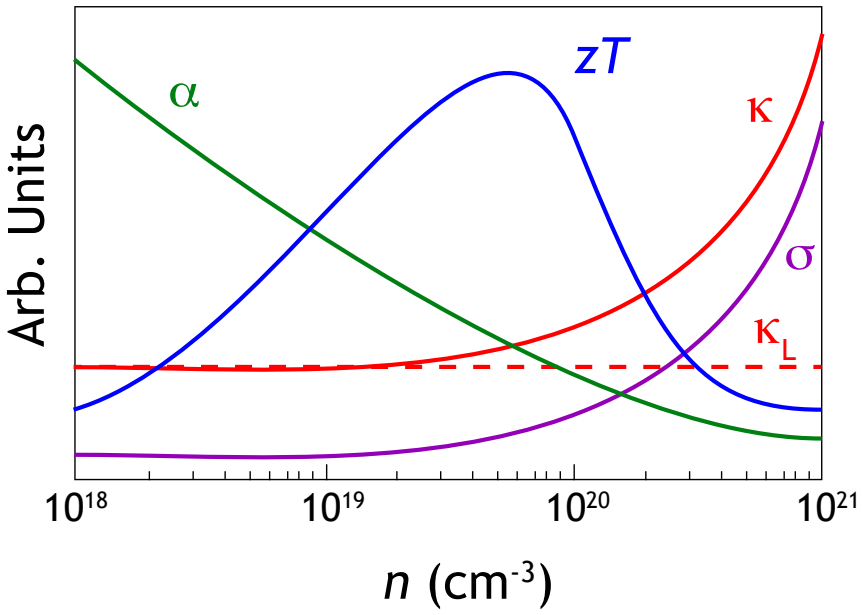

Figure 1.2. Schematic of thermoelectric properties as a function of carrier concentration. The interdependence of these properties necessitates balancing the properties of an insulator and a metal, with optimal performance in the heavily doped semiconductor range.

possible to construct a reasonably accurate effective mass model with only a few measurements of physical properties from a small number of samples, making this a very useful tool in determining the maximum "potential" of any given material and guiding the experimentalist in optimizing its performance. The construction of an effective mass model, commonly referred to as a single parabolic band (SPB) model, is relatively straightforward and the details can be found elsewhere.[18–20]

Given knowledge of the effective mass model, zT can be redefined based on two parameters. The first is the material quality factor ($\mathcal{B}$) and the second is chemical potential (η). $\mathcal{B}$ is dimensionless and proportional to $\frac{\mu_0(m^*/m_e)^{3/2}}{\kappa_L}T^{5/2}$, and being composed of only intrinsic material properties, represents the "potential" for thermoelectric performance.

Therefore, the best possible zT that a material can reach is determined by $\mathcal{B}$ as they increase monotonically together. With this quality factor model in hand, the three main strategies for optimizing thermoelectric performance can be discussed.

The first strategy is to supress the lattice thermal conductivity by increasing the number of phonon scattering sources or the anharmonicity. This can be done by increasing the concentration of grain boundaries, impurities, or nano-precipitates to reduce the thermal conductivity while only slightly impacting electronic transport. This strategy is often most successful in materials such as Si or other traditional semiconductors with inherently high electronic mobility.[21–27] A second stragety is to manipulate the electronic band structure by enhancing anisotropy, valley degeneracy, or effective mass. This is done by alloying the parent compound with one or more additional species to alter the shape and location of bands.[28–33] In addition to these two main strategies, each material can be optimized by tuning the chemical potential (also commonly called Fermi level or carrier concentration tuning). This is done by changing the chemical composition either by adjusting the ratio of elements in the compound (intrinsic doping) or by the substitution of foreign elements (extrinsic doping).[7,34,35]

It can be seen in the equation for zT and $\mathcal{B}$ that the ideal thermoelectric is one which has good electronic conduction but poor thermal conduction, commonly referred to as "electron crystal, phonon glass." This is challenging to achieve due to the coupled nature of κ, ρ, and α. However, complex materials have been exploited as an opportunity to realize good thermoelectric performance.[7,8,36] Due to their complex crystal structures, they often have inherently low lattice thermal conductivity. Often the chemical composition of these compounds is flexible enough to allow either alloying to alter the band structure

or doping to optimize the chemical potential, or both. In the effort to realize high zT materials, the properties of known semiconductors can be optimized using the strategies previously discussed, or new materials with desirable properties can be discovered.

1.3. High-throughput Searches for New Thermoelectric Materials

Reproduced in part from *Energy & Environmental Science* **8**, 983-994 (2015) with permission from the Royal Society of Chemistry.

Previous efforts in the advancements of thermoelectric materials have been led by chemists using a combination of chemical understanding, structure-property relationships, and fortune, which has resulted in relatively slow and incremental improvements. The discovery of new thermoelectric materials is limited by the need to accurately predict both the electron and phonon transport properties entering the thermoelectric figure-of-merit.[7,37–39] While the desired properties inherent to good thermoelectric performance have been known for more than a century,[40] the design problem concerning optimum material structures and chemical compositions remains elusive. Typically most computational work is done after the experiments in an effort to understand and explain the observed phenomena rather than before experiments to predict properties. The few attempts at predicting thermoelectric performance have been limited in scope. To this end, recent efforts have used high-throughput (HT) computations, focusing exclusively on the ground-state electronic structure of known materials, to identify potential thermoelectric candidates.[41–43]

With such a diverse phase space, the need for high-throughput computationally-driven searches for thermoelectric materials is critical. The first broad attempt to search beyond a

single structural class was conducted by *Madsen*, who considered 570 antimonides.[41] This work analyzed the ground-state electronic structure employing the constant relaxation time approximation (CRTA) for solving the electronic Boltzmann transport equations.[44] As its name suggests, the CRTA treats the charge carrier relaxation time τ as an energy-independent term. In reality, an energy-dependent τ is expected for electron-phonon scattering; nevertheless, the CRTA approach is mathematically attractive as it enables one to obtain a reduced power factor ($\alpha^2\rho/\tau$) as a function of chemical potential simply from the electronic band structure. Within this approach, however, the ranking of different materials based on the reduced power factor requires that τ is not only constant for a given material, but also does not vary significantly from one material to the other. Furthermore, calculations of dopant levels, electron or phonon scattering, and the phonon band structure were not included in this work due to their high computational cost. This work, however, succeeded in identifying n-type LiZnSb as a promising thermoelectric due to fairly high band degeneracy; subsequent experimental efforts agreed with these calculations within the experimentally accessible doping range.[45]

An alternative approach to addressing the scattering challenge has been proposed by *Curtarolo* and coworkers, who investigated 2,500 compounds.[43] The approach focuses on highly nanostructured materials by assuming that the bulk carrier mean free path is equal to or larger than the average grain size l. Therefore, if these structures are sufficiently fine-grained ($\sim$5 nm), grain boundary scattering will dominate charge carrier scattering. Electronic structure calculations can then provide a performance metric given by $\alpha^2\rho/l$. This metric can be used to compare predicted performance of different materials and sort promising candidates. Achieving high zT in this approach inherently requires large α, as

the electronic mobility has been significantly reduced owing to enhanced grain boundary scattering.

On the other hand, rigorous calculations of electron–phonon scattering rates have been recently considered for simple materials (e.g. GaAs, GaP, Si, $Si_{1-x}Ge_x$) and were found to agree well with experiments.[46–49] Calculations of the vibrational properties and lattice thermal transport of individual materials have also seen significant advances.[50–55] However, these calculations, although of desired accuracy, are typically material dependent and are sufficiently expensive that high-throughput searches are unlikely to adopt such methods in the near future for structurally complex materials.

1.4. Semi-empirical Model for High-throughput Predictions of Thermoelectric Performance

Reproduced in part from *Energy & Environmental Science* **8**, 983-994 (2015) with permission from the Royal Society of Chemistry. And reproduced in part with permission from *Chemistry of Materials* **29**, 2494-2501 (2017).

The basis for the semi-empirical descriptor emerges from the thermoelectric figure-of-merit, zT, which depends on the Seebeck coefficient, electrical conductivity and the electronic and lattice components of the thermal conductivity:

$$zT = \frac{\alpha^2 \sigma}{\kappa_L + \kappa_e} T. \tag{1.1}$$

Inspection of Eq. 1.1 reveals challenges associated with direct assessment of zT as it depends on both the electronic and vibrational properties, including scattering phenomena. Electronic correlations can further complicate the evaluation of electronic transport. The complexity of the problem is further compounded by the fact that thermoelectric materials span a diverse chemical phase space. Many promising compounds remain to be discovered, preferably *via* efficient methods such as high-throughput computations. Alloys and metastable polymorphs offer further avenues for the discovery of new thermoelectric materials; such compounds highlight the need for computationally-driven searches due to their broad phase space.

A semi-empirical approach that is based on first-principles calculations and offers a relatively simple computational assessment of the intrinsic bulk material properties which govern zT has been proposed and validated.[76] This approach offers a bridge between ab initio calculations and experiments by deriving semi-empirical relations for quantities that are nearly inaccessible to high-throughput computations such as carrier mobility and lattice thermal conductivity. These material properties combine to form a quantitative semi-empirical descriptor β_{SE}. The efficacy of β_{SE} is demonstrated in both predicting known thermoelectric materials, including those that are not used in developing the empirical relations for β_{SE}, and in high-throughput screening for new candidate materials.

In an attempt to develop a tractable computational approach taking into account both κ_L and the energy-dependence of charge carrier scattering and that will allow screening of large, complex materials classes, simple descriptors for thermoelectric performance were revisited. Consideration of the solutions to the Boltzmann transport equation within the

relaxation time approximation yields an expression for zT,

$$zT = \frac{u\beta}{v\beta + 1}, \tag{1.2}$$

where u and v are functions that depend strictly on the chemical potential (η) and charge carrier scattering mechanism, and β is a material-dependent parameter that is independent of charge carrier chemical potential.[56,57] It is clear from inspection of Eq. 1.2 that large zT requires simultaneously maximizing β and optimizing η. β is defined as:

$$\beta = \frac{2e}{\hbar^3}\left(\frac{k_B}{e}\right)^2\left(\frac{k_B}{2\pi}\right)^{3/2}\frac{\mu_0 {m^*_{\mathrm{DOS}}}^{3/2}}{\kappa_L}T^{5/2}, \tag{1.3}$$

where μ_0 is the intrinsic charge carrier mobility and m^*_{DOS} is the density of states effective mass. In SI units, this expression simplifies to:

$$\beta = 5.745 \times 10^{-6}\frac{\mu_0(m^*_{\mathrm{DOS}}/m_e)^{3/2}}{\kappa_L}T^{5/2}. \tag{1.4}$$

Under the assumption that optimal η can be achieved, β is helpful in assessing the maximal zT achievable in a given material. By focusing on compounds which have received significant efforts to optimize the carrier concentration (thereby maximizing u/v and thus zT for a given β), Fig. 1.3 shows that β_{300K} is a good descriptor of maximal zT. Here, β_{300K} is estimaged from experimental values at 300 K due to the relative abundance of room temperature measurements. While this descriptor is fairly independent of temperature and facilitates comparison of materials with different band gaps and peak temperatures, it still necessitates the production of numerous samples to properly quantify β_{300K}. Therefore semi-empirical models for room temperature μ_0 and κ_L were developed

by combining standard DFT calculations, available experimental values (at 300 K), and classical scattering theory. These models serve to develop the semi-empirical approach to β_{300K}, which is denoted by β_{SE}:

$$\beta_{SE} \propto \frac{\mu_0 (m^*_{\mathrm{DOS}}/m_e)^{3/2}}{\kappa_L}. \tag{1.5}$$

At room temperature and above, one would expect a combination of acoustic and optical phonons to dominate charge carrier scattering, which is consistent with the $\mu \propto T^{-1.5}$ observed experimentally at high temperatures in thermoelectric materials and classic semiconductors.[58–61] Electron-phonon scattering is known to be important in semiconductors and depend critically on the elastic properties of the material. In addition, the relaxation times are inversely proportional to the electronic density of states, which implies τ scales with $m^{*-3/2}_{\mathrm{b}}$ within the parabolic band approximation. Motivated by these general features of the electron–phonon scattering mechanisms and taking into account the reciprocal additivity of the relaxation times (Matthiessen's rule), the model for the carrier mobility is postulated as the combination of bulk modulus (B), describing the elastic properties of materials, and m^*_{b} in the following way:

$$\mu_0 = A_0 (B)^s (m^*_{\mathrm{b}})^{-t}, \tag{1.6}$$

where A_0, s and t are empirical parameters which provide a reasonable approximation for the mobility of band conductors. The bulk modulus and m^*_{b} in Eq. 1.6 represent the DFT calculated values with band effective mass derived from the DOS effective mass and the band degeneracy.

The thermal conductivity is determined within the semi-empirical model using ground state calculations and structural data from the Inorganic Crystal Structure Database (ICSD).[62] Assuming Umklapp scattering as the dominant scattering source and using the high temperature heat capacity limit, it can be shown that with a simplified Debye-Callaway model,[63] acoustic phonons can be approximated using:[8]

$$\kappa_{L,ac} = \frac{(6\pi^2)^{2/3}}{4\pi^2} \frac{\overline{M} v_s^3}{T\gamma^2 V^{2/3} n^{1/3}}, \tag{1.7}$$

where $\overline{M}$ is the average atomic mass, v_s the speed of sound, T is the temperature, γ is the Grüneisen parameter, V the volume per atom, and n is the number of atoms in the primitive cell. In most systems, acoustic phonon modes dominate the lattice thermal conductivity. However, omitting the optical modes produces a model which erroneously predicts that κ_L asymptotes to zero in materials with large n. To account for optical modes, it is assumed that their wavelength is related to the mean free path,[64] leading to:

$$\kappa_{L,opt} = \frac{3k_b}{2}\left(\frac{\pi}{6}\right)^{1/3} \frac{v_s}{V^{2/3}}\left(1 - \frac{1}{n^{2/3}}\right), \tag{1.8}$$

where k_b is the Boltzmann constant. Together, $\kappa_{L,ac}$ and $\kappa_{L,opt}$ provide a general expression for $\kappa_{L,tot}$ that can be obtained from ground-state calculations:

$$\kappa_{L,tot} = A_1 \frac{\overline{M} v_s^3}{V^{2/3} n^{1/3}} + A_2 \frac{v_s}{V^{2/3}}\left(1 - \frac{1}{n^{2/3}}\right). \tag{1.9}$$

where A_1 and A_2 are fitted parameters. Here, γ has been incorporated into A_1 as a material-independent quantity. In practice, γ varies from $\sim$0.5 to 3 in most materials and will contribute approximately an order of magnitude scatter to the modeled κ_L.

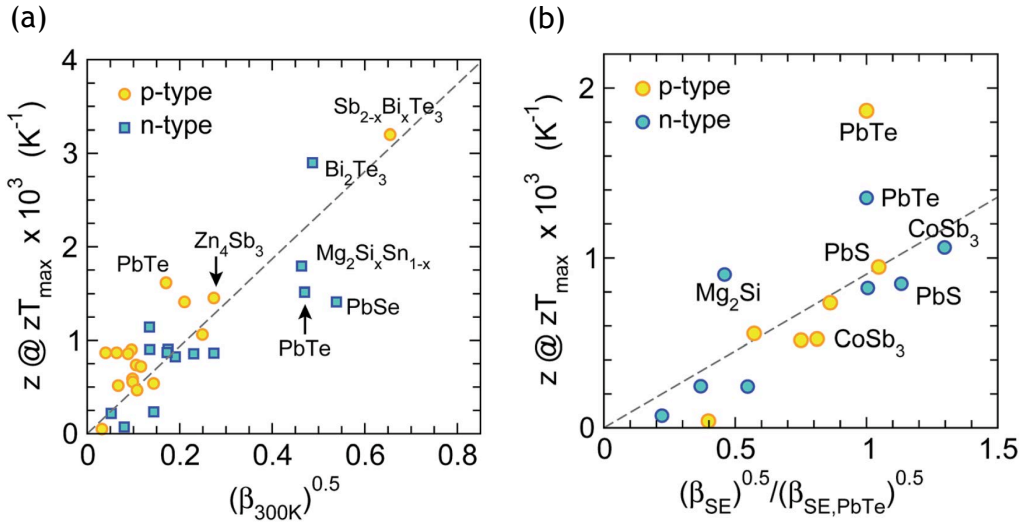

Figure 1.3. (a) Room temperature experimental measurements combined into β_{300K} are a good descriptor of zT across a diverse range of compounds. (b) β_{SE} calculated *via* semi-empirical models is also a robust predictor of thermoelectric performance.

The models for μ_0 and $\kappa_{L,tot}$ were fit using their respective adjustable parameters to experimental values for mobility and lattice thermal conductivity in bulk materials at room temperature. Each model is accurate to within approximately one order of magnitude compared to the experimental values. The resulting predictions using the semi-empirical β_{SE} is nearly as predictive as the experimental β_{300K}, as shown in Fig. 1.3. It is important to note that no predictions for any compounds are dramatically false-negative or false-positive. Further, the real power of β_{SE} is that it only requires relatively simple and computationally inexpensive density functional calculations. Such success provides a promising path forward for high throughput screening of known and hypothetical materials for their thermoelectric performance.

1.5. Summary of Research

The semi-empirical descriptor β is a measure of the maximal zT achievable in a material, provided the system is dopable (1) with the desired carrier type, and (2) to the desired carrier concentration. Therefore this metric can be used to make high-throughput predictions on many thousands of compounds and identify promising candidate thermoelectric materials and eliminate those with little potential.

The need for high-throughput property predictions and development of the β metric is discussed in Chapter 1. In Chapter 3, the semi-empirical model was used to identify a number of compounds that merited experimental investigation for their low thermal conductivity and potential as thermoelectric materials.[65] From these, eight compounds were chosen spanning a wide variety of structures and compositions to be synthesized and characterized. By adding the thermal conductivity of these compounds and an additional literature search to the original dataset, it was possible to refine the lattice thermal conductivity model to include more statistically justified fitting parameters and make more accurate predicitons. This was done primarily by the introduction of a structural parameter that was ignored in the first version of the model. The lattice thermal conductivity predictions generated using this model are significantly better than the previous iteration and two times as accurate as other inexpensive models. Compared with a first-principles model that is only applicable to compounds with simple structures due to the high computational cost, the semi-empirical model is commensurate.

Three layered compounds were chosen for further experimental thermoelectric characterization. In Chapter 4, SnO is shown to be a promising n-type material with a high mobility, low lattice thermal conductivity, and unusual electronic properties. Due to the

limited stability range of SnO compared to SnO_2, the processing conditions necessary to optimize performance are challenging.[66] Chapter 5 focuses on GeSe, a promising p-type material where performance has been limited prior to this work. Co-substitution is demonstrated to unlock an alternative phase which realizes the high potential with a zT near 1.[67] $ZrTe_5$ is investigated in Chapter 6, and although the underlying properties indicate it could be a good material for either p- or n-type thermoelectrics, it suffers from bipolar conduction which limits performance. However, a simple two-band model can be used to explain the properties which have been investigated as exotic phsyics phenomena.[68] All three of these compounds share common features: they have attractive and interesting transport features of interest in thermoelectrics and other applications, their potential performance is predicted to be high based on the semi-empirical model, and they all suffer from issues related to dopability.

The dopability of materials is complicated by the presence of native defects that pin the Fermi level; consequently, the material is either n- or p-type or intrinsically compensated with low carrier concentrations. The descriptor β is equivocal of the doping tendency of the material. Therefore, the realization of the high thermoelectric performance predicted by a large value of β rests upon dopability of the material, which, at present, can be computationally predicted with expensive defect calculations that cannot be performed in a HT fashion. By collecting empirical carrier concentration data, it was possible to fit a statistical model to this literature data that is accurate to within approximately one order of magnitude. The simplicity of this model allows understanding and explaination of the drivers of dopability in diamond-like semiconductors and comparison with previous

efforts. By combining the β and dopability model, idenfication of promising thermoelectric materials and better guidance for both experimental and computational efforts is achieved.

CHAPTER 2

Methods

2.1. Summary

Discussed here is the synthesis and characterization of inorganic polycrystalline thermoelectric materials. While single crystals, nanomaterials, and thin films are the focus of much current thermoelectric research with the goal of producing high zT, there are some advantages to bulk polycrystalline samples. These samples are prepared by mechanical alloying and consolidation, alloying for reproducibility and mass production and are therefore quite practical.

In order to gain a deep understanding of the underlying materials science, synthesis and measurement were maintained as consistently as possible. Summarized in this section are general methods for synthesis of bulk polycrystalline samples. The details of synthesis vary by compound and project, thus they are elaborated in individuals sections below. The same holds true for characterization techniques, mostly carried out using in-house built measurement equipment at Northwestern, with alterations to this procedure discussed separately. Computational methods, details on literature data scrapes, and modeling tools are all discussed on an individual basis.

2.2. General Sample Preparation

One common method for the synthesis of inorganic materials is melting from a mixture of pure elements. With this technique, raw materials are weighed out to form stoichiometric quantities, sealed in an ampoule under vacuum, and placed in a furnace. The furnace is then heated at some rate to an elevated temperature, held for a period of time, and then either slowly cooled or the sample is removed and quenched. The resulting compound is then consolidated through pressing.

Mixing and grinding of materials is also utilized, either before melting or between melting and consolidation. Mixing of raw materials using an agate mortar and pestle distributes the elements fairly uniformly, aiding in full reaction to form the compound during melting or sintering. In situations where mixing of elements is not sufficient, mechanical alloying using a SPEX Sample Prep 8000 Series mixer/mill can be performed. Raw materials (2 to 10 grams) are placed in a 3 inch stainless-steel vial along with 2 or more half inch stainless steel balls. These vials are sealed with o-rings in an inert atmosphere inside the glove box to avoid reaction of elements with oxygen. This dry, high energy ball mill produces homogeneously distribued powder, typically with nanoscale particles. While the typical procedure is to mill before melting, thus reducing the time for a full reaction to occur, it can also take place after melting to reduce particle size before consolidation.

Consolidation takes place using a home-built hot press system. A graphite die is loaded with 1 to 2 grams of pre-reacted powder, with grafoil around the inner diameter and both top and bottom. The die is placed within a copper induction coil, a thermocouple is attached to monitor the temperature, and the vacuum chamber is closed. After a

pump and purge cycle using roughing pump and argon gas, a diffusion pump evacuates any remaining oxygen before refilling with Ar. Under flowing Ar, pressure is applied (typically 45 MPa), and the die is rapidly heated by induction. After applying the desired temperature and pressure for a length of time, they are removed, allowing the die and chamber to cool slowly under flowing argon. The resulting disk shaped pellet is typically 1 to 2 mm thick and is carefully polished to produce flat parallel surfaces with no grafoil contamination. The density is calculated either with the geometry and weight or the Archimedes method, and the pellet is then used for chemical and physical characterization.

2.3. Synthesis Methods for Individual Studies

2.3.1. Capturing Anharmonicity in a Lattice Thermal Conductivity Model for High-throughput Predictions

Eight compounds were synthesized and their thermal conductivity was measured for the first time in bulk polycrystalline form in the present study. The synthesis procedure is described in detail below for each compound. Non-oxide samples were syntehsized by collaborator Brenden Ortiz.

- $Ba_3In_2O_6$: Stoichiometric $BaCO_3$ and In_2O_3 were ground in agate mortar and pestle. Powders were pressed into ½ inch diameter pellets using uniaxial press and steel die at 200 MPa. Pellets were fired for 18 hours at 1000°C, ball milled in a tungsten carbide vial for 1 hour, pressed again into pellet form, and fired at 1350°C for 36 hours.
- Ba_2SnO_4: Stoichiometric $BaCO_3$ and SnO_2 were ground in agate mortar and pestle. Powders were pressed into ½ inch diameter pellets using uniaxial press

and steel die at 200 MPa. Pellets were fired for 18 hours at 1200°C, ball milled in a tungsten carbide vial for 1 hour, pressed again into pellet form, and fired at 1425°C for 24 hours.

- Cu_3TaTe_4: A stoichiometric mixture of Cu granules, Ta and Te chunks was ball milled in a stainless steel vial. The resulting powder was annealed at 600°C for 18 hours followed by hot pressing at 600°C with 3 hour densification followed by 18 hours stress free anneal.
- $Cu_2ZnSiTe_4$: A stoichiometric mixture of Cu granule, Zn powder, Si and Te chunk was ball milled in a tungsten carbide vial. The resulting powder was annealed at 615°C for 72 hours followed by hot pressing at 554°C with 3 hour densification and 18 hour stress free anneal. A small amount (<3%) secondary phase ZnTe (ICSD 77072) observed following refinement.
- InI: A stoichiometric mixture of In and I chunk was ball milled in a stainless steel vial followed by hot pressing at 220°C with 1 hour densification.
- $MoTe_2$: A stoichiometric mixture of Mo powder and Te chunk was ball milled in a stainless steel vial. The resulting powder was annealed at 600°C for 18 hours followed by hot pressing at 600°C with 3 hour densification and 18 hour stress free anneal.
- SnO: $SnCl_2$ was dissolved in HCl, precipitated with NH_4OH, and washed with deionized water.[69] The resulting powder was pressed at 200°C under 300 MPa uniaxial pressure for 2 hours.
- $SrIn_2O_4$: Stoichiometric $SrCO_3$ and In_2O_3 were ground in agate mortar and pestle. Powders were pressed into ½ inch diameter pellets using uniaxial press

and steel die at 200 MPa. Pellets were fired 18 hours at 1000°C, ball milled in a tungsten carbide vial for 1 hour, pressed again into pellet form, and fired at 1350°C for 36 hours.

2.3.2. SnO as a Potential Oxide Thermoelectric Candidate

Tin monoxide was synthesized using a precipitation reaction similar to that described by Kwestroo *et al.,*[69] using $SnCl_2$ as a precursor rather than Sn. Doping was attempted either through the solution synthesis or *via* a solid state method by dry ball-milling with stainless-steel balls in a stainless-steel vial using a SPEX Sample Prep 8000 Series mixer/mill. Powders were placed in a 1/2 inch steel die which was loaded between heated platens. The temperature was increased to 225°C at a rate of ∼100°C per hour and then allowed to slowly cool to room temperature. During the heating and cooling process, a pressure of 250 MPa was maintained. Discs were polished using 1200 grit sandpaper prior to all measurements. An effective medium theory model was used to correct for porosity, assuming small spheres of air uniformly distributed in the matrix.[70]

Incorporation of both *p*- and *n*-type dopants was attempted by solid state reaction. $Sn_{1-x}Sb_xO$, $SnO_{1-x}Cl_x$, or $Sn_{1-x}Ga_xO$ were placed in a stainless-steel vial under argon and milled for five minutes in one minute increments. The resulting powder was then pressed, sealed in a quartz ampule, and annealed for 7 days at 275°C. Alternately, doping the material directly during the solution synthesis was also attempted to achieve $Sn_{1-x}Sb_xO$ or $Sn_{1-x}In_xO$, substituting $InCl_3$ or $SbCl_5$ for $SnCl_2$ as a precursor in the solution synthesis.

2.3.3. High Thermoelectric Performance of New Rhombohedral Phase of GeSe Stabilized Through Alloying with $AgSbSe_2$

Polycrystalline samples $GeAg_xSb_xSe_{1+2x}$ (x=0, 0.05, 0.1, 0.15, 0.2, 0.3) were prepared using a melting-annealing method and spark plasma sintering (SPS) technique. Highly pure elemental powders of Ge (99.999%, Aladdin), Ag (99.9%, Alfa Aesar), Sb (99.999%, Alfa Aesar), and Se (99.999%, Alfa Aesar) were weighed according to the stoichiometric ratio $GeAg_xSb_xSe_{1+2x}$ and ball-milled for 12 h at 450 rpm. The milled powder was sealed in a vacuum quartz tube and heated at 773 K for 30 min with a heating rate of 3 K min^{-1}. Then the materials were melted at 1073 K for 2 hours with a ramp rate of 3 K min^{-1} and annealed at 823 K for 30 min. The samples were ground into fine powders and sintered by SPS at 773 K for 5 min with a heating rate of 20 K min^{-1} and a pressure of 50 MPa. The obtained ingots were cut for thermoelectric property measurement and characterization. The single element doped GeSe samples ($GeAg_ySe_{1+y}$ and $GeSb_zSe_{1+z}$) were prepared by the same process. Samples were syntehsized by collaborator Zhiwei Huang.

2.3.4. Polycrystalline $ZrTe_5$ Parameterized as a Narrow Band Gap Semiconductor for Thermoelectric Performance

Bulk polycrystalline $ZrTe_{5-x}I_x$ samples were produced by solid state reaction of Zr (Alfa Aesar, 99.95%), Te (Alfa Aesar, 99.999%), and TeI_4 (Strem Chemical, 99.9%), followed by hot pressing. Zr was mixed in a stoichiometric ratio with Te and TeI_4, placed in a quartz ampule, evacuated to 10^{-5} mbar, and torch sealed. Using a vertical single zone furnace, the heating profile was 90 K per hour from room temperature to 923 K, dwell time of 12 hours, furnace quench (300 K per hour) to 748 K, dwell for 72 hours, and finally cooling

to room temperature at 90 K per hour. The resulting material was ground in an agate mortar and pestle into a fine powder. Powder was hot pressed in a half inch graphite die using a maximum temperature of 723 K for 2 hours under flowing argon, followed by ambient cooling. A series of grit papers ending in 1200 grit was used to polish residual graphite foils and produce samples of uniform thickness.

2.4. Structural Analysis

To investigate the structure, homogeneity, composition, and presence of secondary phases, characterization was performed on both synthesized powder and consolidated pellets. This was done using X-ray diffraction (XRD) and electron microscopy, both scanning electron micriscopy (SEM) and transmission electron microscopy (TEM).

The individual instruments used for characterization vary by each case. XRD was typically performed using a Rigaku D/MAX diffractometer at the JB Cohen X-ray Diffraction Facility or STOE STADI MP at the Integrated Molecular Structure Education and Research Center (IMSERC), both at Northwestern University. SEM was carried out using a Hitachi S-3400-II in the EPIC facility in the NUANCE Center at Northwestern University.

For the work on GeSe, characterization was carried out by collaborators. The crystal structure was characterized using X-ray diffraction (Empyrean-100) with Cu Kα radiation at room temperature. The phase transition phenomenon of $GeAg_xSb_xSe_{1+2x}$ was investigated by an in-situ XRD system (Riguka D/MAX 2400) from 300 K to 523 K in N_2 atmosphere. The high-angle annular dark field (HAADF) images and selected area electron diffraction patterns (SAED) were collected using an ARM-200CF (JEOL, Tokyo,

Japan) TEM system (200 keV, double spherical aberration (Cs) correctors). The samples for TEM characterization were prepared by mechanical polishing, dimpling and ion milling method with liquid nitrogen.

2.5. Physical Property Measurement

Physical properties of interest for thermoelectric materials were measured, including the Seebeck coefficient, electrical conductivity/resistivity, Hall effect, thermal conductivity, and optical band gap. Again, the individual instruments used for these measurements varied so the instruments used most commonly will be described first, with any deviations discussed separately.

The Seebeck coefficient was measured using the light-pipe method with chromel-niobium thermocouples under vacuum.[71] The various pros and cons of this method in comparison with other techniques, including the cold-finger effect, electrical and thermal contact issues, sample geometry, and measurement error, can be found elsewhere.[20] All instrumentation, sample loading, conditions, and analysis were typical of the lab group, with no major differences to note.

The Hall effect and resistivity are simultaneously measured under dynamic vacuum using a 4-point Van der Pauw (VdP) technique with a 0.8 T magnet.[72] This permits estimation of the sign, concentration, and mobility of charge carriers, allowing the effective mass and possible scattering mechanisms to be determined when measured as a function of temperature. Sample considerations, experimental setup, Hall correction factors, and other details can be found in Ref. 20. All instrumentation, sample loading, conditions, and analysis were typical of the lab group, with no major differences to note.

Diffuse reflectance at room temperature was measured using a Shimadzu UV-3600 UV-VIS-NIR spectrophotometer. The absorption spectra were obtained using the Kubelka-Munk method.[73,74]

Thermal conductivity can be measured with numerous methods, but typical of the thermoelectrics community, the laser flash method was utilized here. A Netzsch LFA 457 was used to measure the diffusivity (D) with the data being fit using a Cowan plus Pulse Correction model. The total thermal conductivity is then given as κ_{tot}=DdC_p where d is the geometrical mass density and C_p is the heat capacity. For most materials, using the Dulong-Petit approximation for the heat capacity is sufficient. The lattice thermal conductivity (κ_L) was calculated from κ_L =κ_{tot}-κ_{e}, where κ_{e}, the electronic thermal conductivity, is given by κ_{e}=$L\sigma T$. L is the Lorenz number calculated by L=1.5+$e^{-|\alpha|/116}$.[75] Again, the principles, preparation, and considerations are discussed elsewhere[20] and all instrumentation, sample loading, conditions, and analysis were typical of the lab group, with no major differences to note.

When samples were not greater than 95% of the theoretical density, an effective medium theory model[70] was used to correct for porosity by treating porosity as small spheres dispersed in a uniform matrix. The thermal conductivity of the matrix material is given by:

$$\kappa_m = \frac{\kappa_c(2\kappa_c + \kappa_a - 3\kappa_a)}{\kappa_c(2 - 3P) + \kappa_a}, \tag{2.1}$$

where m, c, and a represent the matrix, composite, and air, respectively, and P is the porosity. In all cases, non-oxide samples were at least 95% dense and oxide samples were greater than 85% of theoretical density.

For low temperature measurements on $ZrTe_5$ samples, a number of instruments were used to measure the various properties by other collaborators. A Physical Property Measurement System (PPMS, Quantum Design) was used in the van der Pauw configuration as well as with the Thermal Transport Option (TTO). For all PPMS measurements, contacts were made out of silver paste, air-dried, and were ohmic in the temperature range considered. Additional low temperature magnetotransport and Hall measurements were done on square planar devices with four-corner contacts applying the van der Pauw method. The experiment was conducted in a Cryogenic Ltd. cryogen-free 5 Tesla magnet system with helium flow-cryostat using ac lock-in techniques (SR830).

The thermoelectric properties of $GeAg_xSb_xSe_{1+2x}$ were measured by collaborators along two directions (parallel and perpendicular to the pressing direction). There was no evidence of anisotropic behavior in the XRD or property measurements for $GeAg_xSb_xSe_{1+2x}$ samples, therefore only thermoelectric properties along the direction perpendicular to the pressing direction will be discussed. The carrier concentration and mobility measurements were performed using a Hall system (HL5500PC) at 300 K. The electrical conductivity and Seebeck coefficient measurements were performed from 300 K to 710 K in a helium atmosphere (ZEM-3; ULVAC-RIKO, Japan). Heat capacity measurements were performed using a Netzsch STA 449 F3 instrument from 300 K to 710 K at a heating rate of 10 K min^{-1} in continuous N_2 flow.

2.6. Computational Methods

2.6.1. Capturing Anharmonicity in a Lattice Thermal Conductivity Model for High-throughput Predictions

The DFT calculations were performed as previously described in Refs. 76 and 77 on 26 additional compounds. Accurate computational assessment of γ is expensive, making it intractable for high-throughput predictions of complex materials. It was proposed to use local coordination as an estimate of γ. The local coordination of an atomic site in a crystal was established by estimating the number of neighboring atoms directly bonded to it. Neighbors directly bonded to an atomic site are determined based on the shortest neighbor distance. For each atomic site, all neighbors within 10% of the nearest neighbor length are counted towards the site coordination. An average coordination number is then computed for a given crystal structure by summing the coordination number for all the atomic sites and dividing by the total number of atoms.

The density functional theory (DFT) calculations were performed by collaborators with the plane-wave VASP code[78] using the generalized gradient approximation of Perdew-Burke-Ernzerhof (PBE) approach[79] within the projector augmented wave (PAW) formalism.[78] The calculations were performed within the Pylada framework[80] using the previously described approach for structure relaxations.[81] A suitable on-site correction in the form of Hubbard U in the rotationally-invariant form[82] was applied for transition metals. For compounds containing transition metals, a limited search was performed for the magnetic ground state by enumerating over all possible magnetic orders on a primitive cell.

Because the number of configurations scales as 2^N with number of magnetic atoms (N), the total number of configurations was limited to 32, including the ferromagnetic order.

The exchange correlation functionals such as LDA[83] and GGA[79] that are routinely used in computational materials screening do not account for van der Waals (vdW) interactions, which are especially important in quasi-2D materials such as SnSe and SnS. It is well known that using LDA or GGA leads to overbinding and underbinding of the quasi-2D layers in these materials, respectively, and consequently, overestimation and underestimation of B, respectively. The underestimation in GGA is especially severe; in some cases, the value of B can be underestimated by an order of magnitude compared to experiments. For instance, B calculated with GGA for $MoTe_2$ is ∼5 GPa while the experimental value is ∼40 GPa. As a consequence, calculated κ_L with GGA (0.3 $Wm^{-1}K^{-1}$) is more than an order of magnitude smaller than the actual value (4 $Wm^{-1}K^{-1}$).[84] To account for long-range vdW interactions, the optB86 vdW-corrected exchange correlation functional[85] was employed, which significantly improves predictions of κ_L.[77] Structural relaxations were performed with the vdW-corrected functional using a plane-wave cutoff of 400 eV.

2.6.2. SnO as a Potential Oxide Thermoelectric Candidate

DFT calculations were performed by collaborators with the plane-wave VASP code[78] and the generalized gradient approximation of Perdew-Burke-Ernzerhof (PBE) approach[79] within the projector augmented wave (PAW) formalism.[78] Structures were relaxed following a procedure similar to that described in Ref. 81. For transition metals, a Hubbard U in

the rotationally-invariant form was employed as the on-site correction.[82] High-throughput calculations were performed with the Pylada framework.[80]

2.6.3. High Thermoelectric Performance of New Rhombohedral Phase of GeSe Stabilized Through Alloying with $AgSbSe_2$

Density Functional Theory Calculations First-principles calculations for GeSe were carried out b collaborators using density functional theory (DFT) implemented in the Vienna Ab initio Simulation Package (VASP).[86] In all calculations, projector-augmented-wave (PAW) pseudopotentials and generalized gradient approximation of Perdew–Burke–Ernzerhof (PBE)[87,88] for exchange and correlation functionals was adopted. The plane-wave basis sets were truncated at a constant energy cutoff of 405 eV, and Γ-centered k-point meshes with a density of ∼8000 k-points per reciprocal atom (KPPRA). All atomic coordinates were relaxed until the forces on the atoms had declined to 0.001 eV per Å, enforcing a total energy convergence criterion of 1×10^{-8} eV. For plotting the Fermi surface, a Γ-centered k-point mesh with a density ∼20,000 KPPRA was used.

2.7. Literature Data Scrape

2.7.1. Capturing Anharmonicity in a Lattice Thermal Conductivity Model for High-throughput Predictions

As outlined in Ref. 76, the original material dataset is similar to that used in previous studies of high-throughput prediction of κ_L.[89,90] The dataset consisted of 37 compounds spanning from simple structures such as diamond (κ_L=1000 $Wm^{-1}K^{-1}$) to complex ternary Zintl phases such as $Ca_5In_2Sb_6$ (κ_L=1.2 $Wm^{-1}K^{-1}$), but was primarily focused on known

thermoelectric materials and simple binary compounds in the rocksalt, zincblende, and wurtzite structures. To expand the original material dataset, another literature survey was undertaken to find experimental single crystal and bulk polycrystalline thermal conductivity measurements to complete the expanded dataset; the present model does not incorporate grain boundary or dislocation scattering and therefore nanocrystalline and thin film samples are not considered.

2.7.2. Empirical Modeling of Dopability in Diamond-like Semiconductors

An extensive literature search was undertaken to compile a dataset that could be used for statistical modeling. Although a few sources of tabulated carrier concentration exist, these often do not note sample quality or processing conditions even though these are very important in determining carrier concentration in semiconductors. For this reason, careful consideration was given to experimental conditions from which measurements could be relied upon and all measurements for this dataset were scraped from original sources where possible. An attempt was made to use bulk samples produced at or near equilibrium conditions and measured using the Hall effect technique near room temperature and pressure. Nanomaterials, thin films, and other non-equilibrium processing methods were avoided where possible.

With DLS as the model system, the scale for dopability must be defined such that the data are distributed fairly normal so that it can be modeled. The primary goal is to describe the full extent of the achievable dopability range in a compound, from the maximum n-type carrier concentration to the maximum p-type concentration. In some compounds, carrier concentration can be experimentally varied across many orders of

magnitude for both hole and electron majority carriers, while for others the range is narrow or limited to a single type. Although carrier concentration spans many orders of magnitude for both positive and negative values, the primary interest is the range from intrinsic to degenerately doped. Thus, the scale used here ranges from -1 x 10^{21} (degenerate n-type) to 1 x 10^{21} (degenerate p-type), with intrinsic considered any concentration less than $|1$ x $10^{16}|$ (all units given as cm^{-3}). This allows a linear scale from -5 to 0 to 5 to be defined, corresponding to -1 x 10^{21} to ± 1 x 10^{16} to 1 x 10^{21} where every integer value represents an order of magnitude in carrier concentration. Any concentration greater than 1 x 10^{21} was assigned a value of 5 and anything less than 1 x 10^{16} was considered to be 0.

2.8. Modeling Tools

2.8.1. Capturing Anharmonicity in a Lattice Thermal Conductivity Model for High-throughput Predictions

A number of statistical quantities were used to evaluate the model presented herein to compare with experimental data and other high-throughput models.[89,90] The mean absolute error is an unambiguous and natural measure of the average error[91] and therefore, all models in the present work were optimized to reduce the average factor difference (AFD) as given by:

$$\text{AFD} = 10^{x}, x = \frac{1}{m}\sum_{i=1}^{m}|log(t_i) - log(p_i)|, \tag{2.2}$$

where t_i is the true or experimental value, p_i is the predicted value, and m is the number of samples. Due to the κ_L data spanning many orders of magnitude, we are interested in our predictions being equally accurate, on a *logarithmic* scale, for AgCl and diamond (1

and 1000 $Wm^{-1}K^{-1}$, respectively). Using the AFD as defined here gives equal weight to all data, rather than minimizing the absolute error. For example, the log scale was used such that for a given experimental value of 1000, predictions of 500 or 2000 were both a factor of 2 from the "true" value (likewise predictions of 0.5 and 2 for experimental measurement of 1 were both off by a factor of 2 as well).

To assess whether the improved model was predicting κ_L in a linearly increasing relationship with experimental values, the Pearson and Spearman rank correlation coefficients were calculated. The Pearson correlation coefficient is a linear correlation between two variables and is defined as the covariance over the product of the two standard deviations. This was used to measure the degree of linear dependence between the variables and can range from ± 1, inclusive, with 0 indicating no correlation, -1 total negative correlation, and 1 total positive correlation. The Spearman rank correlation can be used instead of the usual Pearson one to assess the relationship between the ordinal ranking of the predicted and experimental κ_L. This is determined by sorting the raw variables in ascending order and assigning a rank to each (using the average position when there is more than one variable with the same value) according to their position in the sorted list. The Spearman rank correlation is then calculated using the same covariance over standard deviation product definition, except with the rank rather than the raw values. Though the same range and interpretations apply, the Spearman rank correlation was used to determine how well the ranking order of one variable predicts that of the other.

2.8.2. Polycrystalline $ZrTe_5$ Parameterized as a Narrow Band Gap Semiconductor for Thermoelectric Performance

To model and analyze the thermoelectric transport data, the effective mass model was used.[18] This model is frequently employed to guide the understanding and optimization of thermoelectrics. However, there are cases where the effective mass model breaks down, namely due to nonparabolic bands or multi-band effects.[28,92,93] We considered two bands contributing to transport and restrict the use of the model to higher temperatures where any possible topological and phase coherence effects are supressed. One valence and one conduction band are used, both with a rigid band shape that does not change with temperature or doping level. In this model, the effective mass and initial doping level for each band were fixed along with the band gap. To calculate the Fermi level at each temperature the charge neutrality condition was used for the chemical potential relationship between two bands with known gap. Charge neutrality is given by:

$$N_d^+ + p = n + N_a^-, \tag{2.3}$$

where N_d^+ and N_a^- are the number of ionized donors and acceptors, respectively, and p and n are the concentrations of holes and electrons. For a given band gap, E_g, the relationship between the reduced chemical potentials of the two bands is given by the expression

$$\eta_1 = -\eta_2 - \frac{E_g}{k_B T}. \tag{2.4}$$

Once the masses, dopant level, and band gap were set and the Fermi level at each temperature was calculated, the properties of each band according to the effective mass

model could be determined. These are given below for a two-band system, though they can be generalized to multi-band with the appropriate summations:

$$\alpha_{tot} = \frac{\alpha_1\sigma_1 + \alpha_2\sigma_2}{\sigma_1 + \sigma_2} \tag{2.5}$$

$$\sigma_{tot} = \sigma_1 + \sigma_2 \tag{2.6}$$

$$R_{H,tot} = \frac{R_{H,1}\sigma_1^2 + R_{H,2}\sigma_2^2}{\sigma_{tot}^2} \tag{2.7}$$

where α, σ, and R_H are the Seebeck coefficient, electrical conductivity, and Hall coefficient, respectively. The subscripts 1 and 2 denote the contribution from each of the two bands (in this case, one conduction and one valence, though this analysis can be applied to two bands of the same type). The total thermal conductivity (κ_{tot}) is then given by:

$$\kappa_{tot} = \kappa_L + T(L_1\sigma_1 + L_2\sigma_2) + T\left((\sigma_1\alpha_1^2 + \sigma_2\alpha_2^2) - \frac{(\sigma_1\alpha_1 + \sigma_2\alpha_2)^2}{\sigma_1 + \sigma_2}\right). \tag{2.8}$$

Here the first term, lattice thermal conductivity (κ_L) was set in the model to have some temperature dependence. At high temperature, Umklapp scattering dominates, which has a T^{-1} dependence. The second term is the electronic thermal conductivity, which depends on the temperature, electrical conductivity, and Lorentz number (L). The third term is bipolar thermal conductivity.

2.8.3. Empirical Modeling of Dopability in Diamond-like Semiconductors

To model this dataset a list of features was first compiled. This includes chemistry-based features from periodic table properties of the consitutuent elements. Added to this feature set were inexpensive calculations from the Open Quantum Materials Database (OQMD)[94,95] and Materials Project (MP)[96–98] collected by collaborators. Lastly, structure and other miscellaneous features were added. Modeling was performed using a number of Python packages, most notably Scikit-learn and StatsModels. Linear regression and leave-one-out cross-validation (LOOCV) were chosen due to a combination of prediciton accuracy and interpretability after comparing the results with other machine learning methods. The primary metric for scoring accuracy used here was the mean absolute error (MAE) which is the average distance between the experimental and predicted value, though mean squared error (MSE) were also evaluated, where smaller values indicate less difference between experiments and predictions.

CHAPTER 3

Capturing Anharmonicity in a Lattice Thermal Conductivity Model for High-throughput Predictions

3.1. Summary of Research

High-throughput, low cost, and accurate predictions of thermal properties of new materials would be beneficial in fields ranging from thermal barrier coatings and thermoelectrics to integrated circuits. To date, computational efforts to predict lattice thermal conductivity (κ_L) are hampered by the complexity associated with computing multiple phonon interactions. In this work, a semi-empirical model for κ_L is developed and validated by fitting density functional theory calculations to experimental data. Experimental values for κ_L come from new measurements on $SrIn_2O_4$, Ba_2SnO_4, $Cu_2ZnSiTe_4$, $MoTe_2$, $Ba_3In_2O_6$, Cu_3TaTe_4, SnO, and InI as well as 55 compounds from across the published literature. To capture the anharmonicity in phonon interactions, a structural parameter is incorporated that enables the model to predict κ_L within a factor of 1.5 of the experimental value across four orders of magnitude in κ_L values and over a diverse chemical and structural phase space, with similar or better accuracy compared to computationally more expensive models.

3.2. Introduction

Thermal properties of materials, namely thermal conductivity and heat capacity, are important for applications ranging from thermal barrier coatings to integrated circuits and light emitting diodes.[99–101] This is especially true in thermoelectric materials where the thermoelectric efficiency is determined by the thermal conductivity and thus low lattice thermal conductivity (κ_L) is desirable.[1,7] However, finding low κ_L materials remains a challenge from an experimental standpoint as synthesis procedures are costly and time consuming.[61] To drive these technologies forward, efficient and accelerated searches with accurate predictions of κ_L of new functional materials are necessary.[102] The ability to accurately predict thermal properties across a wide range of materials with simple calculations would be beneficial for decreasing the time to realization of novel materials. Intuitively, one would expect that κ_L will decrease with increasing atomic mass (heavier atoms) and atoms in primitive unit cell (complex structure).[103,104] Figure 3.1 shows that this is generally the case, though there still exists an order of magnitude variation in κ_L for compounds with similar atomic mass and number of atoms. This demonstrates that intuition is limited and robust calculations require more nuanced theory.

Recently, advances in high-throughput computations have accelerated experimental searches of novel functional materials.[105] However, to make high-throughput predictions, it is necessary to make various assumptions. Heat is transported through multiple-phonon scattering processes, which are commonly determined by solving the Boltzmann transport equation and by calculating group velocities, phonon frequencies, and both harmonic and anharmonic interatomic force constants. This is especially expensive when considering three phonon scattering processes, which requires calculation of third-order anharmonic

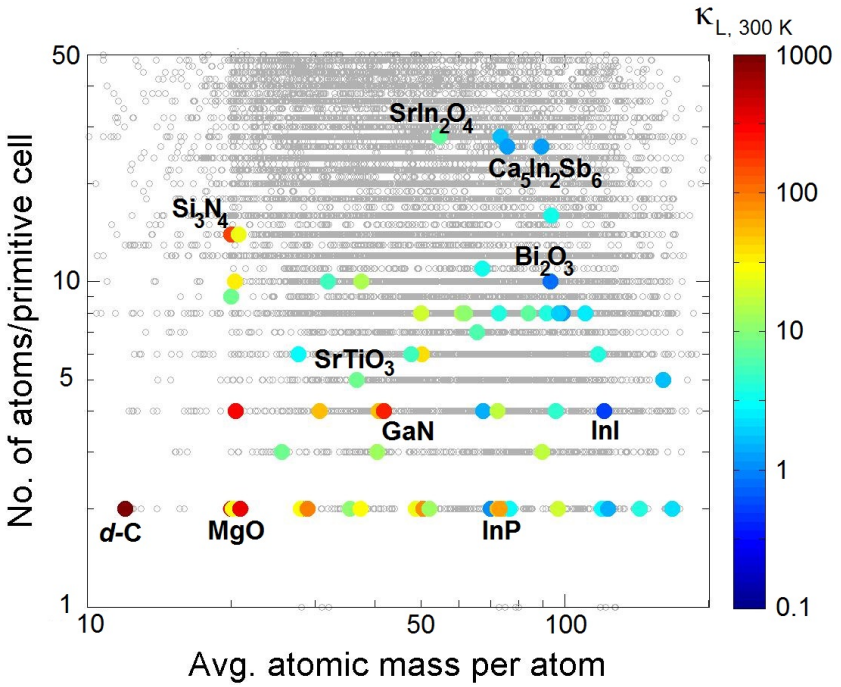

Figure 3.1. Plot of number of atoms in the primitive cell *vs* average atomic mass of 18,135 structures from the Inorganic Crystal Structure Database (open circles). Filled circles denote 63 compounds used in developing the present model with the heat map representing experimental room temperature κ_L ($\mathrm{Wm^{-1}K^{-1}}$).

interatomic force constants.[52,53] Several studies have attempted to predict κ_L for large sets of materials. Seko *et al.* used expensive anharmonic lattice-dynamics calculations to identify low lattice thermal conductivity materials,[106] Carrete *et al.* used *ab initio* calculations and machine-learning algorithms to predict κ_L for half-Heusler compounds,[55] while Madsen *et al.* and Toher *et al.* employed the quasiharmonic Debye approximation to compute thermal properties, including κ_L.[89,90] Previously, a semi-empirical model was developed for determining κ_L, which combines first-principles calculations and experimental measurements and offers an inexpensive route to predicting lattice thermal conductivity.[76] However, anharmonicity was not incorporated in the original model as

the limited size of the original material dataset permitted only a small number of free parameters to be fit.

To improve the accuracy of the prior model,[76] a structural parameter is integrated, which serves as a proxy to capture anharmonicity. This required an expansion of the original material dataset through measurements for the first time on eight bulk polycrystalline materials ($Ba_3In_2O_6$, Ba_2SnO_4, Cu_3TaTe_4, $Cu_2ZnSiTe_4$, InI, $MoTe_2$, SnO, and $SrIn_2O_4$) as well as additional experimental results from the literature. Selection of compounds was driven by the original model predicting low (< 10 $Wm^{-1}K^{-1}$) κ_L and a need for greater structural and chemical diversity in the experimental dataset. The expanded dataset enables anharmonicity to be included and yields a model that performs equally well or better than current methods[89,90] at a fraction of the computational cost. This demonstrates a complete feedback loop with theory guiding material selection, experiments to test predictions, and theory refined by these results.

3.3. Materials Dataset

The original materials dataset used in developing the semi-empirical κ_L model[76] was expanded from 37 to 63 compounds (Fig. 3.2), thereby permitting additional fitting parameters. The expansion was achieved by synthesizing and characterizing eight different compounds, $Ba_3In_2O_6$, Ba_2SnO_4, Cu_3TaTe_4, $Cu_2ZnSiTe_4$, InI, $MoTe_2$, SnO, and $SrIn_2O_4$ in-house as well as by incorporating 18 additional compounds from the literature. As seen in Figure 3.3, the compounds synthesized in-house occupy a diverse chemical and structural space.

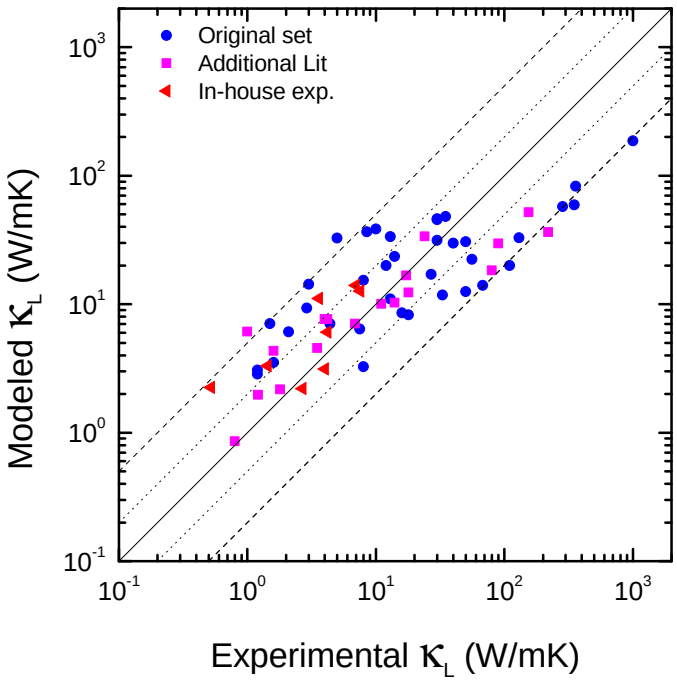

Figure 3.2. Experimental *vs* predicted lattice thermal conductivity for each dataset using original model. There is no significant difference between the datasets. More compounds were added to increase the sample size and add to the number of compounds in the experimental lattice thermal conductivity region of interest for thermoelectrics (1-10 $Wm^{-1}K^{-1}$).

SnO, $MoTe_2$, and InI are all quasi-2D layered materials. Complex ternary oxides such as the n=1 Ruddlesden-Popper (RP) phase Ba_2SnO_4, the oxygen deficient n=2 RP phase $Ba_3In_2O_6$, and $SrIn_2O_4$ which exhibits a continuous network of corner- and edge-shared In octahedra were also investigated. Additionally, chalcogenide materials such as the diamond-like structure $Cu_2ZnSiTe_4$ and cage-like Cu_3TaTe_4 were also included. All of the compounds were predicted to have κ_L on the order of 10 $Wm^{-1}K^{-1}$ or lower using the original model.[76] The XRD patterns and Reitveld refinement for these compounds are shown in Fig. 3.4 and Table 3.1, demonstrating that these compounds were phase pure and match previous reports.

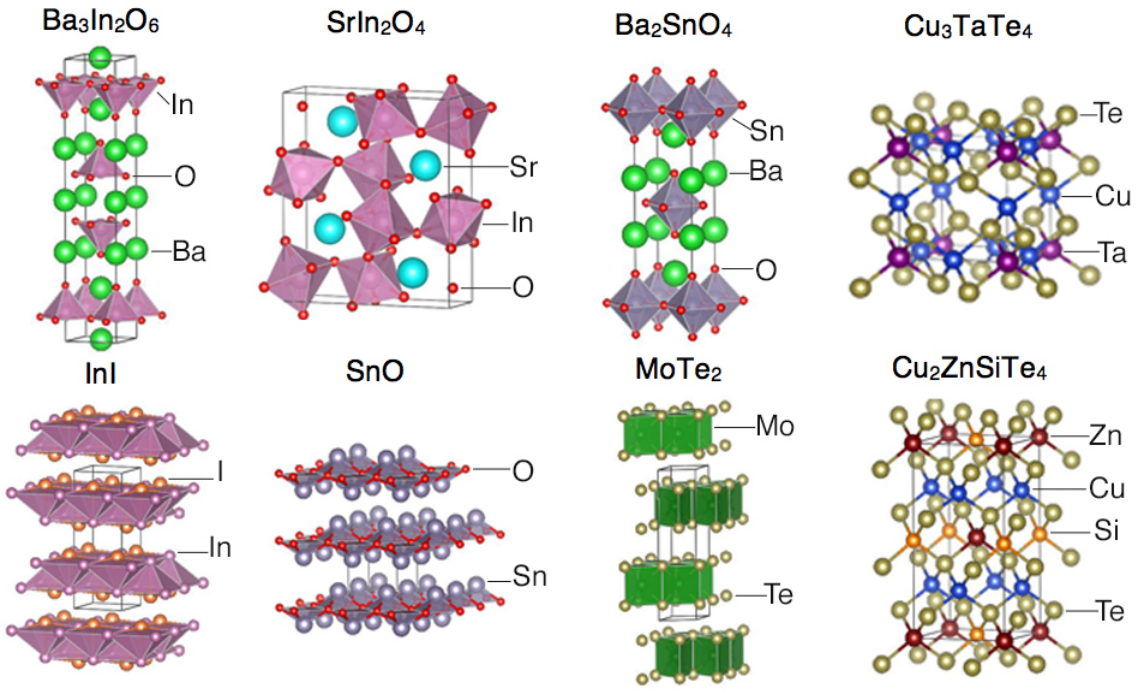

Figure 3.3. Compounds synthesized in this study were chosen for their low predicted κ_L and exhibit a wide range of chemical and structural diversity, ranging across complex oxides, layered materials, and chalcogenides.

Compound	ICSD	a	b	c	GOF	R_p	R_{wp}	a	b	c
$Ba_3In_2O_6$	39267	4.1925(6)	4.1925(6)	21.689(3)	1.63	4.92	7.10	4.188(2)	4.188(2)	21.69(0)
Ba_2SnO_4	27115	4.130(3)	4.130(3)	13.27(1)	1.18	9.81	15.02	4.142(7)	4.142(7)	13.30(2)
Cu_3TaTe_4	80282	5.930(2)	5.930(2)	5.930(2)	1.51,	6.94	8.87	5.926(4)	5.926(4)	5.926(4)
$Cu_2ZnSiTe_4$	656150	5.972(1)	5.972(1)	11.797(4)	2.75	8.03	11.15	5.974(4)	5.974(4)	11.79(4)
InI	38129	4.75(2)	12.76(2)	4.91(2)	1.37	6.89	9.04	4.764(6)	12.77(3)	4.905(0)
$MoTe_2$	24155	3.5182(14)	3.5182(14)	13.9736(40)	2.01	6.14	8.44	3.518(3)	3.518(3)	13.96(1)
SnO	15516	3.7986(1)	3.7986(1)	4.808(2)	1.38	9.48	13.54	3.801(4)	3.801(4)	4.834(4)
$SrIn_2O_4$	16241	9.809	11.449	3.265	0.95	9.31,	5.78	9.829(5)	11.48(7)	3.264(4)

Table 3.1. Compounds matched to ICSD collection code using Jana 2006 with lattice parameters (in Å) along with goodness of fit, profile R-factor, and weighted profile R-factor.

A list of in-house κ_L measurements for the compounds in eight different structure types at room temperature is given in Table 3.2. The κ_L *vs* temperature behavior for these eight compounds, representing a diverse phase and structural space, is shown for the

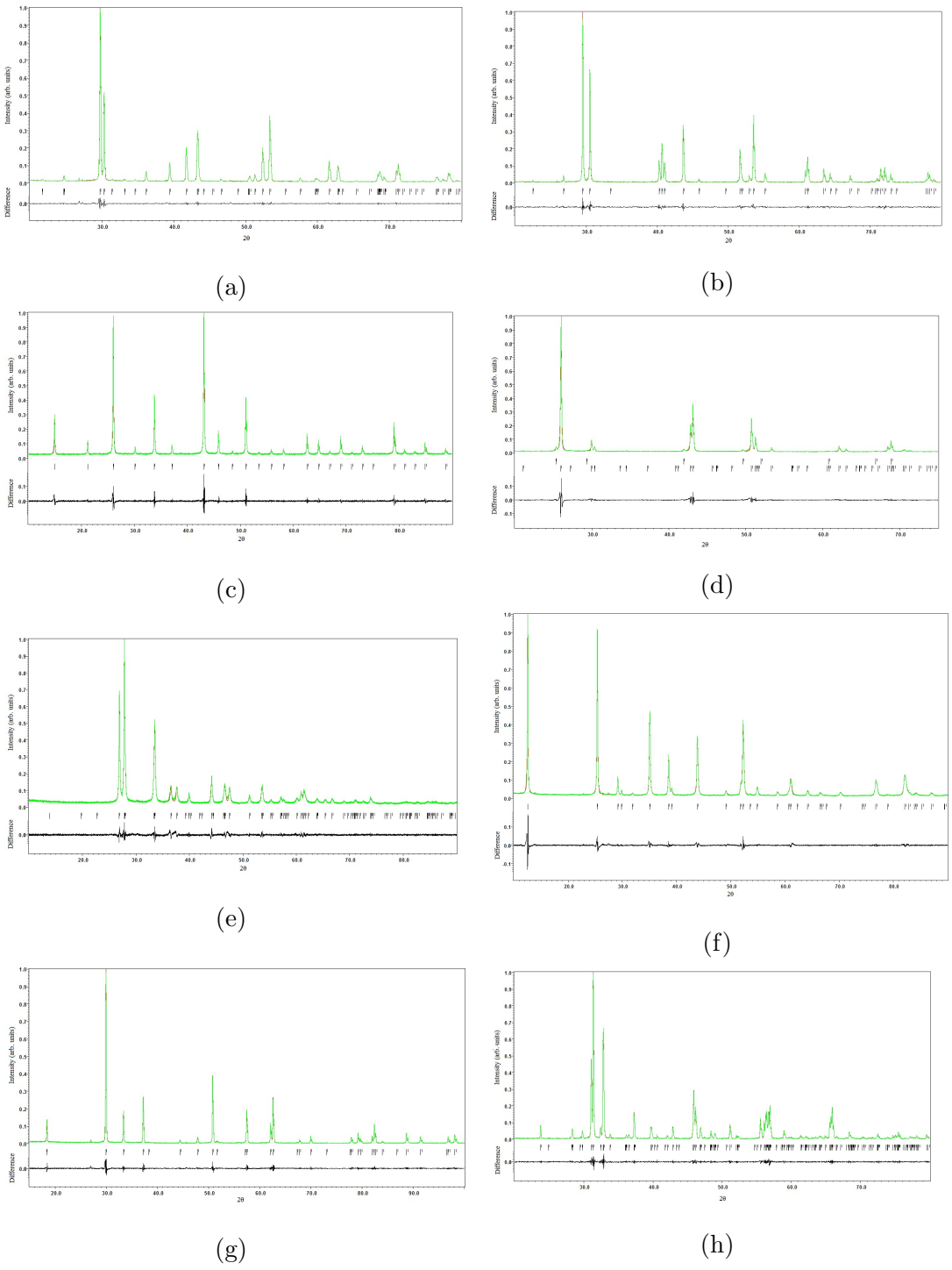

Figure 3.4. Refinement showing observed pattern in green, theoretical pattern in red, and difference pattern below for (a) $Ba_3In_2O_6$, (b) Ba_2SnO_4, (c) Cu_3TaTe_4, (d) $Cu_2ZnSiTe_4$, (e) InI, (f) $MoTe_2$, (g) SnO, and (h) $SrIn_2O_4$.

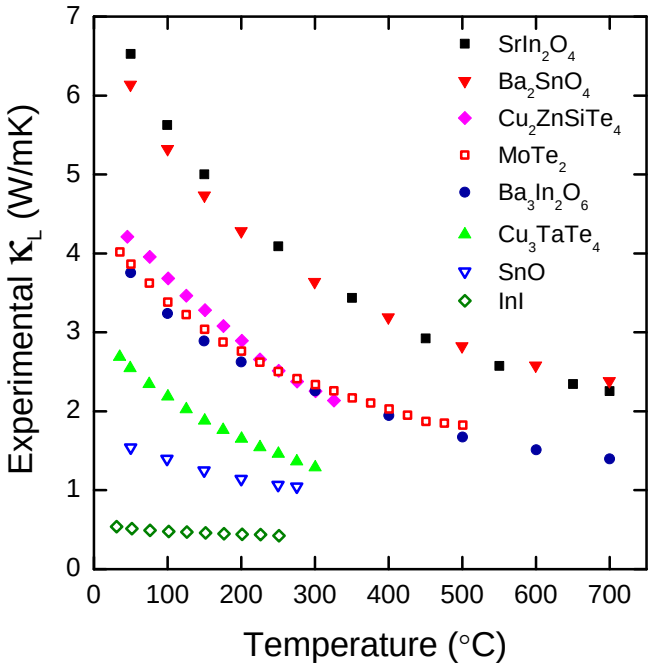

Figure 3.5. Experimental κ_L as a function of temperature for binary to quaternary compounds with various structure types that have not previously been reported in bulk polycrystalline form. Open symbols represent quasi-2D structures while filled symbols are 3D structures.

Compound	Structure type	Measured κ
$Ba_3In_2O_6$	$La_2SrCu_2O_6$	3.76
Ba_2SnO_4	K_2MgF_4	6.13
Cu_3TaTe_4	Cu_3VS_4	2.69
$Cu_2ZnSiTe_4$	Cu_2FeSnS_4	4.21
*InI	TlI	0.54
*$MoTe_2$	MoS_2	4.02
*SnO	PbO	1.54
$SrIn_2O_4$	$CaFe_2O_4$	6.53

Table 3.2. First report of room temperature lattice thermal conductivity for bulk polycrystalline samples with numerous structure types from simple to complex, including both layered materials (indicated with *) and 3D.

first time in Figure 3.5 for bulk, polycrystalline samples. Due to the varying temperature stability of different compounds, the upper temperature limit of the thermal conductivity

Compound	κ_L [W/mK]	Ref.	γ	Ref.	Compound	κ_L [W/mK]	Ref.	γ	Ref.
AgCl	1	[107]	1.9	[103]	InSe	1.8	[108]	1.2	[8]
AlAs	80	[109]	0.66	[110]	γ-$MgAl_2O_4$	24	[110]	1.4	[110]
AlN	285	[111]	0.7	[110]	Mg_2Ge	13	[103]	1.46	[112]
Al_2O_3	35	[113,114]	1.34	[115]	MgO	30	[116]	1.53	[115]
AlP	90	[109]	0.75	[110]	Mg_2Si	8	[103,117]	1.17	[112]
AlSb	56	[110,114]	0.6	[110]	MnO	10	[118]	1.45	[119]
BaO	3	[120]	1.5	[110]	NiO	30	[118]	1.44	[119]
Bi_2O_3	0.8	[121]			PbS	2.9	[110,122]	2	[110]
BP	350	[110]	0.75	[110]	PbSe	4	[123]	1.5	[110]
Bi_2Te_3	1.6	[124]	1.49	[8]	PbTe	2.1	[110,122,125]	1.45	[110]
d-C	1000	[126]	0.75	[110]	Si	130	[110,127]	1.06	[110]
Ca_3AlSb_3	1.6	[128]			SiC (3C)	360	[129]	0.75	[110]
$Ca_5Al_2Sb_6$	1.2	[61]			β-Si_3N_4	155	[110]	0.7	[110]
$Ca_5In_2Sb_6$	1.2	[130]			SiO_2	8	[113]	0.8	[131]
CaO	30	[120]	1.57	[110]	SnO_2	40	[129]		
$CdGeAs_2$	6.86	[132]			SnSe	1.5	[133]		
$CdGeP_2$	11	[134]			SnTe	1.5	[135,136]	2.1	[8]
CdS	16	[110]	0.75	[110]	SrO	12	[110]	1.52	[110]
CdSe	4.4	[110,135]	0.6	[110]	$SrTiO_3$	8.5	[137]		
CdTe	7.5	[110,114]	0.52	[110]	$ZnGeP_2$	18	[134]		
$CuAlO_2$	56	[138]	1.3	[139]	ZnO	50	[110]	0.75	[110]
$CuGaSe_2$	4.2	[140]	1.03	[141]	ZnS	27	[110]	0.75	[110]
Fe_2O_3	11	[142]	1.51	[143]	ZnSb	3.5	[144]	0.76	[145]
GaAs	50	[110,146]	0.75	[110]	ZnSe	33	[103,110]	0.75	[110]
GaN	220	[147]	0.7	[110]	$ZnSiAs_2$	14	[134]		
Ga_2O_3	14	[148]			ZnTe	18	[110]	0.97	[110]
GaP	110	[149]	0.75	[110]	ZrNiSn	17.2	[150]		
InP	68	[110,149]	0.6	[110]					

Table 3.3. Room temperature experimental lattice thermal conductivity (κ_L) and Grüneisen parameter (γ) measurements from the literature used in the improved semi-empirical model.

measurements varies by sample. Additionally, the temperature dependence of the κ_L is consistent with our assumption of Umklapp scattering dominating in this temperature regime.

The resulting comprehensive dataset, which is a combination of the original material dataset, an additional literature search, and in-house experimental measurements, provides a well-rounded dataset and supplements the low κ_L regime. Table 3.3 gives the experimental κ_L values used in the semi-empirical model. All lattice thermal conductivity values used in the semi-empirical model are taken at room temperature (300 K).

3.4. Addition of Structural Parameter for Improving Fit

Using the original model with A_1 and A_2 equal to 2.7×10^{-4} K^{-1} and 1.5×10^{-23} JK^{-1}, respectively, κ_L is predicted fairly well, within half an order of magnitude, as seen in Figure 3.2. There is no difference between the original material dataset, additional literature compounds, and new measurements. They were simply added to supplement and expand the dataset. However, there is a trend that tends to underestimate κ_L for materials with high experimental lattice thermal conductivity and overestimate κ_L for low thermal conductivity materials motivating the addition of a structural parameter for better predictions.

An effort was undertaken to better understand what attributes lead to predictions that deviate significantly from the experimental measurements and whether any material parameters not previously considered in Equation 1.9 should be added to the semi-empirical model. Approximately 40 additional structural and chemical attributes were considered, including space group, Wyckoff multiplicity, elemental mass, atomic number, coordination, and electronegativity, as well as variations on these such as maximum coordination, lightest element relative to the average, maximum minus average atomic number, and standard deviation of electronegativity.

The best version of the previous model was determined by allowing all terms in Equation 1.9 to be fit, producing a baseline AFD of 1.88 as shown in Figure 3.6. This demonstrates the best possible fit achievable with the semi-empirical model previously described, not accounting for data being overfit with too many free parameters. An attribute was added to the model assuming exponential behavior, allowing the exponent to vary from -5 to +5 which is consistent with other terms in the equation. The AFD was minimized to determine the best model with this new attribute included, the first attribute removed and replaced with a second, and the process repeated for all possible attributes. Among all of these possible attributes, coordination number stands out as the most promising addition to reduce the AFD, as seen if Figure 3.6. This demonstrates that among the 37 structural attributes, most would not significantly improve the model if added, but the average coordination number, if introduced into Eq. 1.9, would greatly improve the semi-empirical model accuracy.

It has previously been proposed that the coordination number is related to the Grüneisen parameter;[26,151] the average γ for octahedral coordinated materials is higher than that for tetrahedral compounds, as seen in Figure 3.7. In this dataset, compounds with experimentally measured γ yield values from 0.5 to over 2. Tetrahedrally bonded structures have an average γ of approximately 0.75 whereas octahedrally bonded structures have γ of approximately 1.5. However, in Equation 1.9 the Grüneisen parameter is uniformly incorporated in A_1 to allow for low cost computations, and thus it is a constant for all calculations. This approach contributes significant scatter to the predictions as can be

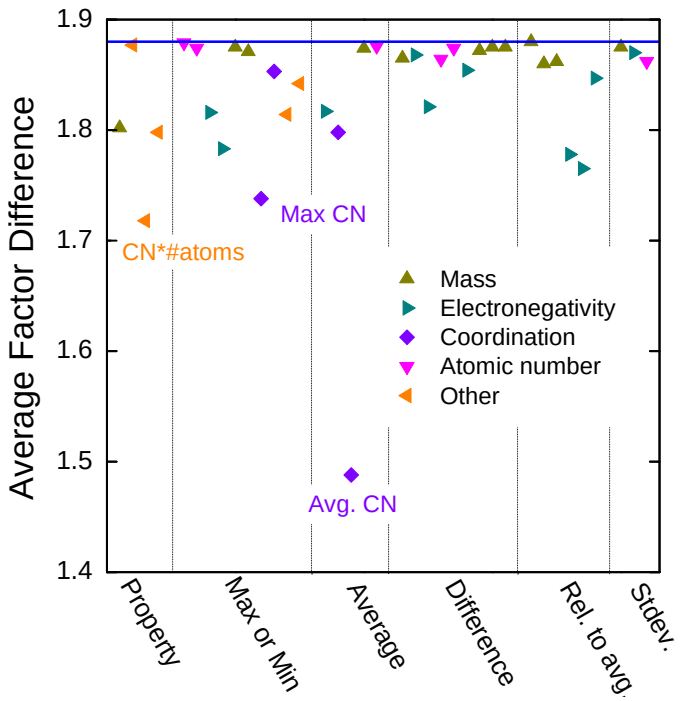

Figure 3.6. The AFD between experimental and modeled κ_L when using additional attributes. A baseline accuracy of 1.88 for the model is shown in blue. When added to the semi-empirical model and allowed to be fit, most attributes do not significantly reduce the AFD, but incorporation of average coordination number (CN) yields notably improved accuracy.

seen in Figure 3.8, which shows the entire κ_L dataset differentiated by average coordination number. Materials with an average coordination of 4 are generally underestimated by the model and those with a coordination of greater than 4 are overestimated.

With the assumption that bonding and local coordination has the largest effect on the Grüneisen parameter, γ can be approximated based on the average coordination number. A functional form for this relationship was chosen such that the estimated γ is lower at small coordination and higher for large coordination as is observed in experimental data:

$$\gamma_{modeled} = \gamma_0(1 - e^{-a(CN - CN_0)}). \tag{3.1}$$

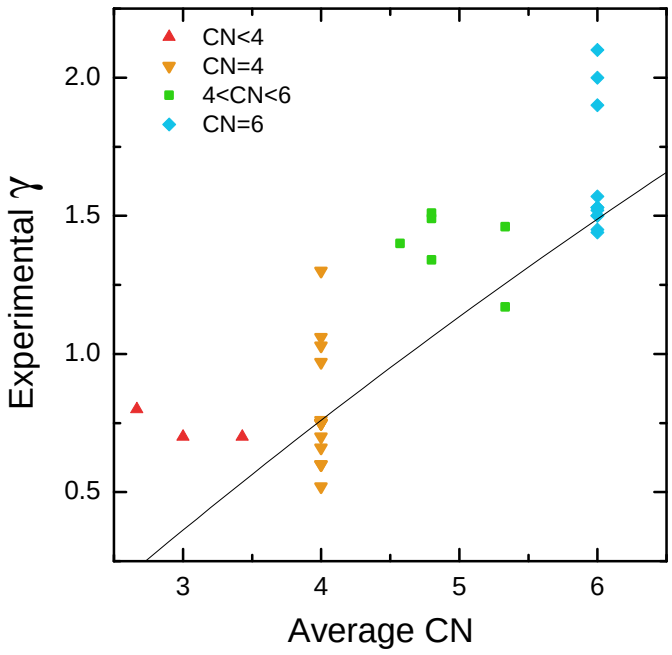

Figure 3.7. The average coordination number is related to the experimental γ. The black line is the equation which best fits the present data, as given in Equation 3.1.

This equation was fit to all experimental γ measurements in this study using the average coordination as previously defined. The parameters, γ_0, a, and CN_0, were refined to minimize the average factor difference between estimated and experimental γ. Due to the large number of experimental measurements at or near 0.75 and 1.5 in the present dataset, the average Grüneisen parameters are 0.76 and 1.53 for tetrahedral and octahedral compounds, respectively. As can be seen by the black line in Figure 3.7, the estimates for γ are close to these averages, though that may not be visibly apparent.

Here the coordination number serves as a simple, computationally inexpensive proxy for the Grüneisen parameter to reduce computational costs; however, we can link coordination and γ from a physical viewpoint. γ is a measure of anharmonicity which arises

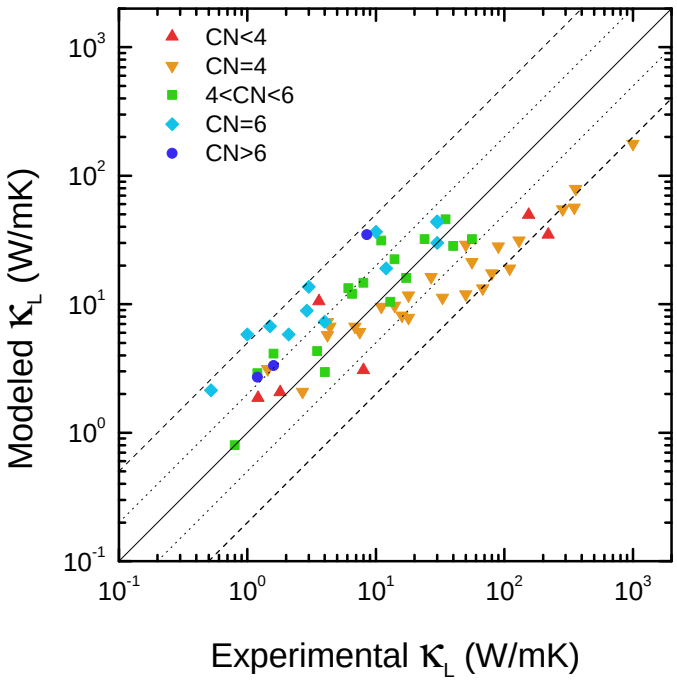

Figure 3.8. Systematic errors in κ_L show a strong correlation with coordination number (color). In general, the thermal conductivity of lower average coordinated materials is underestimated while that of higher coordinated materials is overestimated. A factor of two is shown with a dotted line and half an order of magnitude is shown with a dashed line.

when vibrations of an atom are asymmetric. As Zeier *et al.* argued,[26] these asymmetric vibrations can be found in soft lattices or more open structures that are not as well packed. Compounds with a higher coordination number typically have longer average bond lengths leading to both softer lattices and more space. This trend of higher γ for materials with a higher average coordination is demonstrated in Fig. 3.7, though there are variations due to other more complex factors. Though it has previously been suggested that the electronegativity, bond type, and other attributes influence γ,[152] this study did not find electronegativity or other structural parameters to have a significant impact in reducing the average factor difference in the estimation.

3.5. Refinement of κ_L Model

With the goal of reducing the difference between the experimental and predicted value of κ_L, namely the average factor difference, the semi-empirical model was fit to the existing experimental data. The resulting optimized κ_L model is given by:

$$\kappa_{L,tot} = A_1 \frac{\overline{M} v_s^y}{\gamma^2 V^z n^x} + \frac{3k_b}{2}\left(\frac{\pi}{6}\right)^{1/3} \frac{v_s}{V^z}\left(1 - \frac{1}{n^{2/3}}\right). \tag{3.2}$$

To avoid overfitting of data, the adjusted R^2 was used. The coefficient of determination, R^2, will always increase as the number of explanatory variables increases. However, adjusted R^2 only increases when the addition of another variable improves the model more than would be expected due to random chance. Therefore, the best model is that with the maximum adjusted R^2, which accounts for the number of fitting parameters and samples. While R^2 can range up to a value of 1 indicating the regression perfectly fits the data, $R^2_{adj.}$ will always be less than R^2. To determine which variables to fit in order to optimize the model (Equation 3.2), all terms were held constant while each variable was allowed to vary one at a time. It was found that the free parameter leading to the lowest AFD was A_1. The $R^2_{adj.}$ was determined and a second free parameter was added to the model, allowing both A_1 and the second parameter to vary. This process was repeated until the fifth free parameter led to a decrease in the $R^2_{adj.}$, indicating that four fitted variables, A_1, x, y, and z, lead to the best model without overfitting the data. Allowing the next most important parameter, the exponent on $n_{optical}$, to be a free parameter did not improve the model significantly enough to justify the use of a fifth fitting parameter

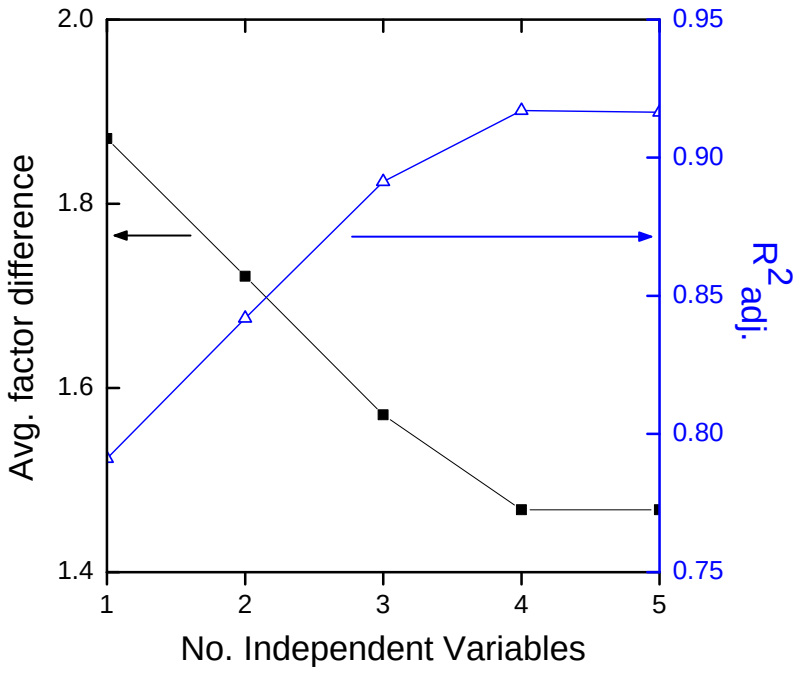

Figure 3.9. The addition of further variables improves the lattice thermal conductivity model as measured by R^2. However, the adjusted R^2 shows the improvements do not warrant additional variables beyond the first four.

according to the $R^2_{adj.}$ criterion. This can be visualized in Figure 3.9, which shows that the four variable model is the optimal choice. The fitting parameters used in the final model are shown in Table 3.4.

The resulting predictions using this model in Figure 3.10 show good agreement between experimental and predicted κ_L, and represent a significant accuracy improvement compared to the original model shown in Figure 3.8. Note that the predicted κ_L values for Figure 3.10 are generated using the "leave one out" method. The new model with four fitting variables was fit to 62 data points and then used to predict the κ_L of the 63^{rd} compound (i.e. the model is fit to all compounds in the study except GaN and then the κ_L of GaN was predicted using this model) and then iterated over the entire dataset.

Variable	Value	Units
γ_0	7.34	N/A
a	0.0586	N/A
CN_0	2.13	N/A
A_1	0.00269	K^{-1}
$(n_{acoustic})^x$	x=1.05	N/A
$(v_{s,acoustic})^y$	y=4.43	N/A
V^z	z=0.334	N/A

Table 3.4. The semi-empirical model for lattice thermal conductivity is based on an evolving set of experimental data and associated calculations and thus the fitted terms are expected to change as the model evolves. For the fits employed within this paper for the complete dataset, the following terms are used when the material parameters are in SI units.

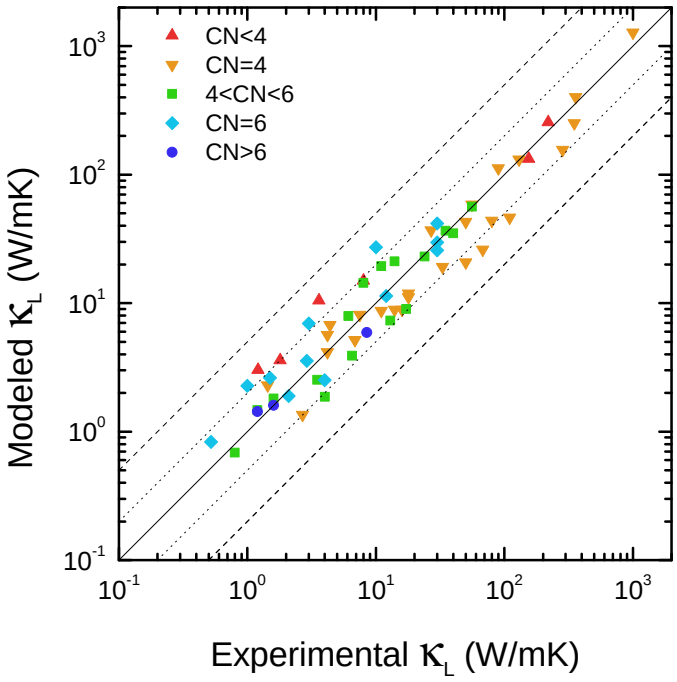

Figure 3.10. The final semi-empirical model of κ_L leads to an average factor difference of only 1.5 from experimental lattice thermal conductivity, a significant improvement achieved through incorporation of a structural parameter.

	AFD	A_1	x	y	z
Test set 1	1.63	0.00217	1.04	4.59	0.356
Test set 2	1.56	0.00202	1.06	4.64	0.357
Test set 3	1.39	0.00196	1.07	4.61	0.329
Test set 4	1.41	0.00230	0.994	4.36	0.340
Average	1.49	0.00225	1.04	4.55	0.345
Reported model	1.48	0.00230	1.03	4.51	0.334

Table 3.5. A summary of the AFD and each of the fitting variables in the cross validation study for each test set as well as the average and the results of fitting the entire dataset.

Furthermore, four-fold cross validation was performed to determine the validity of the semi-empirical model in not just describing but also predicting κ_L. The results are summarized in Table 3.5. Within this dataset, both the leave one out method and cross validation indicate that the model is predictive rather than just descriptive.

The model presented here accurately predicts lattice thermal conductivity across a diverse range of compounds over four orders of magnitude in κ_L. The resulting model has a factor difference of 1.48, a significant improvement over the previous work. While the expansion and diversification of the dataset provided justification for increased fitting parameters according to the adjusted R^2 analysis, the majority of the improvement is driven by the treatment of γ as seen in Fig. 3.6. Here γ was approximated using the average coordination number (Eq. 3.1) and it should be noted that the semi-empirical model simplifies the speed of sound as $v_s \simeq (B/d)^{1/2}$.

For the improved semi-empirical model, the different speed of sound dependence can be explained by the use of a Debye model here whereas the speed of sound actually rolls flat similar to a Born-von Karman model.[8,153,154] Other possible reasons include the presence of velocity or stiffness-dependent scattering or breakdown of the Dulong

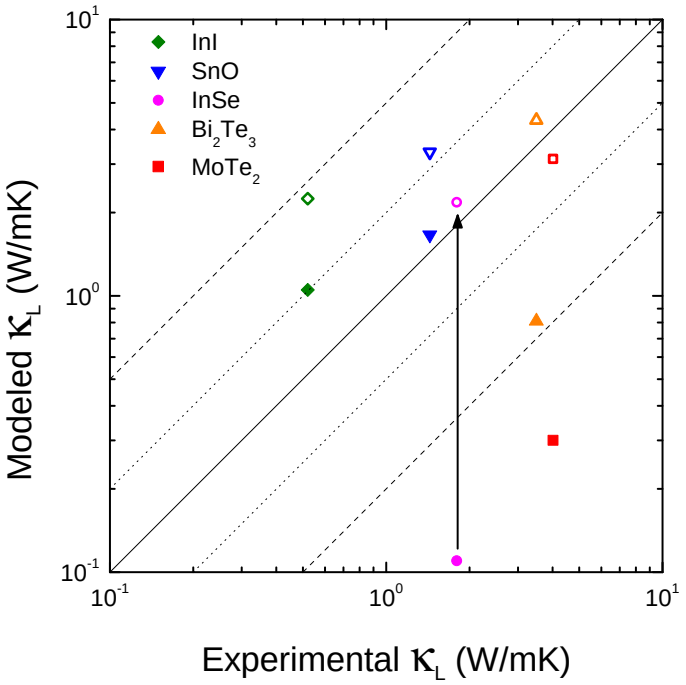

Figure 3.11. Experimental lattice thermal conductivity shown against predicted κ_L with standard functionals (filled symbols) *vs* van der Waals-corrected functionals (open symbols) using the original model from Yan *et al.*. This demonstrates the need for van der Waals-corrected functionals for quasi-2D layered compounds.

Petit approximation. Similarly, although $n^{-2/3}$ is the dependence obtained by Slack for the acoustic branch,[103] the value here is within the bounds of $n^{-1/3}$ and n^{-1} expected for Umklapp and boundary scattering, respectively.[8] Rather than implying boundary scattering, it is likely that the n and V dependence of the improved model indicate a role in scattering strength that is not captured by our simple estimate of the Grüneisen parameter fit.

Note that van der Waals-corrected functionals are necessary to accurately predict the bulk modulus, and thus thermal conductivity, of layered materials. In comparing the predicted and experimental lattice thermal conductivity for these new compounds

and previous literature reports, it was found that there are large differences for some materials. As seen in Figure 3.11, it is necessary to use van der Waals-corrected functionals to accurately compute the bulk modulus and thus lattice thermal conductivity of layered materials.

3.6. Comparison of Refined Model with Previous Efforts

Accurate, low cost, and high-throughput predictions of κ_L are useful for a variety of applications. To highlight the advantages of this semi-empirical model, it is compared to previous high-throughput methods used in the literature. Both Madsen *et al.*[89] and Toher *et al.*[90] employ the quasiharmonic Debye approximation and calculate κ_L according to the equation proposed by Slack.[103] In Ref. 89. they perform full Grüneisen parameter calculations followed by mode-averaging, resulting in fairly accurate but expensive calculations which limits the dataset to only rocksalt, zincblende, and diamond structures (2 atoms per unit cell). In Ref. 90 an alternative approach is taken, screening a much larger set of compounds to rank different classes by order of magnitude. Ref. 90 uses the Mie-Grüneisen equation to calculate γ, requiring just the volume, pressure, number of atoms, and Debye temperature. The result is a much less computationally expensive method that allows a much larger number of calculations to be performed on more complex cells but produces less accurate predictions. Though Refs. 89 and 90 both use the classical exponents on each property, neither consider the $\kappa_{L,opt}$ contribution to the total κ_L.

Due to the use of three different models each using a distinct way of computing the Grüneisen parameter, there is variation in modeled γ for each experimental value, as seen in Figure 3.12. Though this work appears to underestimate γ, the fit used here produces

the minimum possible average factor difference due to numerous γ_{exp} measurements at 0.75 and 1.5 for tetrahedral and octahedral compounds, respectively. Both this work and Ref. 89's mode-averaged γ predictions have strong correlations with experiment (Table 3.7). For both the Pearson and Spearman rank correlation coefficients, a value of 1 shows ideal positive correlation between the experimental. However, these correlation coefficients are only a measure of linear or monotonic relationships between two values and don't account for the offset between experimental and predicted properties and as such, the average factor difference is needed to fully grasp the accuracy of the various models. The inexpensive Mie-Grüneisen method employed by Ref. 90 performs poorly on all metrics, systematically overestimating γ and having a weak correlation with experimental data. The high correlation coefficients and low AFD demonstrate that the simple method presented here is at least as accurate in estimating γ as more computationally expensive high-throughput methods.

Though approximating γ is needed, whether using the quasiharmonic Debye or semi-empirical model, the property of interest is κ_L. To further verify the predictive power of this semi-empirical model and compare it to other models, the same four randomized test sets used for cross validation were compared with other models. Since the training set for the semi-empirical model does not include the test set, this allows for comparison of the AFD between the semi-empirical model and those of Ref. 89 and Ref. 90 within each of the test sets. The results for each of the four test sets are summarized in Table 3.6 which shows that our model performs similarly to the Ref. 89 model and better than the Ref. 90 model within each test set and on average. Additionally, there is no significant variation in the ability of the semi-empirical model to predict κ_L in any given randomized

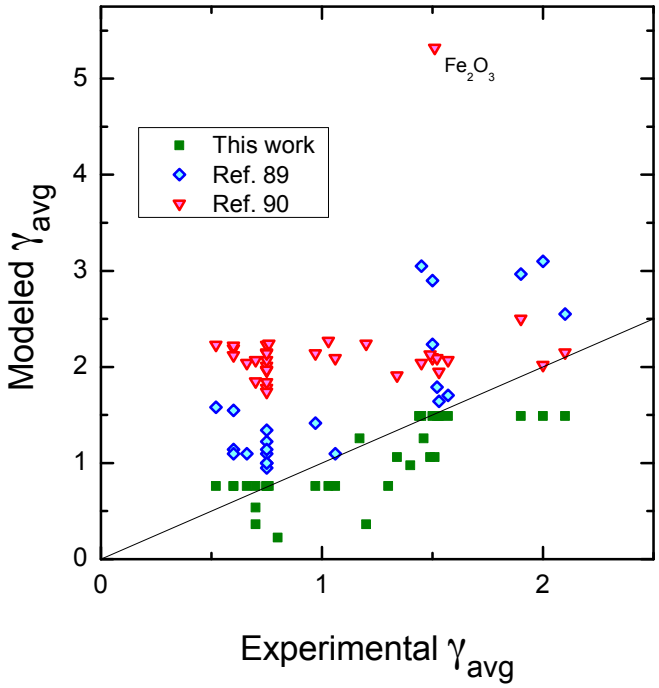

Figure 3.12. Comparison of γ approximations between the semi-empirical model and previous high-throughput efforts. Though simple, the estimation of γ using the coordination number is no less accurate than other high-throughput methods.

set taken from the complete dataset. Also note that the κ_L prediction accuracy is similar for both simple and complex compounds. As summarized in Table 2, the AFD for more complex compounds not considered in other models is 1.51 and 1.52 for the average of the four fold cross validation and the leave one out method, respectively. These are both similar to the 1.48 AFD for the dataset as a whole demonstrating the versatility of this semi-empirical model.

It has been demonstrated through four-fold cross validation that the fitting parameters do not significantly change between the test sets (Table 3.5) and that the predictions for these tests sets compare favorably with other models (Table 3.6). Therefore, κ_L

# compounds	Dataset 1 24		Dataset 2 17		Dataset 3 22
	Ref. 89	SE	Ref. 90	SE	SE
Test set 1	2.03	1.68	3.19	1.55	1.71
Test set 2	1.57	1.52	3.07	1.50	1.61
Test set 3	1.81	1.18	4.08	1.42	1.23
Test set 4	1.53	1.50	3.69	1.42	1.23
Average	1.73	1.47	3.51	1.43	1.51
LOO method	-	1.49	-	1.45	1.52

Table 3.6. Comparison of the average factor difference using four-fold cross validation test sets and the leave one out (LOO) method. Dataset 1 includes the compounds in Ref. 89 and the present semi-empirical (SE) model, Dataset 2 are those in Ref. 90 and the SE model, and Dataset 3 includes those compounds used in the present work but neither Refs. 89 or 90.

predictions are made for a single compound using the leave one out method and compared on a case by case basis with the other models.

The resulting predictions are shown in Figure 3.13 by taking the ratio of predicted to experimental lattice thermal conductivity. Thus predictions of κ_L equal to the experimental value have a value of 1.0 whereas under- and over-estimation by a factor of two are shown as 0.5 and 2.0, respectively. For the compounds considered in all three models (Fig. 3.13a), just Ref. 90 and this work (Fig. 3.13b), and only the present semi-empirical model (Figure 3.14), the compounds are shown in increasing order of experimental thermal conductivity.

As seen in Figure 3.13a and Table 3.7, the semi-empirical model developed herein performs equally well at predicting κ_L. On average, the factor difference between predicted and experimental κ_L for the present model and that used by Ref. 89 is half that of Ref. 90. Similarly, the Pearson and Spearman rank correlation coefficients for these two models are comparable and closer to the ideal value of 1 than that for the Ref. 90 predictions. The

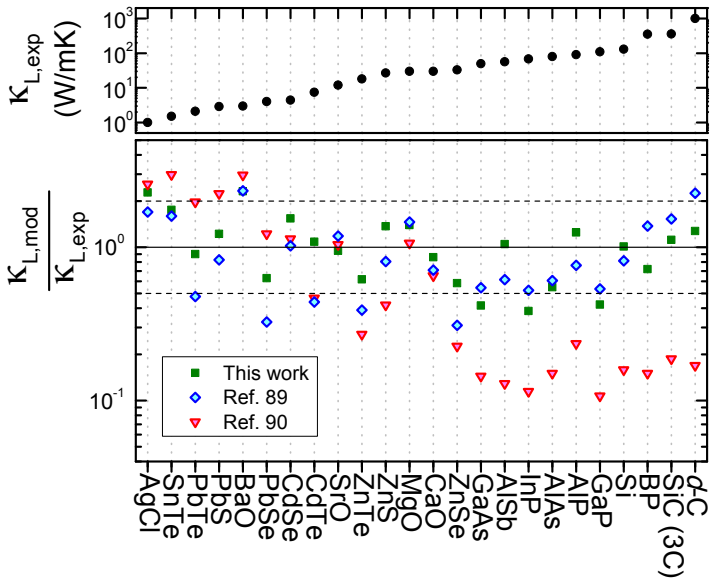

(a)

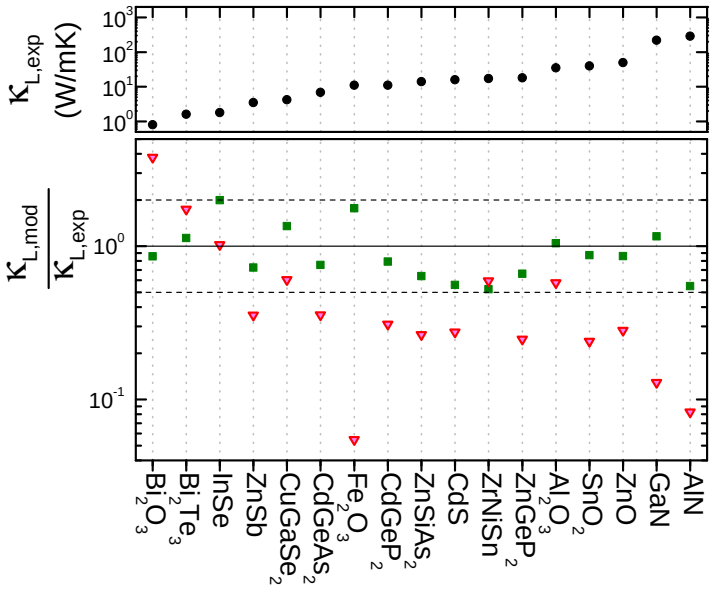

(b)

Figure 3.13. Comparison of predicted κ_L with experimental values finds the method herein combines accuracy with low computational cost. (a) shows those rocksalt, zincblende and diamond structured materials calculated in all models while (b) shows those more complicated structures only handled by the present model and Ref. 79. Horizontal dashed lines show over- and underestimation by a factor of 2 from experimental κ_L.

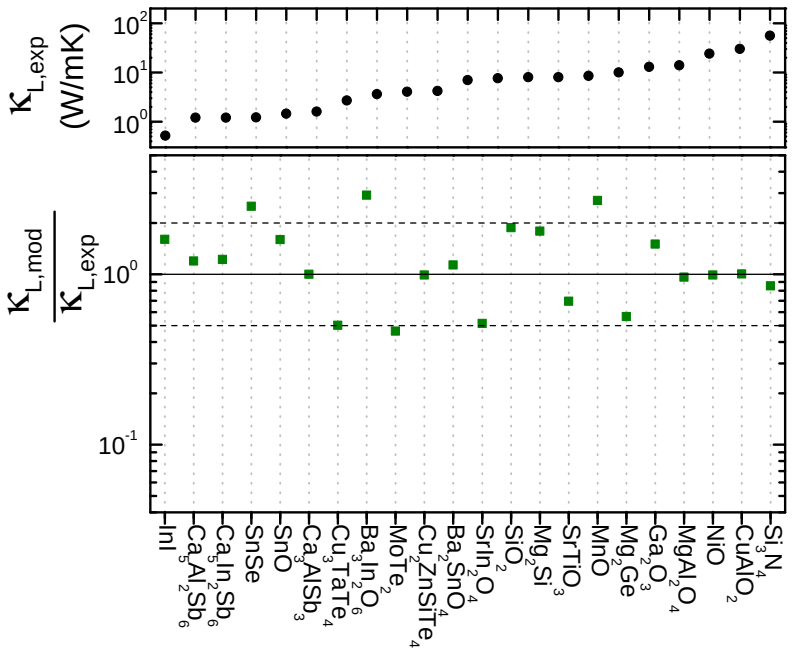

Figure 3.14. Ratio of predicted *vs* experimental lattice thermal conductivity for those compounds only considered in the present study and not in previous efforts. Even for layered compounds, Zintls, and complex oxides, predictions are accurate; most compounds are within a factor of 2 from the experimental measurements, and all within a factor of 3.

κ_L predictions for Ref 89 are accurate for the simple rocksalt, zincblende, and diamond structures but their method is much more computationally expensive (a few orders of magnitude for simple structures and even more costly for complex structures). Ref. 90's method is useful for screening large datasets but overestimates γ and underestimates the lattice thermal conductivity for compounds with experimental $\kappa_L \geq$ 10 $\mathrm{Wm^{-1}K^{-1}}$. A graphical comparison of the accuracy of each of these models on the respective datasets is shown in Figure 3.15.

	This work	Ref. 89	Ref. 90
γ Factor Difference	1.21	1.54	2.17
γ Pearson Correlation	0.815	0.834	0.214
γ Spearman Correlation	0.799	0.654	0.0917
κ_L Factor Difference	1.48	1.71	3.36
κ_L Peason Correlation	0.983	0.983	0.969
κ_L Spearman Correlation	0.953	0.957	0.807

Table 3.7. A summary of the comparison between this work and other previous high-throughput models, for both γ and κ_L. This includes the average factor difference as well as the Pearson and Spearman rank correlation coefficients.

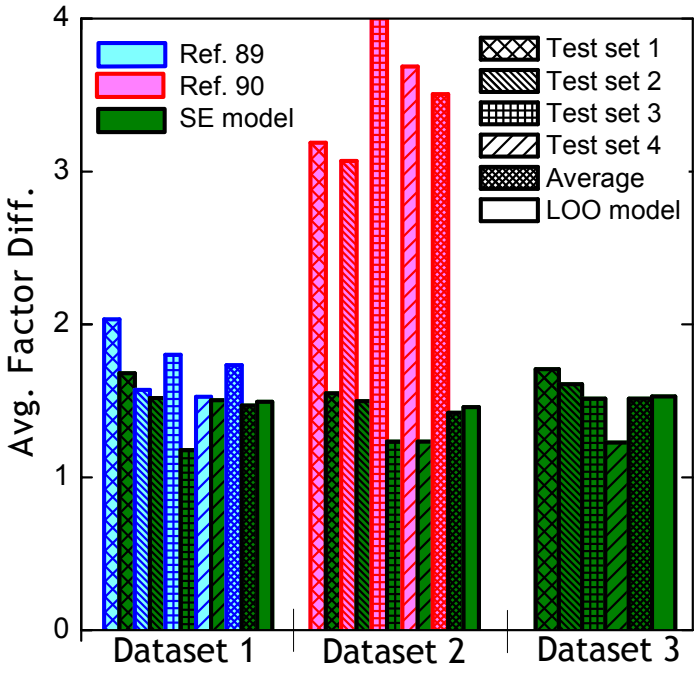

Figure 3.15. Graphical comparison of lattice thermal conductivity average factor difference. Each of three models is represented by a different color, and various hash marks show different cross validation. Here it is easily seen that the SE model performs equally well across simple to complex compounds. For the compounds considered by other models, the SE model is as accurate as an expensive model and much more accurate than an inexpensive model.

3.6.1. Limitations

Given the semi-empirical nature of the model, the predictive power is limited by the data to which the model is fit. Included here are covalent and ionic materials with chemistries ranging from simple elements to complex quaternaries and structural diversity spanning simple crystals (d-C) to complex Zintl phases, cage-like structures, highly anisotropic quasi-2D structures. The current model is applicable to bulk materials but not micro- and nano-structured materials. The model is meant to handle stoichiometric materials so while intermetallic compounds such as half-Heuslers can be handled by the model, κ_L of solid solution alloys such as $Si_{1-x}Ge_x$ cannot be accurately predicted. Small amounts of substituted elements, whether as an alloy or dopant, are not expected to drastically change the κ_L but could affect descriptors used here such as the number of atoms per unit cell. As such, application of our model should be limited to well-defined crystal structures found in databases such as the ICSD, allowing prediction of κ_L of the "parent" material. From these predictions of the stoichiometric compound, alloy scattering models such as that proposed by Klemens[155] or Yang *et al.*[156] can be used for substituted materials.

3.7. Conclusions

Here we 'close the loop' between theory and experiment, yielding a predictive model of thermal conductivity that has an average factor difference of less than 1.5. Beginning with predictions from prior work, the original lattice thermal conductivity material dataset was expanded through the growth and characterization of eight bulk polycrystalline compounds for the first time and incorporation of additional literature results. By growing the dataset to 63 diverse compounds, it was possible to incorporate additional

parameters in the semi-empirical model to account for anharmonicity and the associated phonon-phonon scattering rate. Additionally the model was tested using four fold cross validation and the leave one out method to predict κ_L and compare with other models. The result is a high-throughput, low cost computational method that does not require explicit calculation of the Grüneisen parameter or numerous elastic constants. As the model only requires the bulk modulus to be determined using density functional theory, it is applicable to structurally complex materials. Note that the semi-empirical model works for both layered and 3D materials, though van der Waals functionals must be used for quasi-2D materials to accurately compute the bulk modulus. It should be expected that further refinements of the model will take place when choosing a dataset that is targeted to a specific chemical space.

3.8. Note on Average Factor Difference

The original publication of this paper defined the Average Factor Difference (AFD) with the order of operations being: 1) difference (absolute value difference between experimental and predicted), 2) average, 3) factor (log scale transformation). All analysis in the paper uses this formulation for AFD where the averaging is performed prior to the transformation to a log scale. After further discussion, a more correct formulation would perform the log factor transformation prior to the averaging. It was determined that a submission correction to the journal was not necessary due to the small change in AFD between these two formulations (less than 0.1), rather this will be corrected in the next iteration. All AFD values used in this chapter of my thesis remain the same as those used in the original paper.

CHAPTER 4

SnO as a Potential Oxide Thermoelectric Candidate

This Chapter contains contents reproduced from *Journal of Materials Chemistry C* **5**, 8854-8861 (2017) with permission from the Royal Society of Chemistry.

4.1. Summary of Research

In the search for new thermoelectric materials, high-throughput calculations using a combination of semi-empirical models and first-principles density functional theory present a path to screen large numbers of compounds for the most promising candidates. Using this method, 735 oxide materials were assessed for their thermoelectric performance potential, and SnO was identified as an n-type candidate. Computations indicate a dispersive and doubly degenerate conduction band edge as well as lone pair electrons. Lone pair s-orbital semiconductors have demonstrated unusual properties in their electronic structure and thermal properties, making SnO a material of interest for applications including oxide electronics and thermoelectrics. We report thermal conductivity as low as 0.75 $\mathrm{Wm^{-1}K^{-1}}$ at 525 K for bulk, polycrystalline SnO. The Hall effect and Seebeck coefficient were measured and a high p-type mobility of 30 $\mathrm{cm^2V^{-1}s^{-1}}$ at room temperature for a polycrystalline sample was reported. The stability was computationally assessed, offering insight into the challenges associated with achieving n-type behavior.

4.2. Introduction

Thermoelectric (TE) generators offer a solid-state, clean, and reliable method to harvest energy from waste heat. Traditional thermoelectric materials are predominantly chalcogenides (*e.g.* PbCh, SnCh, Bi_2Ch_3, Sb_2Ch_3, where Ch = S, Se, Te)[51,157,158] and pnictides (*e.g.* $CoSb_3$, $CeFe_4Sb_{12}$, $Yb_{14}MnSb_{11}$, Zn_4Sb_3, Mg_3Sb_2).[32,159–163] However, the elements present in these thermoelectric materials are either toxic (Pb, Sb) or scarce (Te, Bi, Sb) in the earth's crust.[164] In addition, these thermoelectric materials are unstable at higher temperatures or are susceptible to oxidation or sublimation.[165–167] Oxide TEs containing earth-abundant and non-toxic elements are a possible solution to the toxicity and stability issues as oxides are generally stable in oxidizing atmospheres and at high temperatures.[168] However, oxide thermoelectrics with reasonably high zT are rare primarily due to their lower mobilities and larger lattice thermal conductivities compared to chalcogenides and pnictides.

Historically, the search for new thermoelectric materials has been led by empirical approaches using a combination of structure-property relationships, intuition and serendipity.[13] Recent advances in computational approaches have enabled reliable predictions of reciprocal space properties (electrons and phonons)[89,90,169] and accelerated computationally-guided discovery of new thermoelectric materials.[8,43,55,105,170–172] One of the approaches to computationally predicting TE performance is to use a semi-empirical descriptor,[65,76,77] which can be determined from simple first-principles calculations to predict the potential for thermoelectric performance of a material. This approach offers a high-throughput (HT), computationally-tractable way to assess the TE performance of large families of compounds.

In this work, the potential for thermoelectric performance of 735 metal-oxides was assessed using the semi-empirical descriptor β.[76] From this high-throughput search, SnO was identified as a candidate material containing earth-abundant and non-toxic elements based on the predicted value of β. Previous studies of SnO as a functional oxide material include applications as a gas sensor,[173] transparent conducting oxide (TCO),[174] and thin film transistor,[175] indicating the potential use of SnO for oxide electronics. Phase-pure SnO samples were produced to measure the properties. We confirmed experimentally the low lattice thermal conductivity predictions and demonstrated an indirect optical band gap of 0.68 eV. We report the Hall effect and thermoelectric measurements for SnO. Though we were able to dope SnO p-type with two processes to study the thermoelectric properties, n-type doping without significant impurities proved challenging. Computational assessment offered insight into the stability of SnO.

4.3. High-throughput Search

In this work, the quality factor β was calculated for 735 oxides reported in the Inorganic Crystal Structure Database,[62] consisting of s, p, and d block elements. The calculated value of β (only considering those materials with calculated DFT band gaps larger than 10 meV) is shown in Figures 4.1(a) and 4.1(b) as functions of μ_e (intrinsic electron mobility) and μ_h (intrinsic hole mobility) and κ_L, respectively. The data are also available through the open-access database, TEDesignLab (www.tedesignlab.org).[176] The values of β for PbTe, a well-known thermoelectric material, are $\sim$16 for both n- and p-type transport; therefore β for PbTe is used as a reference to gauge the predicted performance of the oxides. The gray markers in Figure 4.1 represent chalcogenides and pnictides. In general,

Compound	**SG**	$\beta(n)$	**Compound**	**SG**	$\beta(p)$
$SiSn_6O_8$	186	23	$HgO^{\S}$	2	26
$PbO^{\S}$	57	16	$LaGaO_3$	62	24
$BaO_2{}^{\ddagger}$	65	15	$Rb_2Co_2O_3$	62	22
$In_2O_3{}^{\ddagger}$	62	12	$Ba_2PbO_4{}^{\S}$	139	19
SnO	129	11	$SrSnO_3$	62	17
$Cd_2SnO_4{}^{\S}$	55	10	$BaPbO_3{}^{\S}$	74	16
$PbHfO_3{}^{\S}$	221	10	$BaO_2{}^{\ddagger}$	65	15
$CdSnO_3{}^{\S}$	62	10	$HfO_2{}^{\ddagger}$	225	13
$SnO_2{}^{\ddagger}$	205	9	$CaGeO_3$	62	13
$PbZrO_3{}^{\S}$	221	9	$SrPbO_3{}^{\S}$	62	12

Table 4.1. Value of n- and p-type β for top ten oxide candidates. SG denotes the space group. Superscript § indicates compound contains toxic elements while ‡ indicates high-pressure or high-temperature phases.

oxides exhibit lower mobility (μ), particularly for holes, and higher lattice thermal conductivity (κ_L) compared to chalcogenides and pnictides. Lower μ and higher κ_L are both undesirable for thermoelectrics, which illustrates the challenge in identifying promising new oxide thermoelectric materials.

Ten n- and p-type oxides with the largest values of β are shown in Table 4.1, the majority of which are either high-pressure or high-temperature phases or contain toxic elements such as Cd, Pb, or Hg. SnO was identified as a n-type candidate oxide containing earth-abundant and non-toxic elements. First-principles calculations indicate that SnO possesses favorable electronic structure and thermal properties for thermoelectrics: (1) dispersive conduction band edge (low effective masses m^*), (2) doubly degenerate conduction band edge, and (3) Sn s lone pairs, which are responsible for anharmonic interactions and consequently, low lattice thermal conductivity.[177] While not identical, the layered structure of SnO (tetragonal) with lone pair electrons is similar to SnS and SnSe (orthorhombic). Both Sn monochalcogenides exhibit good thermoelectric performance as demonstrated in some recent works.[51,157,178]

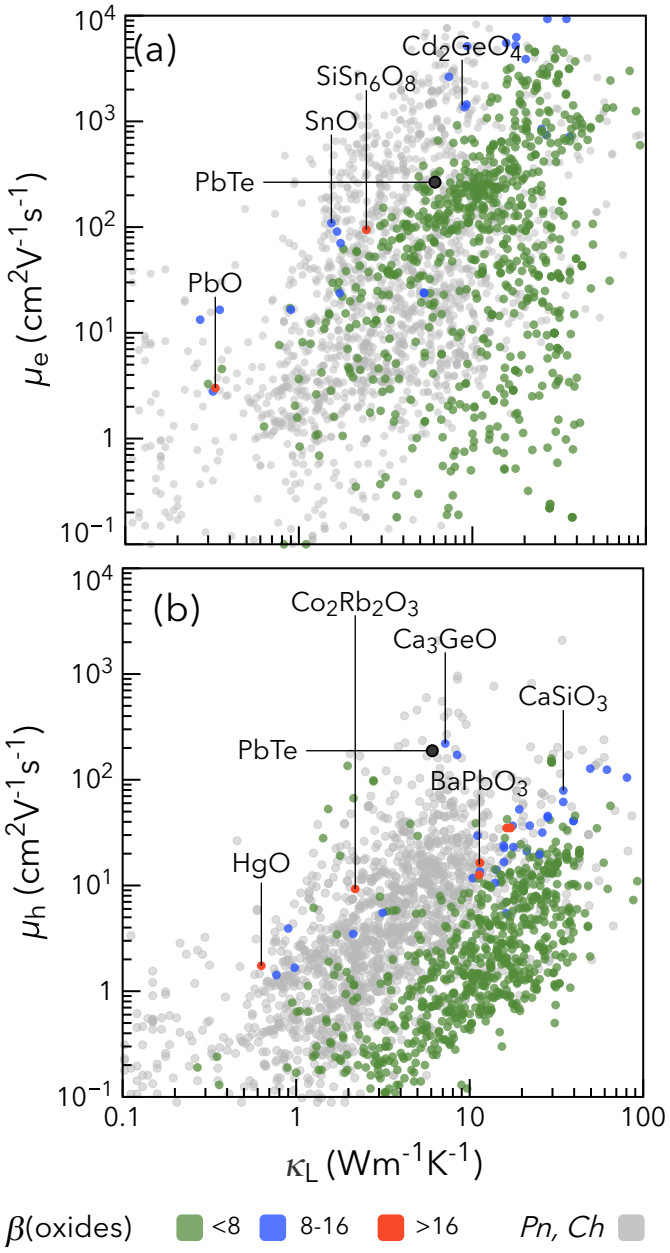

Figure 4.1. Plots of electron (a) and hole (b) mobilities *vs* lattice thermal conductivity (κ_L) in assumed n-type and p-type materials, respectively. Marker color represents calculated value of β for oxides, where β ~8 is $0.5\beta_{PbTe}$ for both p- and n-type transport. Gray markers are all pnictides (Pn) and chalcogenides (Ch) from TEDesignLab. Generally, oxides have lower μ and higher κ_L compared to chalcogenides and pnictides.

4.4. Charge and Phonon Transport Properties

SnO is known to crystallize in three different structures but the structure of interest is the room temperature phase stable in ambient conditions - black SnO (space group 129, $P4/nmm$).[179] The crystal structure of SnO is shown in Figure 4.2, which consists of PbO-like sheets stacked in the c-axis. These sheets are comprised of regular square pyramidal polyhedra capped with tin (II) atoms, arranged in a zig-zag pattern when viewed along the b-axis and a square net when viewed along the c-axis.

Oxides are generally considered poor candidates for thermoelectrics due to the highly ionic bonding, which leads to large band gaps and less dispersive band edges. The latter results in lower charge carrier mobilities compared to traditional thermoelectrics materials that are predominantly chalcogenides and pnictides (Fig. 4.1). SnO exhibits favorable

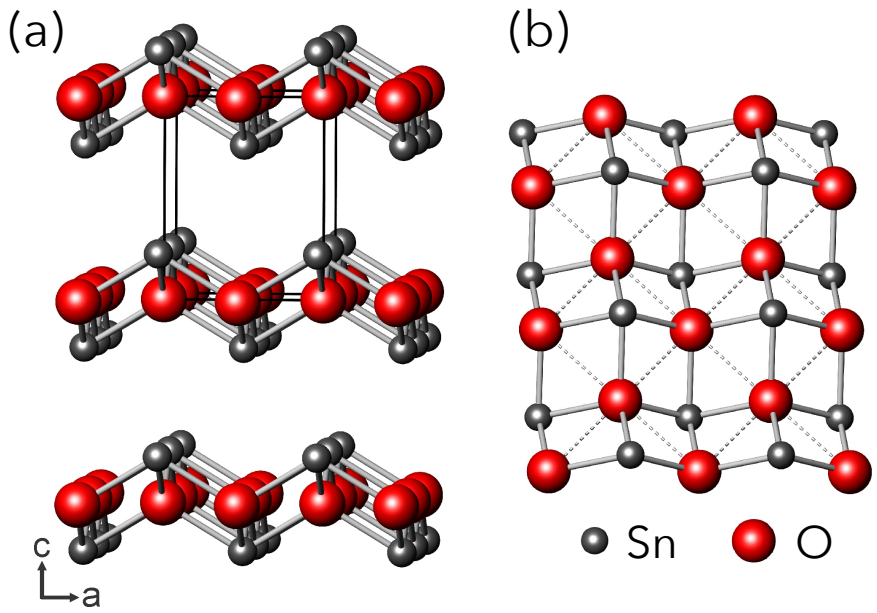

Figure 4.2. (a) The crystal structure of SnO with layers in the a-b plane stacked along the c-axis. (b) The crystal structure viewed along the c-axis

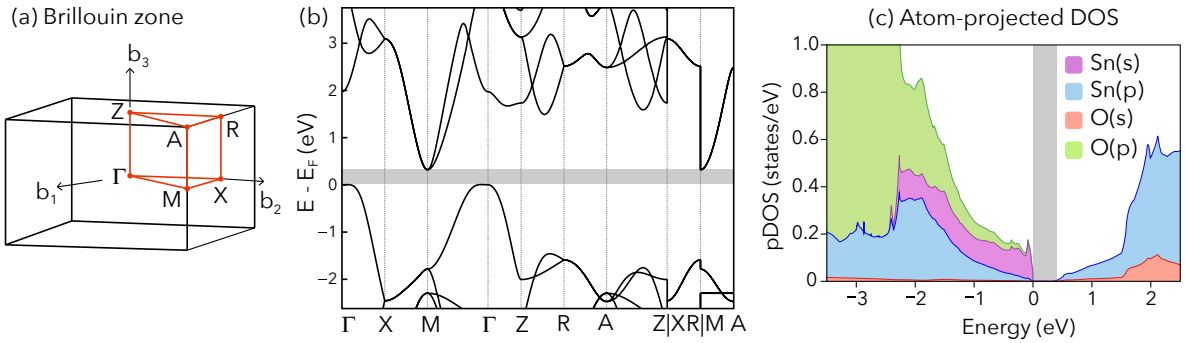

Figure 4.3. (a) Brillouin zone for tetragonal SnO with special k-point paths (b) Calculated band structure along special k-point paths. The shaded region denotes the band gap. The doubly degenerate conduction band edge is dispersive while the valence band edge, which is mainly composed of Sn s lone pairs is flat. (c) The atom-projected density of states (pDOS) shows that the conduction band edge is dominated by Sn p states while the valence band edge is comprised of states derived from O p orbitals and Sn lone pair s electrons.

electronic structure properties as shown in Figure 4.3. Unlike most oxides, SnO has a small band gap (0.68 eV experimental, 0.32 eV calculated) and dispersive band edges. The calculated band structure of SnO (space group 129) in Figure 4.3(b) shows an indirect band gap of 0.32 eV. The highly ionic bonding in oxides also generally leads to large κ_L (Fig. 4.1). However, κ_L has been shown to be low in materials with lone pairs, due to larger phonon anharmonicities,[177] as well as those with layered structures.[180,181] The combination of these leads to a low predicted κ_L of 1.66 $\mathrm{Wm^{-1}K^{-1}}$ at 300 K for SnO using the semi-empirical model.

Due to the layered crystal structure, the electronic structure is expected to be anisotropic in SnO. The conduction band is dispersive in the plane of the layers (along X-Γ-M) as well as out-of-plane (along M-A), with the minima at M doubly degenerate (Figure 4.3b). The overlap of Sn p states leads to an interconnected network (Fig. 4.4(a)) that resides

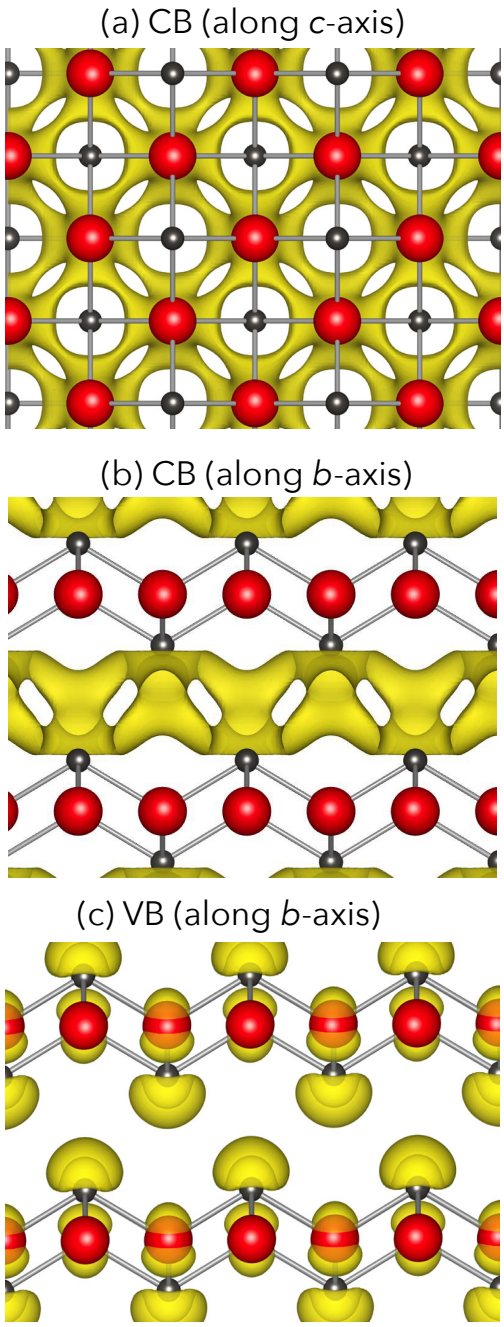

Figure 4.4. Isosurface of charge density within 50 meV from (a) the conduction band minimum viewed along the c-axis, (b) the conduction band minimum viewed along the b-axis, and (c) the valence band maximum viewed along the b-axis.

in the interstitial space between the layers, as seen in Figure 4.4(b). This causes the conduction band to be less anisotropic compared to the valence band. The valence band edge along Γ-M (in-plane) has low dispersion, and the partial charge density of the valence band edge (Figure 4.4c) shows the characteristic "lobes" associated with lone pairs (Sn s). There is no overlap between the lone pairs either in-plane or out-of -plane leading to the observed high effective mass. The dispersive valence band along Γ-Z arises from in-layer overlap between Sn p and O p, as also evidenced by the projected density of states in Figure 4.3(c); the smaller band mass along Γ-Z may allow charge transport in-plane. The high predicted β for n-type SnO (Table 4.1) is the result of a combination of the large carrier mobilities enabled by the dispersive and doubly degenerate conduction band and low lattice thermal conductivity due to the presence of lone pairs and a layered crystal structure.

4.5. Synthesis and Stability

Tin monoxide was synthesized phase-pure (Fig. 4.5) using the solution process method described in the Methods section. Hot pressing the phase-pure powder using the previously described method resulted in samples with a geometric density greater than 85% of the theoretical density. Doping was attempted by substituting Ga for Sn using the solid state reaction (SSR) or In for Sn using the precipitation reaction (PR). In both cases, samples with less than 3 atomic percent dopant (Ga or In) were phase-pure, as observed by XRD, but upon further addition, elemental dopant impurity was observed.

The synthesized SnO was determined to be phase-pure after the precipitation reaction procedure using X-ray diffraction (Fig. 4.5). SnO was stable in air, vacuum, and

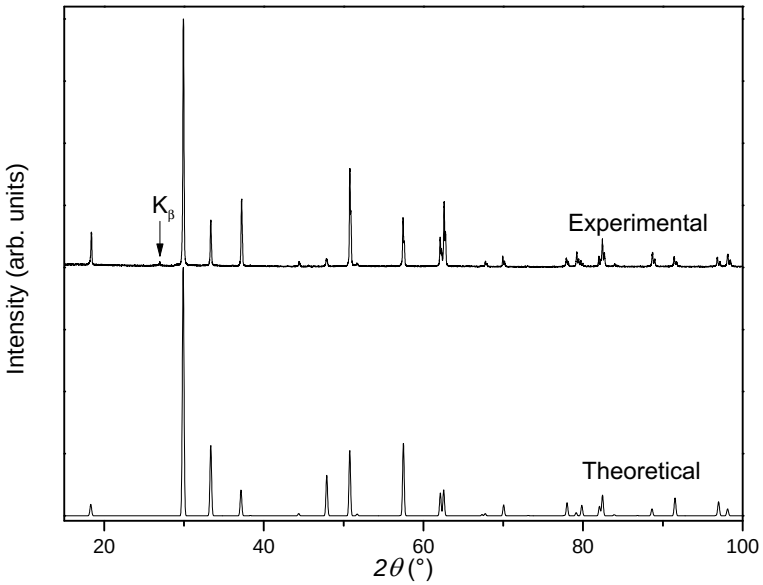

Figure 4.5. The theoretical pattern for SnO (space group 129) as well as the diffraction pattern for phase-pure SnO synthesized using the precipitation reaction synthesis.

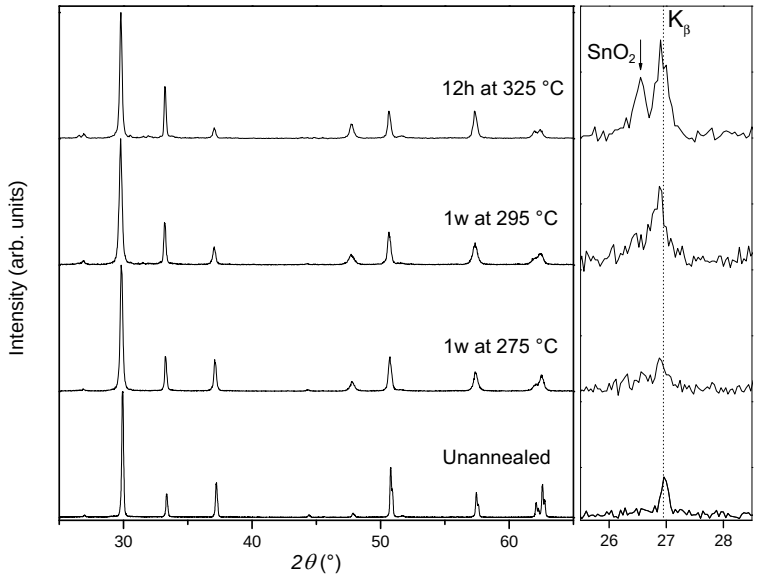

Figure 4.6. The diffraction pattern for the unannealed SnO as well as SnO sealed, evacuated, and then annealed under various conditions. The K_β peak for the main SnO peak is apparent in all diffraction patterns and the main SnO_2 peak is indicated by an asterisk for the 325 °C anneal.

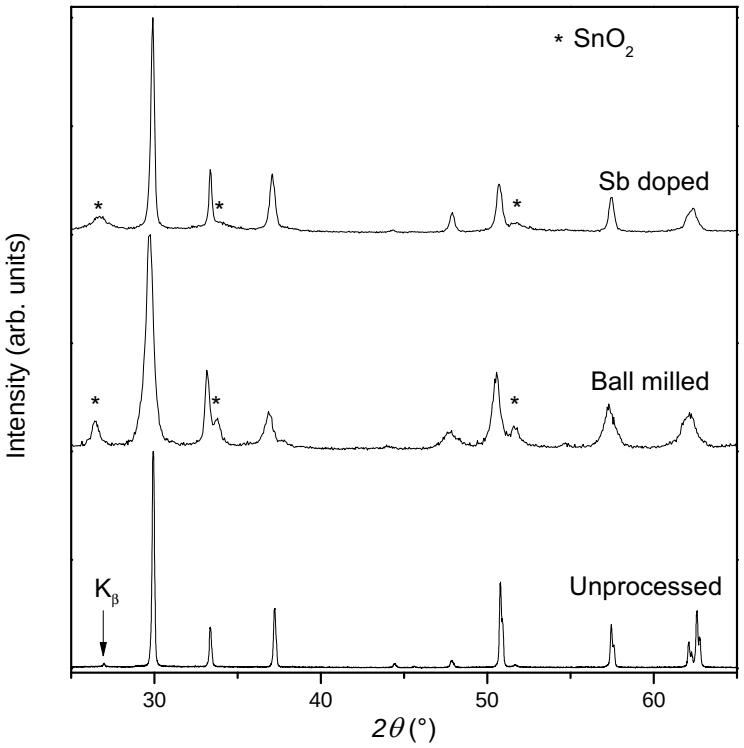

Figure 4.7. The diffraction pattern for the as-synthesized SnO, SnO ball milled for 10 minutes in an argon atmosphere, and SnO doped with Sb during the precipitation reaction. Both the ball milled and Sb doped samples show SnO_2 impurity with the main peaks indicated with an asterisk.

inert atmosphere (argon) up to ∼300°C for one week. However, increasing the annealing temperature to 325 °C caused the decomposition of SnO to begin, as SnO_2 impurities were observed after 12 hours. Figure 4.6 shows the diffraction pattern of unannealed SnO as well as SnO sealed in fused silica tubes evacuated to 10^{-5} mbar and annealed. Additionally, it was found that ball milling for more than a few minutes produced increasing amounts of SnO_2 impurity, as did attempts to dope SnO with Sb (Fig. 4.7). SnO showed no impurities after pressing pellets, and annealing them at 275°C for up to one week did not lead to any further densification.

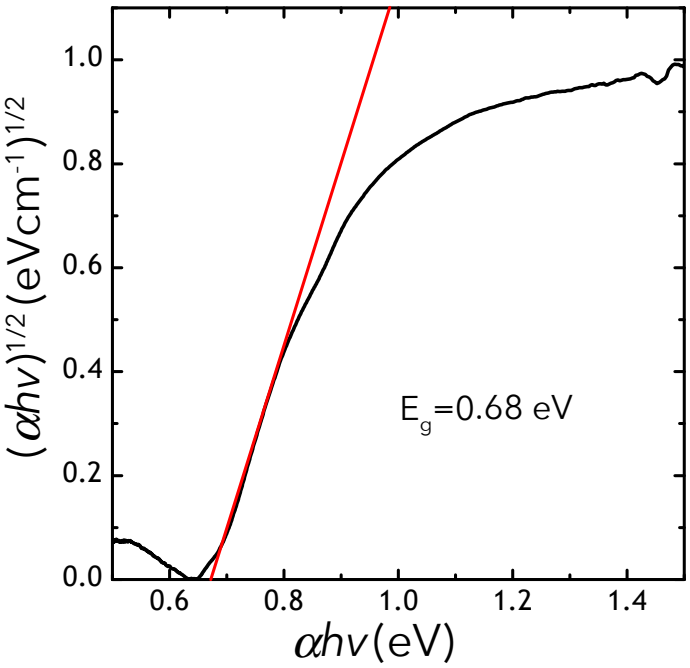

Figure 4.8. The normalized absorption *vs* energy spectra for bulk SnO powder calculated using the Kubelka-Munk method. The indirect gap estimated from diffuse reflectance measurements is approximately 0.68 eV.

4.6. Property Characterization

It has been previously reported that measurements on a SnO thin film show an indirect band gap of ∼0.7 eV and a direct gap of ∼2.7 eV.[182] Diffuse reflectance was measured for bulk SnO powder and the Kubelka-Munk method used to calculate the absorption. The results on bulk SnO powders agree well with the previous DFT and thin film results,[183] as the indirect band gap was determined to be 0.68 eV (Fig. 4.8). The DFT calculated band gap of 0.32 eV is consistent with expectations for DFT to underestimate the band gap.[184]

The electronic transport behavior for undoped SnO is shown as a function of temperature in Figure 4.9. Typical room temperature values for mobility (μ_H) and carrier

concentration (n_H) are approximately 30 $cm^2V^{-1}s^{-1}$ and 1×10^{16} h^+cm^{-3}, respectively. The Hall mobility decreases strongly with temperature suggesting phonon scattering dominates. The relatively high mobility retained in these polycrystalline samples despite porosity and grain boundaries indicates SnO is a good candidate for oxide electronics applications. Previous reports have revealed thermally activated mobility in the room temperature and below range, indicating the possibility of polaron hopping due to the layered crystal structure.[182] However, in the temperature range of these measurements, the temperature dependence of the mobility indicates this is not the case. The carrier concentration behavior as a function of temperature shows thermally activated behavior with a slope that corresponds to a gap of 0.18 eV or a defect state of 0.09 eV.[185] The cause of natural p-type behavior was first believed to be due to tin vacancies.[186] However, defect calculations by Varley *et al.* indicated that hydrogen incorporated during processing would form tin vacancy and hydrogen (V_{Sn}-H) complexes that act as shallow acceptors, 0.07 eV above the valence band maximum.[183] This is similar to our result of an activation energy of ∼0.09 eV from the carrier concentration data, as well as previous reports of defect energy in the range of 90-100 meV.[187]

The thermoelectric properties are shown in Figure 4.10 as a function of temperature for three samples: the undoped SnO, SnO doped with 1 at.% gallium using a solid state reaction (SnO:Ga SSR), and SnO doped with 1 at.% indium during the precipitation reaction (SnO:In PR). The Seebeck coefficient (Fig 4.10 (a)) shows that the gallium and indium are doping the tin monoxide and increasing the p-type behavior as the resistivity drops (Fig 4.10 (b)). The total thermal conductivity is shown in (Fig 4.10 (c)) and agrees well with the prediction of κ_L of 1.66 at 300 K. Due to the low conductivity, the electronic

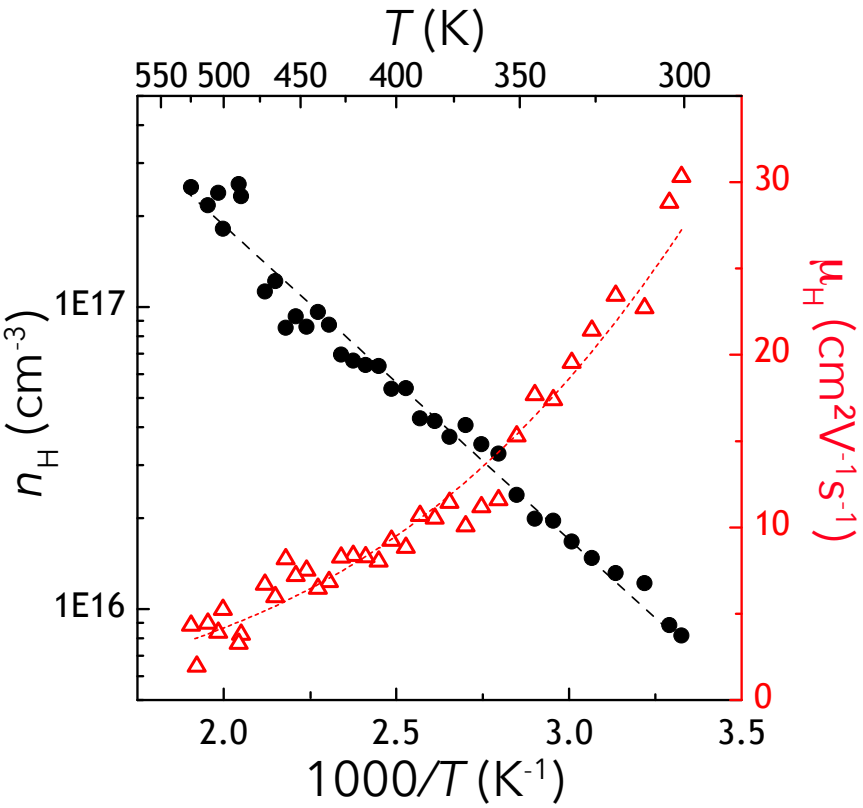

Figure 4.9. Hall data for undoped SnO. The carrier concentration shows thermally activated behavior while the mobility decreases strongly with temperature. Dashed lines provide a guide to the eye.

thermal conductivity is negligible and thus the total thermal conductivity is dominated by the lattice contribution. The lattice thermal conductivity is similar for all samples, though the sample produced by the solid state reaction displays the lowest values. A possible explanation is grain size reduction induced by the ball milling, as this has been shown to decrease thermal conductivity in other systems.[188,189] The zT is shown in Figure 4.10 (d) as a function of temperature. Though the samples doped with Ga and In have somewhat lower thermal conductivity and resistivity, their Seebeck coefficient is significantly lower resulting in a lower zT.

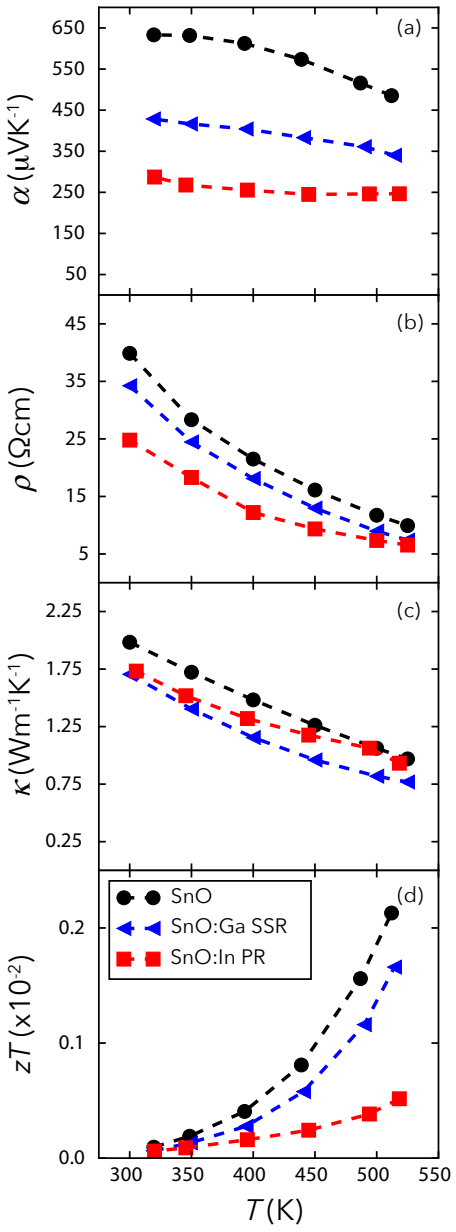

Figure 4.10. (a) The Seebeck coefficient (α) and (b) the resistivity (ρ) are consistent with a thermally activated semiconductor. (c) The total thermal conductivity (κ) is low for an oxide due to the layered structure and decreases with doping due to alloy scattering. (d) The zT decreases with doping due to a sharp drop in the Seebeck coefficient. Dashed lines provide a guide to the eye.

4.7. Dopability and Stability

Although *p*-type doping was achieved using both the solid state and precipitation reactions, better thermoelectric performance is predicted for *n*-type SnO (Table 4.1). Previous reports have indicated that *n*-type doping is possible by the incorporation of >5% antimony in SnO thin films.[187] The native *p*-type self doping of SnO has been attributed to the formation of V_{Sn}-H complexes.[183] For *n*-type doping with Sb to be effective, the substitutional defect (Sb_{Sn}) needs to avoid charge compensation with V_{Sn}-H complexes. Additionally, synthesis must take place in Sn-rich conditions for *n*-type doping since O-rich conditions will facilitate oxidation to SnO_2, as well as the formation of Sn vacancies,[183] resulting in self-compensation that would forbid *n*-type doping.

To realize *n*-type SnO, extrinsic doping with Sb was attempted *via* both solid-state and precipitation reaction routes. Significant impurities in the form of SnO_2 were observed for Sb-doped samples. Although Sb-doped SnO samples have negative Seebeck and Hall coefficients, they contain significant amounts of SnO_2 impurity and thus we cannot confirm if the *n*-type behavior is because of SnO doping or due to the formation of SnO_2, which is natively *n*-type.[190] Synthesis in Sn excess was also attempted but did not produce *n*-type samples. Among the potential halide dopants, Cl was selected due to its size relative to O as well as the low melting temperature of $SnCl_2$ allowing low-temperature processing. Unfortunately, Cl doping of SnO has been unsuccessful in our several attempts but does not rule out the possibility of *n*-type doping of SnO using different deposition and doping procedures and creative chemistry techniques.

The challenges associated with SnO are illustrated in Figure 4.11, which shows the phase stability of the Sn-O binary chemical phase. SnO is in equilibrium with Sn metal

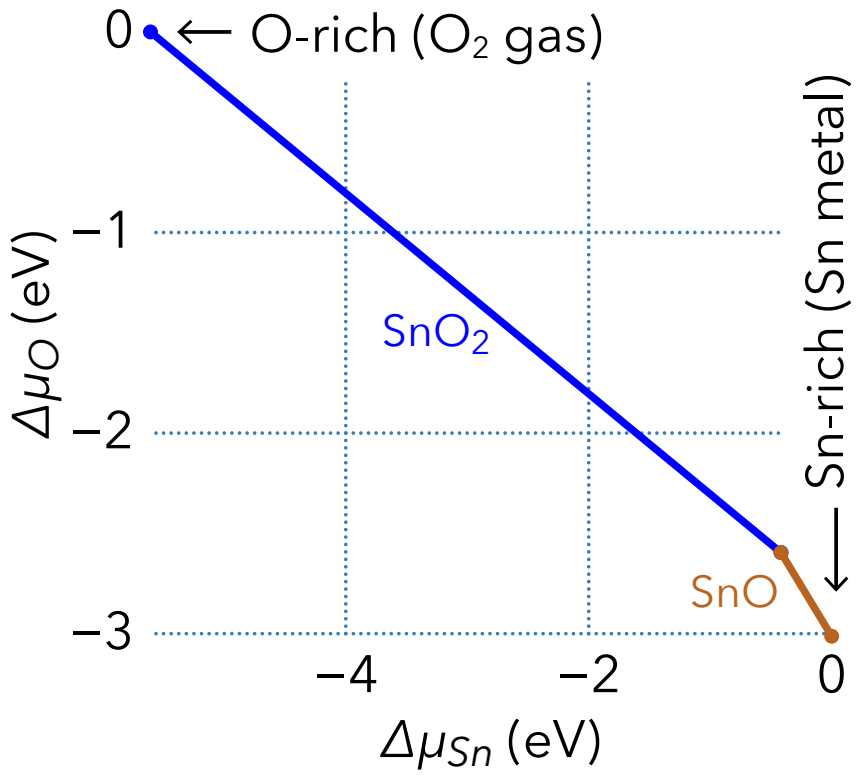

Figure 4.11. Calculated phase diagram of the Sn-O system showing the stability regions of SnO and SnO_2. $\Delta\mu_O$ and $\Delta\mu_{Sn}$ are the chemical potential changes of O and Sn, respectively, from their reference standard states (O_2 gas, Sn metal). $\Delta\mu_O$=0 corresponds to O-rich conditions (equilibrium with O_2 gas) and $\Delta\mu_{Sn}$=0 to Sn-rich conditions (equilibrium with Sn metal). SnO has a narrow region of phase stability and readily oxidizes to SnO_2.

and SnO_2 while SnO_2 is in equilirium with SnO and O_2 gas phase. The range of Sn ($\Delta\mu_{Sn}$) and O ($\Delta\mu_O$) chemical potentials over which SnO is stable is much more narrow compared to SnO_2. Therefore, it is not surprising to find that SnO readily converts to SnO_2 upon heating or ball milling (Fig 4.7). Despite these challenges, we can look to another layered IV-VI semiconductor for insight. While SnSe was reported to have a high p-type zT in single crystal form,[51] first-principles calculations predicted the zT to be even higher for n-type SnSe compared to p-type.[191] Doping SnSe n-type was deemed challenging due to

the strong p-type behavior, yet it was successfully achieved for both polycrystalline[192] and single crystal[193] samples. The limitations of temperature and milling necessitate other processing techniques to realize the potential of SnO as an oxide thermoelectric indicated by predictions. Although achieving phase-pure n-type SnO has been unsuccessful to date, the prediction and subsequent realization of high zT in n-type SnSe, a system similar to SnO, is promising.

4.8. SnO for Oxide Electronics

SnO thin films have been fabricated using a number of techniques but the electrical properties appear to be highly dependent on processing conditions, especially deposition atmosphere and temperature. Hole mobilities of up to 15-25 $cm^2V^{-1}s^{-1}$ at room temperature in thin film form have been previously reported.[194–196] The mobility (30 $cm^2V^{-1}s^{-1}$) reported here is fairly high, especially considering that the sample is bulk, polycrystalline, and not fully dense. This is likely due to the high dispersion along Γ-Z producing a smaller band mass in-plane, as discussed previously. In semiconductors, carrier mobility is a key performance metric[197] and as such, the demonstration of high mobility in oxide materials leads to excitement and investigation for oxide electronic applications. One such possible application for SnO is as a transparent conducting oxide material. While this work reports a high mobility, the carrier concentration is fairly low resulting in a low conductivity. However, defect calculations by Varley *et al.* indicate the possibility to incorporate p-type dopants.[183] This points to the opportunity to realize high p-type mobility bulk samples.

4.9. Conclusions

High-throughput predictions of the semi-empirical metric for thermoelectric performance potential, β, were made for 735 oxide compounds. Tin monoxide was determined as a promising n-type candidate for further work with calculations indicating favorable electronic properties and low thermal conductivity. The thermoelectric properties of bulk, polycrystalline p-type SnO are reported here as a function of temperature. The effect of p-type dopants Ga and In were investigated and led to a reduction in thermal conductivity and resistivity. Efforts to achieve n-type behavior were unsuccessful due to the formation of significant concentrations of SnO_2 during processing. To fully realize the potential of SnO as an oxide thermoelectric, n-type dopants must be incorporated through alternative synthesis techniques. The high p-type mobility demonstrated here offers the possibility of p-type SnO for oxide electronics.

CHAPTER 5

High Thermoelectric Performance of New Rhombohedral Phase of GeSe Stabilized Through Alloying with $AgSbSe_2$

This Chapter contains contents reproduced from *Angewandte Chemie International Edition* **56**, 14113-14118 (2017).

5.1. Summary

GeSe is a IV–VI semiconductor, like the excellent thermoelectric materials PbTe and SnSe. Orthorhombic GeSe has been predicted theoretically to have good thermoelectric performance but is difficult to dope experimentally. Like PbTe, rhombohedral GeTe has a multivalley band structure, which is ideal for thermoelectrics and also promotes the formation of Ge vacancies to provide enough carriers for electrical transport. Herein, we investigate the thermoelectric properties of GeSe alloyed with $AgSbSe_2$, which stabilizes a new rhombohedral structure with higher symmetry that leads to a multivalley Fermi surface and a dramatic increase in carrier concentration. The zT of $GeAg_{0.2}Sb_{0.2}Se_{1.4}$ reaches 0.86 at 710 K, which is 18 times higher than that of pristine GeSe and over four times higher than doped orthorhombic GeSe. Our results open a new avenue towards developing novel thermoelectric materials through crystal phase engineering using a strategy of entropy stabilization of high-symmetry alloys.

5.2. Introduction

Thermoelectric materials, which can directly convert thermal energy to electricity, have been investigated widely as clean and sustainable energy materials.[1,7,198–200] Thermoelectric performance depends on the thermoelectric figure-of-merit $zT = \alpha^2\sigma T/\kappa$, where α is the Seebeck coefficient, σ is the electrical conductivity, T is the absolute temperature, and κ is the total thermal conductivity. Enhancement of zT can be realized through tuning the power factor (PF=$\alpha^2\sigma$) and reducing the thermal conductivity. The power factor can be improved through carrier concentration optimization,[7,201] increasing band degeneracy (tuning crystal structure symmetry[200,202] or band convergence[29,203]) and resonant doping level.[204,205] Thermal conductivity can be reduced by introducing atomic scale point defects,[206] nanostructuring,[158] and all scale hierarchical architecturing.[207] Although Bi_2Te_3 and PbTe based thermoelectric materials exhibit high zT, new thermoelectric materials with earth abundant and less toxic elements are required for largescale applications.[158,208,209]

Recently, SnSe has received extensive attention as a promising thermoelectric material due to its high zT value, which primarily originates from the low thermal conductivity.[51,210–215] GeSe has a similar layered orthorhombic crystal structure ($Pnma$) at room temperature and transforms to cubic ($Fm\overline{3}m$) at 920–930 K.[216,217] Like SnSe and GeSe, GeTe based compounds, including TAGS, are an example of another IV–VI compound that undergoes a high-temperature phase transition (from rhombohedral to cubic) that have been shown to have a high zT over 1.5.[218–222] Density functional theory (DFT) calculations have predicted that, for GeSe doped to the optimal hole carrier concentration of 5×10^{19} cm^{-3}, a zT of 2.5 at 800 K could be achieved, superior to SnSe.[223] However,

the experimental zT for polycrystalline GeSe is only 0.2 at 700 K, primarily due to the low carrier concentration.[224] In principle, the carrier concentration should be tunable by elemental doping, but in practice this has proved challenging. A wide range of elements, including Cu, Ag and Na for p-type as well as Bi, Sb, La, As and I for n-type, have been doped into GeSe, but the maximum carrier concentration reached, 10^{18} cm^{-3} by Ag doping, is still far away from the ideal value from theoretical prediction.[223,224] We herein demonstrate that, by using an alloying strategy, the thermoelectric properties of GeSe-based materials can be dramatically improved. For GeSe, it is found that alloying with $AgSbSe_2$ induces a structural phase transition from the original orthorhombic structure of pristine GeSe to a rhombohedral phase. This transition to a high-symmetry phase, together with the band structure modification, leads to an increase of carrier concentration to 1.2×10^{20} cm^{-3}. As a result, a high power factor of 1105 μWm^{-1}K^{-2} and zT of 0.86 at 710 K for $GeAg_{0.2}Sb_{0.2}Se_{1.4}$ was achieved. This not only confirms GeSe-based materials as promising thermoelectric candidates, but also indicates that the strategy of entropy stabilization of high-symmetry alloys can be exploited as an effective means of improving thermoelectric performance for novel materials.

5.3. Phase Determination

Presented in Fig. 5.1 are the $GeAg_xSb_xSe_{1+2x}$ (x=0, 0.05, 0.1, 0.15, 0.2, 0.3) powder X-ray diffraction (XRD) patterns of at room temperature. Enlarged versions are shown in Fig. 5.2. Pristine GeSe (x=0) shows orthorhombic structure ($Pnma$) at room temperature (a=10.830 Å, b=3.832 Å, c=4.396 Å), which is consistent with previous reports.[224] As x increases to 0.05, the rhombohedral structure ($R3m$) begins to form along with the

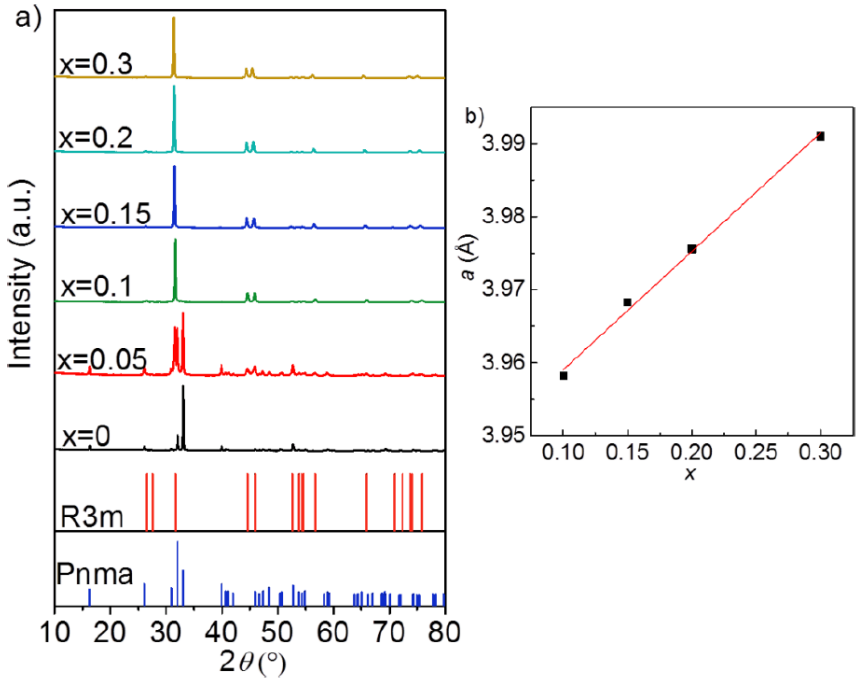

Figure 5.1. a) XRD patterns of $GeAg_xSb_xSe_{1+2x}$ and b) crystal cell parameter ($a = b$) *vs* substitution amount for rhombohedral $GeAg_xSb_xSe_{1+2x}$ (x=0.1, 0.15, 0.2, 0.3).

orthorhombic phase. At x=0.1, the structure is fully rhombohedral with a hexagonal unit cell given as a=b=3.958 Å, and c=10.081 Å. This rhombohedral phase, which can be regarded as the cubic rock salt structure stretched diagonally,[218] is not present in either the GeSe or $AgSbSe_2$ end members.[225,226] Similar to high entropy alloying, where the addition of extra species in the alloy leads to the formation of a high-symmetry phase due to the increased entropy,[227–230] the entropy of GeSe is enhanced after alloying with $AgSbSe_2$, which leads to formation of the rhombohedral phase with a higher-symmetry structure. Interestingly, substituting GeSe with Ag alone increases the carrier concentration but does not cause a phase change, while substituting Sb alone causes a partial phase change at high Sb content (Fig. 5.3).

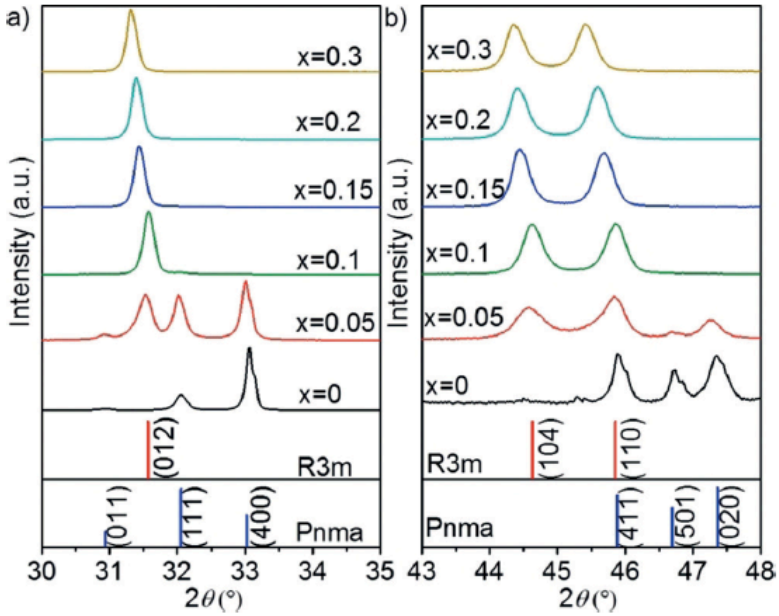

Figure 5.2. Enlarged powder XRD patterns of $GeAg_xSb_xSe_{1+2x}$ (x=0, 0.05, 0.1, 0.15, 0.2, 0.3) samples a) from 30°to 35°and b) from 43°to 48°.

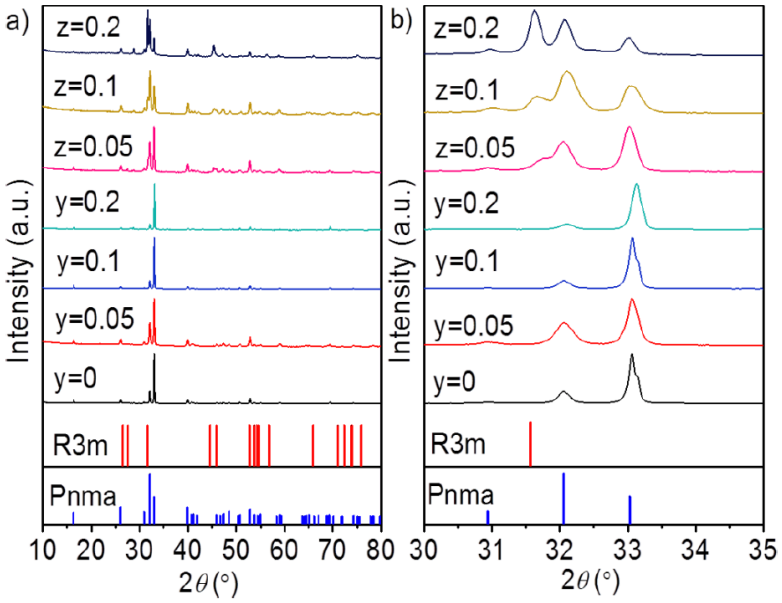

Figure 5.3. a) Full XRD patterns and b) enlarged XRD patterns of Ag doped GeSe ($GeAg_ySe_{1+y}$) and Sb doped GeSe ($GeSb_zSe_{1+z}$) samples (y, z=0, 0.05, 0.1, 0.2).

5.4. Phase Transition

The phase evolution of GeSe in the transition from low to high symmetry is schematically shown in Fig. 5.4a. At high temperature, the structure of GeSe is the symmetric cubic rocksalt but the low temperature phase is an orthorhombic structure that is highly distorted from cubic. This distortion leads to changes in the distance between Ge and Se atoms and a reduction of 6 equidistant neighbors to only three. The change in bond length leads to a bilayer structure forming, with a van der Waals gap between the layers. In contrast, the rhombohedral structure is only a slight distortion from cubic, giving the appearance of opposite cube corners being stretched out. The rhombohedral structure that forms when GeSe is alloyed with $AgSbSe_2$ is only a slight distortion of the Se sublattice relative to that of Ge. This leads to bonding more similar to the symmetric cubic structure rather than the distorted orthorhombic structure. High-angle annular darkfield (HAADF) images (Fig. 5.4b,c) and selected area electron diffraction (SAED) patterns (Fig. 5.4d,e) further confirm the orthorhombic phase for pristine GeSe and rhombohedral phase for $GeAg_{0.2}Sb_{0.2}Se_{1.4}$, which corroborates the peak identification from XRD results. When x>0.1, the main peak at 2θ=31.5° shifts towards smaller angles with increasing content of Ag and Sb, indicating the substitution of Ag and Sb leads to lattice expansion. The refined crystal cell parameters of $GeAg_xSb_xSe_{1+2x}$ ($x\geq$0.1) are presented in Fig. 5.1b. The cell parameter increases linearly with substitution, obeying Vegard's law, which is to be expected when Ag^{1+} and Sb^{3+} substitute for the smaller Ge^{2+}.

For pristine GeSe, the crystal structure changes directly from orthorhombic ($Pnma$) to cubic ($Fm\bar{3}m$) at 920 – 930 K.[216,217] However, for the $AgSbSe_2$ alloyed samples, not only does the more symmetric rhombohedral phase form at room temperature for $x\geq$0.1, it

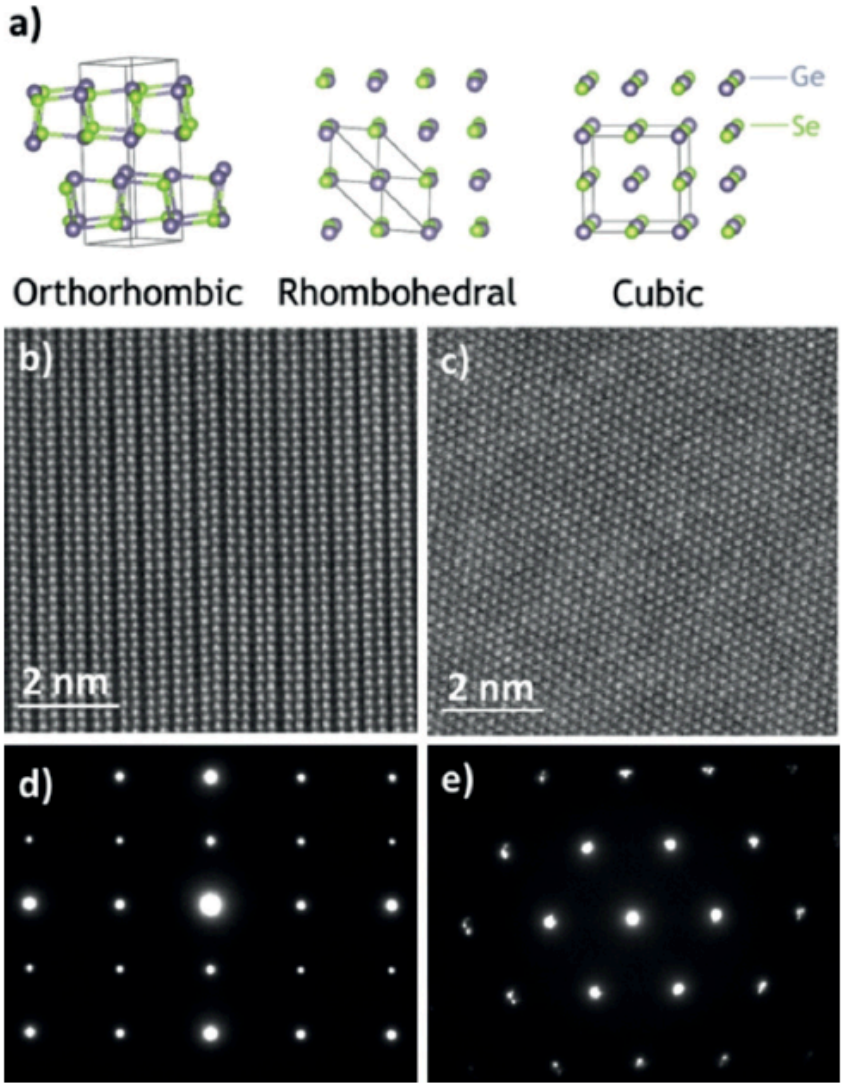

Figure 5.4. a) Schematic of orthorhombic, rhombohedral, and cubic crystal structures of GeSe. HAADF images of b) pristine GeSe and c) $GeAg_{0.2}Sb_{0.2}Se_{1.4}$ projected in the [001] direction. SAED patterns of d) GeSe and e) $GeAg_{0.2}Sb_{0.2}Se_{1.4}$.

leads to a transformation to the cubic phase at a lower temperature (523 K as opposed to 930 K). This can be seen in Fig. 5.5, which shows the XRD pattern as a function of temperature for $GeAg_{0.2}Sb_{0.2}Se_{1.4}$, where the double peaks between 2θ=43-47° move closer.

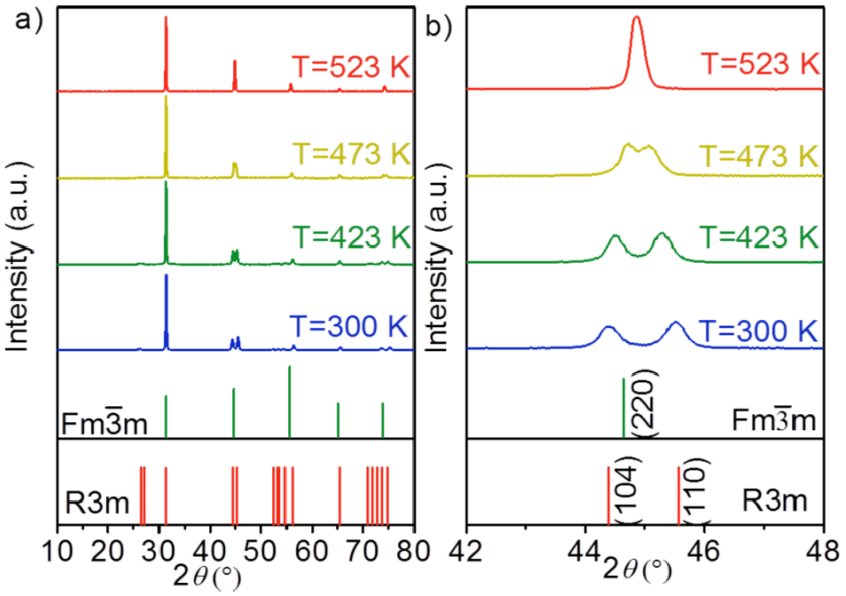

Figure 5.5. a) Temperature-dependent XRD patterns of $GeAg_{0.2}Sb_{0.2}Se_{1.4}$ and b) enlarged XRD patterns from 42°to 48°.

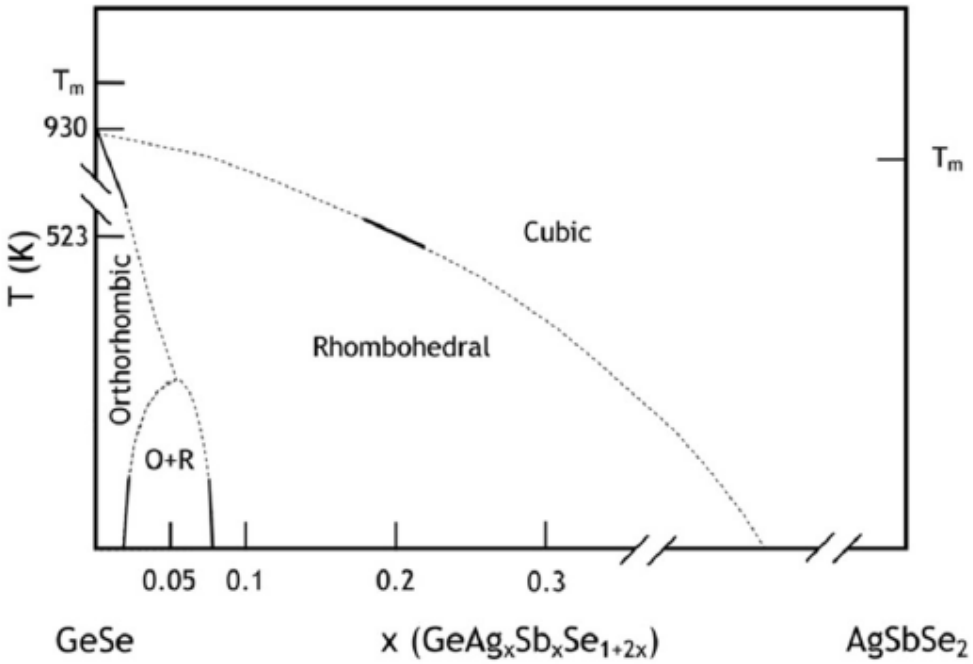

Figure 5.6. Sketch of possible phase diagram for GeSe alloyed with $AgSbSe_2$; lines are inexact.

This indicates that as the temperature increases, the cubic nature of $GeAg_xSb_xSe_{1+2x}$ also increases. This observation is similar to the doping effect of Ag-Sb in GeTe, where the transition temperature from rhombohedral to cubic decreases from 700 K to 510 K by Ag and Sb co-doping.[231,232] A schematic representation of the possible phase space in the GeSe-$AgSbSe_2$ system is shown in Fig. 5.6. More data is needed to determine exact positions of phase boundaries but this demonstrates the relative locations of the orthorhombic, rhombohedral, and cubic phases.

5.5. Electronic Structure and Properties

The band structure calculated by DFT for GeSe in the rhombohedral phase is shown in Fig. 5.7a, which has a band gap of 0.46 eV, compared to a DFT gap of 0.85 eV for orthorhombic GeSe and an experimental band gap of 1.1 eV.[223,233,234] For rhombohedral GeSe, the band structure is quite similar to that of rhombohedral GeTe, a good thermoelectric material (TAGS).[218–222] Rhombohedral GeTe exhibits high carrier concentration due to intrinsic Ge vacancies.[235–237] The formation energy of Ge vacancies in rhombohedral GeTe is low meaning Ge vacancies can form easily.[236,237] A similar phenomenon in rhombohedral GeSe may be expected due to the similar crystal structure, band structure, and bonding nature. The Fermi surface for rhombohedral GeSe (Fig. 5.7c) is much more complex than that for orthorhombic GeSe,[223] showing two sets of threefold symmetric sigma pockets that arise between Γ and P. Rhombohedral GeSe has more pockets contributing to conduction compared to orthorhombic GeSe,[223,227,228] with the multiple bands for rhombohedral GeSe leading to a higher effective mass than orthorhombic GeSe. The calculated effective mass of rhombohedral GeSe is 1.8 m_e compared to 0.75 m_e for

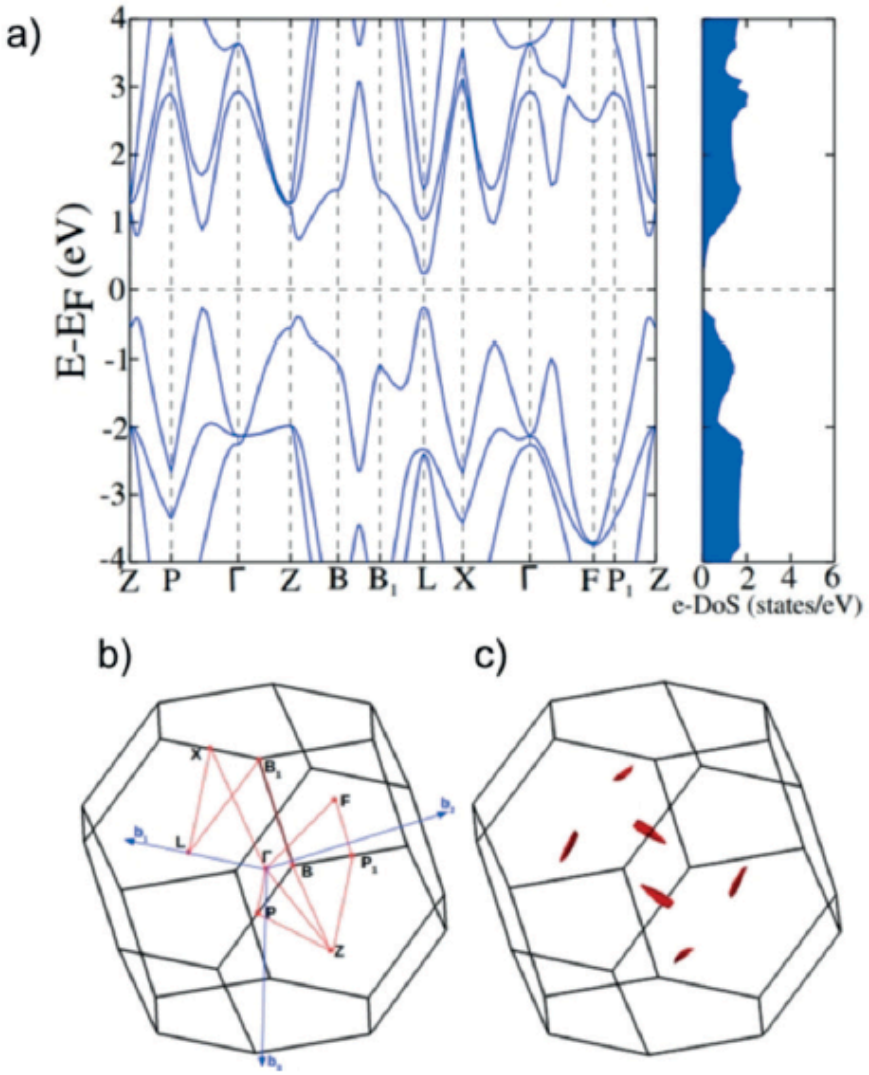

Figure 5.7. a) Calculated electronic band structure and density of states, b) Brillouin zone with high symmetry points, and c) Fermi surface at 2×10^{20} cm^{-3} for rhombohedral GeSe.

orthorhombic GeSe.[224] The contribution of more conduction pockets and the higher effective mass enhances the thermoelectric performance of GeSe in higher-symmetry structures compared to the orthorhombic phase.[29,223,229]

Pristine GeSe has a high Seebeck coefficient typical of a lightly doped p-type semiconductor (Fig. 5.8). The Seebeck coefficient peak corresponds to a Goldsmid-Sharp gap of 0.85 eV, in reasonable agreement with previous measurements and DFT calculations. With the co-substitution of Ag and Sb, the Seebeck coefficient drops dramatically for x=0.05 followed by an increase in S with increasing x. The room temperature carrier concentration for pristine GeSe is quite low, less than 10^{17} cm^{-3}, consistent with previous reports.[224] In GeSe, with $x \geq 0.1$, the room-temperature carrier concentration is quite high even though co-substitution of Ag^{1+} and Sb^{3+} should offset donor and acceptor effects. This value of 10^{20} cm^{-3} is similar to rhombohedral GeTe, where intrinsic Ge vacancies lead to a large number of acceptors, and is evidenced by the reduced Seebeck coefficient. In the single phase rhombohedral region ($x \geq 0.1$), the carrier concentration decreases with increasing x. In addition to the carrier concentration dropping with increased alloying, the mobility decreases significantly in this single phase region, leading to a drop in the conductivity as GeSe is further alloyed with $AgSbSe_2$ in the rhombohedral phase region (Fig. 5.8b).

Doping with silver alone increases the carrier concentration, and thus conductivity, while simultaneously decreasing the Seebeck coefficient, consistent with substitution of Ag^{1+} for Ge^{2+} (Fig. 5.9). The substitution of Ag for Ge in GeSe results in similar carrier concentration, 10^{18} cm^{-3}, and Seebeck coefficient as previous work.[224] Doping with Sb increases the p-type carrier concentration, which is contradictory to expectation for Sb^{3+} substitution on Ge^{2+} sites to be an electron donor.[220] The substitution of Sb^{3+} induces a partial phase transition (Fig. 5.3), with $GeSb_zSe_{1+z}$ samples exhibiting a mixed structure of orthorhombic and rhombohedral phases. The existence of the rhombohedral

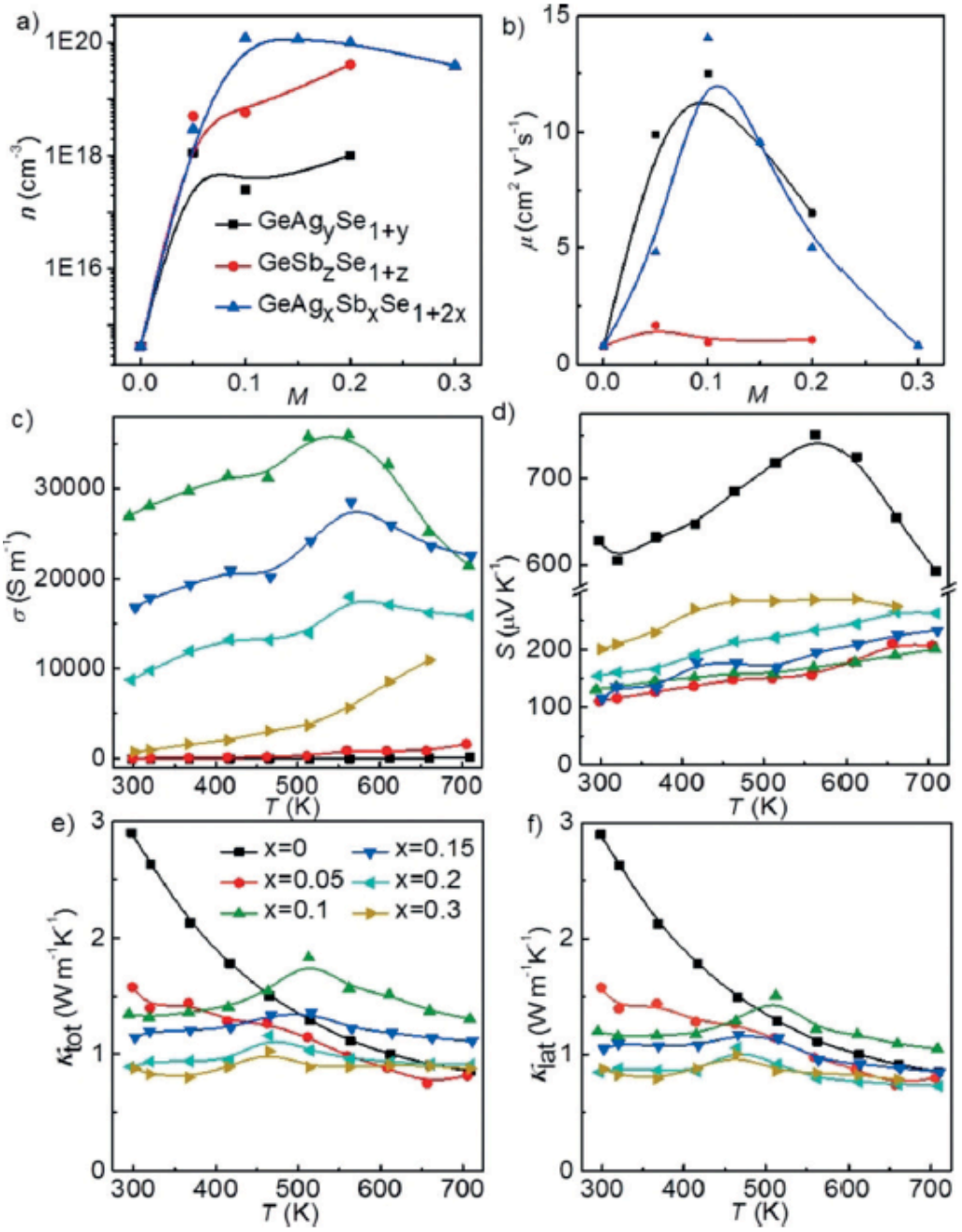

Figure 5.8. a) Hall carrier concentration, and b) mobility versus the substitution values (M) of x, y, z in $GeAg_xSb_xSe_{1+2x}$, $GeSb_ySe_{1+y}$, and $GeAg_zSe_{1+z}$ samples. Temperature-dependent c) electrical conductivity, d) Seebeck coefficient, e) total thermal conductivity, and f) lattice thermal conductivity of $GeAg_xSb_xSe_{1+2x}$ (x=0, 0.05, 0.1, 0.15, 0.2, 0.3) samples.

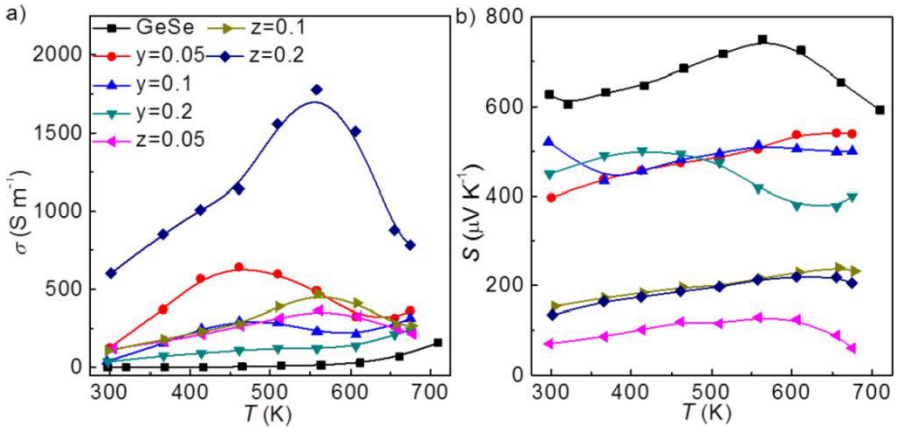

Figure 5.9. Temperature-dependent a) electrical conductivity and b) Seebeck coefficient of $GeAg_ySe_{1+y}$, and $GeSb_zSe_{1+z}$ samples.

phase, which may have abundant intrinsic Ge vacancies, therefore increases the *p*-type carrier concentration of $GeSb_zSe_{1+z}$ samples. The presence of a secondary phase also explains the low mobility in Sb doped samples. Only by alloying GeSe with $AgSbSe_2$ to form $GeAg_xSb_xSe_{1+2x}$ does the complete transformation of orthorhombic to rhombohedral GeSe occur, with the accompanying high carrier concentration and high mobility.

The total thermal conductivity (κ_{tot}) of $GeAg_xSb_xSe_{1+2x}$ as a function of temperature is shown in Fig. 5.8e. The lattice thermal conductivity (κ_L) was calculated by subtracting the electronic thermal conductivity (κ_{e}) (Fig. 5.10) from κ_{tot}. Though κ_{tot} varies between samples, the total thermal conductivity is dominated by the lattice contribution. The κ_L of pristine GeSe is 2.9 $\text{Wm}^{-1}\text{K}^{-1}$ at 300 K and decreases to 0.85 $\text{Wm}^{-1}\text{K}^{-1}$ at 710 K. Our results for pristine GeSe are similar to but slightly higher than previous experimental reports for lattice thermal conductivity of orthorhombic GeSe (1.8 to 0.6 $\text{Wm}^{-1}\text{K}^{-1}$).[224] The heat capacity and diffusivity are shown in Fig. 5.11. Like the lattice thermal conductivity, the diffusivity for pristine GeSe exhibits a strong temperature

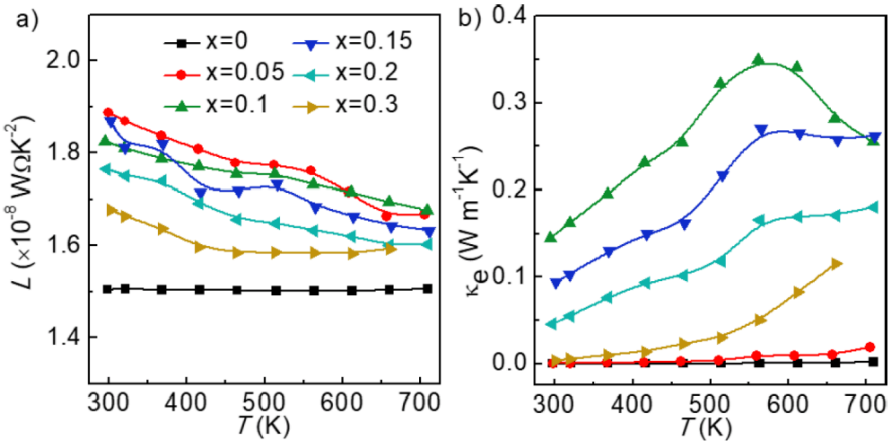

Figure 5.10. Temperature-dependent a) Lorenz number and b) electronic thermal conductivity of $GeAg_xSb_xSe_{1+2x}$ samples.

dependent behavior, which is typical for crystals, while the temperature dependence of the rhombohedral samples is quite flat like a glass. The heat capacity has a baseline that agrees reasonably well with the Dulong–Petit approximation (dashed line in Fig. 5.11a). For the x≥0.1 samples, there is a peak in the heat capacity, corresponding to the phase transition from rhombohedral to cubic, which decreases in temperature with increasing x, in agreement with the possible phase diagram presented in Fig. 5.6. The phase transition leads to the bumps of (κ_L) and (κ_{tot}) for rhombohedral $GeAg_xSb_xSe_{1+2x}$ samples in Fig. 5.8e,f. In the rhombohedral phase samples, both the mobility and lattice thermal conductivity decrease with increasing substitution of $AgSbSe_2$. A possible explanation for this is impurity or point defect scattering due to alloying. The lattice thermal conductivity for polycrystalline GeSe samples is fairly low; however the theoretical prediction for the thermal conductivity of GeSe is nearly two times lower than the experimental values found here and by others,[224] which accounts for most of the difference in maximum zT between predictions and experiments.[223]

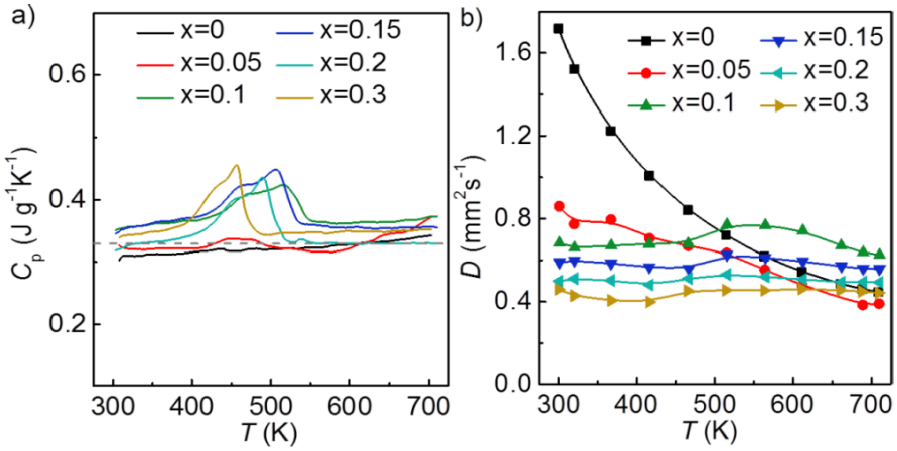

Figure 5.11. a) Heat capacity of $GeAg_xSb_xSe_{1+2x}$. Gray dashed line represents the Dulong-Petit approximation of 0.33 Jg^{-1}K^{-1} for GeSe. b) Thermal diffusivity for $GeAg_xSb_xSe_{1+2x}$ samples.

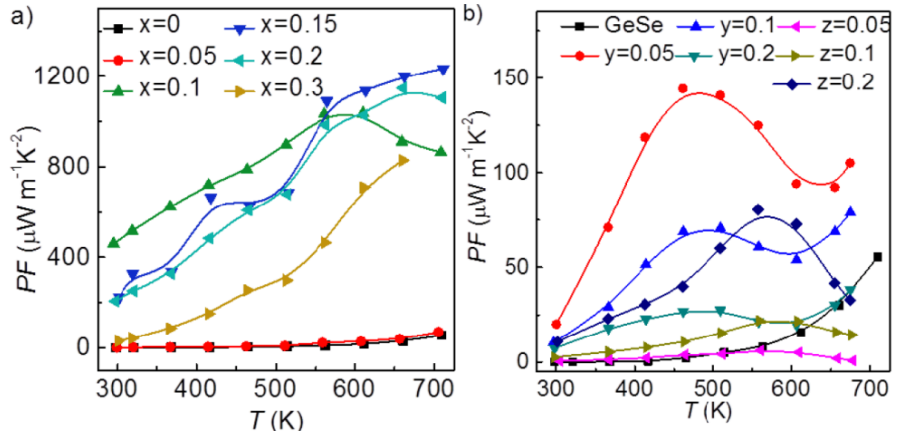

Figure 5.12. a) Power factor of $GeAg_xSb_xSe_{1+2x}$ samples and b) power factor of $GeAg_ySe_{1+y}$ and $GeSb_zSe_{1+z}$ samples.

Alloying GeSe with $AgSbSe_2$ dramatically improves the power factor, from a maximum of 56 μWm^{-1}K^{-2} at 710 K for pristine orthorhombic GeSe to 1233 μWm^{-1}K^{-2} at 710 K for $GeAg_{0.15}Sb_{0.15}Se_{1.3}$, significantly higher than the power factor for any of the single element doped samples (Fig. 5.12). This is due to a combination of the increase in the carrier concentration as well as the increase in degeneracy for the rhombohedral phase

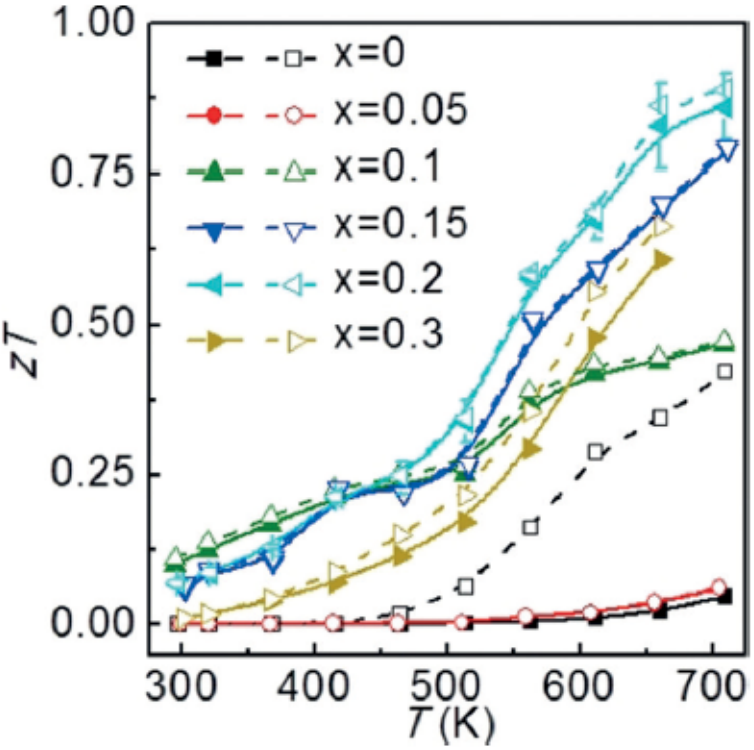

Figure 5.13. Temperature-dependent experimental zT (filled symbols and solid lines) and maximum possible zT from the weighted mobility modelling (open symbols and dashed lines) for $GeAg_xSb_xSe_{1+2x}$ (x=0, 0.05, 0.1, 0.15, 0.2, 0.3) samples.

as compared to the orthorhombic phase. The improvement of the power factor, coupled with a decrease in the lattice thermal conductivity, leads to a maximum zT of 0.86 for $GeAg_{0.2}Sb_{0.2}Se_{1.4}$ at 710 K (Fig. 5.13). This zT value (0.86) is 18 times larger than that of pristine GeSe (0.046) and more than four times higher than the previous reports for GeSe.[224] The high zT of $GeAg_{0.2}Sb_{0.2}Se_{1.4}$ shows thermal stability as shown in Fig. 5.14.

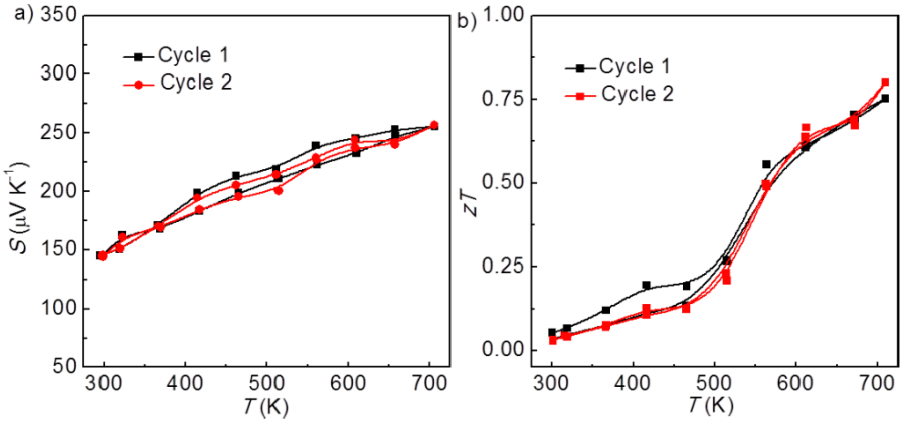

Figure 5.14. Two-cycle heating-cooling a) Seebeck coefficients and b) zT versus T of $GeAg_{0.2}Sb_{0.2}Se_{1.4}$.

5.6. Optimization of GeSe

An effective mass model can be used as a tool to optimize the thermoelectric efficiency.[18] Using transport measurements, the intrinsic material properties can be determined and combined to calculate β and thus the optimum zT. The effective mass of orthorhombic Ag doped GeSe has previously been reported as ~1.0 m_e at 700 K,[224] consistent with our calculation of ~0.75 m_e for $GeAg_ySe_{1+y}$ at room temperature. For the x=0.1 sample, the effective mass and mobility parameter are determined as 1.8 m_e, and 21 $cm^2V^{-1}s^{-1}$, respectively, in the rhombohedral phase at room temperature. Using an effective mass of 1.8 m_e, a Pisarenko plot (Fig. 5.15a) shows the rhombohedral phase samples are well fit by this model. However, without Hall data as a function of temperature, the effective mass and mobility parameter cannot be determined at high temperatures, so instead the weighted mobility is used to determine the quality factor β. Fig. 5.15b shows the maximal zT as a function of Seebeck coefficient at various temperatures for the x=0.1 sample, the first fully rhombohedral sample. This demonstrates that the stabilization

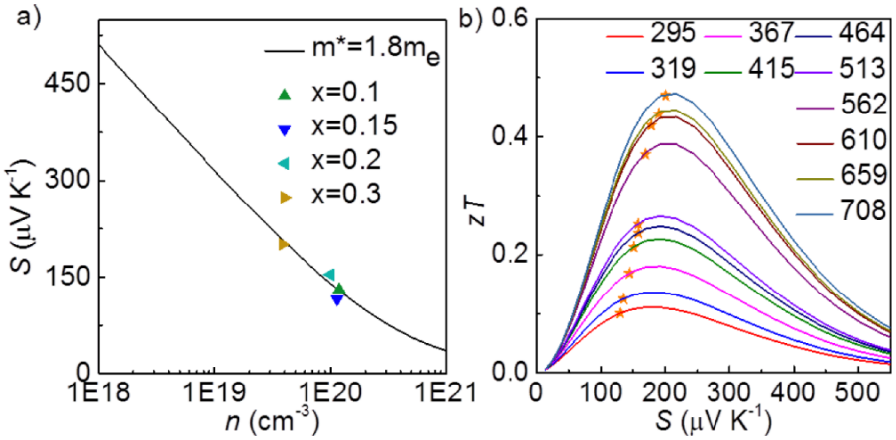

Figure 5.15. a) Pisarenko plot for rhombohedral GeSe showing fit with an effective mass of 1.8 m_e at 300 K and b) zT *vs* Seebeck coefficient for $GeAg_{0.1}Sb_{0.1}Se_{1.2}$. Orange stars represent experimental Seebeck coefficient at each temperature, showing experimental Seebeck coefficient is slightly too low (and thus carrier concentration is too high), though very near the maximum. The legend is temperature in Kelvin.

of the high-symmetry rhombohedral phase allows a carrier concentration very near the optimum. This is the case for all of the rhombohedral samples, which have carrier concentration slightly above the optimum, giving an experimental zT just below the maximum, as shown in Fig. 5.13. This is in contrast with the pristine orthorhombic GeSe sample, which shows a maximum zT significantly higher than the experimental measurement due to the difficulty in doping to a higher carrier concentration, in agreement with previous work.[224]

5.7. Conclusions

Although orthorhombic GeSe has been predicted to have a high zT based on DFT calculations, this has not been experimentally realized due to the difficulty in carrier concentration tuning. By alloying GeSe with $AgSbSe_2$, a new rhombohedral phase is

stabilized at room temperature, an example of entropy stabilization of a high symmetry alloy. This rhombohedral phase is not fully stabilized by substituting either Ag or Sb alone and is not present in either of the end members GeSe or $AgSbSe_2$. Likely due to Ge vacancies, the rhombohedral phase of GeSe has a high carrier concentration, similar to rhombohedral GeTe. An effective mass model is used to show that the carrier concentration for rhombohedral samples is very near the optimum. Combined with this high carrier concentration, the rhombohedral phase, due to the higher symmetry compared to orthorhombic, has a Fermi surface conducive to high thermoelectric performance. This is realized as zT=0.86 for $GeAg_{0.2}Sb_{0.2}Se_{1.4}$ at 710 K owing to the high carrier concentration and low lattice thermal conductivity.

CHAPTER 6

Polycrystalline $ZrTe_5$ Parameterized as a Narrow Band Gap Semiconductor for Thermoelectric Performance

6.1. Summary of Research

Transition metal pentatellurides $HfTe_5$ and $ZrTe_5$ have been studied for their exotic transport properties with much debate over the transport mechanism, band gap, and cause of the resistivity behavior, including a large low-temperature resistivity peak. Single crystals grown by the chemical vapor transport method have shown a n-p transition of the Seebeck coefficient at the same temperature as a peak in the resistivity. We show that behavior similar to that of single crystals can be observed in iodine doped polycrystalline samples, but that undoped polycrystalline samples exhibit drastically different properties; they are p-type over the entire temperature range. Additionally, the thermal conductivity for polycrystalline samples is much lower, 1.5 $Wm^{-1}K^{-1}$, than previously reported for single crystals. It is found that the polycrystalline $ZrTe_5$ system can be modeled as a simple semiconductor with conduction and valence bands both contributing to transport, separated by a band gap of 20 meV. This model demonstrates to first order that a simple two-band model can explain the transition from n to p-type behavior and the cause of the anomalous resistivity peak. Combined with the experimental data, the two-band

model shows that carrier concentration variation is responsible for differences in behavior between samples. Using the two-band model, the thermoelectric performance at different doping levels is predicted, finding $zT = 0.2$ and 0.1 for p and n-type, respectively, at 300 K, and $zT = 0.23$ and 0.32 for p and n-type at 600 K. Given the reasonably high zT that is comparable in magnitude for both n and p-type, a thermoelectric device with a single compound used for both legs is feasible.

6.2. Introduction

Thermoelectric (TE) materials are those that convert a temperature gradient to a voltage or an electrical current flow into a heat flow, with applications in power generation and Peltier cooling. This thermoelectric conversion of heat energy into electrical energy, the Seebeck effect, has been well studied, with compounds optimized for use in various temperature ranges and applications. Mid- and high-temperature thermoelectrics have been well investigated, including PbTe, SiGe, and Zintl compounds.[13,238–241] However, there is a dearth of materials for applications at lower temperatures. To date, TE materials for cooling applications fall into one of three families, $Bi_{1-x}Sb_x$,[242,243] $CsBi_4Te_6$,[244,245] or $(Bi,Sb)_2(Te,Se)_3$.[246,247] Furthermore, construction of thermoelectric generators requires thermal and chemical stability and matching between n and p legs of the device.[248] Recently, there has been interest in the use of layered transition metal pentatellurides for low temperature thermoelectric applications. $ZrTe_5$ and $HfTe_5$ have demonstrated high power factors, though the thermal conductivity is relatively high.[249,250] Measurement on needle-like single crystals showed the thermal conductivity to be in the ∼4-8 $Wm^{-1}K^{-1}$ range at room temperature.[251] In contrast, recent calculations indicated that the lattice

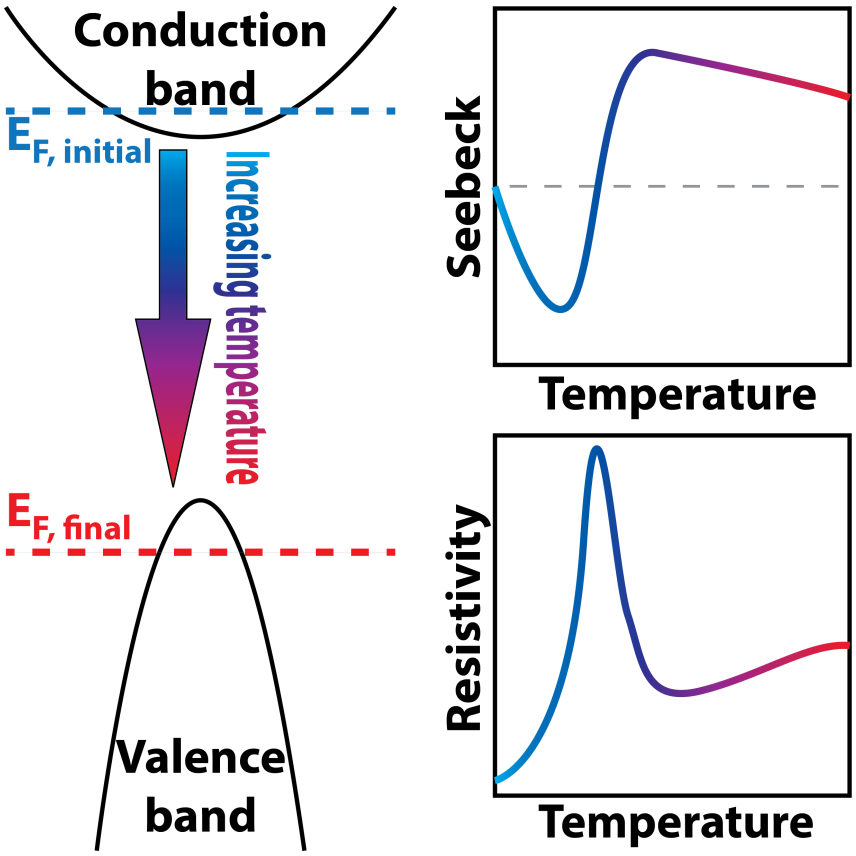

Figure 6.1. Schematic of two-band model for iodine doped polycrystalline sample (or vapor grown single crystals) showing movement of the Fermi level with increasing temperature and the resulting properties.

thermal conductivity should be much lower,[65,76,176] and thus the zT higher than initially thought, warranting further study.[77]

However, the optimization of thermoelectric performance through compositional tuning of the pentatelluride materials has been difficult due to a poor understanding of the underlying transport. Chemical vapor grown single crystals of $ZrTe_5$ exhibit a peak in resistivity (ρ) as a function of temperature and a change in sign of the Seebeck coefficient (α) at approximately 130 K. There have been many explanations for this behavior over the years. Researchers first believed this was due to charge density waves,[252] but

diffraction, magnetic field, and compositional data indicated this was not likely the cause of the peaked resistivity.[6,253] Other explanations have since been advanced but there has not been a consensus on the cause of the transport phenomena.[254,255] The temperature-induced Lifshitz transition has been studied as well as the quantum Hall effect and chiral magnetic effect,[256–261] but there remains a debate over whether pentatellurides are topological insulators with a small band gap or whether they are Dirac semimetals.[262–267]

To more specifically investigate the promise of $ZrTe_5$ as a thermoelectric material, we have produced bulk, polycrystalline $ZrTe_5$ samples. Our undoped samples are p-type over the entire temperature range, though substitution of iodine for tellurium causes a transition to n-type at low temperatures, in agreement with previous reports. Using experimental Seebeck coefficient, thermal conductivity (κ), and Hall data, we find that in the polycrystalline form, these pentatellurides can be modeled as a narrow band gap semiconductor with effective contributions from a single n-type conduction band and a single p-type valence band. We then use our model to explain previous property observations in the literature, and are able to explain the resistivity peak in terms of a n-type to p-type thermally-induced crossover, shown schematically in Fig 6.1. We also investigate predicted thermoelectric properties from this model and show how to optimize the zT for these polycrystalline materials, as well as note their potential use for both n and p-type legs in the same device.

6.3. Synthesis and Characterization

$ZrTe_{5-x}I_x$ samples were prepared by solid state reaction and hot pressing with powder XRD used to monitor sample purity at room temperature (Fig. 6.2). Rietveld refinement

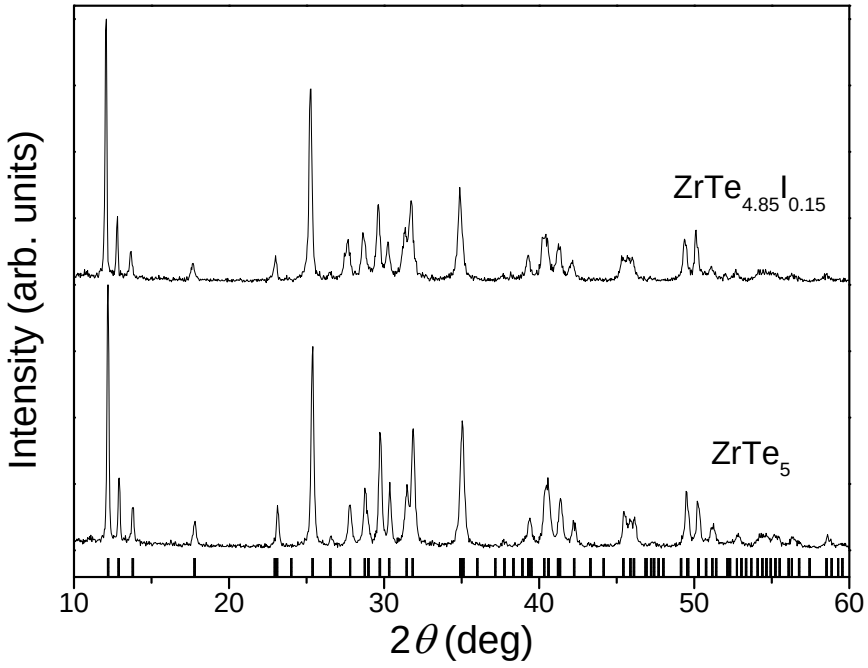

Figure 6.2. X-ray diffraction of $ZrTe_5$ and $ZrTe_{4.85}I_{0.15}$ are shown along with tick marks corresponding to the theoretical peak positions for $ZrTe_5$.

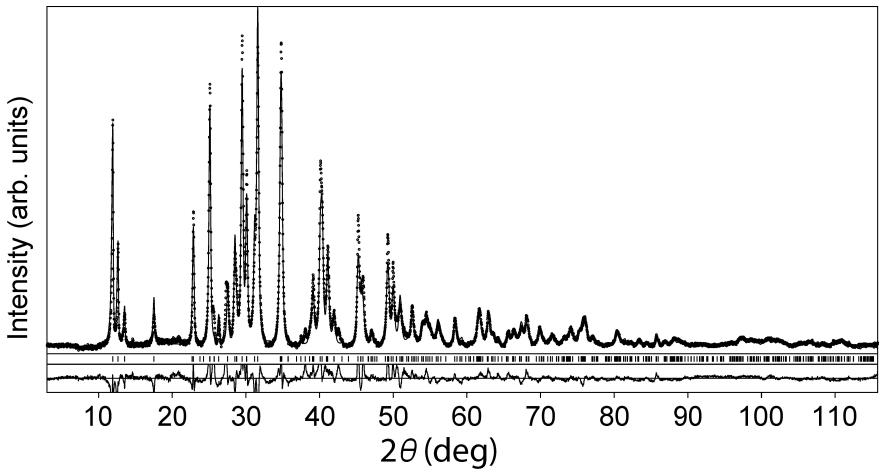

Figure 6.3. Rietveld fit of $ZrTe_5$ (Cu-$K_{\alpha 1}$ radiation). Ticks mark the calculated reflection positions of the target phase while the baseline corresponds to the residuals of a Rietveld refinement ($R_i = 0.08$, $R_p = 0.15$, $R_{wp} = 0.21$) based on the reported crystal structure data. No pronounced preferred orientation was observed by texture analysis. The lattice parameters of this sample were $a = 3.9880(3)$ Å, $b = 14.5283(8)$ Å, $c = 13.7305(9)$ Å.

was performed by the WinCSD program package on the hot-pressed undoped sample and the result is shown in Figure 6.3[268,269]. All compositions labeled in the text and figures are the nominal composition. Samples were nearly phase-pure after solid state reaction as well as following hot pressing. The geometric density of the hot pressed samples was greater than 98% of the theoretical density for $ZrTe_5$. Figure 6.2 shows the X-ray diffraction pattern for the pure and iodine doped $ZrTe_5$ samples as well as the theoretical peak positions,[269] indicating phase-purity for both samples. The Rietveld refinement is shown in Figure 6.3, performed on the undoped sample following hot pressing. From a careful texture analysis, preferred orientation of the grains was not observed, meaning that the polycrystalline sample is a collection of mostly randomly oriented grains. This safely allows modeling of the transport properties as isotropic even though the properties in a single crystal are anisotropic.

6.4. Property Measurements

Figure 6.4 shows the raw measurements of the properties for both $ZrTe_5$ and $ZrTe_{4.85}I_{0.15}$ at all temperatures. Above room temperature, Seebeck measurements are taken using the light-pipe method, resistivity and Hall coefficient are measured using a 4-point van der Pauw technique, and thermal conductivity using an LFA 457 as described in Methods. These measurements are represented as orange "up" triangles and blue "right" triangles for $ZrTe_5$ and $ZrTe_{4.85}I_{0.15}$, respectively. Below room temperature properties were measured in various systems. For $ZrTe_5$, the Seebeck coefficient and resistivity were measured with a Physical Property Measurement System (PPMS, Quantum Design) with the Thermal Transport Option (TTO) and are represented as orange "down" triangles. The

Hall coefficient was measured using a 4-point VdP geometry described previously and are shown as orange diamonds. For $ZrTe_{4.85}I_{0.15}$ the Seebeck coefficient, resistivity, and thermal conductivity measured with PPMS-TTO are shown as blue "left" triangles. The resistivity and Hall coefficient as measured with a PPMS using a 4-point VdP method are shown using blue diamonds.

We have scaled all low temperature measurements to agree with high temperature ones, using a multiplicative factor, in order to have smooth data across the entire temperature range for modeling purposes. In the PPMS-TTO measurement, contacts are painted on and assumed to be point contacts where in reality they are of significant size relative to the sample. This is noticeable in the resistivity for $ZrTe_{4.85}I_{0.15}$ where the value measured using the PPMS-TTO measurement at room temperature (6.53 mOhmcm) is significantly higher than either the PPMS-VdP (2.14) or high temperature VdP (1.71). Even for the low temperature VdP measurements using either the home-built or PPMS systems the ratio of the contact size to sample size is much larger than that employed for the high temperature measurements. Due to the confluence of all these factors we have scaled all low temperature values to agree with high temperature ones, where the measurements for both samples were taken using the same instruments and geometries. Raw data is shown here for the interested reader with smoothed data shown throughout the rest of the text.

Most previous reports of $ZrTe_5$ properties have been for single crystals grown by a chemical vapor transport method. For these crystals, the Seebeck coefficient is linear at low temperature, changes from n to p-type near 130 K, and has an absolute value of ∼100-200 μVK^{-1}, while the temperature-dependent resistivity has a peak around 130 K which is a few times higher than the room temperature value.[249,250,270–276] Recently a tellurium

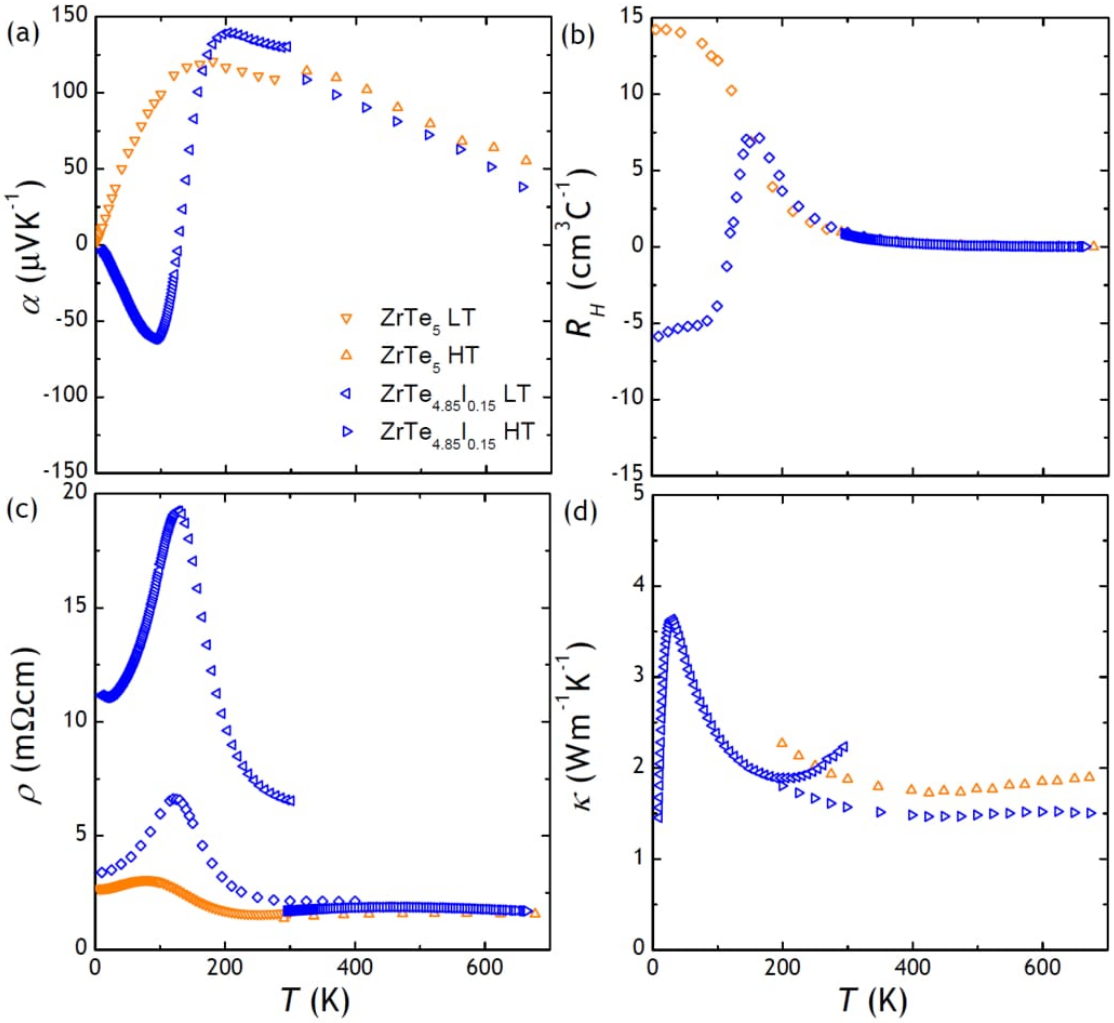

Figure 6.4. Raw data for $ZrTe_5$ and $ZrTe_{4.85}I_{0.15}$ showing low temperature and high temperature data before smoothing. Orange up arrows and blue right triangles are for $ZrTe_5$ and $ZrTe_{4.85}I_{0.15}$, respectively, measured above room temperature as described in the text. Orange down and blue left triangles are for low tempeature measurements using PPMS while diamonds are for van der Pauw measurements. See text for specific details on the instrument used to collect each.

self-flux growth technique was used to synthesize single crystals, an alternative to the traditional vapor transport growth.[256] These flux grown crystals exhibit similar behavior

as chemical vapor transport single crysals in general, though there are some key differences when compared with vapor grown crystals. For example, ρ does not trend toward zero at 0 K, the n-type α is significantly larger in magnitude, and most importantly, the temperature is much lower for the n-p transition and resitivity peak, around 60 K. This indicates that synthesis techniques are very important in determining the properties of $ZrTe_5$. In addition to the influence on differences in the TE properties, both the vapor growth and self-flux techniques produce needle-like single crystals which are small and can present challenges for property measurement and sample loading. Finally, there are seldom reports of the thermoelectric properties above 300 K,[249] which would provide a more complete understanding of the transport.

To resolve these issues, we synthesized $ZrTe_5$ samples by solid state reaction and hot pressing, producing large, bulk, polycrystalline samples for study across the entire temperature range, approximately 0 to 700 K. The Seebeck coefficient and resistivity for polycrystalline $ZrTe_{5-x}I_x$ samples are shown in Figure 6.5. While the $ZrTe_{4.85}I_{0.15}$ sample exhibits properties largely similar to previous reports on chemical vapor grown single crystal samples, the behavior of undoped polycrystalline $ZrTe_5$ is quite different (Fig. 6.5). The Seebeck coefficient for the latter is always positive and the resistivity peak is shifted to a lower temperature, closer to 60 K, in addition to being smaller in magnitude relative to ρ_{300K}.

Shown in Figure 6.6 are sweeps of the Hall resistance vs magnetic field ($\mathcal{B}$) for all temperatures up to 300 K. This confirms the p-type nature of undoped $ZrTe_5$ down to low temperatures. Above approximately 150 K, ρ_{xy} is linear with $\mathcal{B}$ field for $ZrTe_5$, indicating a single carrier dominates. However, at lower temperatures, lines are curved, indicating

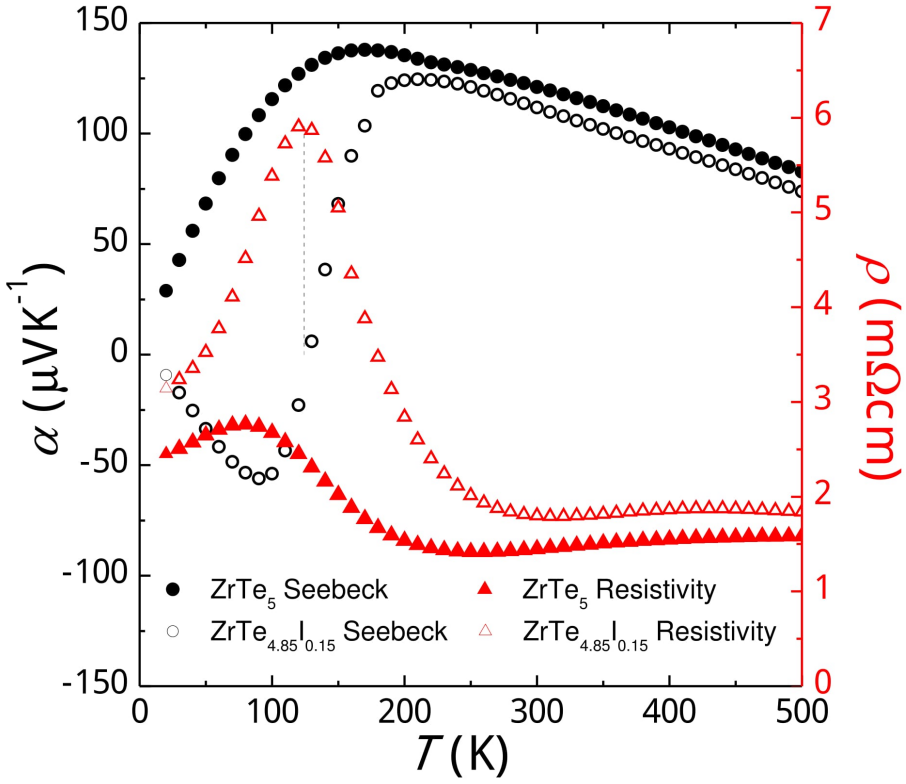

Figure 6.5. Seebeck coefficient and resistivity for polycrytalline $ZrTe_5$ and $ZrTe_{4.85}I_{0.15}$. Dashed line at 130 K indicating resistivity peak and Seebeck coefficient crossing zero for $ZrTe_{4.85}I_{0.15}$. Undoped $ZrTe_5$, by contrast, has a lower temperature resistivity peak and stays p-type over the full temperature range.

multiple carrier types contribute. For $ZrTe_{4.85}I_{0.15}$, the Hall coefficient is negative at low temperatures, crosses zero around 130 K, and becomes linear around 200 K. The trend is in good agreement with previous reports for flux grown single crystals, with transitions shifted to higher temperatures. The 120 K ρ_{xy} trace is positive at negative $\mathcal{B}$ field, crosses to negative around -1 Tesla, goes through zero $\mathcal{B}$ field with a positive slope, and finally crosses back from positive to negative ρ_{xy} at 1 T. This indicates that the p-type mobility is

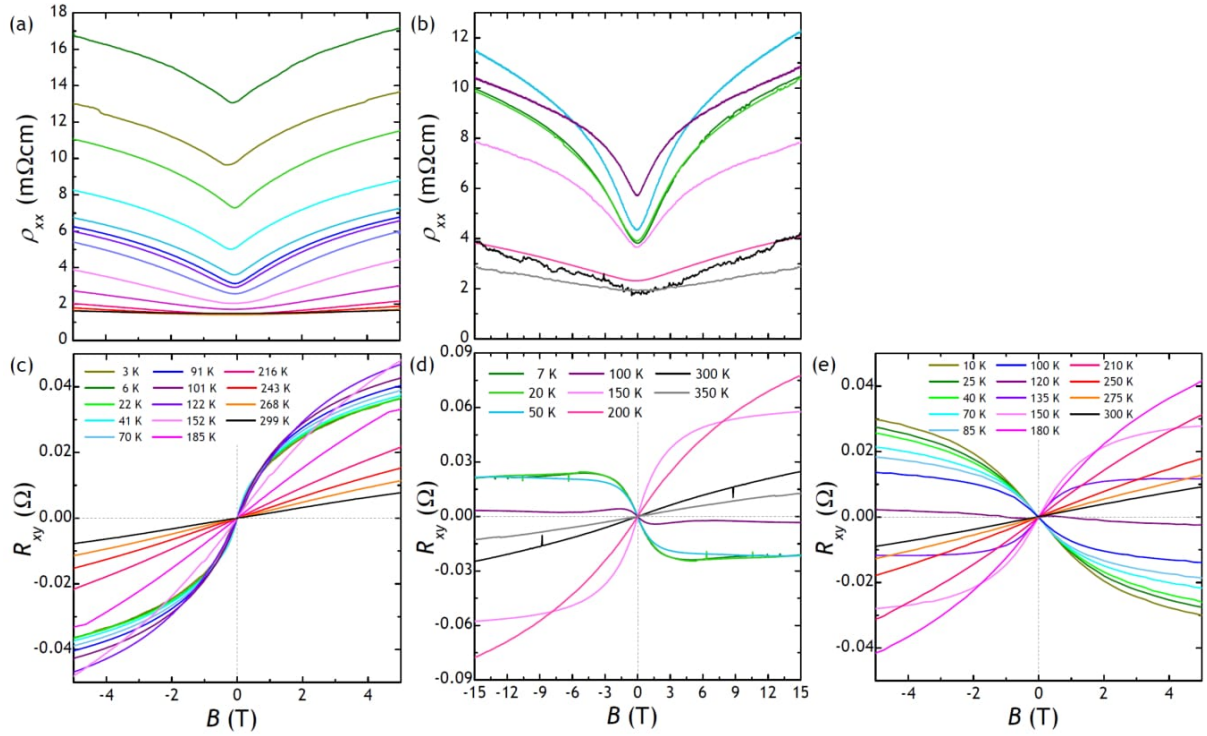

Figure 6.6. Resistivity and Hall resistance for both samples. (a) and (c) are for $ZrTe_5$ while (b) and (d) are for $ZrTe_{4.85}I_{0.15}$. Data in (a)-(d) collected with SR830 and (e) was collected with PPMS.

much higher than the n-type mobility while the concentration is higher for n-type carriers than p-type.

The resistivity (ρ_{xx}) and Hall resistance (R_{xy}) as a function of magnetic field are shown in Figure 6.7 for these polycrystalline samples. At low temperatures, $\rho_{xx}(B)$ shows an antilocalization minimum at $\mathcal{B} = 0$ typically associated with strong spin-orbit coupling typical to the valence band and also the conduction band for narrow-gap materials.[277] This could also be attributed to topological surface states, possibly at grain boundary interfaces. Numerous unconventional effects have previously been observed in single crystals at low temperatures, including the chiral magnetic effect,[259,260] Lifshitz transition,[256,278] Van

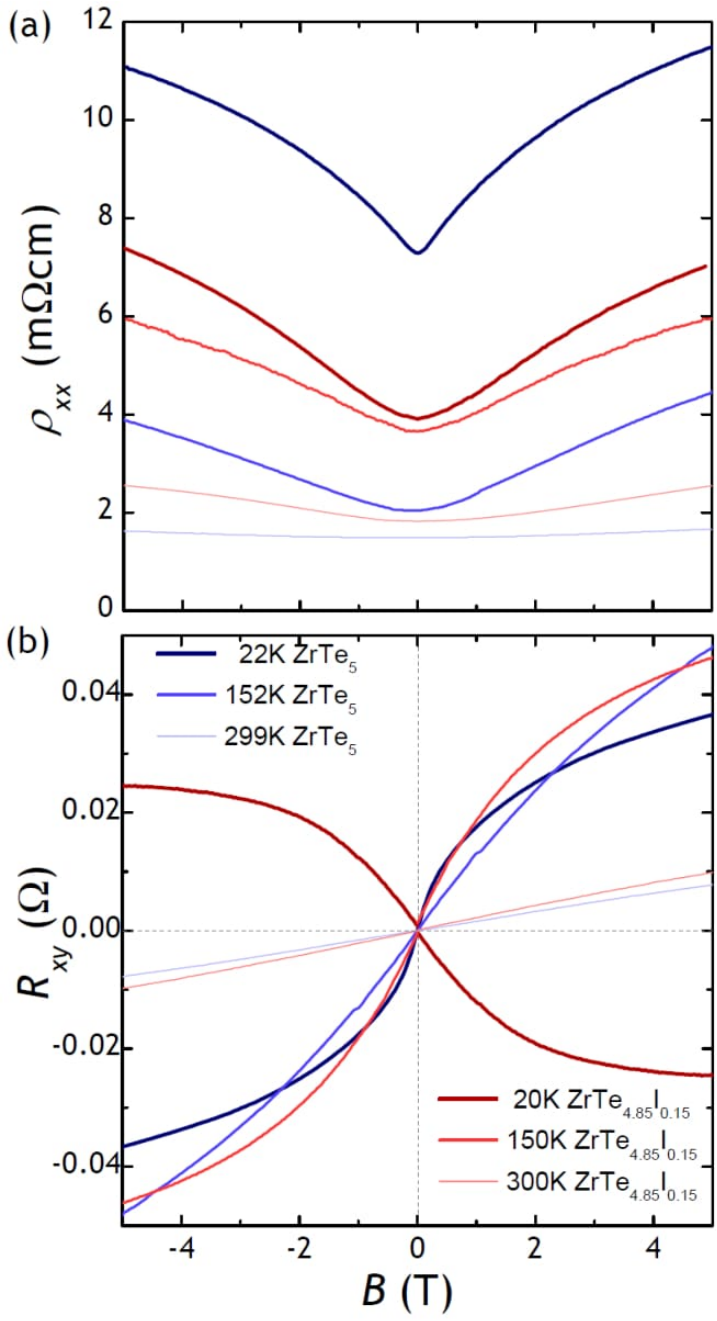

Figure 6.7. Resistivity (a) and Hall resistance (b) for both $ZrTe_5$ and $ZrTe_{4.85}I_{0.15}$ at select temperatures (well below, near, and well above the transition).

Hove singularity,[279,280] Zeeman splitting,[281,282] and topological effects.[262,264,265,277,278,283] This measurement demonstrates that some of the unconventional effects previously observed at low temperatures in single crystals persist in polycrystalline samples as well. However, at higher temperatures, these effects are less important in their contributions to the transport behavior. As the temperature increases, $\rho_{xx}(B)$ in Fig. 6.7(a) is less dependent on magnetic field over the relevant magnetic field range, deviating at most $\pm 25\%$ around the mean value, with a sharp curvature only at the lowest temperature. Thus we define an arbitrary 150 K cutoff above which we argue that a Drude-like model with no consideration of phase-coherent effects can approximate the observed behavior, but below which a more careful model including weak anti-localization would be needed. The Hall resistance for $ZrTe_{4.85}I_{0.15}$ is consistent with previous measurements[256] and with Seebeck coefficient measurements showing n-type conduction at low temperatures and switching to p-type at higher temperatures, while undoped $ZrTe_5$ remains p-type at all temperatures, again consistent with Seebeck coefficient measurements. Both of the polycrystalline samples show non-linearity of R_{xy} with $\mathcal{B}$ at lower temperatures, possibly indicating more than one carrier contributes to conduction. As the temperature increases, R_{xy} becomes linear with $\mathcal{B}$, indicating a single charge carrier dominates.

6.5. Two-band Modeling

Although there are prominent features in the low-temperature magnetotransport associated with spin-orbit coupling and phase coherent scattering, as we shall demonstrate, the higher temperature properties above 150 K can be reproduced with a simple two-band model for all of the transport coefficients in this high temperature range. In addition, the

qualitative trends at low temperature can also be reproduced with the same parametrization. We therefore propose a simplified two-band model that clarifies the significantly different properties observed in $ZrTe_5$ samples produced by different methods (polycrystalline, flux, or vapor grown) and offers insight into the phenomena of the resitivity peak and Seebeck coefficient switching from n to p-type. Using this simple two-band model with one valence and one conduction band, we can describe the thermoelectric properties observed for various samples by changing only the doping level.

The effective mass model used here is similar to the single parabolic band (SPB) model commonly used in thermoelectrics, but considers contributions from two bands (one conduction and one valence). To construct the model, we fix a number of parameters based on previous experimental and computational studies and then determine the mobility needed to explain the experimentally measured transport properties. The Boltzmann transport equations have previously been derived assuming Drude model for mobility and an energy dependent scattering time $\tau = \tau_0 E^{\lambda - 1/2}$ ($\lambda = 0$ for acoustic phonon).[284] For the fits to the polycrystalline $ZrTe_{5-x}I_x$ samples we fix the isotropic electron and hole Seebeck mass as $m_e = 0.5\ m_0$ and $m_h = 0.15\ m_0$, respectively, and the band gap as $E_g = 0.02$ eV. The number of donors for the iodine doped sample is fixed at $N_d = 1.1 \times 10^{18}$ (cm^{-3}) while for the undoped $ZrTe_5$ sample the number of acceptors was $N_a = 4.5 \times 10^{17}$ (cm^{-3}). To appropriately fit the data, it was found that the masses, their ratio, and the band gap, were required to be within a relatively narrow range. For example, it was only possible to fit the model to experimental data when the band gap is set between approximately 0.015 and 0.03 eV. Previous experimental studies using a variety of techniques have found that the band gap of $ZrTe_5$ can be anywhere from 100

meV to a gapless semimetal.[258,259,262–266,278,285] However, recent ARPES studies observed a 40 meV band gap at 255 K which decreases with decreasing temperature,[278] while another measured a gap of 18-29 meV.[286] We found that the model worked best with a gap of 20 meV. As this is an effective mass model, we can not definitively determine each of the parameters without more experimental data, we can only suggest general ranges and ratios of the parameters. Additionally, an isotropic model is used here whereas the transport properties in $ZrTe_5$ are anisotropic.[282,287,288] The transport properties are expected to be anisotropic due to the structure of $ZrTe_5$ and needle-like growth of single crystals. However, the solid state reaction, grinding, and hot pressing procedure used here produces a sample that is not textured, as seen in the Rietveld refinement. Instead the sample is a collection of randomly oriented grains such that the properties for each direction are averaged out, allowing the use of a simpler, isotropic model here.

The experimental properties for both polycrystalline samples, as well as the model using two different doping levels, are shown in Figure 6.8. The model fits the data reasonably well in the 200-600 K range. The resistivity as a function of temperature is well described by this effective mass model across the entire temperature range (Fig. 6.8(a)). The Seebeck coefficient data fits well at high temperature (Fig. 6.8(b)). The model deviates from the experimental data at low temperatures, though this is to be expected. As discussed previously, the unconventional transport effects start to dominate in these polycrystalline samples at low temperature. The modeled Hall coefficient qualitatively reproduces the trends observed in the experimental Hall coefficient (Fig. 6.8(c)), which was determined using a linear fit to the low field R_{xy} *vs* $\mathcal{B}$ data.

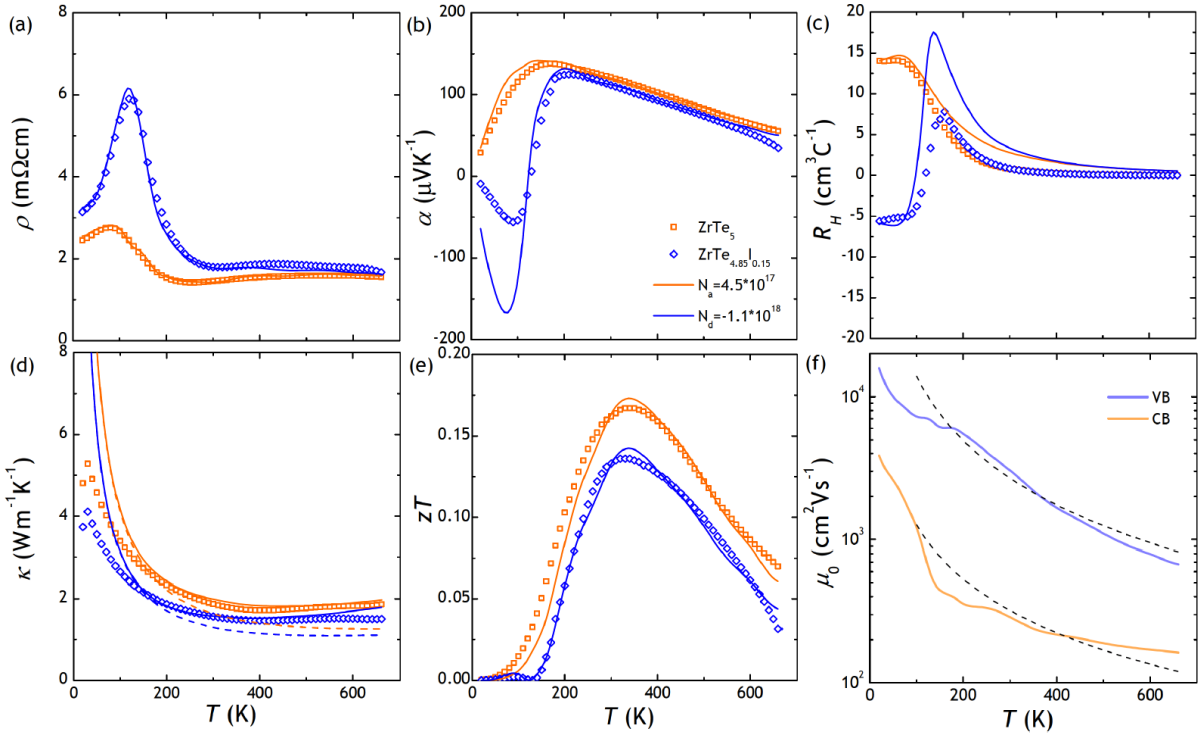

Figure 6.8. Smoothed experimental data (symbols) for (a) resistivity, (b) Seebeck coefficient, (c) Hall coefficient, (d) total thermal conductivity, and (e) zT. Also shown are the modeled properties (lines) with two different carrier concentrations using the parameters listed in the text. In (e) the total (solid) and lattice plus bipolar (dashed) thermal conductivity using the model are shown. The modeled mobility is shown in (f) with dashed lines representing $T^{-3/2}$.

The resistivity and Seebeck coefficient behavior for the $ZrTe_{4.85}I_{0.15}$ sample is very similar to previous reports for chemical vapor grown single crystals, showing n-type behavior at low temperature. The Seebeck coefficient is n-type at low temperature and increasing in magnitude as the Fermi level is initially in the conduction band and moving toward the gap with increasing temperature. The temperature where the Seebeck coefficient crosses zero and the resistivity is at a maximum ($\sim$130 K in this case) is where the Fermi level

nears the middle of the gap. With increasing temperature, the Fermi level continues toward the valence band as the material becomes more p-type. Finally, after the Seebeck coefficient reaches its maximum p-type value it then decreases linearly with temperature, when the Fermi level becomes effectively pinned within the valence band (see Fig. 6.1). As will be demonstrated later, the initial position of the Fermi level in the conduction band is what controls the temperature at which $\alpha = 0$ and the resistivity is peaked. On the other hand, for the undoped polycrystalline $ZrTe_5$, the Seebeck coefficient is always positive due to the Fermi level residing in the valence band. At low temperatures, the Fermi level moves toward the gap leading to the linear increase in α, and eventually is pinned within the valence band.

The model for κ (Fig. 6.8(d)) considers Umklapp scattering as well as the electronic and bipolar contributions to total thermal conductivity. Umklapp scattering dominates at higher temperatures and has a T^{-1} dependence which fits the data well at higher temperatures, in the area of interest for zT predictions. Below 200K, the model fit to experimental data is not as good, partly due to the use of a PPMS for low temperature measurements which uses a direct measurement technique that is uncorrected for radiation. The fit below 200 K is not expected to be exact as the measurement technique differs and other scattering mechanisms (i.e. point defect or boundary scattering) may play a role at lower temperatures. Due to the layered crystal structure, κ is fairly low. Though $ZrTe_5$ was predicted to have a lattice thermal conductivity of 1.8 $Wm^{-1}K^{-1}$ at 300 K,[77] initial reports in single crystal $ZrTe_5$ found $\kappa \sim 8$ $Wm^{-1}K^{-1}$. However, due to the small size and needle-like shape of the single crystals measured previously, there

may be a significant error in the initial report of thermal conductivity. These measurements demonstrate a much lower total thermal conductivity, experimentally confirming the prediction (Fig. 6.8(d)), in line with previous measurements.[289] This difference in the thermal conductivity is expected, due to the polycrystalline nature, but is also partly due to the measurement technique allowed by the larger size and shape of these samples. Our polycrystalline $ZrTe_5$ samples exhibit a total thermal conductivity four times lower than that measured for single crystals along the a-axis, so while the power factor is reduced, the overall zT (Fig. 6.8(e)) is higher.

In most thermoelectric materials, it is sufficient to assume solely acoustic phonon scattering for modeling purposes, as they tend to be investigated at temperatures above 300 K. However for these pentatelluride systems, the thermoelectric behaviors of interest occur below 200 K, where other scattering mechanisms can play a significant role. For example in Si and Ge, ionized impurity scattering dominates the temperature dependence of mobility at low temperatures while acoustic phonon scattering is more important at higher temperatures.[284] The Fermi integrals used in this model are for λ=0, acoustic phonon scattering, since we are primarily concerned with high temperature properties while the model is not expected to fit precisely at low temperatures due to the reasons discussed previously. The mobility used to fit the measured properties is shown in Figure 6.8(f). The modeled mobility for both the conduction and valence bands have a temperature dependence close to $T^{-3/2}$ above 100 K, in agreement with acoustic phonon scattering.

In addition to low temperature effects discussed previously, there is another contribution to the discrepancy between measured and modeled Seebeck and Hall coefficients.

Due to the complex nature of the pentatellurides with a small band gap and layered structure, DFT calculations of band structure have not always been in agreement.[262,265,285,290] Additionally, the calculated band structure is sensitive to the parameters used, including the temperature, stress/strain induced by chemical substitution, and pressure.[258,282,283] However, calculations typically show a single hole pocket centered around Γ with much higher energy than other pockets, while the conduction band has numerous pockets at comparable energy levels. As T increases, these pockets contribute to conduction leading to an increase in the Seebeck effective mass. This is due to carriers being thermally generated across the small gap due to broadening of the Fermi-Dirac distribution with increasing temperature. A better fit to the experimental data can be achieved by either adding a third band or employing a temperature dependent effective mass or band gap. But because exact fits are not expected due to the unconventional effects at low temperatures as previously discussed, the introduction of additional fitting parameters is not warranted. Nonetheless, this model does qualitatively reproduce the trends as a function of temperature for the various property measurements.

6.6. Effect of Varying Carrier Concentration

The two-band model fit to experimental data can be extended to simulate properties at carrier concentrations not used for modeling, as shown in Figure 6.9. This is done by adjusting the initial doping level in the calculations, akin to experimental carrier concentration tuning using external dopants. As the *p*-type carrier concentration is increased, the peak in the Seebeck coefficient moves to a higher temperature and lower magnitude while the resistivity peak decreases in magnitude. As the *n*-type carrier concentration is

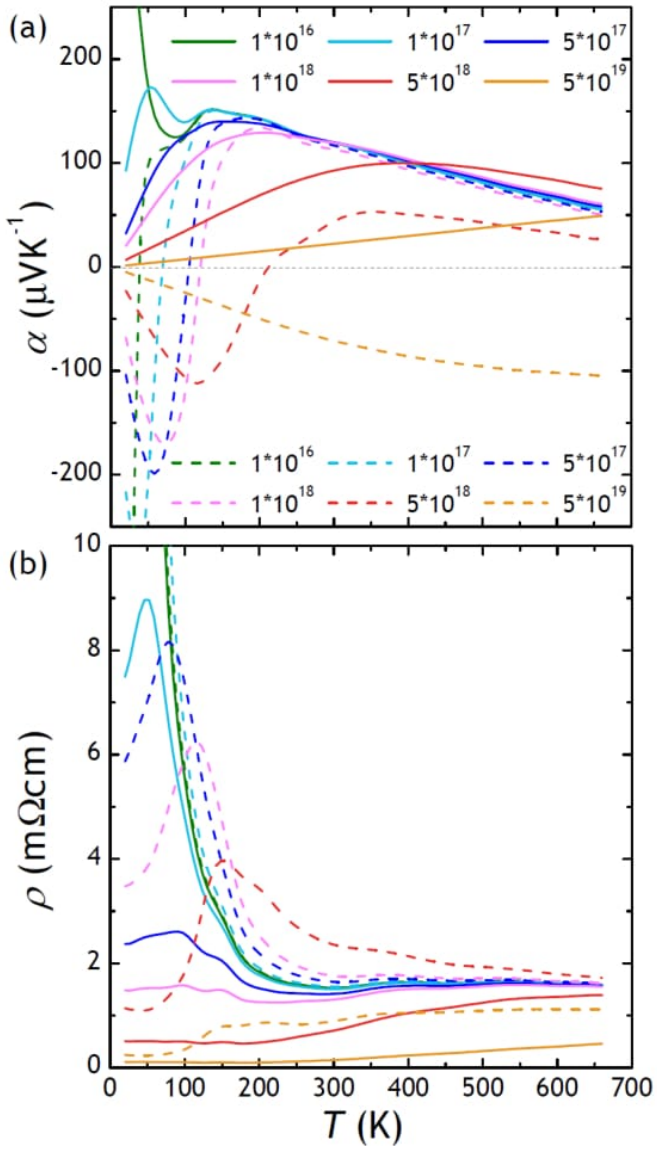

Figure 6.9. The (a) Seebeck coefficient and (b) resistivity as a function of temperature in polycrystalline $ZrTe_5$ for different doping levels (cm^{-3}) of both p (solid) and n-type (dashed) carriers.

increased, the n-type Seebeck coefficient crosses 0 at a higher temperature for higher doping levels, while the resistivity peaks at a lower magnitude but higher temperature. This qualitative behavior is in good agreement with previous measurements on single crystals

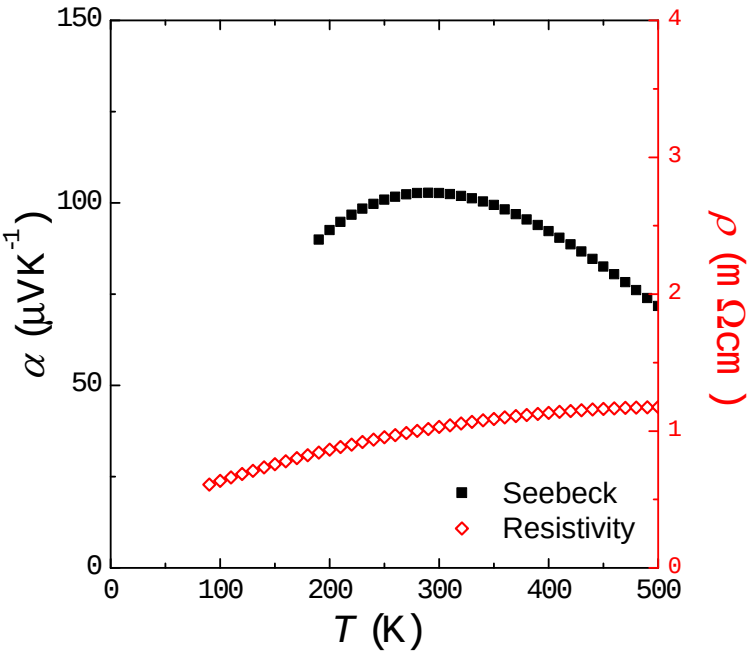

Figure 6.10. Resistivity and Seebeck coefficient data for $Zr_{0.99}Sm_{0.01}Te_5$.

with different carrier concentrations. Reports of iodine-vapor grown crystals show n_H of approximately 1×10^{18} cm^{-3} at room temperature and an n-p transition temperature of about 130 K while self-flux grown single crystals had values of 5×10^{16} cm^{-3} and 60 K.[249,255,256] The trends from the two-band model in Seebeck coefficient and resistivity are also in agreement with experiments where rare earth elements are substituted for the transition metal (Fig. 6.10 and Ref. 291). Figure 6.10 shows the Seebeck coefficient and resistivity for $ZrTe_5$ with samarium substituted for zirconium. These were measured using the home-built systems described previously cooled with liquid nitrogen. This demonstrates the properties for samples with higher p-type carrier concentration, in agreement with the two-band model. The model predicts that at high n-type carrier concentrations, a negative Seebeck will persist to higher temperatures, as has been experimentally found for $Hf_{0.99}Ta_{0.01}Te_5$ up to at least 300 K.[292]

As was previously discussed, the synthesis route used to produce $ZrTe_5$ samples has a dramatic effect on the observed properties. Our model shows that the cause of the various properties found in different crystals is the carrier concentration variation due to processing. The traditional route for making single crystals of $ZrTe_5$, chemical vapor transport synthesis, was thought to produce pure samples. Iodine is used as the vapor transport agent, so even though crystals are washed after this procedure, it is unlikely that all iodine is removed. Substitution of I for Te would act as an electron donor, causing n-type transport at low temperatures before the higher mobility p-type conduction dominates as carriers are thermally activated. Our model demonstrates how variations in the carrier concentration, in this case due to unintentional doping with iodine, change the properties. This is experimentally verified by measurements on undoped and iodine doped polycrystalline samples. Additionally, the differences between Te self-flux grown single crystals and undoped polycrystalline samples can be explained in the context of this model. $ZrTe_5$ is considered a line compound, though there is actually a finite phase width. So while both the flux and solid state reactions consist of only Zr and Te (no I), the ratio of the two elements may vary in the samples produced by different methods. This Zr to Te ratio would lead to changes in carrier concentration due to differences in actual (not nominal) stoichiometry. For example, Te vacancies caused by the high vapor pressure of tellurium would act as electron donors. Our model shows that the temperature and magnitude of the ρ peak, as well as the n-p transition of α can be tuned by adjusting the carrier concentration, accomplished through careful control of the Zr to Te ratio or dopant concentration.

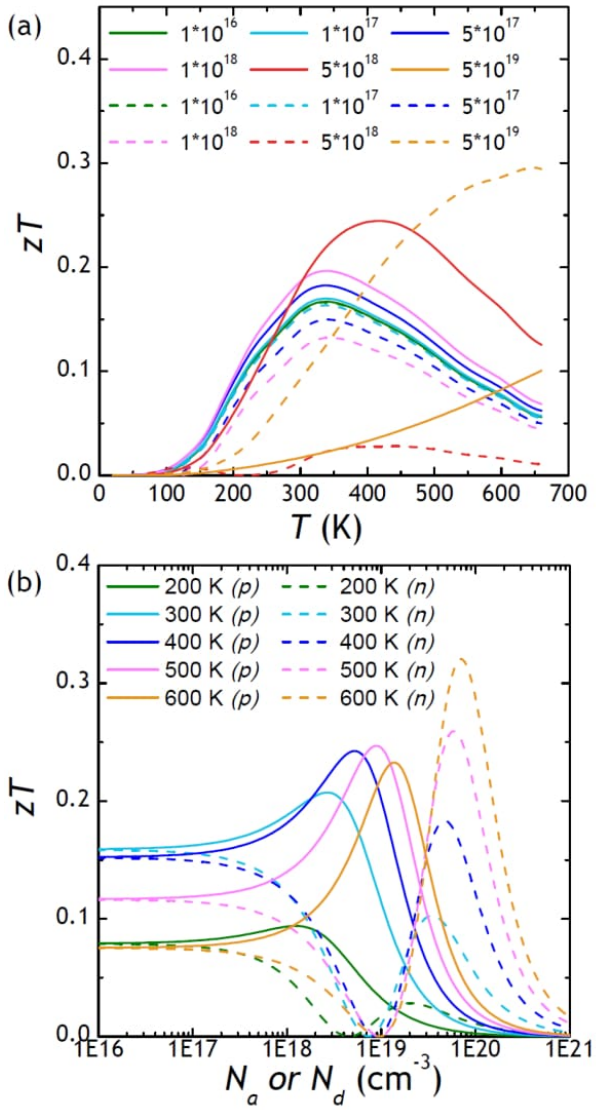

Figure 6.11. For polycrystalline $ZrTe_5$, (a) the zT as a function of temperature at various acceptor (solid) or donor (dashed) levels, and (b) the zT as a function of dopant concentration for temperatures ranging from 200 to 600 K.

6.7. Tuning Model to Optimize Thermoelectric Performance

Due to the reasons previously stated, we do not expect the model to be accurate at low temperatures, but the properties are well fit in the 200-600 K range where the peak zT

is observed. Figure 6.11(a) shows the zT as a function of temperature for various doping levels while Figure 6.11(b) shows zT *vs* doping level for both p and n-type samples at various temperatures. With low doping levels, bipolar conduction sets in by 200 K, leading to modest zT. However, as the doping level is increased, the maximum zT increases as the Fermi level is pinned into one band or the other. Controlling the carrier concentration allows for optimization of the zT in a desired temperature range.

Using the model for predictions, strategies can be devised for optimizing the thermoelectric performance of $ZrTe_5$. By increasing the band gap, minority carrier contributions can be suppressed, increasing the zT to $\sim$0.4 at 300 K. This could be done by substitution of Se for Te, as demonststrated previously.[292] Using our two-band model, we can estimate the zT contributions of each band independently. From this, we observe that engineering the composition such that the mobility of the minority carrier is reduced by a factor of 10 would also increase the 300K zT to approximately 0.35 for p-type. A two to three-fold reduction in the lattice thermal conductivity through grain size reduction, softening of the lattice, alloying, or other strategies would potentially lead to a zT near 1 at room temperature. Furthermore, by controlling the carrier concentration through doping, n and p legs can be made in the $ZrTe_5$ system. This provides the opportunity to make modules out of single compound, thus mitigating issues with chemical and thermal compatibility.

6.8. Conclusions

The details of transport in the $HfTe_5$ and $ZrTe_5$ systems have been debated for many years due to the exotic transport properties observed in single crystals. Measurement of

polycrystalline $ZrTe_5$ samples revealed p-type behavior at all temperatures, leading to a conjecture that the system could be explained as a semiconductor. Doping $ZrTe_5$ with iodine led to properties similar to previous reports on single crystals, with a n to p transition near 130 K, suggesting that prior work on pentatellurides may have been contaminated by residual iodine from the typical iodine vapor transport synthesis. A two-band model was constructed which accurately describes the properties of polycrystalline samples as well as explains the behavior of both flux and vapor grown single crystals. The model has a temperature independent band gap of 0.02 eV, a valence band with a higher mobility, and a conduction band with a higher effective mass. The experimental data is consistent with a semiconductor having a positive finite gap where the anomalous resistivity peak and change in Seebeck coefficient can be simultaneously explained. Finally, the model allows for prediction of zT by carrier concentration tuning and other strategies to optimize the thermoelectric performance. $ZrTe_5$ is promising for practical applications, as a thermoelectric device could be constructed out of single material used for both legs.

CHAPTER 7

Empirical Modeling of Dopability in Diamond-like Semicondutros

This Chapter contains content which has been submitted to a journal. Once it is accepted, permission will be requested.

7.1. Summary

Carrier concentration optimization has been an enduring challenge when developing newly discovered semiconductors for applications (e.g. thermoelectrics, transparent conductors, photovoltaics). This barrier has been particularly pernicious in the realm of high throughput property prediction, where the carrier concentration is often assumed to be a free parameter and the limits are not predicted due to the high computational cost. In this work, we explore the application of machine learning for high-throughput carrier concentration range prediction. Bounding the model within diamond-like semiconductors, the learning set was developed from experimental carrier concentration data on 127 compounds ranging from unary to quaternary. The data was analyzed using various statistical and machine learning methods. Accurate predictions of carrier concentration ranges in diamond-like semiconductors are made within approximately one order of magnitude on average across both p- and n-type dopability. The model fit to empirical data is analyzed to understand what drives trends in carrier concentration which are then compared with

previous computational efforts. Finally, dopability predictions from this model are combined with high-throughput quality factor predictions to identify promising thermoelectric materials.

7.2. Introduction

Control of charge carrier concentration of semiconducting materials is vitally important in a variety of applications, including photovoltaics,[293,294] optoelectronics,[295,296] transistors,[297,298] and thermoelectrics (TE).[7,299] To maximize efficiency, many of these applications require tuning both the type (p- or n-type) as well as the concentration of carriers. For many well-studied systems, the methods of controlling the carrier concentration are well established, both in choice of dopant species and synthetic technique.[300,301] However, the control of carrier concentration is not well understood in novel material systems. Traditionally, experimentalists have relied on basic metrics to guide the choice of doping species, namely ionic charge counting and radius ratio "rules of thumb."[302] These rules may not directly translate to more complex chemistries and structures. Theorists have recently been able to better guide efforts using defect calculations as computational capabilities have improved.[303–307] Despite these improvements, issues remain in the widespread use of these calculations due to their computational costs and inaccuracy. Therefore, methods to address dopability are critical for advances in complex semiconductors.

One such example is the high-throughput prediction of material properties, which has become increasingly common in the thermoelectrics community.[65,90,176,308] Various groups have developed their own models which can predict the optimal potential thermoelectric performance for a material based on its structure and simple density functional theory

(DFT) calculations. One of these metrics, quality factor (β), is a descriptor for the potential of a material to exhibit high thermoelectric performance, and has been previously shown to track well with experimental TE performance.[76] Despite the reasonable accuracy of these models in predicting the potential of a compound's performance, they rely on a key assumption. In order to predict this quality factor, it must be assumed that the chemical potential (i.e. Fermi level) can be sufficiently tuned to the type and concentration of charge carrier that optimizes performance. In the absence of dopability guidance, experimental investigation of high β compounds is inefficient due to the large number of false positive compounds which cannot be doped.

In the discussion of dopability, we find it helpful to identify the distinct sources that limit dopability. The discussion here is in relation to p-type dopability, but the schematic and discussion for n-type would be a mirror image. In the first case, Fig. 7.1a, the red native donor defect represents a hole "killer" defect, one that prevents the Fermi level (E_F) from being driven beyond some energy range, as it spontaneously produces an electron which increases E_F. This donor defect pins the minimum thermodynamically achievable limit of the Fermi level ($E_{F,lim}$) at the location of the red tick, with the possible doping range shown by the red horizantal gradient bar. As the native donor energy ($E_{n,d}$) increases, $E_{F,lim}$ moves towards the valence band, allowing a larger possible doping range shown by the green bar. Eventually, the donor energy is great enough such that the native donor dopability window ($W_{n,d}$) becomes positive, allowing greater p-type carrier concentration. Beyond killer defects, a system may exhibit limited dopability due to the lack of chemical flexibility in the native structure or extrinsic dopants. The Fermi level of the material will be set near the intersection of the lowest energy acceptor and donor

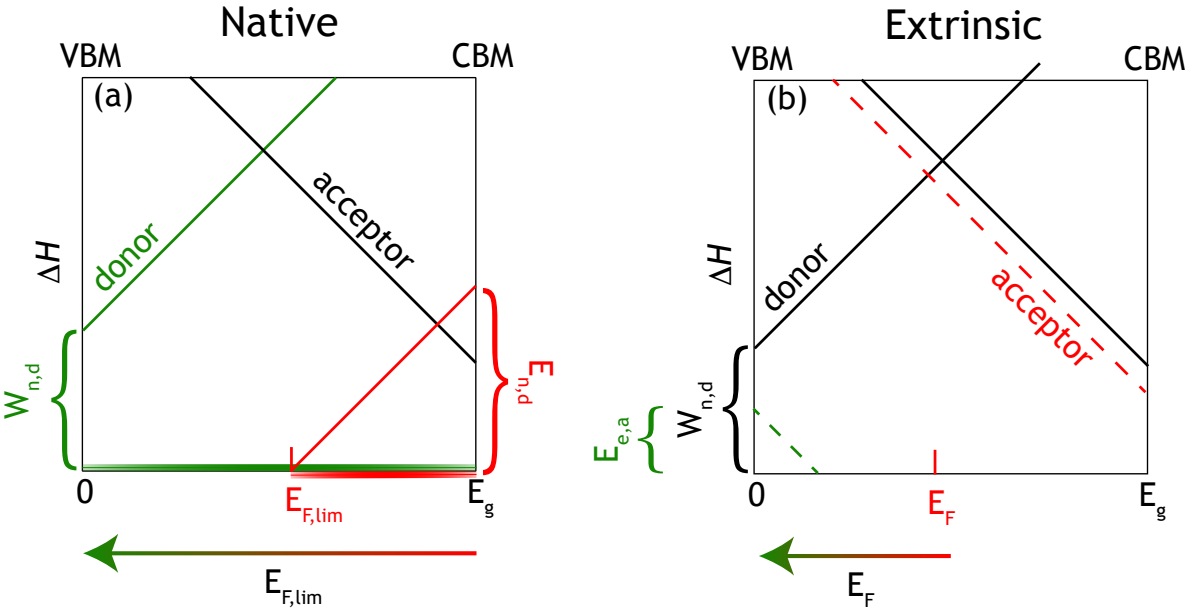

Figure 7.1. (a) Defect diagram schematic showing native defects, including an acceptor defect (black line) and two possible variations of a native donor defect (red and green lines). The intersection at the valence band maximum (VBM) of the native donor defect gives the *p*-type dopability window ($W_{n,d}$). The achievable thermodynamic limit of the Fermi level ($E_{F,lim}$) is set by the charge (which determines slope) of the native donor defect and the conduction band minimum (CBM) defect energy (native donor energy or $E_{n,d}$). (b) Defect diagram schematic showing the effect of extrinsic dopants (dashed colored lines), given native acceptor and donor defects (solid black lines). The Fermi level will be near the intersection of the lowest energy donor and acceptor defects. The red extrinsic acceptor is a poor dopant as it does not significantly lower E_F. A good *p*-type dopant is one where the extrinsic acceptor energy ($E_{e,a}$) is less than or equal to $W_{n,d}$ ($W_{n,d}$ - $E_{e,a} \geq 0$), allowing high *p*-type carrier concentration.

defects, regardless of whether they are native or extrinsic (Fig. 7.1b.). In some cases, the lowest energy extrinsic acceptor dopant is too high to substantially lower the Fermi level, meaning there is no extrinsic dopant which increases the dopability window,[309] represented with the red extrinsic acceptor. This arises when there is significant phase competition for the dopant element and dopant solubility limits are reached. In more well-behaved

systems, high dopant solubility is achieved due to a lack of phase competition and the minimal energetic penalty for dopant incorporation. This scenario yields a dopant where the energy of the extrinsic acceptor ($E_{e,a}$) is lower than the window of the native donor ($W_{n,d}$), drastically altering the Fermi level toward or into the valence band, leading to an associated high p-type carrier concentration (green extrinsic defect).

To date, there have been few efforts in modeling of charge carrier concentration and no comprehensive analytical/physical model exists to estimate dopability of materials. Conventional wisdom posits that large band gap materials are harder to dope, elemental properties such as size and electronegativity should be considered when choosing a substituting species, and that the structure and lattice energy have some effect.[302] Yet little is known about the relationship (sign, magnitude, functional form) between the physical properties and carrier concentration. DFT can predict intrinsic defects and external dopants, guiding experimentalists to regions of phase space and dopants necessary to achieve the desired carrier concentration.[20] In the field of dopability, diamond-like semiconductors (DLS) have received the most computational attention. This includes an amphoteric defect model,[306,310] phenomenological models for doping limits based on universal band alignment,[303,304,309,311] and detailed analysis of defects in individual DLS systems.[312–314] Despite this success, defect calculations can't be used for high-throughput screening due to their computational cost.

One possible solution is the development of semi-empirical models, as they have proven successful in combining experimental data with physics-based models.[65,76] In the absence of an analytic model or high-throughput defect calculations, statistical learning from experimental or computational data can serve as an alternative to create empirical models

and rules of thumb to make predictions of dopability in new compounds. Machine learning has proven successful in understanding and predicting energy and entropy,[315] potentials and forces,[316–318] structure, physical, and elastic properties,[319–324] bandgap,[320,325,326] and defects,[327] as well as enabling high-throughput screening and discovery,[328–332] and guiding experimental synthesis.[333,334]

In order to properly model and interpret dopability, the construction of an empirical dataset for cross-validation is of vital importance. While other physical properties have been tabulated in databases, there are few resources where carrier concentration in semiconductors has been collected. Minimization of the number of uncontrolled variables and maximization of the size of the dataset is helpful in improving accuracy, statistical significance, and applicability to the largest possible group of materials.[326,335] Again, DLS stands out from this perspective as there are a large number of compounds and they are technologically relevant,[336–339] including recent discovery of high β quaternary compounds.[340] DLS compounds have the same tetrahedral local bonding environment and span an impressive fraction of the periodic table.[341,342]

The goal of the following is to establish a broader understanding of the drivers underpinning dopability and a method to predict the possible carrier concentration range in DLS compounds. By performing a careful and extensive literature search with DLS as the model system, the experimentally realized carrier concentration range of 127 compounds have been obtained. Input features for modeling have been generated using structural information, periodic table properties of constituent elements, and widely available inexpensive DFT calculation results. We show using cross validation that accurate predictions

are possible for this dataset across the entire family, with the model capturing experimental trends in subsets of compounds as well. The features determined to be important in the linear regression are explained and matched with intuition and previous computational results. Finally, the dopability prediction engine is applied to additional DLS compounds which have not been experimentally studied to assess their ultimate potential as TE materials.

7.3. Experimental Carrier Concentration Data

The two most important factors in determining dopability are structure and chemistry. For statistical learning, diamond-like semiconductors (DLS) are an ideal system as they allow isolation of one of these factors. The local bonding environment is fixed to tetrahedral coordination while compounds span a broad chemical space. DLS compounds are derived from the silicon structure and range from unary to quaternary in this study. Typically DLS compounds have an average position of Group IV (4 electrons per atom) and an equal number of cations and anions in the unit cell, though there are defect structures which break these rules. With a wide range of elements and numerous stoichiometries (unary, 1-1, 1-1-2, 2-1-3, 3-1-4, 2-1-1-4, 1-2-1-4), DLS is a rich family of compounds. This makes them an ideal model system for statistical learning from a large dataset.

Using DLS as the model system, carrier concentration reports were scraped from literature to create a dataset to be used for statistical modeling. This is because preparation of enough compounds, each with fully explored carrier concentration range, by a single individual or group is not feasible. Therefore, we employ a comprehensive literature

seach from many disciplines, while carefully controlling processing conditions. The resulting dataset is presented in Table 7.1. There are some inherent difficulties in building a dataset in this way that can be broken down into three major groups:

- Samples are produced and measured by different groups, with different preparation methods and goals. This means that there will be variations in sample quality and various types of human error, preparation conditions are sometimes ill-defined, and that carrier concentration is often not the primary goal and instead is just one of many properties reported for a sample.
- There is insufficient data to allow division of intrinsically and extrinsically doped samples, even though we expect that there should be some difference in the limits obtainable by self-doping *vs* introduction of an additional species.
- Experimental reports inherently skew toward unary and binary compounds as these have been investigated more thoroughly than ternary and quaternary compounds even though there are more possible compositions at higher order.

Irrespective of these caveats, we believe this is likely the best dataset one could reasonably expect possible due to the careful control of structure, chemistry, and processing conditions and the large number of samples and chemical constituents present.

Table 7.1. Experimental carrier concentration (cm^{-3}) range for DLS compounds.

Compound	Max n-type	Synthesis	Max p-type	Synthesis	All Refs.
$AgAlTe_2$			1×10^{17}	vacuum anneal [343]	343
$AgCd_2InTe_4$	1×10^{15}	from melt [344]	7.3×10^{16}	polycrytalline pellet [345]	344–346
$AgFeSe_2$	-5×10^{19}	from melt [347]	-1×10^{19}	from melt [347]	341,347
$AgFeTe_2$	-1×10^{19}	from melt [347]	-2×10^{18}	from melt [347]	341,347,348
$AgGaSe_2$	1.7×10^{15}	sputter 450 [349]	6.6×10^{16}	sputter 550 [349]	349–353
$AgGaTe_2$	1×10^{13}	flash evaporation 400 [354]	1×10^{17}	vacuum anneal [343]	343,354–357
$AgInS_2$	-3×10^{20}	vacuum deposition 380 [358]	1×10^{15}	vacuum deposition 380 [358]	350,358–362
$AgInSe_2$	-2.5×10^{18}	thermal evaporation 600 [363]	1.35×10^{15}	magnetron sputtered selenized 300 [364]	350,363–368
$AgInTe_2$	6×10^{15}	melt anneal [369]	1.1×10^{16}	melt anneal [369]	343,369,370
$AgSbSe_2$			8×10^{14}	review [341]	341
$AgSbTe_2$			2×10^{16}	review [341]	341
Ag_2GeSe_3			2×10^{17}	review [348]	348
Ag_2GeTe_3			8×10^{17}	review [348]	348
Ag_2HgSnS_4	-4.6×10^{16}	Bridgman [371]			371
Ag_2SnSe_3	1×10^{16}	polycrystalline pellet [372]	1×10^{18}	review [348]	348,372
Ag_2SnTe_3	5×10^{17}	review [348]	1×10^{20}	polycrystalline pellet [372]	348,372
Ag_2ZnSnS_4	-1.6×10^{14}	chemical bath deposition [373]	-6×10^{12}	chemical bath deposition [373]	373–376
$Ag_2ZnSnSe_4$	-6×10^{18}	thermal evaporation [377]	-9×10^{15}	thermal evaporation [377]	374,377,378
AlAs	-6×10^{18}	vapor growth [379]	1×10^{19}	crystals [362]	362,379–383
AlN	-1×10^{17}	MOVPE 1040, Si doped [384]	4.7×10^{19}	CVD 750, Mg doped [385]	384–388
AlP	-5×10^{19}	vapor transpor [389]t	-5×10^{18}	vapor transport [389]	389,390
AlSb	-1×10^{17}	MBE 430, Te doped [391]	1×10^{19}	MBE 550, Ge doped [392]	380,390–397
BAs	1×10^{17}	vapor transport [398]	1×10^{19}	chemical transport [399]	398,399
BN	-6×10^{16}	review [400]	5×10^{18}	magnetron sputter 1000 [401]	400–405
BP	-2×10^{20}	vapor deposition 950, P excess [406]	1×10^{19}	thermal decomposition 1150 [407]	362,406–418
BSb	-1.5×10^{18}	PLD 200 [419]	-8.6×10^{17}	PLD 400 [419]	419
BeTe	1×10^{14}	autoclave synthesis [420]	1×10^{20}	MBE 400, N doped [421]	362,420,421
C	1.8×10^{14}	CVD 850 [422]	3×10^{21}	CVD 500 [423]	422–428
$CdGa_2Se_4$			9×10^{11}	Bridgman [429]	429

Continued on next page

Table 7.1 – continued from previous page

Compound	Max n-type	Synthesis	Max p-type	Synthesis	All Refs.
$CdGeAs_2$	-4×10^{18}	single crystals [430]	2×10^{17}	gradient freeze [431]	348,430–438
$CdGeP_2$	-1×10^{20}	Bridgmann [134]	2×10^{18}	from melt, Mn doped [439]	134,436,439,440
$CdIn_2S_4$	-1.25×10^{19}	Bridgman [441]	-7.2×10^{15}	vaport transport [442]	441–446
$CdIn_2Se_4$	-1.5×10^{19}	zone leveling [447]	-3.9×10^{15}	PLD 100 [448]	447,448
$CdIn_2Te_4$	-3.5×10^{15}	Bridgman [449]	-2.5×10^{11}	Bridgman [450]	348,449,449–452
CdS	-1.1×10^{21}	review [303]	1.1×10^{17}	review [303]	303,453–465
CdSe	-1.3×10^{19}	electrodeposition 500, Cd excess [466]	1×10^{17}	MBE 230, N doped [467]	362,465–479
$CdSiAs_2$	1×10^{9}	CVT [480]	2.4×10^{18}	CVT, B doped [481]	437,480–486
$CdSiP_2$	-1×10^{15}	review [341]	-1×10^{14}	review [341]	341
$CdSnAs_2$	-5×10^{18}	from melt [487]	5×10^{18}	zone recrystallization [488]	487–495
$CdSnP_2$	-8×10^{17}	cooled from melt [496]	-3.6×10^{15}	gradient freeze [497]	496–499
CdTe	-2×10^{18}	Stockbarger, I doped [500]	1×10^{17}	vapor growth [501]	362,465,479,500,500–543
$CuAlS_2$	-7.4×10^{16}	vapor transport [544]	6.3×10^{19}	polycrystalline pellet, Zn doped [545]	350,544–546
$CuAlSe_2$	5×10^{13}	vapor grown [547]	4×10^{18}	MBE 800 [548]	547,548
$CuAlTe_2$	5×10^{12}	directional freezing [549]	8.8×10^{14}	CVD [550]	549,550
CuBr	8×10^{15}	polycrystalline pellet [551]	9×10^{17}	polycrystalline pellet [552]	551,552
$CuCd_2GaS_4$	1×10^{15}	polycrystalline pellet [553]	1×10^{16}	polycrystalline pellet [553]	553
$CuCd_2GaTe_4$			5×10^{18}	from melt [554]	554
$CuCd_2InS_4$	1×10^{15}	polycrystalline pellet [553]	1×10^{16}	polycrystalline pellet [553]	553
$CuCd_2InSe_4$	8.7×10^{15}	Bridgman [555]	1.9×10^{18}	polycrystalline pellet [345]	345,555–557
$CuCd_2InTe_4$	7.4×10^{18}	polycrystalline pellet [558]	5×10^{19}	polycrystalline pellet [345]	344–346,555,558
CuCl	-1×10^{19}	magnetron sputter [559]	-2×10^{15}	magnetron sputtering [559]	559–561
$CuFeS_2$	-3×10^{21}	polycrystalline [562]	7×10^{20}	polycrystalline pellet [563]	562–573
$CuFeSe_2$	2×10^{19}	from melt [347]	2×10^{20}	from melt [347]	341,347
$CuFeTe_2$	5×10^{19}	from melt [347]	5×10^{21}	review [574]	341,347
$CuGaS_2$	4.2×10^{11}	melt grown [575]	5.4×10^{17}	vapor grown [575]	303,350,575,576
$CuGaSe_2$	-1×10^{16}	Ge implantation, Zn anneal [577]	1.2×10^{19}	MOVPE 570 [578]	350,577–584
$CuGaTe_2$	2×10^{17}	flash evaporation 400 [354]	1.1×10^{20}	Bridgman [585]	354,550,585–589
$CuGe_4P_3$			4×10^{20}	crystal [590]	590
CuI	1×10^{18}	sputter 350 [591]	1×10^{19}	sputter 350 [591]	591

Continued on next page

Table 7.1 – continued from previous page

Compound	Max n-type	Synthesis	Max p-type	Synthesis	All Refs.
$CuInS_2$	-1×10^{18}	Bridgman [592]	2×10^{19}	melt and thermal evaporation [593]	350,358,576,592–599
$CuInSe_2$	-7×10^{18}	flash evaporation 490 [600]	1×10^{19}	Bridgman [601]	348,350,582,583,593,600–609
$CuInTe_2$	-2×10^{17}	directional freezing [610]	7.5×10^{19}	Bridgman [611]	303,339,550,585,589,593,610–619
$CuSbSe_2$			5×10^{15}	review [341]	341
$CuZn_2InTe_4$	9.5×10^{18}	polycrystalline pellet [345]	3.7×10^{19}	polycrystalline pellet [558]	345,558
Cu_2CdGeS_4	4×10^{14}	directional solidification [620]	6×10^{16}	directional solidification [620]	620
$Cu_2CdGeSe_4$	6.4×10^{19}	polycrystalline pellet [621]	1.2×10^{21}	polycrystalline pellet [621]	621
$Cu_2CdGeTe_4$			1.5×10^{20}	polycrytalline pellet [340]	340
$Cu_2CdSiTe_4$			8.1×10^{19}	polycrytalline pellet [340]	340
Cu_2CdSnS_4	3×10^{17}	sputter and sulfurize 550 [622]	5×10^{20}	spray pyrolysis 500 [623]	622–628
$Cu_2CdSnSe_4$	2.3×10^{18}	polycrystalline pellet [629]	2×10^{20}	polycrystalline pellet [629]	627,629–631
$Cu_2CdSnTe_4$			2×10^{20}	polycrytalline pellet [340]	340
Cu_2CoSnS_4	2×10^{16}	spin coat and sulfurize 500 [632]	5×10^{16}	drop cast and sulfurize 550 [633]	632,633
$Cu_2FeGeSe_4$			1×10^{19}	from melt [634]	634,635
Cu_2FeSnS_4	1×10^{16}	spray pyrolysis and sulfurize 500 [636]	1.1×10^{18}	cast and anneal 550 [637]	626,633,636–640
$Cu_2FeSnSe_4$	8.7×10^{19}	solvothermal 200 [641]	8×10^{20}	spray pyrolysis and selenize 500 [640]	640,641
$Cu_2Ga_4Te_7$	1×10^{18}	from melt [642]	8.3×10^{19}	polycrystalline pellet [643]	643
Cu_2GeS_3	5.6×10^{15}	vapor transport [644]	3×10^{17}	review [348]	348,644,645
Cu_2GeSe_3	1.5×10^{17}	review [348]	1.4×10^{21}	polycrystalline pellet, Ga doped [646]	348,646–654
Cu_2GeTe_3			3×10^{21}	from melt [653]	653
$Cu_2HgGeTe_4$	8×10^{19}	polycrystalline pellet [340]	6×10^{20}	polycrytalline pellet [340]	340
$Cu_2HgSiTe_4$			2.3×10^{20}	polycrytalline pellet [340]	340
$Cu_2HgSnSe_4$	9×10^{18}	normal freezing [556]	4×10^{19}	polycrystalline pellet [655]	556,655
$Cu_2HgSnTe_4$	1.6×10^{20}	polycrystalline pellet [340]	4×10^{20}	polycrytalline pellet [655]	340,655
$Cu_2In_4Te_7$			5.3×10^{18}	polycrystalline pellet [656]	656
$Cu_2MgSnSe_4$	3.2×10^{18}	polycrystallibe pellet [657]	2.5×10^{20}	polycrystalline pellet [657]	657
Cu_2MnGeS_4			4×10^{17}	vapor transport [658]	658
Cu_2MnSnS_4	4.7×10^{18}	spray pyrolysis 500 [659]	8.5×10^{19}	spray pyrolysis and sulfurize 500 [660]	659,660
$Cu_2MnSnSe_4$			3.8×10^{19}	spray pyrolysis and selenize 500 [660]	637,660
Cu_2NiSnS_4	3.9×10^{18}	dip coat and sulfurize 525 [661]	6.3×10^{18}	dip coat and sulfurize 525 [661]	661

Continued on next page

Table 7.1 – continued from previous page

Compound	Max n-type	Synthesis	Max p-type	Synthesis	All Refs.
Cu_2SnS_3	6×10^{17}	review [348]	2.5×10^{21}	polycrystalline pellet, Zn doped [662]	348,644,662–672
Cu_2SnSe_3	-1×10^{18}	liquid phase reactive sinter, In doped [673]	2.9×10^{21}	polycrystalline pellet [674]	348,653,654,673–684
Cu_2SnSe_4	3.3×10^{18}	polycrystalline pellet [685]	1×10^{21}	Bridgman [686]	685,686
Cu_2SnTe_3			1×10^{21}	from melt [684]	684
Cu_2ZnGeS_4	7.8×10^{18}	vapor transport [687]	1.5×10^{19}	vapor transport [687]	687
$Cu_2ZnGeSe_4$	1×10^{18}	polycrystalline pellet [688]	1×10^{21}	polycrystalline pellet [688]	688–691
$Cu_2ZnGeTe_4$			3.5×10^{20}	polycrytalline pellet [340]	340
$Cu_2ZnSiTe_4$			5.5×10^{20}	polycrytalline pellet [340]	340
Cu_2ZnSnS_4	1×10^{16}	traveling heater [692]	8×10^{19}	magnetron sputter 500 [693]	624,637,692–694,694–716
$Cu_2ZnSnSe_4$	4.4×10^{16}	sputter and selenize 600 [717]	1.8×10^{21}	polycrystalline pellet [718]	378,637,717–732
$Cu_2ZnSnTe_4$	2.9×10^{20}	crystals [733]	3.3×10^{20}	polycrystalline pellet [340]	340,733
Cu_3AsS_4	1×10^{16}	polycrystalline pellet [734]	7.8×10^{19}	review [348]	348,362,734,735
Cu_3AsSe_4	3×10^{17}	polycrystalline pellet [734]	2.7×10^{18}	review [348]	348,734
Cu_3PS4	1×10^{16}	polycrystalline pellet [736]	1.8×10^{17}	vapor transport [737]	734,736–738
Cu_3PSe_4	3.3×10^{16}	PLD and anneal [739]	6×10^{17}	polycrystalline pellet [734]	734,736,739
Cu_3SbS_4	1×10^{16}	polycrystalline pellet [734]	1×10^{21}	polycrystalline pellet [740]	362,734,740–742
Cu_3SbSe_4	3×10^{17}	from melt [743]	3.2×10^{20}	polycrystalline pellet [744]	348,743–753
GaAs	-2×10^{19}	MBE 400, Si doped [380]	5×10^{19}	MBE 800, C doped [380]	380,390,400,471,754
GaN	-4×10^{20}	MBE 1100, Ge doped [755]	5×10^{17}	PSD 480 [756]	383,755–774
GaP	-4×10^{18}	monocrystalline [775]	2×10^{19}	vapor grown, Zn doped [776]	396,775–778
GaSb	-2×10^{18}	Czochralski, Te excess [779]	1×10^{19}	MOVPE 560, C doped [780]	396,397,400,779–785
Ge	-8×10^{19}	solvent growth, As doped [786]	6×10^{19}	sputtered 600, Mn doped [787]	400,786–789
$HgGa_2S_4$			1×10^{8}	vapor transport [790]	790
$HgIn_2Te_4$	-1.5×10^{17}	Bridgman [791]	-3.5×10^{15}	Bridgman [348]	348,791–793
HgS	-3×10^{19}	vacuum deposition, 185 [794]	-1×10^{18}	vacuum deposition 185 [794]	465,794–796
HgSe	-1×10^{19}	review [797]	-3.5×10^{17}	zone melt [798]	465,797–800
HgTe	-6×10^{17}	Bridmann [801]	1×10^{19}	review [797]	465,796,797,801–805
InAs	-8×10^{20}	review [362]	5×10^{20}	review [362]	362,383,396,400,806–813
InN	-8×10^{21}	tube flow method 600 [814]	-3×10^{17}	MBE 380 [815]	396,759,814–824
InP	-4×10^{19}	Czochralski [825]	7.6×10^{18}	diffusion, Zn doped [826]	362,383,390,396,400,813,825–836

Continued on next page

Table 7.1 – continued from previous page

Compound	Max n-type	Synthesis	Max p-type	Synthesis	All Refs.
InSb	-1.5×10^{19}	Te doped single crystal [837]	1×10^{20}	pure crystals [838]	362,396,400,813,837–853
$MgGeAs_2$	-3×10^{18}	MBE260-610, Ge rich [854]	2×10^{19}	MBE260-610, Mg rich [854]	854
$MnGa_2Te_4$			1×10^{13}	directional crystallization [855]	855
$MnIn_2Te_4$			1×10^{12}	directional crysallization [855]	855
Si	-1×10^{20}	review [856]	5×10^{19}	review [856]	400,856,857
SiC (3C)	-2×10^{20}	Czochralski [858]	-1×10^{16}	Czochralski [858]	858–878
Sn (α)	-3×10^{19}	grown from Hg solution [879]	3.1×10^{19}	Hg solution, Ga doped [880]	879–881
$ZnGeAs_2$	1×10^{18}	Bridgman, As annealed [882]	8×10^{19}	cooled from melt [883]	438,882–887
$ZnGeN_2$	-1×10^{19}	vapor-liquid-solid method [888]	1×10^{18}	CVD 850 [889]	888,889
$ZnGeP_2$	1.5×10^{10}	Bridgman [890]	1×10^{18}	directional crystallization [436]	134,436,437,440,491,890–894
$ZnIn_2S_4$			1×10^{17}	vapor transport [895]	895,896
$ZnIn_2Se_4$	-8×10^{16}	vaport transport [897]	-4×10^{13}	evaporated 426 [898]	897–899
ZnO	-1.1×10^{21}	PLD, 400, Al doped [900]	9×10^{16}	MBE, 525, N doped [901]	900–924
ZnS	-5×10^{19}	solvent growth 400, I doped [303]	-4.8×10^{16}	I vapor transport, Zn anneal [925]	303,925–930
ZnSe	-1.5×10^{19}	MBE 280, Cl doped [931]	1×10^{18}	MBE 300, N doped [932]	307,925,929,931–939
$ZnSiAs_2$	2×10^{14}	Bridgman [940]	5×10^{17}	vapor transport [941]	134,940–944
$ZnSiP_2$	-4.8×10^{18}	CVT, Te doped [945]	5×10^{17}	vapor transport [946]	348,945–953
$ZnSnAs_2$	5×10^{17}	crystals [954]	3×10^{21}	from melt [489]	348,489,954–959
$ZnSnN_2$	-1×10^{21}	MBE 400 [960]	-2.3×10^{17}	magnetron sputtering 400 anneal [961]	960–967
$ZnSnP_2$	6.6×10^{16}	cooled from melt [968]	1.4×10^{17}	melt grown [969]	968–971
$ZnSnSb_2$	1×10^{19}	from solution, Zn excess [972]	1×10^{21}	from solution, Sn excess [972]	972,973
ZnTe	-4×10^{17}	MOVEPE 380, Al doped [974]	1×10^{20}	MBE 280, Te excess [931]	465,541,931,935,974–988

Due to carrier concentration spanning many orders of magnitude, both n and p-type, experimental data must be appropriately scaled before modeling. By using the -5 to +5 scale discussed in Methods to describe carrier concentration, the distribution is fairly normal in DLS compounds, allowing more accurate modeling, as shown in Fig. 7.2. There appears to be two distinct sides to the distribution, with more p-type than n-type compounds. This is due to historical bias, as more Cu-containing than Ag-containing ternary and quaternary compounds have been investigated.

The dopability dataset scraped from literature reports of carrier concentration is presented in Fig. 7.3. The width of each bar represents dopability range for 127 compounds found in the comprehensive literature search. While the theoretical limits on dopability are determined by defects and chemistry (see Fig. 7.1), there are also practical limits due to historical research which we call "persistence." The more times a compound has been reported, the more likely it is that someone has pushed the dopability limit. This is highlighted by the color shading in Fig. 7.3. The persistence is quite varied, from 1 report of carrier concentration in a compound to dozens, with the average or median value being $\sim$5 per compound. For compounds which have not been measured with high persistence, for only a single application, or that have not been made with the explicit goal of exploring the the full dopability range, it is likely that only a single distribution (n-type, intrinsic, or p-type) has been investigated. Whether intentionally or not, compounds which have been studied extensively are more likely to have been sampled in each distribution, thus pushing the dopability limits (Fig. 7.10). While one may intuit that the low-persistence compounds could be ignored, we provide two virtual experiments (Fig. 7.11) that demonstrate we should not ignore these compounds in modeling the dataset and instead use this

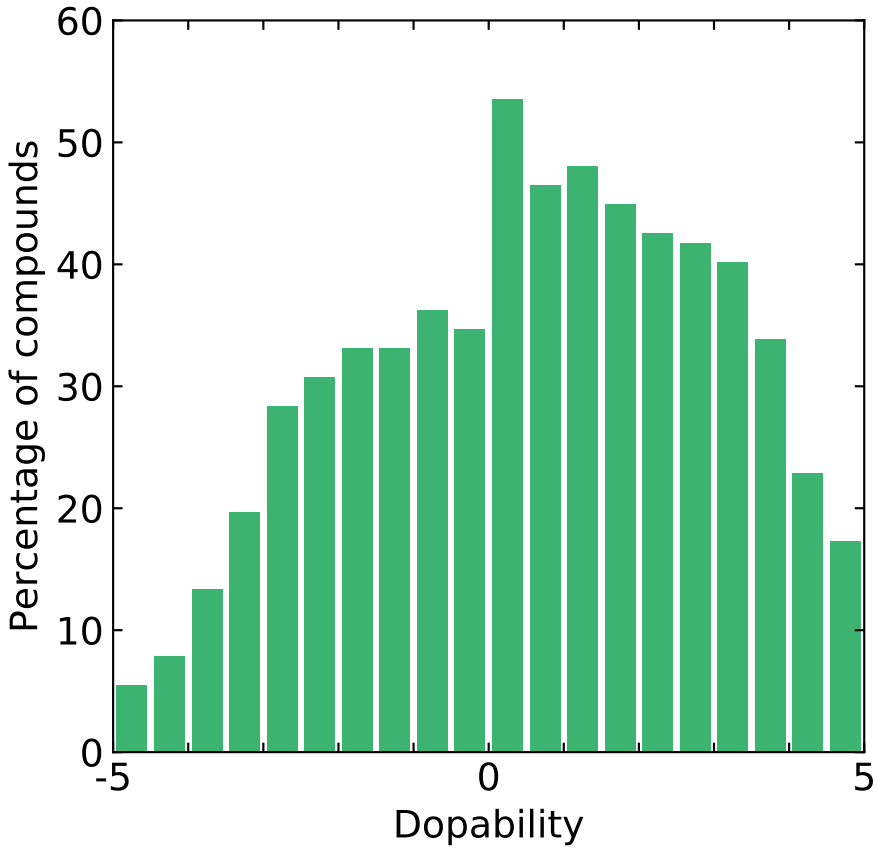

Figure 7.2. **Experimental Data Collection and Scaling** Dopability in DLS compounds follows a fairly normal distribution when put on the -5 to 5 scale as described. This also demonstrates that there are more p-type DLS compounds than n-type, largely due to the ternary and quaternary Cu containing compounds.

persistence value in weighing the data for fitting. The effect of persistence and historical bias and how we should handle this issue will be discussed in later sections.

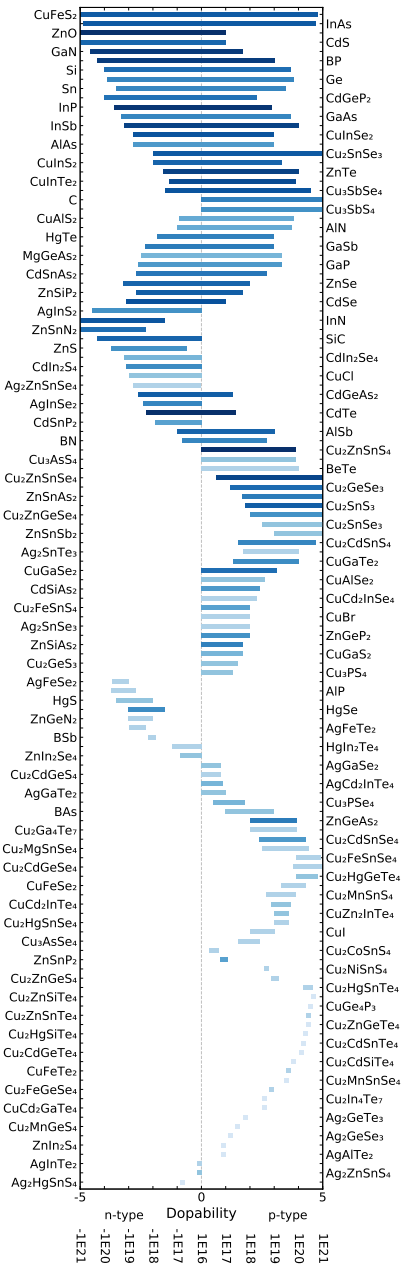

Figure 7.3. Experimental dopability range for diamond-like semiconductors collected from literature data. Left end of bar represents highest n-type carrier concentration while right side shows highest p-type achieved. Top to bottom order chosen to minimize both the difference in dopability range and the left/right displacement of the bar. Compounds with more experimental measurements are darker blue.

7.4. Feature Preparation for Modeling

A set of features for each compound to serve as inputs to the model were assembled from periodic table properties, DFT calculations, and other sources gathered by hand. A flowchart describing feature preparation is shown in Fig. 7.4. All of the elements in a compound are considered as one group from which elements are further split into one of two additional groups: anion (the element which is from the rightmost column on the periodic table), and cations (all other elements). Features for these groups are determined based on a set of properties and a set of mathematical relationships as listed by applying each math function to each property for each compound. In this set of compounds, there is only a single anion in any given system, thus each of the periodic properties for the anion are also added to the feature set. Additionally a pairwise comparison between the anion and each cation present in a compound was also added to the feature set.

Beyond these periodic table properties obtained using Pymatgen's featurizer,[989] inexpensive DFT properties were added to the feature set from the Open Quantum Materials Database[94,95] and Materials Project[96–98] including formation energy, band gap, bulk modulus, shear modulus, and band offset terms, and Madelung energy. Furthermore, the Bader charge analysis code[990–993] was used to calculate the Bader charge for each element in the compounds and a set of properties were determined in the same way as the periodic properties. Finally, a few hand selected features were added such as describing the number of unique elements in a compound, the structure (based on diamond, zinc-blende, wurtzite, or defect), or the presence of unique atoms such as copper or silver.

The resulting 116 features were standardized and scaled to unit variance (sklearn.preprocessing.StandardScaler) prior to the bivariate correlation being calculated

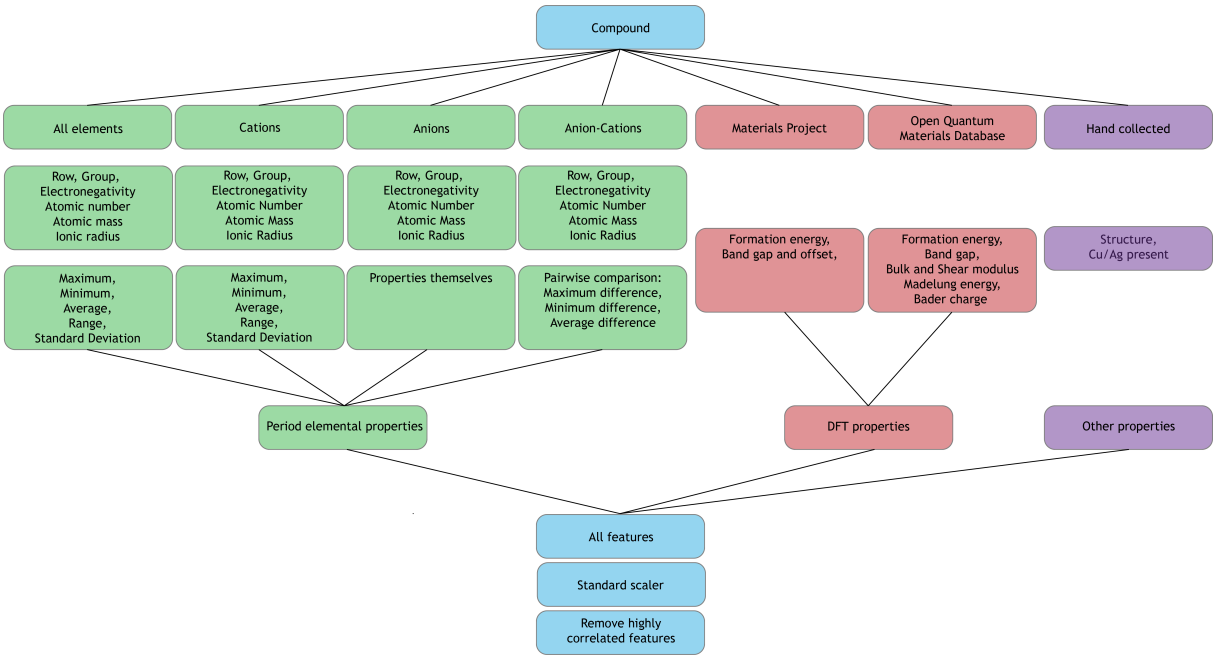

Figure 7.4. Flowchart for feature preparation in modeling DLS compound dopability. For each compound, features from periodic table information, DFT calculations, and other infomration is assembled. Once this is done for all compounds, the features are scaled based on the mean and variance, their cross-correlation is determined, and highly correlated features are removed.

for each pair of features. Then one of the features was removed if the pair had a correlation greater than $|0.9|$. The resulting set of 42 uncorrelated features were used for further analysis. It should be mentioned that it is impossible to definitively determine which property or feature is the one that controls dopability among two or more that are highly correlated with each other, we can only say that at least one of these correlated features is important.

7.5. Model Selection: The Case for Simplicity

Having established that the experimental dopability depends on a multitude of features, the most appropriate type of model for this problem must be chosen. Here a

discussion of the pros, cons, and assumptions of various model types is warranted. For any model, there are trade-offs between the interpretability of a model and the assumptions or constraints that are necessary. On one end of this spectrum is a linear model which is highly interpretable but presumes that there is no interaction between the inputs and that the relationship between the response and the input is linear. While this type of model is simple, robust, and easy to interpret, we might presume that there would in reality be some interaction between various material properties and that at least some of them are likely to have a non-linear effect on carrier concentration. Given these two drawbacks to a linear model, a possible alternative is random forest which does not necessitate a linear relationship. Random forest models are typically a good choice for ease of use in that they require little parametric tuning and are robust to outliers and overfitting. The trade-off though is the computational cost for large datasets and the loss of interpretability. On the far end of the spectrum is deep learning or neural networks which work well for large datasets and complex interactions both between multiple varaiables and between each variable and the response. The downside of neural networks is that they require larger datasets for training and testing, additional parameter tuning, and are much like a "black box". But for certain problems, the increase in prediction accuracy for neural networks is worth the loss of interpretability.

Model selection was performed by implementing a gridspace search over basic parameters to optimize each of the model types, using the mean absolute error (MAE) on the test set to score performance (lower MAE means less difference between experimental and predicted values). All modeling was done using Python Scikit-learn (sklearn) with the same set of inputs and targets using k-fold cross validation with k=5. For linear

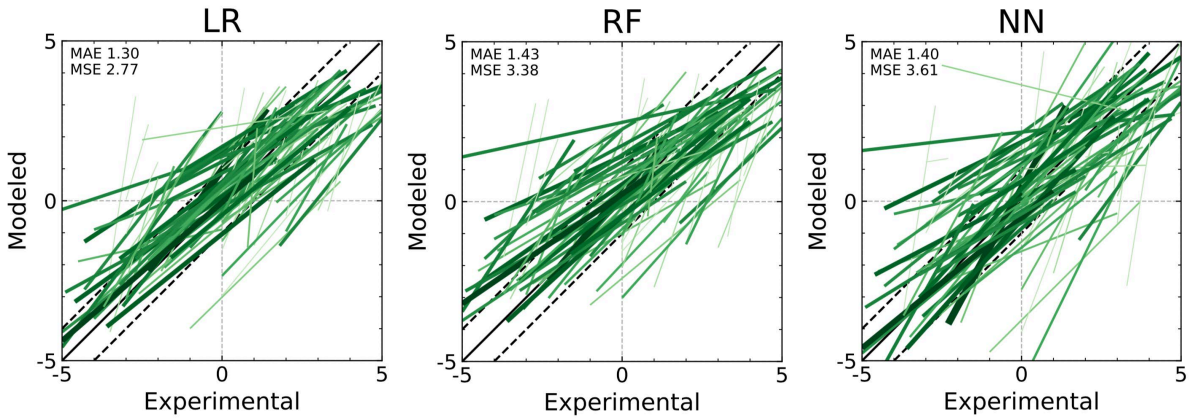

Figure 7.5. A comparison of basic optimization for linear regression (LR), random forest (RF), and neural network (NN) models. The green line represents dopability range for each individual compound, joining the scatterpoint ends which represent the maximum n-type (left) and maximum p-type (right) carrier concentrations. Compounds with more experimental reports of carrier concentration have lines that are thicker and darker green. Solid black line represents perfect prediction accuracy, dashed lines correspond to one order of magnitude difference.

regression the L1 regularizer ($alpha$=0.125) was varied, for random forest the number of trees ($n_{estimators}$=200) was varied, and for the neural network with three hidden layers, it was the number of neurons in each of the layers ($hidden\_layer\_sizes$=200). Shown in Fig. 7.5 is the first-pass optimized version of each model type (optimized parameters given in parentheses in previous sentence). While each model is likely to be improved with more careful parameter tuning, this shows that the accuracy of the predictions from each of the models is similar. Since the linear model is simple and interpretable, it is attractive as we are interested in not just making predictions, but in understanding the properties that lead to dopability. Therefore the linear model is the one of choice given that it is similar or even slightly better than the random forest and neural network models.

While these more complex models are generally believed to be more accurate for most situations, there could be reasons why that is not the case here. One must first consider the dataset. In a materials science scenario such as this, the limiting step in building a dataset is not in generating features but in collecting samples. Whether this involves synthesis and characterization of new samples or assembling measurements from literature reports, this is a very time-intensive process. On the other hand, generating more features is much less expensive, whether it involves large-batch DFT calculations or including additional features or mathematical relationships between those properties of each element. This is contrary to many data science cases where the response is known for hundreds or millions of samples but only a limited number of inputs can be collected. In this dopability dataset, we start with more features than samples, though final modeling is performed at approximately a 2:1 samples to inputs ratio after removing highly correlated features and samples with insufficient data. While random forest and neural network models excel in large, complex scenarios, some argue that they are not as well suited for small datasets where overfitting can be an issue. Additionally, the bias/variance tradeoff must always be considered, with simpler models generally having high bias/low variance and more complex models having low bias/high variance. While a simple linear model may have a high bias and underfit the data, it will likely produce less variance in predictions beyond the training set.

7.6. Refinement of Linear Model

Using leave-one-out cross validation, a model was fit to the diamond-like semiconductor dopability data using LASSO. Shown in Fig. 7.6 are the mean coefficient values and

the mean plus or minus the standard deviation for each of the features. The inputs are all of the uncorrelated features and shown here are all features with at least one non-zero coefficient. The standard deviation is very tight, demonstrating the training of the model is robust in terms of the dataset and iteration. The top to bottom order of the features is in descending order of the sum of the absolute value of the coefficients, indicating some relative order of importance.

Following adoption of this model, further refinement is necessary. While the sklearn LASSO (least absolute shrinkage and selection operator) model performs some feature selection, it lacks functionality that is important. The nature of the data collection for dopability in this study leads to differences in the confidence we should have about the dopability range in compounds. Those that have been studied more for various applications naturally have larger carrier concentration ranges while those that have only a few literature measurements have narrow reported experimental dopability windows. This will be discussed in more detail in later sections. Therefore we would like to apply a sample weighting scheme that places more weight in training the model on compounds which have more experimental measurements. We would also like to place confidence intervals on the predictions due to uncertainty in the experimenal measurements. Linear regression and other models predict the mean value, while we are interested in the extreme limits of dopability, therefore confidence and prediction intervals were calculated to determine reasonable estimates of these limits.

Further refinement is performed using the weighted least squares (WLS) function in StatsModels which allows the use of weighting and calculation of confidence and prediction intervals. Refinement was done by simultaneously performing a gridspace search over

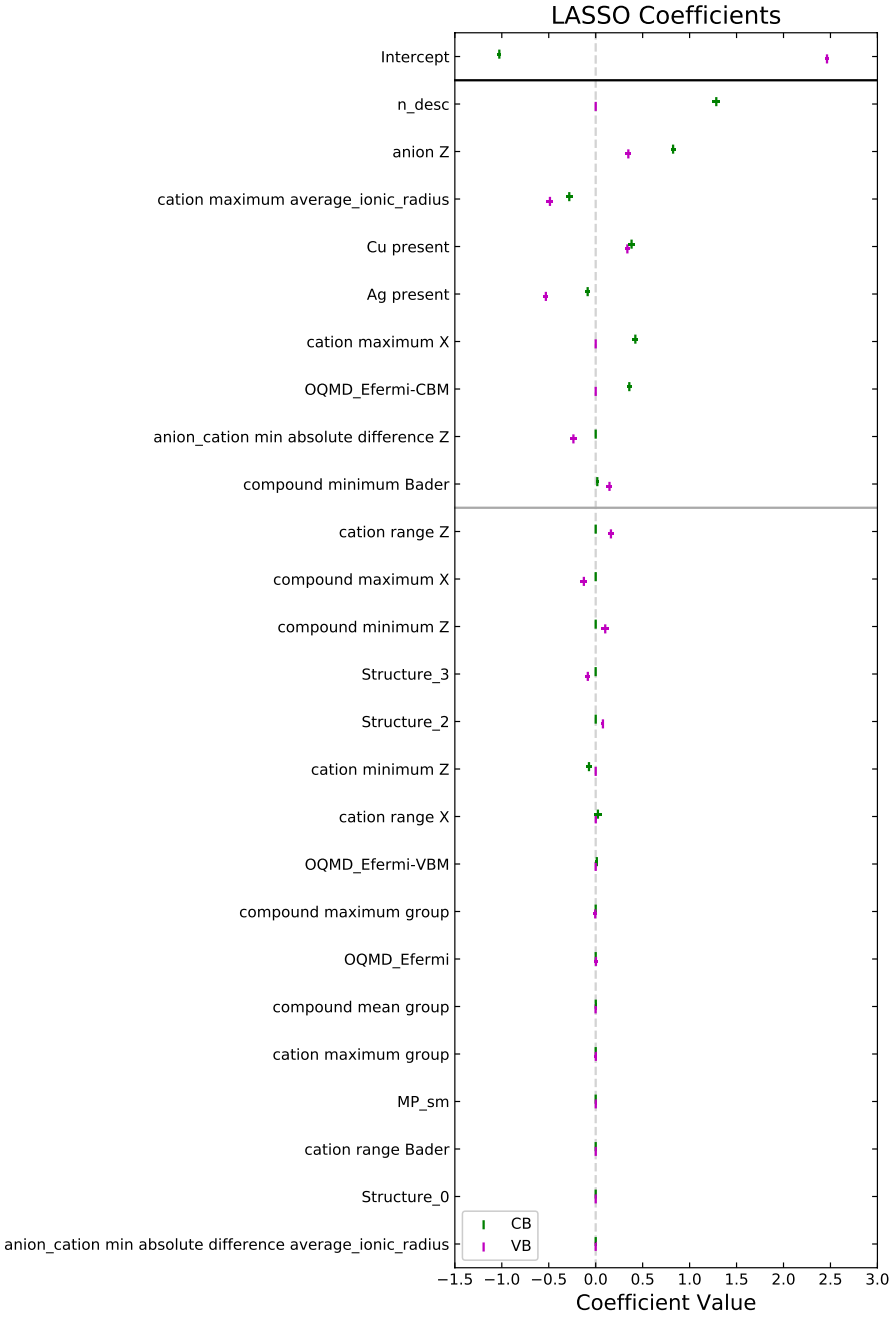

Figure 7.6. Non-zero coefficients for unrefined linear regression (no additional feature selection or sample weighting) using uncorrelated feature list. Model fit using LASSO with L1 regularizer set to *alpha*=0.125 and leave-one-out cross validation. Vertical bar represent the mean coefficient and horizontal bar is the mean plus/minus the standard deviation.

sample weights while removing features with coefficients near zero as determined by the LASSO model. Monitoring of the MAE, MSE, and adjusted R^2 using LOOCV was carried out. The best predictions without overfitting are the model where the MAE and MSE are minimized and the adjusted R^2 is maximized. For this dataset, the optimum features will be discussed later and the optimum weight was determined to be $(N/N_{max})^{0.2}$ where N is the number of literature reports for a given compound and N_{max} is the maximum number of experimental reports (95 for CdTe). This means that in training the linear regression model, CdTe is weighted as being approximately 2x more important than compounds which have only one experimental report of carrier concentration. Transformations of the features prior to introduction to the model were also attempted such as log base 10, natural log, polynomial expansion, and a combination of these, but no improvement was observed.

7.7. Comparison of Experimental and Predicted Dopability

The resulting predictions of the optimized model using leave-one-out cross-validation (LOOCV) are shown in Fig. 7.7. This figure contains only the subset of DLS compounds for which both experimental dopability data could be found as well as properties from DFT databases (OQMD and MP) had been calculated, and defect structures were removed. The experimental range is shown with a blue bar representing the maximum extent of dopability in both directions observed in a given compound. A seperate model is used to predict the maximum dopability on each side, with the predicted dopability range being all values between these maxima and given by the red bar. Since this model predicts the mean value for dopability, where we are interested in the maximum extent, a 50%

prediction interval is given by the grey error bars. The prediction interval is calculated individually for each type (n/p) and compound, but in this dataset the bars are largely the same length, indicating the compounds are fairly evenly distributed across the feature space. As the left and right sides of this dopability range are predicted separately, there is a difference between the accuracy of these individual models. The MAE of the CB is 1.16, while for the VB it is 1.22, giving an average MAE of 1.19 (about one order of magnitude in carrier concentration on average), demonstrating the model is roughly equally predictive of both n- and p-type carrier concentration. The predictive quality of this model has thus been established using LOOCV demonstrating the ability to predict dopability using this data collection and statistical fitting method.

Careful observation of the experimental dopability dataset reveals some trends and these trends are captured by the model. A few of these trends are highlighted here and are discussed in more detail in the next section.. The first trend that is captured is in the Group IV compounds, where Si, Ge, and Sn all have quite large carrier concentration ranges across n and p-type while C can only be made p-type and SiC only n-type. Second, in binary materials, there is a clear trend in II-VI compounds where dopability shifts from left to right (n towards p-type) as you move down the anion group which is not observed in experimental III-V data. Third, compounds of the II-IV-V_2 family show a similar trend in the experimental data for those with Zn but not those with Cd. Finally, in I-III-VI_2 compounds, Cu-containing compounds are much more p-type whereas Ag ones are intrinsic or n-type. The predictions for all of these sub-families of DLS match qualitatively with the observation of experimental trends and are discussed in more detail in the following section.

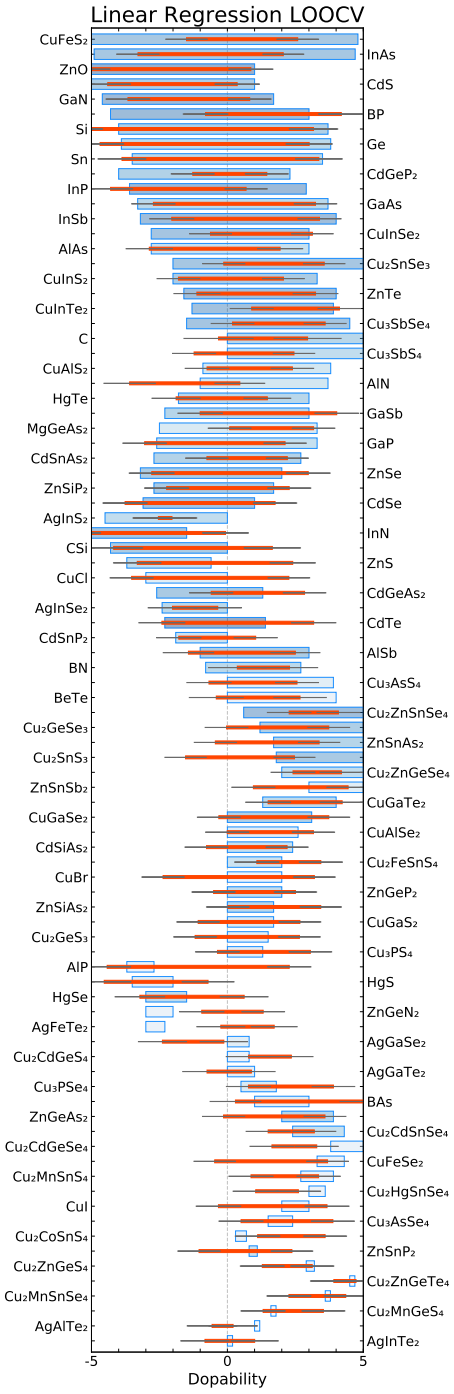

Figure 7.7. For each compound, the experimental range is shown in blue and the prediction in red (shade of blue denotes experimental persistence). Grey error bar style lines represent a 50% prediction interval for both the n and p-type models. Top to bottom order is the same as in Fig. 7.3.

7.8. Experimental Trends Captured by Model

Trends in the experimental carrier concentration ranges of subgroups of the DLS family can be observed, as seen in Fig. 7.8. In Group IV compounds and Cu or Ag I-III-VI_2 compounds there is a distinct dilineation of the carrier type (n or p-type) and in select binary and ternary compounds there are periodic trends. These are largely captured by the model and discussed in more detail here.

The first observation is that Si, Ge, and Sn all have quite a large carrier concentration range for both n and p-type while C and SiC can only be made a single type (all experimental measurements are for 3C SiC which has the zincblende-type structure and is the structure which has carrier concentration reported most commonly). For n-type diamond or p-type SiC, there are few reports and those that are available were deemed unsatisfactory for these purposes due to non-equilibrium processing conditions. Carbon is doped fairly easily p-type using B, but it is much more challenging to achieve reasonable n-type carrier concentration. Nitrogen is the most logical donor element but N_C is a deep donor due to the formation of a dangling bond on one of the carbon neighbors and a lone-pair on the nitrogen.[994] Another potential n-type dopant, phosphorus, has a smaller donor level but it is still fairly deep, 0.6 eV, leading to low carrier concentration. Complicating the n-type dopability in C is that the lattice constant is quite small so substitution causes deformation in the region of the dopant leading to low solubility of dopants. In SiC, n-type carrier concentration is readily varied by incorporation of N, which acts as a shallow donor, through the gas phase. In 4H SiC, reasonable p-type carrier concentrations have been achieved with Al as the acceptor and vapor phase epitaxy, but no bulk samples produced under near-equilibrium processing conditions having modest

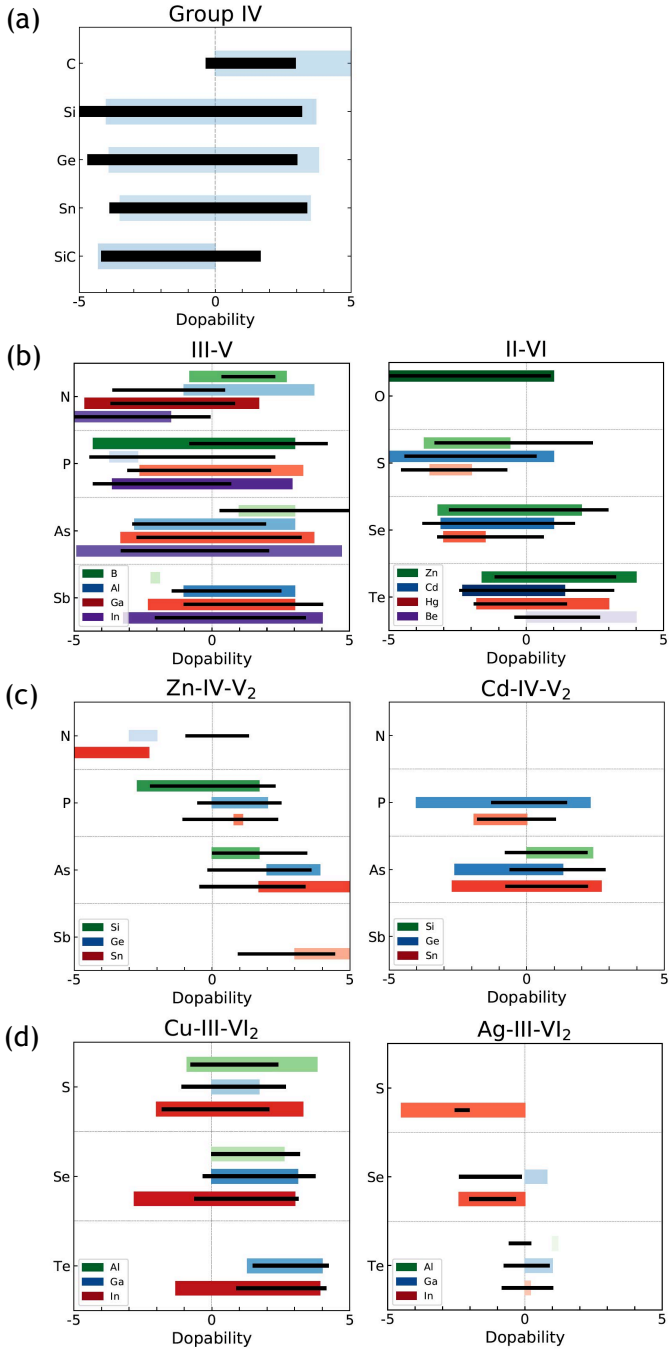

Figure 7.8. Observations of trends in experimental dopability data are reproduced by this model. In (a) and (d), the charge carrier type is correctly predicted, while in (b) and (c) the periodic trends are replicated. All experimental ranges presented in color, with darkness representing number of measurements, and predictions shown using the black bar.

p-type carrier concentrations have been reported based on our literature search. These are both examples where there are no "killer" defects but the carrier concentration is limited due to dopant solubility issues. The linear model largely predicts the dopability in each of these compounds correctly. Si, Ge, and Sn have large dopability ranges for both experiments and predictions. For C, the predictions and experiments are mostly p-type only, and for SiC they are both mostly n-type. It is interesting to note that for C, the n-type tail is nearly non-existant, in agreement with the experimental results as discussed, indicating the model has captured the solubility limitation even though there is no killer defect. On the other hand, we should expect that p-type SiC in the 3C structure is achievable to 1×10^{18} cm^{-3} plus or minus an order of magnitude based on the combination of predictions from this model and experimental realization in 4H SiC.

Due to the larger number of binary compounds the trends in carrier concentration are more apparent but are also somewhat convoluted. Looking at the right panel in Fig. 7.8b, two trends emerge in the experimental data. The first is that experimental carrier concentration shifts from left to right (n-type to p-type) as you move down the anion group. This is most apparent by viewing each bin as a whole or by looking at only the Zn or Cd compounds. This matches both the predictions and the coefficients (see Features 2 and 5 which relate to the atomic number and Bader charge of the anion). The second trend is that as you move down the cation group, the shift is from right to left (p to n-type), which again matches the predictions and the linear model (see Features 3, 7, and 8 which relate to the ionic radius electronegativity, and atomic number of a cation becoming more similar to that of the anion). There is also a trend in the predictions caused by the model coefficients to trend toward a smaller dopability range as you move

down the cation group but this is less apparent in the experimental data, likely due to the lack of measurements outside of the Se containing II-VI compounds. Interestingly, these same trends are not as visible in the III-V DLS experimental data. The left to right shift based on the anion as well as the right to left shift based on the cation are both much less pronounced in the experimental data, though they still appear in the predicted dopability due to the model being the same. Our hypothesis is that the dopability limits have been pushed further in these compounds due to their more extensive use in a variety of applications.

The dopability in ternary compounds has been studied less intensely than in binary ones, leading to fewer literature reports of carrier concentration on average. Additionally, although more combinations of elements in the structure type are possible, a smaller fraction have dopability reports. Nonetheless, it is interesting to observe the top left to bottom right shift of experimental dopability in Zn-IV-V_2 compounds, noticeably in the P and As groups, which is not present in the Cd-IV-V_2 compounds. As mentioned previously, Cu and Ag seem to behave fundamentally differently in ternary and quaternary chalcogenides. There are fewer quaternary compounds with sufficient experimental data but a comparison of I-III-VI_2 compounds offers ample evidence. Comparing Cu/Ag analogues with the same III and VI species shows that the center of mass of the experimental dopability for the Ag version is always further left than the Cu one; this is again captured by the model. It should be noted that the only Cu-III-VI_2 compounds with even moderate n-type carrier concentration are those containing In. This may be an example of the "persistence effect" as these are most investigated leading to the dopability limits being pushed further. Parsing how features in the model influence the predictions in ternary

compounds is even more challenging than for binary compounds due to the added complexity, necessitating further experimental investigation and defect calculations to help elucidate the trends and their causes.

7.9. Model Interpretation

Rather than serving only as a prediction engine, the hope is that some physical insight can be gained through interpretation of the resulting model. As this is a linear regression, it has an intercept (baseline n/p-type dopability) and a number of features that modify the intercept based on the coefficient value associated with each of them. Therefore, Fig. 7.9 can be interpreted by looking at the sign and magnitude of the coefficient value of each feature in relation to that of the intercept. Features whose coefficients are opposite in sign to their intercept contribute to lowering the carrier concentration range for either the n/p-type side. The eight features of Fig. 7.9 constitute the set which provide the best fit (lowest MAE) before overfitting begins by the addition of more features. Each of the features and their associated coefficient values will be discussed individually but viewed together, there are three drivers of dopability in this model: substitutional defects, other chemistry related features (including lattice and electronic energy), and practical limits due to historical persistence.

The first set of coefficients to discuss are those that are partly related to the persistence limitation and more broadly the historical bias of prior experimental work: the intercept, Feature 1, and Feature 4. The sign of the intercept is as we should expect, negative for n-type and positive for p-type. A large number of p-type Cu-containing compounds form the learning set (over 45%), thereby making the intercept for the p-type prediction quite

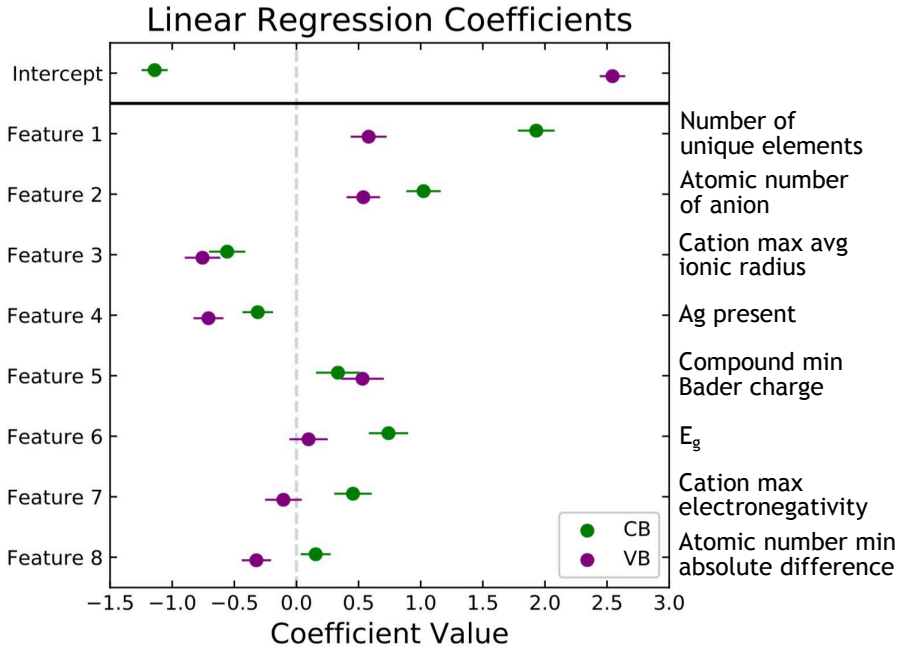

Figure 7.9. Linear regression intercepts and coefficients that were most important in determining carrier concentration ranges. Separate models were fit for n-type (CB) shown in green and p-type (VB) in purple. Error bars represent a 50% confidence interval for the coefficients. Features are in descending order based on the sum of the absolute value of the coefficients.

large. Conversely, the low individual persistence of these Cu-containing compounds yields a narrow dopability window and thus a smaller n-type intercept.

Feature 1 represents the number of unique elements in a compound; both coefficients are positive and the n-type value is significantly larger than the p-type value. In other words, the range shrinks and becomes more p-type with increasing number of unique elements. Unary and binary compounds have been well studied and thus their experimental dopability range is quite large, while ternary and quaternary compounds have less reports in the literature and smaller experimental dopability ranges. The impact of number of unique elements is not *a priori* obvious; as the number of sites increases, there are more

possible sites to dope but also more possible substitutional defects that could pin the Fermi level. Again, the Cu-containing compounds induce this shift due to their native p-type behavior and limited persistence.

Feature 4 is whether silver is present in the compound, driving the dopability more n-type with a smaller range. Since many of the Ag containing compounds have low p-type carrier concentration (more intrinsic) or are n-type, the presence of silver as one of the elements in the composition drives both the CB and VB more negative (Feature 4). As the model is heavily biased by Cu-containing compounds, the presence of Ag thus requires a correction to overcome this difference. Once again, persistence is relevant as the Ag-compounds likewise have limited persistence and a small range.

The next set of features all relate to the cations and their similarity to the anion: Feature 3 is the maximum cation average ionic radius, Feature 7 is the maximum electronegativity of the cations, and Feature 8 is the minimum absolute pair-wise difference in atomic number between the anion and each cation. The effect of Features 7 and 8 are quite similar; when there is cation that is more like the anion in electronegativity or atomic number, the carrier concentration is pushed toward intrinsic and the compound has a lower dopability range. This can be seen as the mean VB coefficient for both of these features is negative and the mean CB coefficient is positive, both opposite of the VB/CB intercept. Since the VB coefficient for Feature 3 is negative (opposite VB intercept) and more negative than the CB coefficient, the dopability range decreases and shifts toward n-type when there is a cation with a similar ionic radius as the anion. Our interpretation of these trends is that these three features, each relating to having at least one cation that is similar to an anion, whether in size, electronegativity or atomic radius, reduce the

dopability range. Such reduced range may be due to the emergence of low energy 'killer' compensating defects.

The other important features are related to chemistry but not closely linked to the concept of substitutional defects. Feature 2 is the atomic number of the anion; therefore the trend is that as the anionic species is found further to the right and bottom of the periodic table, the compound is more p-type and has a smaller dopability range. Feature 5 is the minimum Bader for the compound, and in this case, the minimum Bader charge is always that of the anion. The Bader charge is an approximation of the total electronic charge of an atom and depends on both the chemistry and structure of the compound. The coefficients for the linear model imply that as the anionic element becomes more positive (i.e. less negatively charged), the anion less strongly holds the electrons and the compound becomes more p-type and the dopability range increases. This matches our intuition that compounds that are more covalent and less ionic are more dopable. Similarly, Feature 6 is the band gap from OQMD, with larger band gaps leading to a slightly more p-type material but one with a much smaller dopability range, again matching our intuition.

Phase competition has been found to affect dopability in materials.[995] The number of elements plays a role in phase competition as there are likely to be more possible compounds in the phase diagram as the number of elements increases; as such, this prior work can be related to Feature 1. Another factor that enters into dopability is the energy of the lattice,[304,306] captured in this model by the Bader charge in Feature 5. It has long been assumed that compounds with larger band gaps are harder to dope, however more recent work has found that the band offset and the position of the band extrema relative to the Fermi stabilization or pinning energy is what controls doping limits.[303,306,309,996] These

computational efforts find universal band alignment relate dopability in DLS compounds to the relative position of the VBM and CBM, creating 'Pauling-esque' rules. However, these are not linked directly to the elements that are present and the trends in associated properties of those elements and compounds, therefore the remaining features are not directly comparable to previous computational work.

7.10. The Effect of Persistence

The compound-by-compound predictions generated using this model are shown in Fig. 7.7. However, by grouping these compounds based on the number of times the carrier concentration has been reported in the literature, an interesting trend emerges. In Fig. 7.10, the predictions are broken into roughly equally sized groups based on the number of experimental measurements in the literature for each compound. This illustrates the motivation behind using sample weighting in fitting the linear regression model. By grouping compounds, it becomes apparent that those with many measurements are predicted more accurately. For these compounds, we can be more confident that the experimental dopability range has been fully explored. The lines for these compounds are at approximately a 45 degree angle or less, indicating that the total dopability range is modeled accurately or even underpredicted. This trend toward underpredicting dopability limits in well-studied compounds can also be seen by the endpoints of the green lines. In the bottom left quadrant of the panel the lines end within or above the dashed order-of-magnitude lines while in the top right quadrant the lines generally end within or below the dashed lines. This means that the model is, on average, underestimating the maximum n/p carrier concentration limits observed experimentally for compounds with many measurements. On the

other end of the spectrum it can be seen that the compounds with few measurements have lines that are generally much greater than 45 degrees, even approaching vertical. This is because these compounds have very limited dopability range as reported experimentally. This is due to the lack of literature measurements, even when we would expect their true dopability limits to be larger. This is the "persistence limitation," that the dopability limits are not fully explored in compounds with fewer reports of carrier concentration. Our expectations are captured by the model, which predicts larger dopability ranges than have been reported experimentally for these compounds.

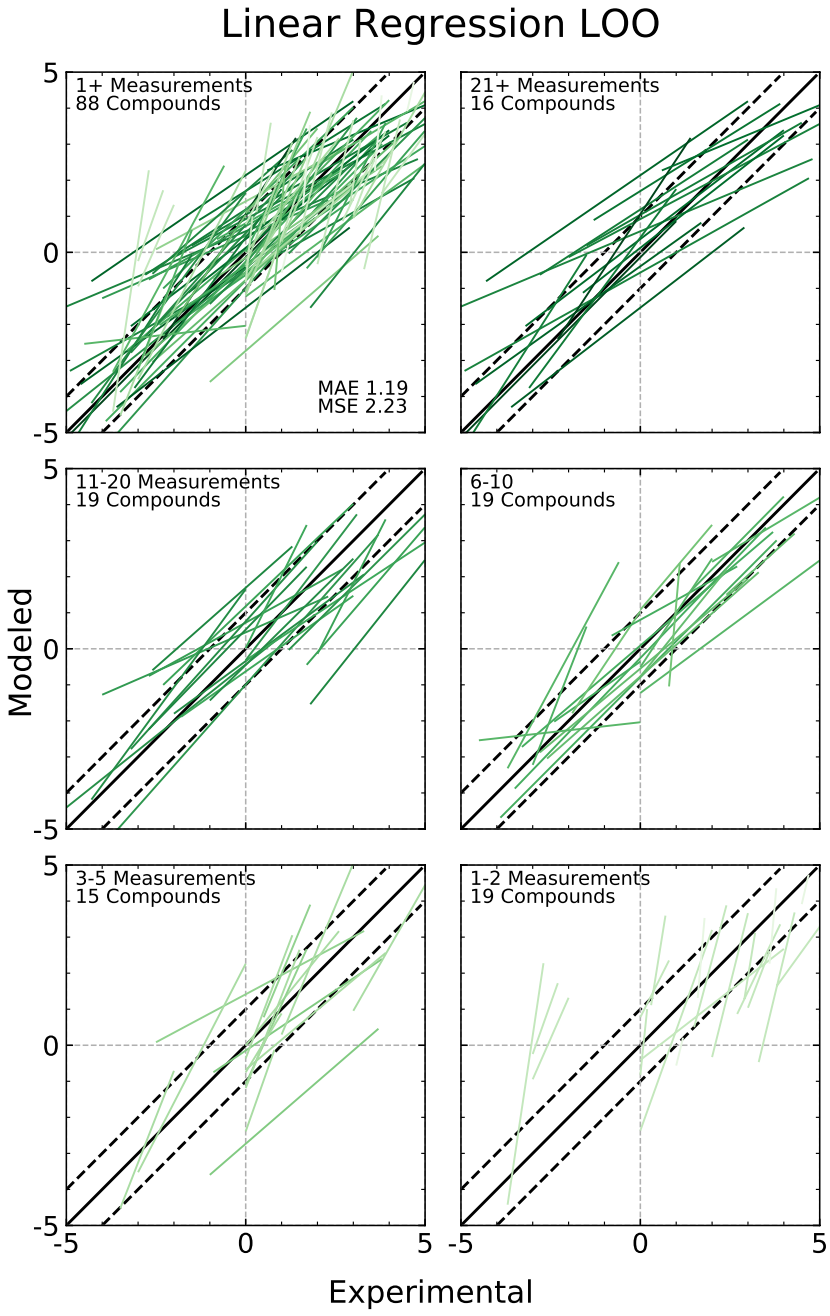

Figure 7.10. Optimized linear regression model showing compounds grouped into roughly equal sized bins by the number of experimental measurements (darker green indicates more measurements). Compounds with more measurements are predicted better than those with few measurements. This indicates that the doping limits have not been fully explored in compounds that have less persistence.

7.11. Virtual Experiments

Such observations elicit a clear question. Even with using a sample weighting scheme for training and scoring the model, could it be improved by removing from the dataset entirely those compounds which have few experimental measurements? If we are to believe that every compound has some positive finite dopability range, then we are training the model with samples for which we know theoretical dopability is larger than what has so far been reported in the literature (i.e. the values we are training the model on are wrong). For those with only a few measurements, it is likely that the theoretical range has not been fully explored experimentally. Taking this to the extreme, compounds measured only once have no range experimentally (they are given an arbitrarily small range of 0.1 for the purposes of visualization), even though they have at least some theoretical dopability range. This idea was explored by conducting two virtual experiments and comparing each of them to the predictions of the weighted model using the entire dataset.

In Fig. 7.11a, the panels with the title "All" are those with the predictions generated using the standard LOO model using the entire dataset. Each panel shows only a subset of the compounds, with those on the left including a larger percentage of the dataset (all compounds with 3 or more measurements) and those on the right showing fewer (only those compounds with 21 or more measurements). The panels with titles "Confident" are predictions using LOO but removing part of the data and showing what is not removed. Therefore, the top and bottom panels show the same set of compounds, the difference is that the top panel is fit using all compounds in the dataset, and the bottom panel is fit using only the compounds shown in that panel (compounds we are more confident in the dopability limits due to persistence). What can be seen is that toward the left, when the

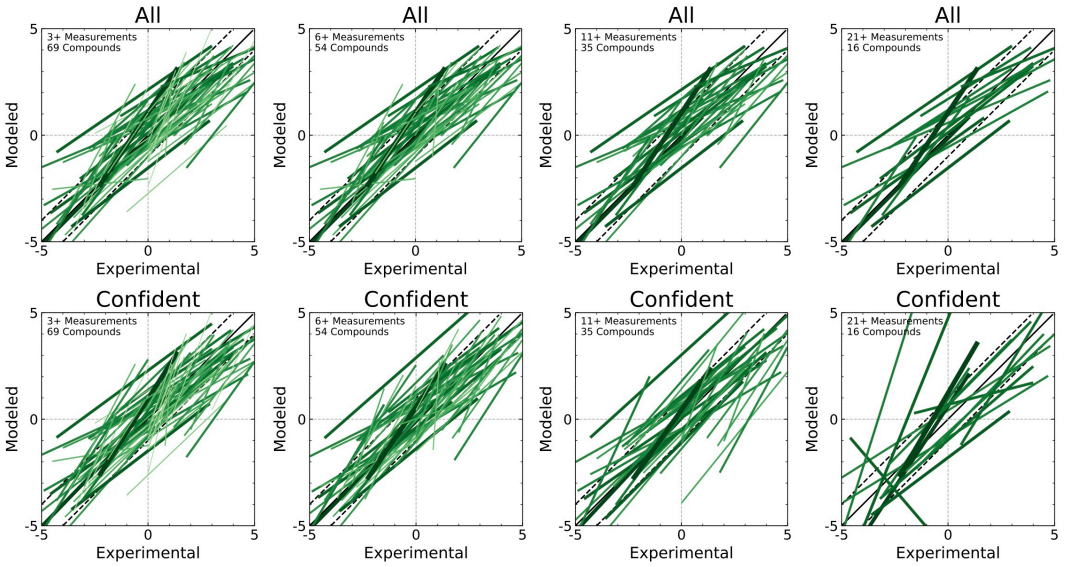

(a)

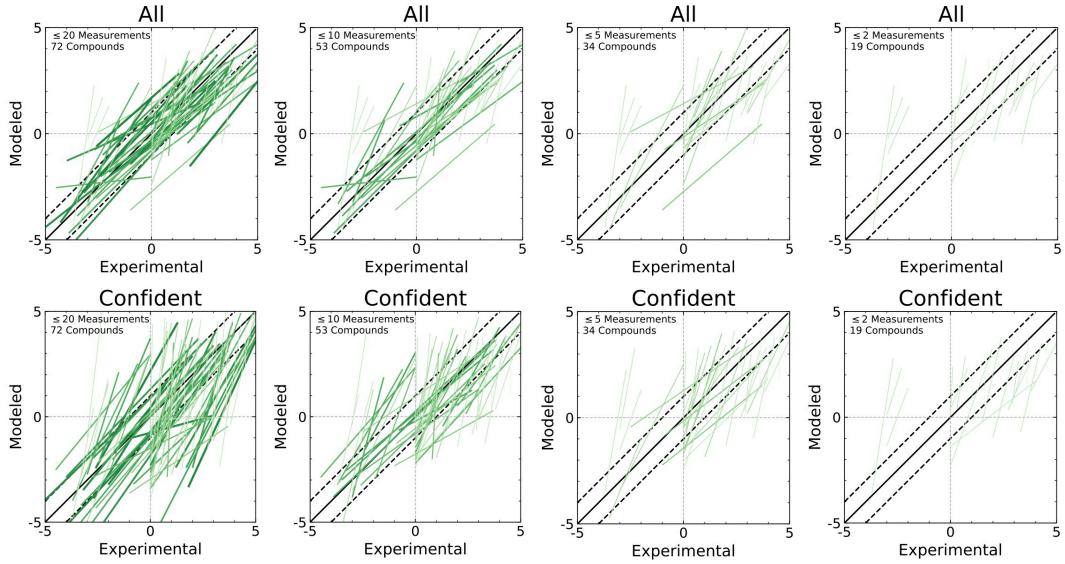

(b)

Figure 7.11. Two virtual experiments to test the effect of persistence in experimental measurements and whether the model can be improved by not fitting model to compounds where the dopability bounds have not been fully explored. Compounds with more experimental measurements shown using darker and thicker lines. These results indicate that predictions are not improved when low persistence samples are removed, indicating that while the information they contain is imperfect, it is still useful or important.

dataset is more complete, the predictions are largely the same. But as compounds are removed from the set used for training the model, the predictions get worse, even though the compounds that were removed are those we are less confident the dopability limits have been fully explored experimentally.

A second virtual experiment is shown in Fig. 7.11b that attempts to answer a similar question from a different angle. Here we hold an entire group of compounds out, train the model on all compounds that have been experimentally measured more times than some mask, and then predict the limits of the compounds that have been measured less than the mask. Using this work-flow, the "Confident" panels were generated by holding back some subset of compounds, training a single model on those compounds which have been measured a sufficient number of times, and then predicting on the held back compounds. These are then compared with the standard LOO predictions made using the entire dataset shown in the plots labeled "All". The result is similar as that in 7.11a; with a small group of compounds held back, the predictions are virtually the same, but as more compounds are held out of the training set, the predictions get worse.

The same conclusion is reached by looking at the results of these two tests. Fig 7.11a shows that removing compounds we are not confident about does not improve the prediction accuracy for well studied compounds, Fig. 7.11b shows that masking compounds we are not confident about does not improve the prediction accuracy for those compounds that are not well studied. The implication of these two virtual experiments is that we should not remove compounds from the dataset, even ones in which we have little confidence in the experimental dopability limits, because while the information this set of compounds contains is imperfect, it is still important.

7.12. High-throughput Dopability Predictions

Combining dopability predictions with quality factor predictions allows the identification of potential new TE materials in the DLS family. While the optimized version of the dopability model includes features and weighting that do not lend well to high-throughput predictions, a simplified version can be used. A model for dopability constructed utilizing only a feature set created using the formula and chemistry-based inputs and LOOCV has a prediction accuracy reasonably similar to the optimized model (MAE/MSE of 1.34/3.05 compared to 1.19/2.23). This model was then used in tandem with β[176] to generate predictions for DLS compounds, with results shown in Fig. 7.12. Out of a total of 188 DLS compounds considered in this study, the dopabiilty learning set was based on 127 compounds. This yields 61 compounds that had no experimental dopability information; both β and dopability could then be predicted for these compounds. An additional 67 compounds were part of the dopability learning set and had β predictions but had a a persistence of less than 5 papers. In this latter case, the dopability prediction may highlight opportunities for extending the known doping range in promising β compounds.

The first notable observation is that both the model predictions and experimental values (where they exist) indicate there are far more DLS compounds that are dopable to an appropriate p-type carrier concentration range to be useful for thermoelectric applications. Furthermore, there are far more DLS compounds with β predicted to be 10 or greater as n-type than p-type. The average hole mobility is $\sim$two orders of magnitude lower than the electron mobility and the valence band mass is about one order of magnitude higher than the conduction band on average. This leads to many materials with high potential n-type performance and fewer with high p-type β. Unfortunately, it appears far fewer

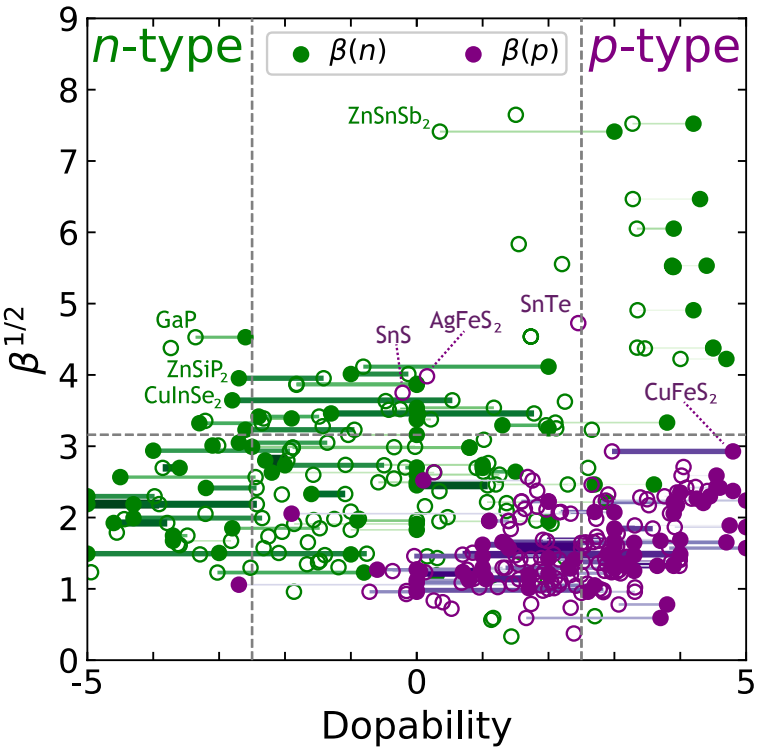

Figure 7.12. Predicted quality factor (β) *vs* dopability for compounds in the diamond-like structure. Filled circles are experimental dopability, open circles are predicted. Horizontal colored lines connect experimental and predicted values of dopability, with color and thickness of line showing persistence. Dashed gray lines represent approximate benchmarks for good TE performance (carrier concentration>|3 x 10^{18}| cm^{-3} and β>10), meaning promising materials are in the regions labeled *n*-type and *p*-type.

compounds can be realized *n*-type to a reasonably high carrier concentrations. Many of these are quaternary Cu containing compounds which have been made *p*-type only, and while the quality factor indicates they have the potential to be very good thermoelectric materials, the dopability predictions show it is very unlikely they can be made *n*-type to realize that potential. However, the high quantity of low persistence quaternary Cu

compounds may bias this conclusion; further studies of extrinsic doping in these materials is needed to establish the attainable carrier concentration bounds.

Fig. 7.12 also demonstrates there are a number of binary and ternary compounds which could be interesting thermelectric materials where the dopability limits have not been fully explored experimentally. For example, β calculations indicate GaP could be a good thermoelectric, with both experimental and predicted dopability in the approriate range. $ZnSnSb_2$ is predicted to have a much larger carrier concentration window than found to date experimentally and could be a good thermoelectric if pushed from p-type through intrinsic to n-type. This also indicates that $CuInSe_2$, which has had recent attention as a p-type thermoelectric, should be looked at instead as an n-type TE. Likewise p-type $CuFeS_2$ and $AgFeS_2$ could be promising TE materials. SnTe[997–999] and SnS[191,1000] have both received significant interest as TE materials in their typical structures (rocksalt and orthorhombic, respectively) and our predictions indicate they could exhibit high performance if stabilized in the diamond-like structure.

7.13. Conclusions

In this work, we show that dopability ranges can be predicted to approximately one order of magnitude against experimental results through linear modeling. The accuracy of a simple linear model is found to be similar to more complex machine learning techniques and allows greater interpretability regarding the features and properties that control dopability in diamond-like semiconductors. A number of features indicate substitutional defects play a major role in driving carrier concentration ranges toward intrinsic ranges and features such as band gap and Bader charge match either 'rules-of-thumb' or

previous computational findings. Compounds that possess both promising thermoelectric quality factor (β) and complementary dopability are identified. Our results serve as a caution against pursuing a subset of high β compounds that have unfavorable dopability ranges. For compounds or subgroups of DLS where persistence is historically low, this work serves to inspire further experimental interrogation of carrier concentration limits when the predicted dopability range is far greater than the experimentally realized limits. These results also indicate where detailed defect calculation efforts are most impactful. We note that the predictive dopability model is not inherently limited to DLS compounds; an expanded learning set could incorporate structural descriptors so that the model could be applied to a more diverse set of compounds, including all thermoelectric materials.

CHAPTER 8

Summary and Recommendation for Future Work

In this work, I have shown how a metric for estimating the potential for thermoelectric performance β can be developed. This is useful to serve as a guide for both experimentalists and computationalists to investigate compounds with high potential as TEs and eliminate those that are unlikely to ever be useful. Experimental investigation of some of these potentially interesting compounds was carried out; each compound has its own unique challenges and opportunities:

- SnO has the potential to be among the best n-type oxide thermoelectric compounds. In this work we were unable to dope it to the appropriate carrier type and density due to stability issues. Other processing techniques may make these carrier concentrations experimentally accessible to realize high performance.
- The potential of GeSe as a thermoelectric was realized by co-substitution to unlock the rhombohedral phase that permits the optimum carrier concentration to be attained. Further work on GeSe should be focused on lattice thermal conductivity reduction and possibly completing the phase transformation to cubic.
- The exotic transport properties of $ZrTe_5$ were shown to be explainable using a simple two-band model. This model indicates that high performance could be realized in the pentatelluride system by lowering lattice thermal conductivity or reducing bipolar conduction, either through reduction of the minority carrier

mobility or opening the band gap further. Work here should focus on alloying with $HfTe_5$ or substitution of S/Se for Te.

Further work in modeling both β (including lattice thermal conductivity) and dopability should focus on completing a feedback loop of property predictions, experimental characterization and validation, and using these new measurements to refine the model. For prediction accuracy to improve, the addition of more experimental data is quite important as it allows more fitting parameters to be statistically justified and decreases the number of out-of-sample compounds. This increased flexibility and applicability supports further learning of what determines a given property and how to design a material to attain the desired characteristics. For the κ_L model, more modeling could be done to determine what features are missing from the physics-based equation. The effect of persistence and historical bias needs to be isolated from the chemical and structural drivers of dopability if possible. Additional work could be done by predicting the probability that compounds could be doped to a certain threshold to aid separating persistence or combining dopability estimation with β. The dataset should also be expanded to include more types of compounds outside of diamond-like semiconductors. The inclusion of inputs which serve as proxies for structure, along with literature data of corresponding material classes, would permit the application of this model to a broader set of compounds which should include all known thermoelectric materials. This may provoke the discovery of new TEs.

I have shown that models can be developed which use inexpensive inputs and are fit to empirical literature data through a rigorous statistical procedure. These models aid in the discovery of novel materials with high potential as thermoelectrics. The success

of these models, which are similar in accuracy and can be applied to a much broader class of compounds compared with more computationally expensive first-principles, should inspire their use in other fields. In situations where there are analytical expressions, a semi-empirical model can be fit with a grasp on the underlying physics. When no such expressions exist, the use of simple statistical models allows interpretation of the primary drivers that play a role in determining the target property. When the goal is learning and not just prediction, both accuracy and interpretability should be considered in selection of a model type for each case, meaning that sometimes linear models will be superior to more trendy machine learning.

References

[1] L. E. Bell, *Science*, 2008, **321**, 1457–1461.

[2] E. Velmre, Electronics Conference (BEC), 2010 12th Biennial Baltic, 2010, pp. 17–24.

[3] J. Peltier, *Ann. Chim. Phys*, 1834, **56**, 371.

[4] J. Martin, T. Tritt and C. Uher, *Journal of Applied Physics*, 2010, **108**, 14.

[5] A. V. Da Rosa, *Fundamentals of renewable energy processes*, Academic Press, 2012.

[6] F. J. DiSalvo, R. M. Fleming and J. V. Waszczak, *Phys. Rev. B*, 1981, **24**, 2935.

[7] G. J. Snyder and E. S. Toberer, *Nat. Mater.*, 2008, **7**, 105–114.

[8] E. S. Toberer, A. Zevalkink and G. J. Snyder, *Journal of Materials Chemistry*, 2011, **21**, 15843–15852.

[9] F. Kreith, 1962.

[10] A. F. Ioffe, L. Stil'Bans, E. Iordanishvili, T. Stavitskaya, A. Gelbtuch and G. Vineyard, *Physics Today*, 1959, **12**, 42.

[11] H. J. Goldsmid, in *Introduction to thermoelectricity*, Springer, 2016, pp. 1–7.

[12] D. M. Rowe, in *CRC Handbook of Thermoelectrics*, CRC press, 1995, pp. 31–37.

[13] D. M. Rowe, *CRC handbook of thermoelectrics*, CRC press, 1995.

[14] C. Goupil, W. Seifert, K. Zabrocki, E. Müller and G. J. Snyder, *Entropy*, 2011, **13**, 1481–1517.

[15] C. B. Vining, *Nature materials*, 2009, **8**, 83.

[16] T. C. Holgate, R. Bennett, T. Hammel, T. Caillat, S. Keyser and B. Sievers, *Journal of Electronic Materials*, 2015, **44**, 1814–1821.

[17] S. K. Yee, S. LeBlanc, K. E. Goodson and C. Dames, *Energy & Environmental Science*, 2013, **6**, 2561–2571.

[18] A. F. May and G. J. Snyder, in *Materials, preparation, and characterization in thermoelectrics*, CRC Press, 2012, pp. 1–18.

[19] S. D. Kang and G. J. Snyder, *arXiv preprint arXiv:1710.06896*, 2017.

[20] S. Ohno, *Ph.D. thesis*, California Institute of Technology, 2017.

[21] S. K. Bux, R. G. Blair, P. K. Gogna, H. Lee, G. Chen, M. S. Dresselhaus, R. B. Kaner and J.-P. Fleurial, *Advanced Functional Materials*, 2009, **19**, 2445–2452.

[22] Z. Chen, B. Ge, W. Li, S. Lin, J. Shen, Y. Chang, R. Hanus, G. J. Snyder and Y. Pei, *Nature communications*, 2017, **8**, 13828.

[23] Z. Chen, Z. Jian, W. Li, Y. Chang, B. Ge, R. Hanus, J. Yang, Y. Chen, M. Huang, G. J. Snyder *et al.*, *Advanced Materials*, 2017, **29**, 1606768.

[24] Z. Wang, J. E. Alaniz, W. Jang, J. E. Garay and C. Dames, *Nano letters*, 2011, **11**, 2206–2213.

[25] H. Wang, A. D. LaLonde, Y. Pei and G. J. Snyder, *Advanced Functional Materials*, 2013, **23**, 1586–1596.

[26] W. G. Zeier, A. Zevalkink, Z. M. Gibbs, G. Hautier, M. G. Kanatzidis and G. J. Snyder, *Angew. Chem., Int. Ed.*, 2016, **55**, 6826–6841.

[27] O. Delaire, J. Ma, K. Marty, A. F. May, M. A. McGuire, M.-H. Du, D. J. Singh, A. Podlesnyak, G. Ehlers, M. Lumsden *et al.*, *Nature materials*, 2011, **10**, 614.

[28] A. F. May, D. J. Singh and G. J. Snyder, *Phys. Rev. B*, 2009, **79**, 153101.

[29] Y. Pei, X. Shi, A. LaLonde, H. Wang, L. Chen and G. J. Snyder, *Nature*, 2011, **473**, 66.

[30] Y. Pei, H. Wang and G. J. Snyder, *Advanced materials*, 2012, **24**, 6125–6135.

[31] W. Liu, X. Tan, K. Yin, H. Liu, X. Tang, J. Shi, Q. Zhang and C. Uher, *Physical review letters*, 2012, **108**, 166601.

[32] Y. Tang, Z. M. Gibbs, L. A. Agapito, G. Li, H.-S. Kim, M. B. Nardelli, S. Curtarolo and G. J. Snyder, *Nat. Mater.*, 2015, **14**, 1223–1228.

[33] C. Fu, T. Zhu, Y. Pei, H. Xie, H. Wang, G. J. Snyder, Y. Liu, Y. Liu and X. Zhao, *Advanced Energy Materials*, 2014, **4**, 1400600.

[34] J. Shuai, H. Geng, Y. Lan, Z. Zhu, C. Wang, Z. Liu, J. Bao, C.-W. Chu, J. Sui and Z. Ren, *Proceedings of the National Academy of Sciences*, 2016, **113**, E4125–E4132.

[35] G. S. Pomrehn, A. Zevalkink, W. G. Zeier, A. Van De Walle and G. J. Snyder, *Angewandte Chemie International Edition*, 2014, **53**, 3422–3426.

[36] E. S. Toberer, C. A. Cox, S. R. Brown, T. Ikeda, A. F. May, S. M. Kauzlarich and G. J. Snyder, *Advanced Functional Materials*, 2008, **18**, 2795–2800.

[37] C. J. Vineis, A. Shakouri, A. Majumdar and M. G. Kanatzidis, *Advanced Materials*, 2010, **22**, 3970–3980.

[38] A. Minnich, M. Dresselhaus, Z. Ren and G. Chen, *Energy & Environmental Science*, 2009, **2**, 466–479.

[39] S. Curtarolo, G. L. Hart, M. B. Nardelli, N. Mingo, S. Sanvito and O. Levy, *Nature materials*, 2013, **12**, 191.

[40] E. Altenkirch, *Physikalische Zeitschrift*, 1909, **10**, 560.

[41] G. K. Madsen, *Journal of the American Chemical Society*, 2006, **128**, 12140–12146.

[42] J. Yang, H. Li, T. Wu, W. Zhang, L. Chen and J. Yang, *Advanced Functional Materials*, 2008, **18**, 2880–2888.

[43] S. Wang, Z. Wang, W. Setyawan, N. Mingo and S. Curtarolo, *Phys. Review X*, 2011, **1**, 021012.

[44] G. K. Madsen and D. J. Singh, *Computer Physics Communications*, 2006, **175**, 67–71.

[45] E. S. Toberer, A. F. May, C. J. Scanlon and G. J. Snyder, *Journal of Applied Physics*, 2009, **105**, 063701.

[46] J. Sjakste, N. Vast and V. Tyuterev, *Physical review letters*, 2007, **99**, 236405.

[47] F. Murphy-Armando and S. Fahy, *Physical Review B*, 2008, **78**, 035202.

[48] O. Restrepo, K. Varga and S. Pantelides, *Applied Physics Letters*, 2009, **94**, 212103.

[49] Z. Wang, S. Wang, S. Obukhov, N. Vast, J. Sjakste, V. Tyuterev and N. Mingo, *Physical Review B*, 2011, **83**, 205208.

[50] Y. Zhang, E. Skoug, J. Cain, V. Ozoliņš, D. Morelli and C. Wolverton, *Physical Review B*, 2012, **85**, 054306.

[51] L.-D. Zhao, S.-H. Lo, Y. Zhang, H. Sun, G. Tan, C. Uher, C. Wolverton, V. P. Dravid and M. G. Kanatzidis, *Nature*, 2014, **508**, 373–377.

[52] D. Broido, M. Malorny, G. Birner, N. Mingo and D. Stewart, *Appl. Phys. Lett.*, 2007, **91**, 231922 1–3.

[53] W. Li, N. Mingo, L. Lindsay, D. A. Broido, D. A. Stewart and N. A. Katcho, *Phys. Rev. B*, 2012, **85**, 195436 1–5.

[54] L. Lindsay, D. Broido and T. Reinecke, *Physical review letters*, 2012, **109**, 095901.

[55] J. Carrete, W. Li, N. Mingo, S. Wang and S. Curtarolo, *Phys. Rev. X*, 2014, **4**, 011019 1–9.

[56] H. Goldsmid and R. Douglas, *Br. J. Appl. Phys.*, 1954, **5**, 386.

[57] R. Chasmar and R. Stratton, *Int. J. of Electron.*, 1959, **7**, 52–72.

[58] M. Cardona and Y. Y. Peter, *Fundamentals of semiconductors*, Springer, 2005.

[59] A. F. May, E. S. Toberer, A. Saramat and G. J. Snyder, *Physical Review B*, 2009, **80**, 125205.

[60] E. S. Toberer, A. F. May, B. C. Melot, E. Flage-Larsen and G. J. Snyder, *Dalton Transactions*, 2010, **39**, 1046–1054.

[61] E. S. Toberer, A. Zevalkink, N. Crisosto and G. J. Snyder, *Adv. Funct. Mater.*, 2010, **20**, 4375–4380.

[62] A. Belsky, M. Hellenbrandt, V. L. Karen and P. Luksch, *Acta Crystallogr., Sect. B: Struct. Sci.*, 2002, **58**, 364–369.

[63] J. Callaway, *Phys. Rev.*, 1959, **113**, 1046.

[64] D. G. Cahill, S. K. Watson and R. O. Pohl, *Physical Review B*, 1992, **46**, 6131.

[65] S. A. Miller, P. Gorai, B. R. Ortiz, A. Goyal, D. Gao, S. A. Barnett, T. O. Mason, G. J. Snyder, Q. Lv, V. Stevanović and E. S. Toberer, *Chem. Mater.*, 2017, **29**, 2494–2501.

[66] S. A. Miller, P. Gorai, U. Aydemir, T. O. Mason, V. Stevanović, E. S. Toberer and G. J. Snyder, *Journal of Materials Chemistry C*, 2017, **5**, 8854–8861.

[67] Z. Huang, S. A. Miller, B. Ge, M. Yan, S. Anand, T. Wu, P. Nan, Y. Zhu, W. Zhuang, G. J. Snyder *et al.*, *Angewandte Chemie International Edition*, 2017, **56**, 14113–14118.

[68] S. A. Miller, I. Witting, U. Aydemir, L. Peng, A. J. Rettie, P. Gorai, D. Y. Chung, M. G. Kanatzidis, M. Grayson, V. Stevanović *et al.*, *Physical Review Applied*, 2018, **9**, 014025.

[69] W. Kwestroo and P. Vromans, *Journal of Inorganic and Nuclear Chemistry*, 1967, **29**, 2187–2190.

[70] L. Gong, Y. Wang, X. Cheng, R. Zhang and H. Zhang, *International Journal of Heat and Mass Transfer*, 2014, **68**, 295–298.

[71] C. Wood, D. Zoltan and G. Stapfer, *Rev. Sci. Instrum.*, 1985, **56**, 719–722.

[72] K. A. Borup, E. S. Toberer, L. D. Zoltan, G. Nakatsukasa, M. Errico, J.-P. Fleurial, B. B. Iversen and G. J. Snyder, *Rev. Sci. Instrum.*, 2012, **83**, 123902.

[73] P. Kubelka, *J. Opt. Soc. Am.*, 1948, **38**, 448–448.

[74] P. Kubelka and F. Munk, *Z. Tech. Phys*, 1931, **12**, 593–601.

[75] H.-S. Kim, Z. M. Gibbs, Y. Tang, H. Wang and G. J. Snyder, *APL materials*, 2015, **3**, 041506.

[76] J. Yan, P. Gorai, B. Ortiz, S. Miller, S. A. Barnett, T. Mason, V. Stevanović and E. S. Toberer, *Energy Environ. Sci.*, 2015, **8**, 983–994.

[77] P. Gorai, E. S. Toberer and V. Stevanović, *J. Mater. Chem. A*, 2016, **4**, 11110–11116.

[78] G. Kresse and J. Furthmüller, *Comput. Mater. Sci.*, 1996, **6**, 15–50.

[79] J. P. Perdew, K. Burke and M. Ernzerhof, *Phys. Rev. Lett.*, 1996, **77**, 3865.

[80] *A Python framework for high-throughput first-principles calculations*, `https://github.com/pylada`.

[81] V. Stevanović, S. Lany, X. Zhang and A. Zunger, *Physical Review B*, 2012, **85**, 115104.

[82] S. Dudarev, G. Botton, S. Savrasov, C. Humphreys and A. Sutton, *Physical Review B*, 1998, **57**, 1505.

[83] W. Kohn and L. J. Sham, *Phys. Rev.*, 1965, **140**, A1133.

[84] L. Brixner, *Journal of Inorganic and Nuclear Chemistry*, 1962, **24**, 257–263.

[85] J. Klimes, D. R. Bowler and A. Michaelides, *J. Phys. Condens. Matter*, 2010, **22**, 022201.

[86] G. Kresse and J. Furthmüller, *Physical review B*, 1996, **54**, 11169.

[87] J. P. Perdew and Y. Wang, *Physical Review B*, 1992, **45**, 13244.

[88] J. P. Perdew, J. A. Chevary, S. H. Vosko, K. A. Jackson, M. R. Pederson, D. J. Singh and C. Fiolhais, *Physical Review B*, 1992, **46**, 6671.

[89] G. K. Madsen, A. Katre and C. Bera, *Phys. Status Solidi A*, 2015, 802–807.

[90] C. Toher, J. J. Plata, O. Levy, M. De Jong, M. Asta, M. B. Nardelli and S. Curtarolo, *Phys. Rev. B*, 2014, **90**, 174107 1–14.

[91] C. J. Willmott and K. Matsuura, *Clim. Res.*, 2005, **30**, 79–82.

[92] D. J. Singh and W. E. Pickett, *Phys. Rev. B*, 1994, **50**, 11235.

[93] D. J. Singh and I. I. Mazin, *Phys. Rev. B*, 1997, **56**, R1650.

[94] J. E. Saal, S. Kirklin, M. Aykol, B. Meredig and C. Wolverton, *Jom*, 2013, **65**, 1501–1509.

[95] S. Kirklin, J. E. Saal, B. Meredig, A. Thompson, J. W. Doak, M. Aykol, S. Rühl and C. Wolverton, *npj Comput. Mater.*, 2015, **1**, 15010.

[96] A. Jain, S. P. Ong, G. Hautier, W. Chen, W. D. Richards, S. Dacek, S. Cholia, D. Gunter, D. Skinner, G. Ceder and K. a. Persson, *APL Mater.*, 2013, **1**, 011002.

[97] M. de Jong, W. Chen, T. Angsten, A. Jain, R. Notestine, A. Gamst, M. Sluiter, C. Krishna Ande, S. van der Zwaag, J. J. Plata, C. Toher, S. Curtarolo, G. Ceder, K. A. Persson and M. Asta, *Sci. Data*, 2015, **2**, year.

[98] M. de Jong, W. Chen, H. Geerlings, M. Asta and K. A. Persson, *Sci. Data*, 2015, **2**, year.

[99] R. Darolia, *Int. Mater. Rev.*, 2013, **58**, 315–348.

[100] S. P. Gurrum, S. K. Suman, Y. K. Joshi and A. G. Fedorov, *IEEE Trans. Device Mater. Reliab.*, 2004, **4**, 709–714.

[101] M. Arik, C. A. Becker, S. E. Weaver and J. Petroski, *Proc. SPIE*, 2004, 64–75.

[102] J. M. Rondinelli, N. A. Benedek, D. Freedman, A. Kavner, E. E. Rodriguez, E. Toberer and L. Martin, *Am. Ceram. Soc. Bull.*, 2013, **92**, 14–21.

[103] G. A. Slack, *Solid State Phys.*, 1979, **34**, 1–71.

[104] M. Roufosse and P. Klemens, *Phy. Rev. B*, 1973, **7**, 5379–5386.

[105] A. Jain, Y. Shin and K. A. Persson, *Nat. Rev. Mater.*, 2016, **1**, 15004 1–13.

[106] A. Seko, A. Togo, H. Hayashi, K. Tsuda, L. Chaput and I. Tanaka, *Phys. Rev. Lett.*, 2015, **115**, 205901 1–5.

[107] M. Anis-ur Rehman and A. Maqsood, *International journal of thermophysics*, 2003, **24**, 867–883.

[108] X. Hou, S. Chen, Z. Du, X. Liu and J. Cui, *RSC Advances*, 2015, **5**, 102856–102862.

[109] E. Steigmeier and I. Kudman, *Physical Review*, 1966, **141**, 767.

[110] D. T. Morelli and G. A. Slack, in *High thermal conductivity materials*, Springer, 2006, pp. 37–68.

[111] G. A. Slack, R. A. Tanzilli, R. Pohl and J. Vandersande, *Journal of Physics and Chemistry of Solids*, 1987, **48**, 641–647.

[112] D. Bessas, R. Simon, K. Friese, M. Koza and R. Hermann, *Journal of Physics: Condensed Matter*, 2014, **26**, 485401.

[113] D. R. Lide, *Handbook of chemistry and physics 85 Boca Raton (Fla.)*, London, New York: CRC Press, 2004.

[114] L. Garbato and A. Rucci, *Chemical Physics Letters*, 1979, **61**, 542–544.

[115] N. Soga *et al.*, *Journal of the American Ceramic Society*, 1966, **49**, 355–359.

[116] A. Slifka, B. Filla and J. Phelps, *Journal of Research of the National Institute of Standards and Technology*, 1998, **103**, 357.

[117] S. K. Bux, M. T. Yeung, E. S. Toberer, G. J. Snyder, R. B. Kaner and J.-P. Fleurial, *Journal of Materials Chemistry*, 2011, **21**, 12259–12266.

[118] G. Slack and R. Newman, *Phys. Rev. Lett.*, 1958, **1**, 359.

[119] S. Agrawal, J. Narain and J. Shanker, *physica status solidi (b)*, 1984, **123**, 497–501.

[120] O. Madelung, U. Rössler and M. Schulz, *Springer Materials—The Landolt-Börnstein Database*, DOI, 2010.

[121] V. Fedorov and I. I. Davydov, *High Temperature Science*, 1979, **16**, 654–660.

[122] H. Wang, E. Schechtel, Y. Pei and G. J. Snyder, *Advanced Energy Materials*, 2013, **3**, 488–495.

[123] J. Androulakis, D.-Y. Chung, X. Su, L. Zhang, C. Uher, T. C. Hasapis, E. Hatzikraniotis, K. M. Paraskevopoulos and M. G. Kanatzidis, *Physical Review B*, 2011, **84**, 155207.

[124] H. Goldsmid, *Proceedings of the Physical Society*, 1958, **72**, 17.

[125] A. D. LaLonde, Y. Pei and G. J. Snyder, *Energy Environ. Sci.*, 2011, **4**, 2090–2096.

[126] R. Berman, P. Hudson and M. Martinez, *Journal of Physics C: Solid State Physics*, 1975, **8**, L430.

[127] C. Glassbrenner and G. A. Slack, *Physical Review*, 1964, **134**, A1058.

[128] A. Zevalkink, E. S. Toberer, W. G. Zeier, E. Flage-Larsen and G. J. Snyder, *Energy & Environ. Sci.*, 2011, **4**, 510–518.

[129] M. E. Levinshtein, S. L. Rumyantsev and M. S. Shur, *Properties of Advanced Semiconductor Materials: GaN, AIN, InN, BN, SiC, SiGe*, John Wiley & Sons,

2001.

[130] A. Zevalkink, J. Swallow and G. J. Snyder, *Dalton Transactions*, 2013, **42**, 9713–9719.

[131] G. F. Davies, *J. Geophys. Res.*, 1972, **77**, 4920–4933.

[132] E. Osmanov, Y. V. Rud and M. Stryalkovskii, *physica status solidi (b)*, 1968, **26**, 85–90.

[133] S. Popuri, M. Pollet, R. Decourt, F. Morrison, N. Bennett and J. Bos, *Journal of Materials Chemistry C*, 2016, **4**, 1685–1691.

[134] K. Masumoto, S. Isomura and W. Goto, *Journal of Physics and Chemistry of Solids*, 1966, **27**, 1939–1947.

[135] D. Spitzer, *Journal of Physics and chemistry of Solids*, 1970, **31**, 19–40.

[136] T. Smith, J. Birch and J. Collins, *Journal of Physics C: Solid State Physics*, 1976, **9**, 4375.

[137] A. Pucci and K. R. Wandelt, *Physics and Engineering of New Materials*, Springer Science & Business Media, 2009, vol. 127.

[138] C. Liu and D. T. Morelli, *Journal of electronic materials*, 2011, **40**, 678–681.

[139] J. Pellicer-Porres, D. Martinez-Garcia, A. Segura, P. Rodriguez-Hernandez, A. Munoz, J. Chervin, N. Garro and D. Kim, *Physical Review B*, 2006, **74**, 184301.

[140] L. Garbato and A. Rucci, *Chemical Physics Letters*, 1979, **64**, 350–351.

[141] C. Rincón, M. Valeri-Gil and S. Wasim, *physica status solidi (a)*, 1995, **147**, 409–415.

[142] E. Takegoshi, Y. Hirasawa and S. Imura, *Bulletin of JSME*, 1984, **27**, 2455–2462.

[143] S.-H. Shim and T. S. Duffy, *American Mineralogist*, 2002, **87**, 318–326.

[144] P. M. Böttger, K. Valset, S. Deledda and T. G. Finstad, *Journal of electronic materials*, 2010, **39**, 1583–1588.

[145] L. Bjerg, B. B. Iversen and G. K. Madsen, *Physical Review B*, 2014, **89**, 024304.

[146] R. Carlson, G. Slack and S. Silverman, *J. Appl. Phys.*, 1965, **36**, 505–507.

[147] A. Jeżowski, B. Danilchenko, M. Boćkowski, I. Grzegory, S. Krukowski, T. Suski and T. Paszkiewicz, *Solid state communications*, 2003, **128**, 69–73.

[148] E. G. Víllora, K. Shimamura, T. Ujiie and K. Aoki, *Applied Physics Letters*, 2008, **92**, 2118.

[149] S. A. Aliev, Nashelsk.Ay and S. S. Shalyt, *Soviet Physics Solid State,Ussr*, 1965, **7**, 1287.

[150] C. Uher, J. Yang, S. Hu, D. Morelli and G. Meisner, *Phys. Rev. B*, 1999, **59**, 8615.

[151] R. Jeanloz and M. Roufosse, *J. Geophys. Res.: Solid Earth*, 1982, **87**, 10763–10772.

[152] B. Huang and M. Kaviany, *J. Appl. Phys.*, 2006, **100**, 123507 1–12.

[153] M. Born and T. Von Karman, *Z. Phys*, 1912, **13**, 297–309.

[154] J.-H. Pöhls, M. B. Johnson and M. A. White, *Physical Chemistry Chemical Physics*, 2016, **18**, 1185–1190.

[155] P. Klemens, *Proc. Phys. Soc. London, Sec. A*, 1955, **68**, 1113–1128.

[156] J. Yang, G. Meisner and L. Chen, *Appl. Phys. Lett.*, 2004, **85**, 1140–1142.

[157] Y. Pei, A. LaLonde, S. Iwanaga and G. J. Snyder, *Energy Environ. Sci.*, 2011, **4**, 2085–2089.

[158] B. Poudel, Q. Hao, Y. Ma, Y. Lan, A. Minnich, B. Yu, X. Yan, D. Wang, A. Muto, D. Vashaee, X. Chen, J. Liu, M. S. Dresselhaus, G. Chen and Z. Ren, *Science*, 2008, **320**, 634–638.

[159] Y. Tang, R. Hanus, S.-w. Chen and G. J. Snyder, *Nat. Commun.*, 2015, **6**, 1–7.

[160] P. Qiu, J. Yang, R. Liu, X. Shi, X. Huang, G. Snyder, W. Zhang and L. Chen, *J. Appl. Phys.*, 2011, **109**, 063713.

[161] E. S. Toberer, S. R. Brown, T. Ikeda, S. M. Kauzlarich and G. J. Snyder, *App. Phys. Lett.*, 2008, **93**, 062110.

[162] E. S. Toberer, P. Rauwel, S. Gariel, J. Taftø and G. J. Snyder, *J. Mater. Chem.*, 2010, **20**, 9877–9885.

[163] J. Zhang, L. Song, S. H. Pedersen, H. Yin, L. T. Hung and B. B. Iversen, *Nature Commun.*, 2017, **8**, 13901.

[164] M. W. Gaultois, T. D. Sparks, C. K. Borg, R. Seshadri, W. D. Bonificio and D. R. Clarke, *Chem. Mater.*, 2013, **25**, 2911–2920.

[165] H. Yin, M. Christensen, B. Pedersen, E. Nishibori, S. Aoyagi and B. B. Iversen, *J. Electron. Mater.*, 2010, **39**, 1957–1959.

[166] H. Dong, X. Li, X. Huang, Y. Zhou, W. Jiang and L. Chen, *Ceram. Int.*, 2013, **39**, 4551–4557.

[167] D. Zhao, C. Tian, S. Tang, Y. Liu and L. Chen, *J. Alloys Compd.*, 2010, **504**, 552–558.

[168] J. W. Fergus, *J. Eur. Ceram. Soc.*, 2012, **32**, 525–540.

[169] F. Zhou, W. Nielson, Y. Xia and V. Ozoliņš, *Phys. Rev. Lett.*, 2014, **113**, 185501.

[170] I. Opahle, A. Parma, E. J. McEniry, R. Drautz and G. K. H. Madsen, *New Journal of Physics*, 2013, **15**, 105010.

[171] W. Chen, J.-H. Pöhls, G. Hautier, D. Broberg, S. Bajaj, U. Aydemir, Z. M. Gibbs, H. Zhu, M. Asta, G. J. Snyder, B. Meredig, M. A. White, K. Persson and A. Jain, *J. Mater. Chem*, 2016, **100**, 4414–4426.

[172] H. Zhu, G. Hautier, U. Aydemir, Z. M. Gibbs, G. Li, S. Bajaj, J.-H. Pöhls, D. Broberg, W. Chen, A. Jain, M. A. White, M. Asta, G. J. Snyder, K. Persson and G. Ceder, *J. Mater. Chem. C*, 2015, **3**, 10554–10565.

[173] V. X. Hien, J.-H. Lee, J.-J. Kim and Y.-W. Heo, *Sens. Actuators B*, 2014, **194**, 134–141.

[174] L. Y. Liang, Z. M. Liu, H. T. Cao and X. Q. Pan, *ACS Appl. Mater. Interfaces*, 2010, **2**, 1060–1065.

[175] K. Okamura, B. Nasr, R. A. Brand and H. Hahn, *J. Mater. Chem.*, 2012, **22**, 4607–4610.

[176] P. Gorai, D. Gao, B. Ortiz, S. Miller, S. A. Barnett, T. Mason, Q. Lv, V. Stevanović and E. S. Toberer, *Comput. Mater. Sci.*, 2016, **112**, 368–376.

[177] E. J. Skoug and D. T. Morelli, *Phys. Rev. Lett.*, 2011, **107**, 235901.

[178] C. Bera, S. Jacob, I. Opahle, N. H. Gunda, R. Chmielowski, G. Dennler and G. K. Madsen, *PCCP*, 2014, **16**, 19894–19899.

[179] M. Moreno and R. Mercader, *Phys. Rev. B*, 1994, **50**, 9875.

[180] S. Kim, J. M. Zuo, N. T. Nguyen, D. C. Johnson and D. G. Cahill, *J. Mater. Res.*, 2008, **23**, 1064–1067.

[181] C. Chiritescu, D. G. Cahill, C. Heideman, Q. Lin, C. Mortensen, N. T. Nguyen, D. Johnson, R. Rostek and H. Böttner, *J. Appl. Phys*, 2008, **104**, 033533.

[182] Y. Ogo, H. Hiramatsu, K. Nomura, H. Yanagi, T. Kamiya, M. Hirano and H. Hosono, *Appl. Phys. Lett.*, 2008, **93**, 2113.

[183] J. Varley, A. Schleife, A. Janotti and C. Van de Walle, *Appl. Phys. Lett.*, 2013, **103**, 082118.

[184] J. P. Perdew, *Int. J. Quantum Chem.*, 1985, **28**, 497–523.

[185] J. F. Shackelford and M. K. Muralidhara, *Introduction to Materials Science for Engineers*, Pearson/Prentice Hall Upper Saddle River, 2005.

[186] A. Togo, F. Oba, I. Tanaka and K. Tatsumi, *Phys. Rev. B*, 2006, **74**, 195128.

[187] H. Hosono, Y. Ogo, H. Yanagi and T. Kamiya, *Electrochem. Solid-State Lett.*, 2011, **14**, H13–H16.

[188] J. Son, M. Oh, B. Kim, S. Park, B. Min, M. Kim and H. Lee, *Journal of Alloys and Compounds*, 2013, **566**, 168–174.

[189] F. Li, J.-F. Li, L.-D. Zhao, K. Xiang, Y. Liu, B.-P. Zhang, Y.-H. Lin, C.-W. Nan and H.-M. Zhu, *Energy & Environmental Science*, 2012, **5**, 7188–7195.

[190] D. Morgan and D. Wright, *Br. J. Appl. Phys.*, 1966, **17**, 337.

[191] R. Guo, X. Wang, Y. Kuang and B. Huang, *Phys. Rev. B*, 2015, **92**, 115202.

[192] Q. Zhang, E. K. Chere, J. Sun, F. Cao, K. Dahal, S. Chen, G. Chen and Z. Ren, *Adv. Energy Mater.*, 2015, **5**, 1500360.

[193] A. T. Duong, G. D. Van Quang Nguyen, S. K. Van Thiet Duong, J. Y. Song, J. K. Lee, J. E. Lee, S. Park, T. Min, J. Lee, J. Kim and S. Cho, *Nat. Commun.*, 2016, **7**, 13713.

[194] J. A. Caraveo-Frescas, P. K. Nayak, H. A. Al-Jawhari, D. B. Granato, U. Schwingenschlogl and H. N. Alshareef, *ACS Nano*, 2013, **7**, 5160–5167.

[195] Y. Pei, W. Liu, J. Shi, Z. Chen and G. Wang, *J. Electron. Mater.*, 2016, **45**, 5967–5973.

[196] J.-Y. Kim, B. Bae and E.-J. Yun, *Sci. Adv. Mater.*, 2016, **8**, 272–277.

[197] X. Yu, T. J. Marks and A. Facchetti, *Nat. Mater.*, 2016, **15**, 383–396.

[198] T. M. Tritt, *Science*, 1999, **283**, 804–805.

[199] J. R. Sootsman, D. Y. Chung and M. G. Kanatzidis, *Angewandte Chemie International Edition*, 2009, **48**, 8616–8639.

[200] G. Tan, L.-D. Zhao and M. G. Kanatzidis, *Chemical reviews*, 2016, **116**, 12123–12149.

[201] Y. Pei, Z. M. Gibbs, A. Gloskovskii, B. Balke, W. G. Zeier and G. J. Snyder, *Advanced energy materials*, 2014, **4**, year.

[202] J. Zhang, R. Liu, N. Cheng, Y. Zhang, J. Yang, C. Uher, X. Shi, L. Chen and W. Zhang, *Advanced Materials*, 2014, **26**, 3848–3853.

[203] L. Zhao, H. Wu, S. Hao, C.-I. Wu, X. Zhou, K. Biswas, J. He, T. P. Hogan, C. Uher, C. Wolverton *et al.*, *Energy & Environmental Science*, 2013, **6**, 3346–3355.

[204] J. P. Heremans, B. Wiendlocha and A. M. Chamoire, *Energy & Environmental Science*, 2012, **5**, 5510–5530.

[205] C. M. Jaworski, V. Kulbachinskii and J. P. Heremans, *Physical Review B*, 2009, **80**, 233201.

[206] L. Hu, T. Zhu, X. Liu and X. Zhao, *Advanced Functional Materials*, 2014, **24**, 5211–5218.

[207] K. Biswas, J. He, I. D. Blum, C.-I. Wu, T. P. Hogan, D. N. Seidman, V. P. Dravid and M. G. Kanatzidis, *Nature*, 2012, **489**, 414.

[208] F. Hao, P. Qiu, Y. Tang, S. Bai, T. Xing, H.-S. Chu, Q. Zhang, P. Lu, T. Zhang, D. Ren *et al.*, *Energy & Environmental Science*, 2016, **9**, 3120–3127.

[209] J. P. Heremans, V. Jovovic, E. S. Toberer, A. Saramat, K. Kurosaki, A. Charoenphakdee, S. Yamanaka and G. J. Snyder, *Science*, 2008, **321**, 554–557.

[210] S. Sassi, C. Candolfi, J.-B. Vaney, V. Ohorodniichuk, P. Masschelein, A. Dauscher and B. Lenoir, *Applied Physics Letters*, 2014, **104**, 212105.

[211] C.-L. Chen, H. Wang, Y.-Y. Chen, T. Day and G. J. Snyder, *Journal of Materials Chemistry A*, 2014, **2**, 11171–11176.

[212] Y. Li, X. Shi, D. Ren, J. Chen and L. Chen, *Energies*, 2015, **8**, 6275–6285.

[213] L.-D. Zhao, G. Tan, S. Hao, J. He, Y. Pei, H. Chi, H. Wang, S. Gong, H. Xu, V. P. Dravid *et al.*, *Science*, 2015, aad3749.

[214] K. Peng, X. Lu, H. Zhan, S. Hui, X. Tang, G. Wang, J. Dai, C. Uher, G. Wang and X. Zhou, *Energy & Environmental Science*, 2016, **9**, 454–460.

[215] T.-R. Wei, G. Tan, X. Zhang, C.-F. Wu, J.-F. Li, V. P. Dravid, G. J. Snyder and M. G. Kanatzidis, *Journal of the American Chemical Society*, 2016, **138**, 8875–8882.

[216] H. Wiedemeier and P. Siemers, *Zeitschrift für anorganische und allgemeine Chemie*, 1975, **411**, 90–96.

[217] M. Sist, C. Gatti, P. Nørby, S. Cenedese, H. Kasai, K. Kato and B. B. Iversen, *Chemistry–A European Journal*, 2017, **23**, 6888–6895.

[218] Y. Chen, C. Jaworski, Y. Gao, H. Wang, T. Zhu, G. Snyder, J. Heremans and X. Zhao, *New Journal of Physics*, 2014, **16**, 013057.

[219] J. Li, X. Zhang, S. Lin, Z. Chen and Y. Pei, *Chemistry of Materials*, 2016, **29**, 605–611.

[220] M. Samanta and K. Biswas, *Journal of the American Chemical Society*, 2017, **139**, 9382–9391.

[221] M. Samanta, S. Roychowdhury, J. Ghatak, S. Perumal and K. Biswas, *Chemistry–A European Journal*, 2017, **23**, 7438–7443.

[222] D. Wu, L.-D. Zhao, S. Hao, Q. Jiang, F. Zheng, J. W. Doak, H. Wu, H. Chi, Y. Gelbstein, C. Uher *et al.*, *Journal of the American Chemical Society*, 2014, **136**, 11412–11419.

[223] S. Hao, F. Shi, V. P. Dravid, M. G. Kanatzidis and C. Wolverton, *Chemistry of Materials*, 2016, **28**, 3218–3226.

[224] X. Zhang, J. Shen, S. Lin, J. Li, Z. Chen, W. Li and Y. Pei, *Journal of Materiomics*, 2016, **2**, 331–337.

[225] H. Ipser, M. Gambino and W. Schuster, *Monatshefte für Chemie/Chemical Monthly*, 1982, **113**, 389–398.

[226] S. Geller and J. Wernick, *Acta Crystallographica*, 1959, **12**, 46–54.

[227] C. M. Rost, E. Sachet, T. Borman, A. Moballegh, E. C. Dickey, D. Hou, J. L. Jones, S. Curtarolo and J.-P. Maria, *Nature communications*, 2015, **6**, 8485.

[228] J.-W. Yeh, S.-K. Chen, S.-J. Lin, J.-Y. Gan, T.-S. Chin, T.-T. Shun, C.-H. Tsau and S.-Y. Chang, *Advanced Engineering Materials*, 2004, **6**, 299–303.

[229] R. Liu, H. Chen, K. Zhao, Y. Qin, B. Jiang, T. Zhang, G. Sha, X. Shi, C. Uher, W. Zhang *et al.*, *Advanced Materials*, 2017, **29**, 1702712.

[230] J.-K. Lee, H.-J. Youn and K. S. Hong, *Journal of materials research*, 1999, **14**, 83–89.

[231] H. Okamoto, *Journal of phase equilibria*, 2000, **21**, 496–496.

[232] B. Cook, M. Kramer, X. Wei, J. Harringa and E. Levin, *Journal of Applied Physics*, 2007, **101**, 053715.

[233] A. Elkorashy, *physica status solidi (b)*, 1986, **135**, 707–713.

[234] D. Vaughn, D. Sun, S. M. Levin, A. J. Biacchi, T. S. Mayer and R. E. Schaak, *Chemistry of Materials*, 2012, **24**, 3643–3649.

[235] D. Damon, M. Lubell and R. Mazelsky, *Journal of Physics and Chemistry of Solids*, 1967, **28**, 520–522.

[236] A. H. Edwards, A. C. Pineda, P. A. Schultz, M. G. Martin, A. P. Thompson, H. P. Hjalmarson and C. J. Umrigar, *Physical Review B*, 2006, **73**, 045210.

[237] J. E. Boschker, R. Wang and R. Calarco, *CrystEngComm*, 2017, **19**, 5324–5335.

[238] C. B. Vining, W. Laskow, J. O. Hanson, R. R. Van der Beck and P. D. Gorsuch, *J. Appl. Phys.*, 1991, **69**, 4333–4340.

[239] S. R. Brown, S. M. Kauzlarich, F. Gascoin and G. J. Snyder, *Chem. Mater.*, 2006, **18**, 1873–1877.

[240] S. Ohno, U. Aydemir, M. Amsler, J.-H. Pöhls, S. Chanakian, A. Zevalkink, M. A. White, x. K. Bux, C. Wolverton and G. J. Snyder, *Adv. Funct. Mater.*, 2017, **27**, 1606361.

[241] C. A. Uvarov, J. F. Rauscher and S. M. Kauzlarich, *Sci. Adv. Mater.*, 2011, **3**, 646–651.

[242] H. Jin, C. M. Jaworski and J. P. Heremans, *App. Phys. Lett.*, 2012, **101**, 053904.

[243] S. Cho, A. DiVenere, G. K. Wong, J. B. Ketterson and J. R. Meyer, *Phys. Rev. B*, 1999, **59**, 10691.

[244] D.-Y. Chung, T. P. Hogan, M. Rocci-Lane, P. Brazis, J. R. Ireland, C. R. Kannewurf, M. Bastea, C. Uher and M. G. Kanatzidis, *J. Am. Chem. Soc.*, 2004, **126**, 6414–6428.

[245] L. Lykke, B. B. Iversen and G. K. H. Madsen, *Phys. Rev. B*, 2006, **73**, 195121.

[246] D. A. Wright, *Nature*, 1958, **181**, 834–834.

[247] D. Kusano and Y. Hori, *J. Jpn. Inst. Met.*, 2002, **66**, 1063–1065.

[248] S. LeBlanc, *Sustain. Mater. Technol.*, 2014, **1**, 26–35.

[249] R. T. Littleton IV, T. M. Tritt, J. W. Kolis and D. R. Ketchum, *Phys. Rev. B*, 1999, **60**, 13453.

[250] N. D. Lowhorn, T. M. Tritt, E. E. Abbott and J. W. Kolis, *Appl. Phys. Lett.*, 2006, **88**, 022101.

[251] B. M. Zawilski, R. T. Littleton IV and T. M. Tritt, *Appl. Phys. Lett.*, 2000, **77**, 2319–2321.

[252] E. F. Skelton, T. J. Wieting, S. A. Wolf, W. W. Fuller, D. U. Gubser, T. L. Francavilla and F. Levy, *Solid State Commun.*, 1982, **42**, 1–3.

[253] S. Okada, T. Sambongi, M. Ido, Y. Tazuke, R. Aoki and O. Fujita, *J. Phys. Soc. Jpn.*, 1982, **51**, 460–467.

[254] M. Rubinstein, *Phys. Rev. B*, 1999, **60**, 1627.

[255] P. Shahi, D. J. Singh, J. P. Sun, L. X. Zhao, G. F. Chen, J.-Q. Yan, D. G. Mandrus and J.-G. Cheng, *arXiv preprint arXiv:1611.06370*, 2016.

[256] H. Chi, C. Zhang, G. Gu, D. E. Kharzeev, X. Dai and Q. Li, *New J. Phys.*, 2017, **19**, 015005.

[257] W. Yu, Y. Jiang, J. Yang, Z. L. Dun, H. D. Zhou, Z. Jiang, P. Lu and W. Pan, *Sci. Rep.*, 2016, **6**, 35357.

[258] H. Weng, X. Dai and Z. Fang, *Phys. Rev. X*, 2014, **4**, 011002.

[259] Q. Li, D. E. Kharzeev, C. Zhang, Y. Huang, I. Pletikosić, A. V. Fedorov, R. D. Zhong, J. A. Schneeloch, G. D. Gu and T. Valla, *Nature Phys.*, 2016, **12**, 550–555.

[260] H. Wang, C.-K. Li, H. Liu, J. Yan, J. Wang, J. Liu, Z. Lin, Y. Li, Y. Wang, L. Li, D. Mandrus, X. C. Xie, J. Feng and J. Wang, *Phys. Rev. B*, 2016, **93**, 165127.

[261] H. Wang, H. Liu, Y. Li, Y. Liu, J. Wang, J. Liu, Y. Wang, L. Li, J. Yan, D. Mandrus, X. C. Xie and J. Wang, *arXiv preprint arXiv:1704.00995*, 2017.

[262] Z. Fan, Q.-F. Liang, Y. B. Chen, S.-H. Yao and J. Zhou, *Sci. Rep.*, 2017, **7**, 45667.

[263] D. N. McIlroy, S. Moore, D. Zhang, J. Wharton, B. Kempton, R. Littleton, M. Wilson, T. M. Tritt and C. G. Olson, *J. Phys. Condens. Matter*, 2004, **16**, L359.

[264] X.-B. Li, W.-K. Huang, Y.-Y. Lv, K.-W. Zhang, C.-L. Yang, B.-B. Zhang, Y. B. Chen, S.-H. Yao, J. Zhou, M.-H. Lu, L. Sheng, S.-C. Li, J.-F. Jia, Q.-K. Xue, Y.-F. Chen and D.-Y. Xing, *Phys. Rev. Lett.*, 2016, **116**, 176803.

[265] R. Wu, J.-Z. Ma, S.-M. Nie, L.-X. Zhao, X. Huang, J.-X. Yin, B.-B. Fu, P. Richard, G.-F. Chen, Z. Fang, X. Dai, H.-M. Weng, T. Qian, H. Ding and S. H. Pan, *Phys. Rev. X*, 2016, **6**, 021017.

[266] A. Pariari and P. Mandal, *Sci. Rep.*, 2017, **7**, 40327.

[267] G. Zheng, J. Lu, X. Zhu, W. Ning, Y. Han, H. Zhang, J. Zhang, C. Xi, J. Yang, H. Du, K. Yang, Y. Zhang and M. Tian, *Phys. Rev. B*, 2016, **93**, 115414.

[268] L. Akselrud and Y. Grin, *J. Appl. Crystallogr.*, 2014, **47**, 803–805.

[269] H. Fjellvåg and A. Kjekshus, *Solid State Commun.*, 1986, **60**, 91–93.

[270] R. T. Littleton IV, T. M. Tritt, C. R. Feger, J. Kolis, M. L. Wilson, M. Marone, J. Payne, D. Verebeli and F. Levy, *Appl. Phys. Lett.*, 1998, **72**, 2056–2058.

[271] M. Izumi, K. Uchinokura, E. Matsuura and S. Harada, *Solid State Commun.*, 1982, **42**, 773–778.

[272] M. Izumi, T. Nakayama, K. Uchinokura, S. Harada, R. Yoshizaki and E. Matsuura, *J. Phys. C: Solid State Phys.*, 1987, **20**, 3691.

[273] W. W. Fuller, S. A. Wolf, T. J. Wieting, R. C. LaCoe, P. M. Chaikin and C. Y. Huang, *J. Phys. Colloq.*, 1983, **44**, C3–1709.

[274] R. T. Littleton IV, T. M. Tritt, J. W. Kolis, D. R. Ketchum, N. D. Lowhorn and M. B. Korzenski, *Phys. Rev. B*, 2001, **64**, 121104.

[275] T. E. Jones, W. W. Fuller, T. J. Wieting and F. Levy, *Solid State Commun.*, 1982, **42**, 793–798.

[276] T. M. Tritt, N. D. Lowhorn, R. T. Littleton IV, A. Pope, C. R. Feger and J. W. Kolis, *Phys. Rev. B*, 1999, **60**, 7816.

[277] J. Wang, A. M. DaSilva, C.-Z. Chang, K. He, J. K. Jain, N. Samarth, X.-C. Ma, Q.-K. Xue and M. H. W. Chan, *Phys. Rev. B*, 2011, **83**, 245438.

[278] Y. Zhang, C. Wang, L. Yu, G. Liu, A. Liang, J. Huang, S. Nie, X. Sun, Y. Zhang, B. Shen, J. Liu, H. Weng, L. Zhao, G. Chen, X. Jia, C. Hu, Y. Ding, W. Zhao, Q. Gao, C. Li, S. He, L. Zhao, F. Zhang, S. Zhang, F. Yang, Z. Wang, Q. Peng, X. Dai, Z. Fang, Z. Xu, C. Chen and X. J. Zhou, *Nature Commun.*, 2017, **8**, 15512.

[279] R. Y. Chen, S. J. Zhang, J. A. Schneeloch, C. Zhang, Q. Li, G. D. Gu and N. L. Wang, *Phys. Rev. B*, 2015, **92**, 075107.

[280] L. Moreschini, J. C. Johannsen, H. Berger, J. Denlinger, C. Jozwiack, E. Rotenberg, K. S. Kim, A. Bostwick and M. Grioni, *Phys. Rev. B*, 2016, **94**, 081101.

[281] R. Y. Chen, Z. G. Chen, X.-Y. Song, J. A. Schneeloch, G. D. Gu, F. Wang and N. L. Wang, *Phys. Rev. Lett.*, 2015, **115**, 176404.

[282] Y. Liu, X. Yuan, C. Zhang, Z. Jin, A. Narayan, C. Luo, Z. Chen, L. Yang, J. Zou, X. Wu, S. Sanvito, Z. Xia, L. Li, Z. Wang and F. Xiu, *Nature Commun.*, 2016, **7**, 12516.

[283] Y. Zhou, J. Wu, W. Ning, N. Li, Y. Du, X. Chen, R. Zhang, Z. Chi, X. Wang, X. Zhu, P. Lu, C. Ji, X. Wan, Z. Yang, J. Sun, W. Yang, M. Tian, Y. Zhang and H.-k. Mao, *Proc. Natl. Acad. Sci. U.S.A.*, 2016, **113**, 2904–2909.

[284] W. Shockley, *Electrons and holes in semiconductors*, van Nostrand, 1953.

[285] G. N. Kamm, D. J. Gillespie, A. C. Ehrlich, T. J. Wieting and F. Levy, *Phys. Rev. B*, 1985, **31**, 7617.

[286] H. Xiong, J. A. Sobota, S.-L. Yang, H. Soifer, A. Gauthier, M.-H. Lu, Y.-Y. Lv, S.-H. Yao, D. Lu, M. Hashimoto, P. S. Kirchmann, Y.-F. Chen and Z.-X. Shen, *Phys. Rev. B*, 2017, **95**, 195119.

[287] G. Qiu, Y. Du, A. Charnas, H. Zhou, S. Jin, Z. Luo, D. Y. Zemlyanov, X. Xu, G. J. Cheng and P. D. Ye, *Nano Lett.*, 2016, **16**, 7364–7369.

[288] Y.-Y. Lv, F. Zhang, B.-B. Zhang, B. Pang, S.-H. Yao, Y. B. Chen, L. Ye, J. Zhou, S.-T. Zhang and Y.-F. Chen, *J. Crys. Growth*, 2017, **457**, 250–254.

[289] M. K. Hooda and C. S. Yadav, *Appl. Phys. Lett.*, 2017, **111**, 053902.

[290] M.-H. Whangbo, F. J. DiSalvo and R. M. Fleming, *Phys. Rev. B*, 1982, **26**, 687.

[291] N. D. Lowhorn, T. M. Tritt, E. E. Abbott and J. W. Kolis, Thermoelectrics, 2005. ICT 2005. 24th International Conference on, 2005, pp. 41–45.

[292] R. T. Littleton IV, *Ph.D. thesis*, Clemson University, 2001.

[293] M. Chan, S. Lai, M. Fung, C. Lee and S. Lee, *Appl. Phys. Lett.*, 2007, **90**, 023504.

[294] J. Oh, H.-C. Yuan and H. M. Branz, *Nat. Nanotechnol.*, 2012, **7**, 743.

[295] P. Avouris and J. Chen, *Mater. Today*, 2006, **9**, 46–54.

[296] O. V. Khokhlev, K. A. Bulashevich and S. Y. Karpov, *Phys. Status Solidi (A)*, 2013, **210**, 1369–1376.

[297] E. Pankratov and E. Bulaeva, *Rev. Theor. Sc.*, 2013, **1**, 58–82.

[298] V. Derycke, R. Martel, J. Appenzeller and P. Avouris, *Appl. Phys. Lett.*, 2002, **80**, 2773–2775.

[299] G.-H. Kim, L. Shao, K. Zhang and K. P. Pipe, *Nat. Mater.*, 2013, **12**, 719.

[300] E. S. Toberer, A. F. May and G. J. Snyder, *Chem. Mater.*, 2009, **22**, 624–634.

[301] Y. Pei, A. D. LaLonde, N. A. Heinz, X. Shi, S. Iwanaga, H. Wang, L. Chen and G. J. Snyder, *Adv. Mater.*, 2011, **23**, 5674–5678.

[302] A. Rocket, in *Defects in Semiconductors*, Springer US, Boston, MA, 2008, pp. 289–356.

[303] S. Zhang, S.-H. Wei and A. Zunger, *J. Appl. Phys.*, 1998, **83**, 3192–3196.

[304] A. Zunger, *Appl. Phys. Lett.*, 2003, **83**, 57–59.

[305] T. R. Paudel, A. Zakutayev, S. Lany, M. d'Avezac and A. Zunger, *Adv. Funct. Mater.*, 2011, **21**, 4493–4501.

[306] W. Walukiewicz, *Physica B: Condens. Matter*, 2001, **302**, 123–134.

[307] W. Faschinger, S. Ferreira and H. Sitter, *J. Cryst. Growth*, 1995, **151**, 267–272.

[308] M. W. Gaultois, A. O. Oliynyk, A. Mar, T. D. Sparks, G. J. Mulholland and B. Meredig, *arXiv preprint arXiv:1502.07635*, 2015.

[309] S. Zhang, S.-H. Wei and A. Zunger, *Physica B: Condens. Matter*, 1999, **273**, 976–980.

[310] W. Walukiewicz, *J. Vac. Sci. & Technol. B: Microelectron. Process. Phenom.*, 1987, **5**, 1062–1067.

[311] C. G. Van de Walle and J. Neugebauer, *Nature*, 2003, **423**, 626.

[312] C. G. Van de Walle and J. Neugebauer, *J. Appl. Phys.*, 2004, **95**, 3851–3879.

[313] C. G. Van de Walle, *Phys. Rev. Lett.*, 2000, **85**, 1012.

[314] S. Lany, J. Osorio-Guillén and A. Zunger, *Phys. Rev. B*, 2007, **75**, 241203.

[315] F. Legrain, J. Carrete, A. van Roekeghem, S. Curtarolo and N. Mingo, *Chem. Mater.*, 2017, **29**, 6220–6227.

[316] C. Chen, Z. Deng, R. Tran, H. Tang, I.-H. Chu and S. P. Ong, *Phys. Rev. Mater.*, 2017, **1**, 043603.

[317] Z. Li, J. R. Kermode and A. De Vita, *Phys. Rev. Lett.*, 2015, **114**, 096405.

[318] A. Takahashi, A. Seko and I. Tanaka, *Phys. Rev. Mater.*, 2017, **1**, 063801.

[319] A. Seko, H. Hayashi, K. Nakayama, A. Takahashi and I. Tanaka, *Phys. Rev. B*, 2017, **95**, 144110.

[320] Y. Zhang and C. Ling, *npj Comput. Mater.*, 2018, **4**, 25.

[321] L. M. Ghiringhelli, J. Vybiral, S. V. Levchenko, C. Draxl and M. Scheffler, *Phys. Rev. Lett.*, 2015, **114**, 105503.

[322] M. De Jong, W. Chen, R. Notestine, K. Persson, G. Ceder, A. Jain, M. Asta and A. Gamst, *Sci. Rep.*, 2016, **6**, 34256.

[323] A. Mannodi-Kanakkithodi, T. D. Huan and R. Ramprasad, *Chem. Mater.*, 2017, **29**, 9001–9010.

[324] X. Ma, Z. Li, L. E. Achenie and H. Xin, *J. Phys. Chem. Lett.*, 2015, **6**, 3528–3533.

[325] Y. Zeng, S. J. Chua and P. Wu, *Chem. Mater.*, 2002, **14**, 2989–2998.

[326] P. Dey, J. Bible, S. Datta, S. Broderick, J. Jasinski, M. Sunkara, M. Menon and K. Rajan, *Comput. Mater. Sci.*, 2014, **83**, 185–195.

[327] B. Medasani, A. Gamst, H. Ding, W. Chen, K. A. Persson, M. Asta, A. Canning and M. Haranczyk, *npj Comput. Mater.*, 2016, **2**, 1.

[328] Z. Li, S. Wang, W. S. Chin, L. E. Achenie and H. Xin, *J. Mater. Chem. A*, 2017, **5**, 24131–24138.

[329] P. Raccuglia, K. C. Elbert, P. D. Adler, C. Falk, M. B. Wenny, A. Mollo, M. Zeller, S. A. Friedler, J. Schrier and A. J. Norquist, *Nature*, 2016, **533**, 73.

[330] A. D. Sendek, Q. Yang, E. D. Cubuk, K.-A. N. Duerloo, Y. Cui and E. J. Reed, *Energy Environ. Sci.*, 2017, **10**, 306–320.

[331] A. O. Oliynyk, E. Antono, T. D. Sparks, L. Ghadbeigi, M. W. Gaultois, B. Meredig and A. Mar, *Chem. Mater.*, 2016, **28**, 7324–7331.

[332] W. Lu, R. Xiao, J. Yang, H. Li and W. Zhang, *J. Materiomics*, 2017, **3**, 191–201.

[333] E. Kim, K. Huang, A. Tomala, S. Matthews, E. Strubell, A. Saunders, A. McCallum and E. Olivetti, *Sci. Data*, 2017, **4**, 170127.

[334] E. Kim, K. Huang, S. Jegelka and E. Olivetti, *npj Comput. Mater.*, 2017, **3**, 53.

[335] G. Pilania, A. Mannodi-Kanakkithodi, B. Uberuaga, R. Ramprasad, J. Gubernatis and T. Lookman, *Sci. Rep.*, 2016, **6**, 19375.

[336] Q. Guo, G. M. Ford, W.-C. Yang, B. C. Walker, E. A. Stach, H. W. Hillhouse and R. Agrawal, *J. Am. Chem. Soc.*, 2010, **132**, 17384–17386.

[337] M. G. Panthani, V. Akhavan, B. Goodfellow, J. P. Schmidtke, L. Dunn, A. Dodabalapur, P. F. Barbara and B. A. Korgel, *J. Am. Chem. Soc.*, 2008, **130**, 16770–16777.

[338] J. Fan, H. Liu, X. Shi, S. Bai, X. Shi and L. Chen, *Acta Mater.*, 2013, **61**, 4297–4304.

[339] R. Liu, L. Xi, H. Liu, X. Shi, W. Zhang and L. Chen, *Chem. Commun.*, 2012, **48**, 3818–3820.

[340] B. R. Ortiz, W. Peng, L. C. Gomes, P. Gorai, T. Zhu, D. M. Smiadak, G. J. Snyder, V. Stevanović, E. Ertekin, A. Zevalkink *et al.*, *Chem. Mater.*, 2018.

[341] J. L. Shay and J. H. Wernick, *Ternary Chalcopyrite Semiconductors: Growth, Electronic Properties, and Applications: International Series of Monographs in The Science of The Solid State*, Elsevier, 2017, vol. 7.

[342] E. Parthé, *Crystal chemistry of tetrahedral structures*, CRC Press, 1964.

[343] B. Tell, J. Shay and H. Kasper, *Physical Review B*, 1974, **9**, 5203.

[344] F. Ferrara, F. Ledda, P. Manca and G. Pegna, *Il Nuovo Cimento D*, 1983, **2**, 1674–1680.

[345] J. J. Curry and S. Pollack, *Journal of Physics and Chemistry of Solids*, 1970, **31**, 1235–1246.

[346] P. Manca and L. Garbato, *Solar cells*, 1986, **16**, 101–121.

[347] V. Zhuze, V. Sergeeva and E. Shtrum, *New semiconductor compounds*, 1958.

[348] L. Berger and V. Prochukhan, *Ternary Diamond-like Semiconductors*, Consultants Bureau, New York, 1969.

[349] H. Karaagac and M. Parlak, *Applied Surface Science*, 2011, **257**, 5731–5738.

[350] B. Tell, J. Shay and H. Kasper, *Journal of Applied Physics*, 1972, **43**, 2469–2470.

[351] C. Merschjann, M. Mews, T. Mete, A. Karkatzinou, M. Rusu, B. Korzun, S. Schorr, P. Schubert-Bischoff, S. Seeger, T. Schedel-Niedrig *et al.*, *Journal of Physics: Condensed Matter*, 2012, **24**, 175801.

[352] Y. S. Murthy, O. M. Hussain, S. Uthanna, B. S. Naidu and P. J. Reddy, *Physics Letters A*, 1991, **152**, 311–314.

[353] K.-M. Nigge, F. Baumgartner and E. Bucher, *Solar energy materials and solar cells*, 1996, **43**, 335–343.

[354] B. Kuhn, K. Friemelt, K. Fess and E. Bucher, *physica status solidi (a)*, 1997, **160**, 151–158.

[355] R. Kumar and R. Bedi, *Journal of materials science*, 2005, **40**, 455–459.

[356] R. Kumar, A. Singh, A. Mahajan, R. Bedi and T. Singh, 2000.

[357] A. Yusufu, K. Kurosaki, A. Kosuga, T. Sugahara, Y. Ohishi, H. Muta and S. Yamanaka, *Applied Physics Letters*, 2011, **99**, 061902.

[358] K. Hattori, K. Akamatsu and N. Kamegashira, *Journal of applied physics*, 1992, **71**, 3414–3418.

[359] Y. Akaki, S. Kurihara, M. Shirahama, K. Tsurugida, T. Kakeno and K. Yoshino, *Journal of Materials Science: Materials in Electronics*, 2005, **16**, 393–396.

[360] R. Beaulieu, J. Loferski, B. Roessler *et al.*, *Thin Solid Films*, 1980, **67**, 341–345.

[361] N. Joshi, L. Martinez and R. Echeverria, *Journal of Physics and Chemistry of Solids*, 1981, **42**, 281–285.

[362] O. Madelung, U. Rössler and M. Schulz, *Springer Materials—The Landolt-Börnstein Database*, 1999.

[363] H. Matsuo, K. Yoshino and T. Ikari, *physica status solidi (c)*, 2006, **3**, 2644–2647.

[364] M. Kaleli, T. Çolakoğlu and M. Parlak, *Applied Surface Science*, 2013, **286**, 171–176.

[365] R. Bedi, D. Pathak, D. Kaur *et al.*, *Zeitschrift fur Kristallographie Supplements*, 2008, **2008**, 177–183.

[366] H. T. Shaban and M. K. Gergs, *Materials Sciences and Applications*, 2014, **5**, 292.

[367] B. Tell and H. Kasper, *Journal of Applied Physics*, 1974, **45**, 5367–5370.

[368] K. Yoshino, A. Kinoshita, Y. Shirahata, M. Oshima, K. Nomoto, T. Yoshitake, S. Ozaki and T. Ikari, Journal of Physics: Conference Series, 2008, p. 042042.

[369] C. Bellabarba and S. Wasim, *physica status solidi (a)*, 1981, **66**, year.

[370] Y. Aikebaier, K. Kurosaki, T. Sugahara, Y. Ohishi, H. Muta and S. Yamanaka, *Materials Science and Engineering: B*, 2012, **177**, 999–1002.

[371] O. Parasyuk, S. Chykhrij, V. Bozhko, L. Piskach, M. Bogdanyuk, I. Olekseyuk, L. Bulatetska and V. Pekhnyo, *Journal of alloys and compounds*, 2005, **399**, 32–37.

[372] R. Davila and B. Fernandez, *TERNARY AND MULTINARY COMPOUNDS*, 1998, **152**, 531–534.

[373] L.-Y. Yeh and K.-W. Cheng, *Thin Solid Films*, 2014, **558**, 289–293.

[374] T. Jing, Y. Dai, X. Ma, W. Wei and B. Huang, *The Journal of Physical Chemistry C*, 2015, **119**, 27900–27908.

[375] C. Ma, H. Guo, K. Zhang, Y. Li, N. Yuan and J. Ding, *Materials Letters*, 2017, **207**, 209–212.

[376] C. Ma, H. Guo, K. Zhang, N. Yuan and J. Ding, *Materials Letters*, 2017, **186**, 390–393.

[377] K.-W. Cheng, *Journal of the Taiwan Institute of Chemical Engineers*, 2017, **75**, 199–208.

[378] T. Gershon, Y. S. Lee, P. Antunez, R. Mankad, S. Singh, D. Bishop, O. Gunawan, M. Hopstaken and R. Haight, *Advanced Energy Materials*, 2016, **6**, 1502468.

[379] M. Ettenberg, A. Sigai, A. Dreeben and S. Gilbert, *Journal of The Electrochemical Society*, 1971, **118**, 1355–1358.

[380] R. Newman, *Materials Science and Engineering: B*, 1999, **66**, 39–45.

[381] N. Chand, T. Henderson, J. Klem, W. T. Masselink, R. Fischer, Y.-C. Chang and H. Morkoĉ, *Physical Review B*, 1984, **30**, 4481.

[382] A. Sigai, M. Abrahams and J. Blanc, *Journal of The Electrochemical Society*, 1972, **119**, 952–956.

[383] G. Hass, M. H. Francombe and R. W. Hoffman, *Physics of Thin Films: Advances in Research and Development*, Elsevier, 2013.

[384] Y. Taniyasu, M. Kasu and N. Kobayashi, *Applied physics letters*, 2002, **81**, 1255–1257.

[385] Y.-B. Tang, X.-H. Bo, J. Xu, Y.-L. Cao, Z.-H. Chen, H.-S. Song, C.-P. Liu, T.-F. Hung, W.-J. Zhang, H.-M. Cheng *et al.*, *Acs Nano*, 2011, **5**, 3591–3598.

[386] A. Polyakov, N. Smirnov, A. Govorkov, A. Markov, T. Yugova, A. Dabiran, A. Wowchak, B. Cui, A. Osinsky, P. Chow *et al.*, *Journal of Applied Physics*, 2008, **104**, 053702.

[387] S. B. Thapa, *Annual Report 2007*, 2007, 85.

[388] N. H. Tran, B. H. Le, S. Zhao and Z. Mi, *Applied Physics Letters*, 2017, **110**, 032102.

[389] F. Reid, S. Miller and H. Goering, *Journal of The Electrochemical Society*, 1966, **113**, 467–469.

[390] F. Reid and R. Willardson, *International Journal Of Electronics*, 1958, **5**, 54–61.

[391] E. Vaughan, S. Addamane, D. Shima, G. Balakrishnan and A. Hecht, *Journal of Electronic Materials*, 2016, **45**, 2025–2030.

[392] B. R. Bennett, W. Moore, M. Yang and B. Shanabrook, *Journal of Applied Physics*, 2000, **87**, 7876–7879.

[393] W. Allred, W. Mefferd and R. Willardson, *Journal of The Electrochemical Society*, 1960, **107**, 117–122.

[394] K. Rustagi, P. Merle, D. Auvergne and H. Mathieu, *Solid State Communications*, 1976, **18**, 1201–1203.

[395] E. I. Vaughan, *Thin film AlSb carrier transport properties and room temperature radiation response*, The University of New Mexico, 2016.

[396] C.-Y. Lee, *Physical Review B*, 1987, **35**, 4511.

[397] S. Subbanna, G. Tuttle and H. Kroemer, *Journal of electronic materials*, 1988, **17**, 297–303.

[398] T. Chu and A. Hyslop, *Journal of The Electrochemical Society*, 1974, **121**, 412–415.

[399] T. Chu and A. Hyslop, *Journal of Applied Physics*, 1972, **43**, 276–279.

[400] M. S. Shur, *Handbook series on semiconductor parameters*, World Scientific, 1996, vol. 1.

[401] D. Litvinov, C. A. Taylor II and R. Clarke, *Diamond and related materials*, 1998, **7**, 360–364.

[402] M. Lu, A. Bousetta, A. Bensaoula, K. Waters and J. Schultz, *Applied physics letters*, 1996, **68**, 622–624.

[403] S. Majety, T. Doan, J. Li, J. Lin and H. Jiang, *AIP Advances*, 2013, **3**, 122116.

[404] K. Teii, T. Hori, Y. Mizusako and S. Matsumoto, *ACS applied materials & interfaces*, 2013, **5**, 2535–2539.

[405] T. Yamada, C. E. Nebel and T. Taniguchi, Vacuum Nanoelectronics Conference (IVNC), 2010 23rd International, 2010, pp. 1–2.

[406] K. Shohno, M. Takigawa and T. Nakada, *Journal of Crystal Growth*, 1974, **24**, 193–196.

[407] T. Chu, J. Jackson, A. Hyslop and S. Chu, *Journal of Applied Physics*, 1971, **42**, 420–424.

[408] T. Chu, M. Gill and S. S. Chu, *Journal of The Electrochemical Society*, 1976, **123**, 259–262.

[409] T. Chu, 1975.

[410] M. Iwami, N. Fujita and K. Kawabe, *Japanese Journal of Applied Physics*, 1971, **10**, 1746.

[411] N. Kato, W. Kammura, M. Iwami and K. Kawabe, *Japanese Journal of Applied Physics*, 1977, **16**, 1623.

[412] Y. Kumashiro, Y. Okada and S. Gonda, *Journal of Crystal Growth*, 1984, **70**, 507–514.

[413] Y. Kumashiro, M. Hirabayashi, T. Koshiro and Y. Okada, *Journal of the Less Common Metals*, 1988, **143**, 159–165.

[414] Y. Kumashiro, *The Rigaku Journal*, 1990, **7**, year.

[415] Y. Kumashiro, T. Yao and S. Gonda, *Journal of Crystal Growth*, 1984, **70**, 515–518.

[416] B. Padavala, C. Frye, X. Wang, Z. Ding, R. Chen, M. Dudley, B. Raghothamachar, P. Lu, B. Flanders and J. Edgar, *Crystal Growth & Design*, 2015, **16**, 981–987.

[417] B. Stone and D. Hill, *Physical Review Letters*, 1960, **4**, 282.

[418] T. Takenaka, M. Takigawa and K. Shohno, *Japanese Journal of Applied Physics*, 1975, **14**, 579.

[419] S. Das, R. Bhunia, S. Hussain, R. Bhar, B. Chakraborty and A. Pal, *Applied Surface Science*, 2015, **353**, 439–448.

[420] W. Yim, J. Dismukes, E. Stofko and R. Paff, *Journal of Physics and Chemistry of Solids*, 1972, **33**, 501–505.

[421] H.-J. Lugauer, F. Fischer, T. Litz, A. Waag, U. Zehnder, W. Ossau, T. Gerhard, G. Landwehr, C. Becker, R. Kruse *et al.*, *Materials Science and Engineering: B*, 1997, **43**, 88–91.

[422] J. Barjon, E. Chikoidze, F. Jomard, Y. Dumont, M.-A. Pinault-Thaury, R. Issaoui, O. Brinza, J. Achard and F. Silva, *physica status solidi (a)*, 2012, **209**, 1750–1753.

[423] M. Werner, R. Locher, W. Kohly, D. Holmes, S. Klose and H. Fecht, *Diamond and Related Materials*, 1997, **6**, 308–313.

[424] M. Gabrysch, S. Majdi, A. Hallén, M. Linnarsson, A. Schöner, D. Twitchen and J. Isberg, *physica status solidi (a)*, 2008, **205**, 2190–2194.

[425] M. Katagiri, J. Isoya, S. Koizumi and H. Kanda, *Applied physics letters*, 2004, **85**, 6365–6367.

[426] H. Kato, S. Yamasaki and H. Okushi, *Diamond and related materials*, 2007, **16**, 796–799.

[427] Z. Teukam, J. Chevallier, C. Saguy, R. Kalish, D. Ballutaud, M. Barbé, F. Jomard, A. Tromson-Carli, C. Cytermann, J. E. Butler *et al.*, *Nature Materials*, 2003, **2**, 482.

[428] P.-N. Volpe, J. Pernot, P. Muret and F. Omnès, *Applied Physics Letters*, 2009, **94**, 092102.

[429] H. Horinaka, A. Uemura and N. Yamamoto, *Journal of Crystal Growth*, 1990, **99**, 785–789.

[430] O. Emelyanenko and I. Polushina, *physica status solidi (b)*, 1969, **36**, K13–K15.

[431] L. Bai, C. Xu, N. Giles, K. Nagashio and R. Feigelson, *Journal of applied physics*, 2006, **99**, 013512.

[432] W. Huang, B. Zhao, S. Zhu, Z. He, B. Chen, Z. Zhen and Y. Pu, *Journal of Alloys and Compounds*, 2016, **656**, 818–824.

[433] H. Kildal, *CdGeAs2 and CdGeP2 Chalcopyrite Materials for Infrared Nonlinear Optics*, Stanford univ ca microwave lab technical report, 1972.

[434] I. Polushina, Y. V. Rud, T. Ushakova and V. Y. Rud, *Physics of the Solid State*, 1999, **41**, 1084–1087.

[435] T. Pollak, *Infrared Applications of Semiconductors Three*, 2000, **3**, 427.

[436] B. Bairamov, V. Y. Rud and Y. V. Rud, *MRS Bulletin*, 1998, **23**, 41–44.

[437] V. Y. Rud and Y. V. Rud, *Japanese Journal of Applied Physics*, 1993, **32**, 672.

[438] L. Kilanski, A. Reszka, M. Górska, V. Domukhovski, A. Podgórni, B. Kowalski, W. Dobrowolski, I. Fedorchenko, A. Aronov and S. Marenkin, *Journal of Physics: Condensed Matter*, 2016, **28**, 495802.

[439] V. Novotortsev, A. Y. Mollaev, I. Kamilov, R. Arslanov, U. Zalibekov, S. Marenkin and S. Varnavskii, *Inorganic materials*, 2006, **42**, 826–829.

[440] A. Miller and W. Clark, *Le Journal de Physique Colloques*, 1975, **36**, C3–73.

[441] S. Endo and T. Irie, *Journal of Physics and Chemistry of Solids*, 1976, **37**, 201–209.

[442] A. Aresti and A. Congiu, *physica status solidi (a)*, 1973, **16**, year.

[443] J. R. Mohamed and L. Amalraj.

[444] S. Baek, T. Jeong, C. Youn, K. Hong, J. Park, D. Shin and Y. Yoo, *Journal of crystal growth*, 2004, **262**, 259–264.

[445] K. Allakhverdiev, V. Antonov, E. SALAEV and R. NANI, *TEMPERATURE DEPENDENCES OF HALL-EFFECT AND ELECTRICAL CONDUCTIVITY OF CDIN2S4 SINGLE-CRYSTALS*, 1972.

[446] J. A. Beun, R. Nitsche and M. Lichtensteiger, *Physica*, 1961, **27**, 448–452.

[447] L. Koval, E. Arushanov and S. Radautsan, *physica status solidi (a)*, 1972, **9**, K73–K75.

[448] D. Sudha, S. Dhanapandian, C. Manoharan and A. Arunachalam, *Results in physics*, 2016, **6**, 599–605.

[449] S. Ou, S. Eshraghi, O. Stafsudd and A. Gentile, *Journal of applied physics*, 1985, **57**, 355–358.

[450] G. Couturier, A. El Farji, F. Lestournelle and J. Launay, *Journal of applied physics*, 1991, **70**, 4472–4475.

[451] G. Couturier, B. Jean, J. Lambert, J. Launay and P. Joffre, *Journal of applied physics*, 1993, **73**, 1813–1818.

[452] P. Gorley, Z. Grushka, O. Grushka, P. Gorley and I. Zabolotsky, *Semiconductor physics quantum electronics & optoelectronics*, 2010, 444–447.

[453] K. Bohnert, G. Schmieder, S. El-Dessouki and C. Klingshirn, *Solid State Communications*, 1978, **27**, 295–299.

[454] H. Grimmeiss, E. Janzén and N. Kullendorff, *Solid State Communications*, 1980, **35**, 727–728.

[455] J. Hasson and A. Many, *Physical Review Letters*, 1975, **35**, 792.

[456] V. Klimov, P. H. Bolivar and H. Kurz, *Physical Review B*, 1995, **52**, 4728.

[457] F. Kroger, H. Vink and J. Volger, *Physica*, 1954, **3**, 1095–1099.

[458] C. Lokhande and S. Pawar, *Solid State Communications*, 1982, **44**, 1137–1139.

[459] K. Matsuura and I. Tsurumi, *Journal of the Physical Society of Japan*, 1975, **39**, 1543–1546.

[460] P. Merchant and C. Elbaum, *Physical Review B*, 1979, **19**, 2992.

[461] B. Sethi, O. Sharma, P. Goyal and P. Mathur, *Journal of Physics C: Solid State Physics*, 1981, **14**, 1649.

[462] A. Shikalgar and S. Pawar, *Solid State Communications*, 1979, **32**, 361–368.

[463] Y. J. Shin, S. K. Kim, B. H. Park, T. S. Jeong, H. K. Shin, T. S. Kim and P. Y. Yu, *Physical Review B*, 1991, **44**, 5522.

[464] N. Stoffel, *Physical Review B*, 1983, **28**, 3306.

[465] N. K. Abrikosov, *Semiconducting II–VI, IV–VI, and V–VI Compounds*, Springer, 2013.

[466] H. Wynands and M. Cocivera, *Journal of The Electrochemical Society*, 1992, **139**, 2052–2057.

[467] T. Ohtsuka, J. Kawamata, Z. Zhu and T. Yao, *Applied physics letters*, 1994, **65**, 466–468.

[468] W. Callister, C. Varotto and D. Stevenson, *physica status solidi (a)*, 1972, **12**, 267–271.

[469] P. Gl, T. Dietl, T. Fromherz, G. Bauer, I. Miotkowski *et al.*, *Physical Review B*, 1994, **49**, 7797.

[470] L. Huldt and S. Boija, *Solid State Communications*, 1970, **8**, 699–701.

[471] M. Lee and H. Drew, *Solid state communications*, 1987, **62**, 825–828.

[472] M. Levy and M. Sarachik, *Journal of applied physics*, 1991, **69**, 2703–2704.

[473] M. Levy, W. Lee, M. Sarachik and S. Geschwind, *Physical Review B*, 1992, **45**, 11685.

[474] M. Pawlak, *Applied Physics A*, 2015, **118**, 173–176.

[475] A. Roy, M. Levy, X. Guo, M. Sarachik, R. Ledesma and L. Isaacs, *Physical Review B*, 1989, **39**, 10185.

[476] R. Tenne, R. Jäger-Waldau, M. Lux-Steiner, E. Bucher, J. Rioux and C. Levy-Clement, *Physical Review B*, 1990, **42**, 1763.

[477] Y. Zhang, P. Dai and M. Sarachik, *Physical Review B*, 1992, **45**, 9473.

[478] Y. Zhang, O. Dai, M. Levy and M. Sarachik, *Physical review letters*, 1990, **64**, 2687.

[479] R. Hall and H. Woodbury, *Journal of Applied Physics*, 1968, **39**, 5361–5365.

[480] M. Avirović, M. Lux-Steiner, U. Elrod, J. Hönigschmid and E. Bucher, *Journal of crystal growth*, 1984, **67**, 185–194.

[481] F. Baumgartner, M. Lux-Steiner, G. Doell, E. Bucher, F. Meier and A. Vaterlaus, *Journal of crystal growth*, 1991, **109**, 314–317.

[482] G. Averkieva, N. Goryunova, V. Prochukan, Y. V. Rud and M. Serginov, *physica status solidi (b)*, 1969, **34**, K5–K8.

[483] G. Averkieva, N. Goryunova, V. Prochukhan, Y. V. Rud and M. Serginov, *physica status solidi (a)*, 1971, **5**, 571–576.

[484] G. AVERKIEVA, N. GORIUNOVA, V. Prochukhan, S. Ryvkin, M. Serginov and I. SHRETER, *SOVIET PHYSICS-SEMICONDUCTORS*, 1971, **5**, 151.

[485] C. Dovletmuradov, K. Ovezov, V. Prochukhan, Y. Rud and M. Serginov, *Soviet Physics-Semiconductors*, 1976, **10**, 986–989.

[486] M. Serginov, N. Goryunova, V. Prochukhan, Y. V. Rud and K. Sanin, *physica status solidi (a)*, 1970, **2**, K75–K78.

[487] A. Strauss and A. Rosenberg, *Journal of Physics and Chemistry of Solids*, 1961, **17**, 278–283.

[488] C. Dovletmuradov, A. A. Lebedev, Y. V. Rud, M. Serginov and V. E. Skoryukin, *Fiz. Tekh. Poluprovodn*, 1981, **15**, 2357–2361.

[489] D. Gasson, P. Holmes, I. Jennings, B. Marathe and J. Parrott, *Journal of Physics and Chemistry of Solids*, 1962, **23**, 1291–1302.

[490] O. Voevodina, A. Vyatkin, V. Voevodin, Y. I. Otman and V. Ots, *Soviet Physics Journal*, 1973, **16**, 923–927.

[491] V. G. Voevodin, O. V. Voevodina, S. A. Bereznaya, Z. V. Korotchenko, N. C. Fernelius, J. T. Goldstein and M. C. Ohmer, *MRS Online Proceedings Library Archive*, 2001, **692**, year.

[492] W. Spitzer, J. Wernick and R. Wolfe, *Solid-State Electronics*, 1961, **2**, 96–99.

[493] M. Matyáš and P. Höschl, *Cechoslovackij fiziceskij zurnal B*, 1962, **12**, 788–795.

[494] T. POLYANSKAYA, S. GA, T. VM and S. YV, *INVESTIGATION OF DEPENDENCE OF HALL COEFFICIENT ON MAGNETIC INDUCTION IN P-TYPE CDSNAS2*, 1967.

[495] S. Mamaev, D. Nasledov and V. Galavanov, *SOVIET PHYSICS-SOLID STATE*, 1962, **3**, 2473–2478.

[496] S. Knight, E. Buehler and I. Camlibel, *Journal of Applied Physics*, 1972, **43**, 3422–3424.

[497] G. A. Medvedkin, T. Nishi and K. Sato, *Japanese Journal of Applied Physics*, 2000, **39**, 6301.

[498] G. A. Medvedkin, T. Nishi and K. Sato, *Sov. Phys. Solid State*, 1989, **31**, 606.

[499] E. Ziegler, W. Siegel and G. Kühnel, *physica status solidi (a)*, 1980, **57**, 625–629.

[500] B. Segall, M. Lorenz and R. Halsted, *Physical Review*, 1963, **129**, 2471.

[501] V. Popovych, I. Virt, D. Tsutsura, Z. Tsybrii, F. Sizov, O. Parfenjuk and M. Ilashchuk, *physica status solidi c*, 2006, **3**, 717–721.

[502] N. Agrinskaya and V. Kozub, *Solid state communications*, 1994, **91**, 853–857.

[503] K. Arai, S. Hagiwara, K. Murase, T. Hirato and Y. Awakura, *Journal of the Electrochemical Society*, 2005, **152**, C237–C242.

[504] M. Carmody and A. Gilmore, *Contract*, 2011, **303**, 275–3000.

[505] A. Carter, G. Carver, R. Nicholas, J. Portal and R. Stradling, *Solid State Communications*, 1977, **24**, 55–60.

[506] A. de Castro and R. Turtelli, *Solid state communications*, 1983, **47**, 475–478.

[507] R. Collins and T. McGill, *Journal of Vacuum Science & Technology A: Vacuum, Surfaces, and Films*, 1983, **1**, 1633–1636.

[508] L. S. Dang, G. Neu and R. Romestain, *Solid State Communications*, 1982, **44**, 1187–1190.

[509] A. J. Al-Douri, F. Al-Shakily, A. A. Alnajjar and M. F. Alias, *Advances in Condensed Matter Physics*, 2011, **2011**, year.

[510] P. Emanuelsson, P. Omling, B. Meyer, M. Wienecke and M. Schenk, *Physical Review B*, 1993, **47**, 15578.

[511] F. Fischer, A. Waag, G. Bilger, T. Litz, S. Scholl, M. Schmitt and G. Landwehr, *Journal of crystal growth*, 1994, **141**, 93–97.

[512] E. Gombia, F. Bissoli, M. Zha, A. Zappettini, T. Görög and L. Zanotti, *physica status solidi (c)*, 2003, 881–884.

[513] H. Jimenez-Gonzalez, R. Aggarwal and P. Becla, *Physical Review B*, 1992, **45**, 14011.

[514] M. Grynberg, S. Huant, G. Martinez, J. Kossut, T. Wojtowicz, G. Karczewski, J. Shi, F. Peeters and J. Devreese, *Physical Review B*, 1996, **54**, 1467.

[515] M. Helm, W. Knap, W. Seidenbusch, R. Lassnig, E. Gornik, R. Triboulet and L. Taylor, *Solid state communications*, 1985, **53**, 547–550.

[516] D. Hommel, A. Waag, S. Scholl and G. Landwehr, *Applied physics letters*, 1992, **61**, 1546–1548.

[517] C. Huber, J. Perez and T. Huber, *Physical Review B*, 1987, **36**, 5933.

[518] G. Khattak, J. Majid, C. Scott and D. Shaw, *Solid state communications*, 1992, **84**, 1073–1076.

[519] L. Kranz, C. Gretener, J. Perrenoud, R. Schmitt, F. Pianezzi, F. La Mattina, P. Blösch, E. Cheah, A. Chirilă, C. M. Fella *et al.*, *Nature communications*, 2013, **4**, 2306.

[520] P. Lemasson, *Solid State Communications*, 1982, **43**, 627–631.

[521] N. Lovergine, P. Prete, L. Tapfer, F. Marzo and A. Mancini, *Crystal Research and Technology*, 2005, **40**, 1018–1022.

[522] S. Maximovsky, I. Revocatova, V. Salman, M. Selezneva and P. Lebedeu, *Revue de Physique Appliquée*, 1977, **12**, 161–165.

[523] M. Miyake, K. Murase, T. Hirato and Y. Awakura, *Journal of Electroanalytical Chemistry*, 2004, **562**, 247–253.

[524] M. Miyake, K. Murase, T. Hirato and Y. Awakura, *Journal of The Electrochemical Society*, 2003, **150**, C413–C419.

[525] B. Monemar, E. Molva and L. S. Dang, *Physical Review B*, 1986, **33**, 1134.

[526] M. Niraula, A. Nakamura, T. Aoki and Y. Hatanaka, *physica status solidi (b)*, 2002, **229**, 83–87.

[527] D. De Nobel, *Phase equilibria and semiconducting properties of cadmium telluride*, na, 1958.

[528] B. Paez, *physica status solidi (b)*, 2000, **220**, 221–225.

[529] O. Panchuk, A. Savitskiy, P. Fochuk, Y. Nykonyuk, O. Parfenyuk, L. Shcherbak, M. Ilashchuk, L. Yatsunyk and P. Feychuk, *Journal of crystal growth*, 1999, **197**, 607–611.

[530] K. Pastor and E. Gołdys, *Solid state communications*, 1985, **55**, 671–674.

[531] V. Patil, P. More, D. Sutrave, G. Shahane, R. Mulik and L. Deshmukh, *Materials chemistry and physics*, 2000, **65**, 282–287.

[532] E. Saucedo, L. Fornaro, N. Sochinskii, A. Cuña, V. Corregidor, D. Granados and E. Diéguez, *IEEE Transactions on Nuclear Science*, 2004, **51**, 3105–3110.

[533] C. Gély-Sykes, C. Corbel and R. Triboulet, *Solid state communications*, 1991, **80**, 79–83.

[534] T. Taguchi, J. Yamamoto, J. Shirafuji and Y. Inuishi, *Solid State Communications*, 1976, **19**, 1037–1039.

[535] T. Takebe, H. Ono, J. Saraie and T. Tanaka, *Solid State Communications*, 1981, **37**, 391–394.

[536] M. Traversa, F. Marzo, P. Prete, L. Tapfer, A. Cappello, N. Lovergine and A. Mancini, *physica status solidi (c)*, 2006, **3**, 754–757.

[537] I. Turkevych, R. Grill, J. Franc, E. Belas, P. Höschl and P. Moravec, *Semiconductor science and technology*, 2002, **17**, 1064.

[538] S.-H. Wei, J. Ma, T. Gessert and K. K. Chin, Photovoltaic Specialists Conference (PVSC), 2011 37th IEEE, 2011, pp. 002833–002836.

[539] M. Wienecke, H. Berger and M. Schenk, *Materials Science and Engineering: B*, 1993, **16**, 219–222.

[540] S. Yamada, *Journal of the Physical Society of Japan*, 1960, **15**, 1940–1944.

[541] B. L. Crowder and W. N. Hammer, *Phys. Rev.*, 1966, **150**, 541–545.

[542] T. Baron, S. Tatarenko, K. Saminadayar, N. Magnea and J. Fontenille, *Applied physics letters*, 1994, **65**, 1284–1286.

[543] T. Baron, K. Saminadayar and N. Magnea, *Journal of applied physics*, 1998, **83**, 1354–1370.

[544] S. H. Chaki, K. S. Mahato and M. Deshpande, *Chinese Journal of Physics*, 2014, **52**, 1588–1601.

[545] M.-L. Liu, F.-Q. Huang, L.-D. Chen, Y.-M. Wang, Y.-H. Wang, G.-F. Li and Q. Zhang, *Applied physics letters*, 2007, **90**, 072109.

[546] M.-L. Liu, F.-Q. Huang and L.-D. Chen, *Scripta Materialia*, 2008, **58**, 1002–1005.

[547] S. Chichibu, M. Shishikura, J. Ino and S. Matsumoto, *Journal of applied physics*, 1991, **70**, 1648–1655.

[548] Y. Morita and T. Narusawa, *Japanese Journal of Applied Physics*, 1991, **30**, L1238.

[549] E. Gombia, F. Leccabue and C. Pelosi, *Materials Letters*, 1984, **2**, 429–431.

[550] E. Gombia, F. Leccabue, C. Pelosi, D. Seuret and O. Vigil, *Progress In Crystal Growth And Characterization*, 1984, **10**, 225–233.

[551] K. Singh, V. K. Singh and B. Yadav.

[552] P. Knauth, Y. Massiani and M. Pasquinelli, *physica status solidi (a)*, 1998, **165**, 461–465.

[553] L. Marushko, L. Piskach, Y. Romanyuk, O. Parasyuk, I. Olekseyuk, S. Volkov and V. Pekhnyo, *Journal of Alloys and Compounds*, 2010, **492**, 184–189.

[554] A. Aresti, L. Garbato, P. Manca and A. Rucci, *Journal of The Electrochemical Society*, 1977, **124**, 766–768.

[555] O. V. Parasyuk, Z. Lavrynyuk, O. Zmiy and Y. Romanyuk, *Journal of crystal growth*, 2009, **311**, 2381–2384.

[556] T. Hirai, K. Kurata and Y. Takeda, *Solid-State Electronics*, 1967, **10**, 975–981.

[557] L. Garbato, F. Ledda, P. Manca, A. Rucci and A. Spiga, *Progress in Crystal Growth and Characterization*, 1984, **10**, 199–205.

[558] G. S. Nolas, M. S. Hassan, Y. Dong and J. Martin, *Journal of Solid State Chemistry*, 2016, **242**, 50–54.

[559] R. K. Vijayaraghavan, *Ph.D. thesis*, Dublin City University, 2011.

[560] L. O'Reilly, A. Mitra, G. Natarajan, O. Lucas, P. McNally, S. Daniels, D. Cameron, A. Bradley and A. Reader, *Journal of crystal growth*, 2006, **287**, 139–144.

[561] F. O. Lucas, P. J. McNally, S. Daniels and D. M. Taylor, *Journal of Materials Science: Materials in Electronics*, 2009, **20**, 144–148.

[562] I. K. Khabibullin, E. Schmidt and V. Matukhin, *Semiconductors*, 2009, **43**, 1650.

[563] Y. Li, T. Zhang, Y. Qin, T. Day, G. Jeffrey Snyder, X. Shi and L. Chen, *Journal of Applied Physics*, 2014, **116**, 203705.

[564] J. Lamazares, F. Gonzalez-Jimenez, E. Jaimes, L. D'Onofrio, R. Iraldi, G. Sanchez-Porras, M. Quintero, J. Gonzalez, J. Woolley and G. Lamarche, *Journal of Magnetism and Magnetic Materials*, 1992, **104**, 997–998.

[565] G. Pitt and M. Vyas, *Solid State Communications*, 1974, **15**, 899–902.

[566] D. Liang, R. Ma, S. Jiao, G. Pang and S. Feng, *Nanoscale*, 2012, **4**, 6265–6268.

[567] T. Teranishi and K. Sato, *Le Journal de Physique Colloques*, 1975, **36**, C3–149.

[568] N. Tsujii and T. Mori, *Applied Physics Express*, 2013, **6**, 043001.

[569] H. Xie, X. Su, G. Zheng, Y. Yan, W. Liu, H. Tang, M. G. Kanatzidis, C. Uher and X. Tang, *The Journal of Physical Chemistry C*, 2016, **120**, 27895–27902.

[570] H. Xie, X. Su, G. Zheng, T. Zhu, K. Yin, Y. Yan, C. Uher, M. G. Kanatzidis and X. Tang, *Advanced Energy Materials*, 2017, **7**, 1601299.

[571] H. Xie, X. Su, Y. Yan, W. Liu, L. Chen, J. Fu, J. Yang, C. Uher and X. Tang, *NPG Asia Materials*, 2017, **9**, e390.

[572] L. Kradinova, A. Polubotko, V. Popov, V. Prochukhan, Y. V. Rud and V. Skoryukin, *LOW-TEMPERATURE ELECTRONIC-PROPERTIES OF CUFES2 AND ITS BAND DIAGRAM AT THE GAMMA-POINT*, 1987.

[573] L. Kradinova, A. Polubotko, V. Popov, V. Prochukhan, Y. V. Rud and V. Skoriukin, *Semiconductor science and technology*, 1993, **8**, 1616.

[574] K. G. Nikiforov, *Progress in crystal growth and characterization of materials*, 1999, **39**, 1–104.

[575] P. W. Yu, D. Downing and Y. Park, *Journal of Applied Physics*, 1974, **45**, 5283–5288.

[576] B. Tell, J. Shay and H. Kasper, *Physical review B*, 1971, **4**, 2463.

[577] J. Schön, J. Oestreich, O. Schenker, H. Riazi-Nejad, M. Klenk, N. Fabre, E. Arushanov and E. Bucher, *Applied physics letters*, 1999, **75**, 2969–2971.

[578] E. Arushanov, S. Siebentritt, T. Schedel-Niedrig and M. C. Lux-Steiner, *Journal of applied physics*, 2006, **100**, 063715.

[579] L. Mandel, R. Tomlinson, M. Hampshire and H. Neumann, *Solid State Communications*, 1979, **32**, 201–204.

[580] B. Mansour and M. El-Hagary, *Thin Solid Films*, 1995, **256**, 165–170.

[581] S. Schuler, S. Siebentritt, S. Nishiwaki, N. Rega, J. Beckmann, S. Brehme and M. C. Lux-Steiner, *Physical review B*, 2004, **69**, 045210.

[582] S. R. Kodigala, *Cu (In1-xGax) Se2 Based thin film solar cells*, Academic Press, 2011, vol. 35.

[583] J. Schön, C. Kloc and E. Bucher, *Thin solid films*, 2000, **361**, 411–414.

[584] H. Matsushita, H. Jitsukawa, H. Sugano, T. Takizawa and S. Endo, *TERNARY AND MULTINARY COMPOUNDS*, 1998, **152**, 535–538.

[585] B. Kuhn, W. Kaefer, K. Fess, K. Friemelt, C. Turner, M. Wendl and E. Bucher, *physica status solidi (a)*, 1997, **162**, 661–671.

[586] S. Wasim, G. Marcano and G. S. Pérez, *physica status solidi (a)*, 1983, **78**, 423–430.

[587] T. Plirdpring, K. Kurosaki, A. Kosuga, T. Day, S. Firdosy, V. Ravi, G. J. Snyder, A. Harnwunggmoung, T. Sugahara, Y. Ohishi *et al.*, *Advanced Materials*, 2012, **24**, 3622–3626.

[588] J. Cui, Y. Li, Z. Du, Q. Meng and H. Zhou, *Journal of Materials Chemistry A*, 2013, **1**, 677–683.

[589] B. Šantić, *physica status solidi (a)*, 1992, **133**, 137–146.

[590] J. Mac Donald, G. Saunders, M. Omar and B. Pamplin, *physica status solidi (a)*, 1985, **89**, year.

[591] S. Inudo, M. Miyake and T. Hirato, *physica status solidi (a)*, 2013, **210**, 2395–2398.

[592] S. Mittleman and R. Singh, *Solid State Communications*, 1977, **22**, 659–662.

[593] A. A. El Soud, H. Zayed and L. Soliman, *Thin Solid Films*, 1993, **229**, 232–236.

[594] H. Hsu, M. Yang, R. Tang, T. Hsu and H. Hwang, *Journal of Crystal Growth*, 1984, **70**, 427–432.

[595] T. Hsu, J. Lee and H. Hwang, *Journal of applied physics*, 1990, **68**, 283–287.

[596] S. Kim, W. Jeong, G. Park, Y. Back, Y. Jeong and Y. Yoo, *Synthetic Metals*, 1995, **71**, 1747–1748.

[597] D. C. Look and J. C. Manthuruthil, *Journal of Physics and Chemistry of Solids*, 1976, **37**, 173–180.

[598] Y. Ogawa, S. Uenishi, K. Tohyama and K. Ito, *Solar energy materials and solar cells*, 1994, **35**, 157–163.

[599] A. Opanowicz and B. Kóscielniak-Mucha, *physica status solidi (a)*, 1988, **105**, K135–K139.

[600] R. Kristensen, S. Sahu and D. Haneman, *Solar energy materials*, 1988, **17**, 329–345.

[601] G. Porras and S. Wasim, *physica status solidi (a)*, 1980, **59**, year.

[602] C. Djega-Mariadassou, R. Lesueur, J. Leloup and J. Albany, *Physics Letters A*, 1978, **65**, 455–457.

[603] K. Hong, T. Jeong and C. Youn, *Journal of applied physics*, 2006, **100**, 123518.

[604] H. Neumann and R. Tomlinson, *Solid state communications*, 1986, **57**, 591–594.

[605] H. Neumann, R. Tomlinson, E. Nowak and N. Avgerinos, *physica status solidi (a)*, 1979, **56**, K137–K140.

[606] G. Sánchezporras and S. Wasim, *physica status solidi (a)*, 1992, **133**, 509–514.

[607] C. Rincon and G. S. Perez, *Solar Cells*, 1986, **16**, 363–368.

[608] H. Shaban, M. Mobarak and M. Nassary, *Physica B: Condensed Matter*, 2007, **389**, 351–354.

[609] V. Lyahovitskaya, Y. Feldman, K. Gartsman, H. Cohen, C. Cytermann and D. Cahen, *Journal of applied physics*, 2002, **91**, 4205–4212.

[610] H. Neumann, R. Tomlinson, E. Nowak, E. Elliott and L. Howarth, *Kristall und Technik*, 1981, **16**, K112–K114.

[611] S. Wasim, G. S. Porras and H. Neumann, *Solid state communications*, 1985, **54**, 239–240.

[612] N. Cheng, R. Liu, S. Bai, X. Shi and L. Chen, *Journal of Applied Physics*, 2014, **115**, 163705.

[613] L. Haworth, I. Al-Saffar and R. Tomlinson, *physica status solidi (a)*, 1987, **99**, 603–610.

[614] L. Kazmerski and Y. Juang, *Journal of Vacuum Science and Technology*, 1977, **14**, 769–776.

[615] A. Kosuga, T. Plirdpring, R. Higashine, M. Matsuzawa, K. Kurosaki and S. Yamanaka, *Applied Physics Letters*, 2012, **100**, 042108.

[616] Y. Li, Q. Meng, Y. Deng, H. Zhou, Y. Gao, Y. Li, J. Yang and J. Cui, *Applied Physics Letters*, 2012, **100**, 231903.

[617] Y. Luo, J. Yang, Q. Jiang, W. Li, D. Zhang, Z. Zhou, Y. Cheng, Y. Ren and X. He, *Advanced Energy Materials*, 2016, **6**, 1600007.

[618] S. Wasim and J. Albornoz, *physica status solidi (a)*, 1988, **110**, 575–583.

[619] S. Wasim, A. L. Vielma and C. Rincon, *Solid state communications*, 1984, **51**, 935–937.

[620] G. Davidyuk, O. Parasyuk, S. Semenyuk and Y. E. Romanyuk, *Inorganic materials*, 2003, **39**, 919–923.

[621] R. Chetty, J. Dadda, J. de Boor, E. Mueller and R. C. Mallik, *Intermetallics*, 2015, **57**, 156–162.

[622] H. Guo, Y. Li, X. Fang, K. Zhang, J. Ding and N. Yuan, *Materials Letters*, 2016, **162**, 97–100.

[623] M. Rouchdi, E. Salmani, N. Hassanain and A. Mzerd, *Optical and Quantum Electronics*, 2017, **49**, 165.

[624] K. Ito and T. Nakazawa, *Japanese Journal of Applied Physics*, 1988, **27**, 2094.

[625] S. R. Kodigala, *Thin film solar cells from earth abundant materials: growth and characterization of Cu2 (ZnSn)(SSe) 4 thin films and their solar cells*, Newnes, 2013.

[626] K. Mokurala and S. Mallick, *RSC Advances*, 2017, **7**, 15139–15148.

[627] W. Zhao, G. Wang, Q. Tian, L. Huang, S. Gao and D. Pan, *Solar Energy Materials and Solar Cells*, 2015, **133**, 15–20.

[628] L. Meng, Y. Li, B. Yao, Z.-H. Ding, G. Yang, R.-J. Liu, R. Deng and L. Liu, *Journal of Physics D: Applied Physics*, 2015, **48**, 445105.

[629] Q. Chen, Y. Yan, H. Zhan, W. Yao, Y. Chen, J. Dai, X. Sun and X. Zhou, *Journal of Materiomics*, 2016, **2**, 179–186.

[630] F. Liu, J. Zheng, M. Huang, L. He, W. Ao, F. Pan and J. Li, *Scientific reports*, 2014, **4**, 5774.

[631] B. Wang, Y. Li, J. Zheng, M. Xu, F. Liu, W. Ao, J. Li and F. Pan, *Scientific reports*, 2015, **5**, 9365.

[632] M. Krishnaiah, P. Bhargava and S. Mallick, *RSC Advances*, 2015, **5**, 96928–96933.

[633] K. Mokurala, S. Mallick and P. Bhargava, *Journal of Power Sources*, 2016, **305**, 134–143.

[634] M. Quintero, R. Tovar, A. Barreto, E. Quintero, A. Rivero, J. Gonzalez, G. S. Porras, J. Ruiz, P. Bocaranda, J. Broto *et al.*, *Physica Status Solidi B Basic Research*, 1998, **209**, 135–144.

[635] G. Sánchez Porras, M. Quintero, R. Barrios, J. Gonzalez, R. TovarSánchez Porras and J. Ruiz, *physica status solidi (b)*, 1999, **215**, 1067–1073.

[636] R. R. Prabhakar, N. Huu Loc, M. H. Kumar, P. P. Boix, S. Juan, R. A. John, S. K. Batabyal and L. H. Wong, *ACS applied materials & interfaces*, 2014, **6**, 17661–17667.

[637] B. Ananthoju, J. Mohapatra, M. K. Jangid, D. Bahadur, N. Medhekar and M. Aslam, *Scientific reports*, 2016, **6**, 35369.

[638] G. Chen, J. Li, S. Chen, Z. Huang, M. Wu, J. Zhao, W. Wang, H. Lin and C. Zhu, *Materials Chemistry and Physics*, 2017, **188**, 95–99.

[639] H. Hou, H. Guan and L. Li, *Journal of Materials Science: Materials in Electronics*, 2017, **28**, 7745–7748.

[640] D. B. Khadka and J. Kim, *Journal of Alloys and Compounds*, 2015, **638**, 103–108.

[641] B. Zhang, M. Cao, L. Li, Y. Sun, Y. Shen and L. Wang, *Materials Letters*, 2013, **93**, 111–114.

[642] A. Congiu, L. Garbato and P. Manca, *Materials Research Bulletin*, 1973, **8**, 293–299.

[643] T. Plirdpring, K. Kurosaki, A. Kosuga, M. Ishimaru, A. Harnwunggmoung, T. Sugahara, Y. Ohishi, H. Muta and S. Yamanaka, *Applied Physics Letters*, 2011, **98**, 172104.

[644] M. Khanafer, O. Gorochov and J. Rivet, *Materials Research Bulletin*, 1974, **9**, 1543–1552.

[645] X. Jin, L. Zhang, G. Jiang, W. Liu and C. Zhu, *Solar Energy Materials and Solar Cells*, 2017, **160**, 319–327.

[646] J. Cho, X. Shi, J. R. Salvador, G. P. Meisner, J. Yang, H. Wang, A. A. Wereszczak, X. Zhou and C. Uher, *Physical Review B*, 2011, **84**, 085207.

[647] J. Y. Cho, X. Shi, J. Salvador, J. Yang and H. Wang, *Journal of Applied Physics*, 2010, **108**, 073713.

[648] J. J. Lee, C. S. Yang, Y. S. Park, K. H. Kim and W. T. Kim, *Journal of applied physics*, 1999, **86**, 2914–2916.

[649] S. Endo, I. Sudo and T. Irie, *Japanese Journal of Applied Physics*, 1971, **10**, 218.

[650] G. Marcano, D. Bracho, C. Rincón, G. S. Pérez and L. Nieves, *Journal of Applied Physics*, 2000, **88**, 822–828.

[651] M. Villarreal, B. Fernández, M. Pirela and A. Velásquez-Velásquez, *Revista Mexicana de Física*, 2007, **53**, 303–306.

[652] D. Zhao, J. Ning, S. Li and M. Zuo, *Journal of Nanomaterials*, 2016, **2016**, year.

[653] W. Scott, *Journal of Electronic Materials*, 1974, **3**, 209–223.

[654] L. Palatnik, V. Koshkin, L. Galchinetskii, V. Kolesnikov and Y. F. Komnik, *Soviet Physics-Solid State*, 1962, **4**, 1052–1053.

[655] J. Navrátil, V. Kucek, T. Plecháček, E. Černošková, F. Laufek, Č. Drašar and P. Knotek, *Journal of electronic materials*, 2014, **43**, 3719–3725.

[656] T. Plirdpring, K. Kurosaki, A. Kosuga, M. Ishimaru, Y. Ohishi, H. Muta and S. Yamanaka, *physica status solidi (RRL)-Rapid Research Letters*, 2012, **6**, 154–156.

[657] V. Pavan Kumar, E. Guilmeau, B. Raveau, V. Caignaert and U. Varadaraju, *Journal of Applied Physics*, 2015, **118**, 155101.

[658] Y. Shapira, E. McNiff Jr, N. Oliveira Jr, E. Honig, K. Dwight and A. Wold, *Physical Review B*, 1988, **37**, 411.

[659] X. Wang, T. Liu, H. Guan, F. Yu and H. Hou, *OPTOELECTRONICS AND ADVANCED MATERIALS-RAPID COMMUNICATIONS*, 2015, **9**, 1190–1193.

[660] R. R. Prabhakar, S. Zhenghua, Z. Xin, T. Baikie, L. S. Woei, S. Shukla, S. K. Batabyal, O. Gunawan and L. H. Wong, *Solar Energy Materials and Solar Cells*, 2016, **157**, 867–873.

[661] K. Mokurala, S. Mallick, P. Bhargava, S. Siol, T. R. Klein and M. F. van Hest, *Journal of Alloys and Compounds*, 2017, **725**, 510–518.

[662] Y. Shen, C. Li, R. Huang, R. Tian, Y. Ye, L. Pan, K. Koumoto, R. Zhang, C. Wan and Y. Wang, *Scientific reports*, 2016, **6**, 32501.

[663] N. Aihara, H. Araki, A. Takeuchi, K. Jimbo and H. Katagiri, *physica status solidi c*, 2013, **10**, 1086–1092.

[664] L. L. Baranowski, P. Zawadzki, S. Christensen, D. Nordlund, S. Lany, A. C. Tamboli, L. Gedvilas, D. S. Ginley, W. Tumas, E. S. Toberer *et al.*, *Chemistry of Materials*, 2014, **26**, 4951–4959.

[665] L. L. Baranowski, K. McLaughlin, P. Zawadzki, S. Lany, A. Norman, H. Hempel, R. Eichberger, T. Unold, E. S. Toberer and A. Zakutayev, *Physical Review Applied*, 2015, **4**, 044017.

[666] J. Chaudhari, S. Patel and U. Joshi, IOP Conference Series: Materials Science and Engineering, 2016, p. 012165.

[667] J. Han, Y. Zhou, Y. Tian, Z. Huang, X. Wang, J. Zhong, Z. Xia, B. Yang, H. Song and J. Tang, *Frontiers of Optoelectronics*, 2014, **7**, 37–45.

[668] P. Zhao and S. Cheng, *Advances in Materials Science and Engineering*, 2013, **2013**, year.

[669] D. Tiwari, T. Chaudhuri, T. Shripathi and U. Deshpande, AIP Conference Proceedings, 2012, pp. 1039–1040.

[670] D. Tiwari, T. K. Chaudhuri, T. Shripathi, U. Deshpande and V. Sathe, *Applied Physics A*, 2014, **117**, 1139–1146.

[671] T. S. Reddy, R. Amiruddin and M. S. Kumar, *Solar Energy Materials and Solar Cells*, 2015, **143**, 128–134.

[672] J. Li, J. Huang, Y. Zhang, Y. Wang, C. Xue, G. Jiang, W. Liu and C. Zhu, *RSC Advances*, 2016, **6**, 58786–58795.

[673] W. Wubet and D.-H. Kuo, *Advanced Materials Research*, 2015, **1101**, 153.

[674] C. Raju, M. Falmbigl, P. Rogl, P. Heinrich, E. Royanian, E. Bauer and R. C. Mallik, *Materials Chemistry and Physics*, 2014, **147**, 1022–1028.

[675] G. S. Babu, Y. K. Kumar, Y. B. K. Reddy and V. S. Raja, *Materials chemistry and physics*, 2006, **96**, 442–446.

[676] K. M. Kim, H. Tampo, H. Shibata and S. Niki, *Thin Solid Films*, 2013, **536**, 111–114.

[677] D.-H. Kuo and W. Wubet, *Journal of Solid State Chemistry*, 2014, **218**, 44–49.

[678] D.-H. Kuo, W.-D. Haung, Y.-S. Huang, J.-D. Wu and Y.-J. Lin, *Thin Solid Films*, 2010, **518**, 7218–7221.

[679] X. Lu and D. T. Morelli, *Journal of electronic materials*, 2012, **41**, 1554–1558.

[680] G. Marcano, C. Rincón, L. De Chalbaud, D. Bracho and G. S. Pérez, *Journal of Applied Physics*, 2001, **90**, 1847–1853.

[681] J. Ning, D. Wu and D. Zhao, *Applied Sciences*, 2017, **7**, 1043.

[682] C. Rincón, G. Marcano, R. Casanova, G. Delgado, G. Marín and G. Sánchez-Pérez, *physica status solidi (b)*, 2016, **253**, 697–704.

[683] Z. Tang, Y. Nukui, K. Kosaka, N. Ashida, H. Uegaki and T. Minemoto, *Journal of Alloys and Compounds*, 2014, **608**, 213–219.

[684] G. Marcano, B. Fernández, D. Bracho and A. Mora, *TERNARY AND MULTINARY COMPOUNDS*, 1998, **152**, 579–582.

[685] W. Li, S. Lin, X. Zhang, Z. Chen, X. Xu and Y. Pei, *Chemistry of Materials*, 2016, **28**, 6227–6232.

[686] G. Marcano, C. Rincón, G. Marın, R. Tovar and G. Delgado, *Journal of applied physics*, 2002, **92**, 1811–1815.

[687] M. Guc, E. Lähderanta, E. Hajdeu-Chicarosh, S. Levcenko, M. A. Shakhov, I. Zakharchuk, E. Arushanov and K. G. Lisunov, *Scientific Reports*, 2017, **7**, 10685.

[688] W. G. Zeier, A. LaLonde, Z. M. Gibbs, C. P. Heinrich, M. Panthofer, G. J. Snyder and W. Tremel, *Journal of the American Chemical Society*, 2012, **134**, 7147–7154.

[689] G. S. Mary, G. H. Chandra, M. A. Sunil and M. Gupta, *Journal of Electronic Materials*, 2018, **47**, 800–810.

[690] R. Chetty, A. Bali, O. Femi, K. Chattopadhyay and R. Mallik, *Journal of Electronic Materials*, 2016, **45**, 1625–1632.

[691] W. G. Zeier, T. Day, E. Schechtel, G. J. Snyder and W. Tremel, *Functional Materials Letters*, 2013, **6**, 1340010.

[692] A. Nagaoka, K. Yoshino, H. Taniguchi, T. Taniyama and H. Miyake, *Journal of Crystal Growth*, 2012, **341**, 38–41.

[693] F. Liu, K. Zhang, Y. Lai, J. Li, Z. Zhang and Y. Liu, *Electrochemical and Solid-State Letters*, 2010, **13**, H379–H381.

[694] C. Chan, H. Lam and C. Surya, *Solar Energy Materials and Solar Cells*, 2010, **94**, 207–211.

[695] S. Chen, A. Walsh, X.-G. Gong and S.-H. Wei, *Advanced Materials*, 2013, **25**, 1522–1539.

[696] S. Das and K. C. Mandal, Photovoltaic Specialists Conference (PVSC), 2012 38th IEEE, 2012, pp. 002668–002673.

[697] T. P. Dhakal, C.-Y. Peng, R. R. Tobias, R. Dasharathy and C. R. Westgate, *Solar Energy*, 2014, **100**, 23–30.

[698] J. Gonzalez, G. Ribeiro, E. Viana, P. Fernandes, P. Salomé, K. Gutierrez, A. Abelenda, F. Matinaga, J. Leitao and A. Da Cunha, *Journal of Physics D: Applied Physics*, 2013, **46**, 155107.

[699] W. H. Oo, J. Johnson, A. Bhatia, E. Lund, M. Nowell and M. A. Scarpulla, *Journal of Electronic Materials*, 2011, **40**, 2214.

[700] A. Ibraheam, Y. Al-Douri, A. S. Mohammed, D. Prakash, U. Hashim and K. Verma, *Int J Electrochem Sci*, 2015, **10**, 9863–9876.

[701] F. Liu, Y. Li, K. Zhang, B. Wang, C. Yan, Y. Lai, Z. Zhang, J. Li and Y. Liu, *Solar Energy Materials and Solar Cells*, 2010, **94**, 2431–2434.

[702] H. Lui, K. Leung, W. Fong and C. Surya, Photovoltaic Specialists Conference (PVSC), 2010 35th IEEE, 2010, pp. 001977–001981.

[703] E. Mkawi, K. Ibrahim, M. Ali and A. S. Mohamed, *Int. J. Electrochem. Sci*, 2013, **8**, 359–368.

[704] M. Patel, I. Mukhopadhyay and A. Ray, *Journal of Physics D: Applied Physics*, 2012, **45**, 445103.

[705] T. Prabhakar and N. Jampana, *Solar Energy Materials and Solar Cells*, 2011, **95**, 1001–1004.

[706] J. J. Scragg, P. J. Dale and L. M. Peter, *Electrochemistry Communications*, 2008, **10**, 639–642.

[707] S. W. Shin, S. Pawar, C. Y. Park, J. H. Yun, J.-H. Moon, J. H. Kim and J. Y. Lee, *Solar energy materials and solar cells*, 2011, **95**, 3202–3206.

[708] G. G. Silvena, B. John, R. A. S. Christinal, M. S. Kumar, S. Chakravarty and A. L. Rajesh, *Journal of Inorganic and Organometallic Polymers and Materials*, 2017, **27**, 1556–1562.

[709] S. K. Swami, A. Kumar and V. Dutta, *Energy Procedia*, 2013, **33**, 198–202.

[710] T. Tanaka, T. Nagatomo, D. Kawasaki, M. Nishio, Q. Guo, A. Wakahara, A. Yoshida and H. Ogawa, *Journal of Physics and Chemistry of Solids*, 2005, **66**, 1978–1981.

[711] Z.-Y. Xiao, Y.-F. Li, B. Yao, R. Deng, Z.-H. Ding, T. Wu, G. Yang, C.-R. Li, Z.-Y. Dong, L. Liu *et al.*, *Journal of Applied Physics*, 2013, **114**, 183506.

[712] W. Xinkun, L. Wei, C. Shuying, L. Yunfeng and J. Hongjie, *Journal of Semiconductors*, 2012, **33**, 022002.

[713] M.-Y. Yeh, P.-H. Lei, S.-H. Lin and C.-D. Yang, *Materials*, 2016, **9**, 526.

[714] X. Zhang, G. Guo, C. Ji, K. Huang, C. Zha, Y. Wang, L. Shen, A. Gupta and N. Bao, *Scientific reports*, 2014, **4**, 5086.

[715] Z. Zhou, Y. Wang, D. Xu and Y. Zhang, *Solar Energy Materials and Solar Cells*, 2010, **94**, 2042–2045.

[716] M. Patel and A. Ray, *Physica B: Condensed Matter*, 2012, **407**, 4391–4397.

[717] W.-L. Chen, D.-H. Kuo and T. T. A. Tuan, *Journal of Electronic Materials*, 2017, **46**, 1481–1487.

[718] R. Chetty, M. Falmbigl, P. Rogl, P. Heinrich, E. Royanian, E. Bauer, S. Suwas and R. C. Mallik, *physica status solidi (a)*, 2013, **210**, 2471–2478.

[719] K.-H. Kim and I. Amal, *Electronic Materials Letters*, 2011, **7**, 225.

[720] D.-H. Kuo and M. Tsega, *Japanese Journal of Applied Physics*, 2014, **53**, 035801.

[721] Y. Li, Q. Han, T. W. Kim and W. Shi, *Journal of sol-gel science and technology*, 2014, **69**, 260–265.

[722] L. Shao, J. Zhang, C. Zou and W. Xie, *Physics Procedia*, 2012, **32**, 640–644.

[723] X. Shi, F. Huang, M. Liu and L. Chen, *Applied Physics Letters*, 2009, **94**, 122103.

[724] T. Tanaka, T. Sueishi, K. Saito, Q. Guo, M. Nishio, K. M. Yu and W. Walukiewicz, *Journal of Applied Physics*, 2012, **111**, 053522.

[725] M. Tsega and D.-H. Kuo, *Applied Physics Express*, 2012, **5**, 091201.

[726] K. Wei, 2015.

[727] R. Adhi Wibowo, E. Soo Lee, B. Munir and K. Ho Kim, *physica status solidi (a)*, 2007, **204**, 3373–3379.

[728] R. A. Wibowo, W. S. Kim, E. S. Lee, B. Munir and K. H. Kim, *Journal of Physics and Chemistry of Solids*, 2007, **68**, 1908–1913.

[729] Y. Yang, X. Kang, L. Huang, S. Wei and D. Pan, *The Journal of Physical Chemistry C*, 2015, **119**, 22797–22802.

[730] Y. Dong, B. Eckert, H. Wang, X. Zeng, T. M. Tritt and G. S. Nolas, *Dalton Transactions*, 2015, **44**, 9014–9019.

[731] M.-L. Liu, F.-Q. Huang, L.-D. Chen and I.-W. Chen, *Applied Physics Letters*, 2009, **94**, 202103.

[732] K. Wei and G. S. Nolas, *ACS applied materials & interfaces*, 2015, **7**, 9752–9757.

[733] T. T. Kovalyuk, E. V. Maistruk, H. P. Parkhomenko and P. D. Maryanchuk.

[734] J. Heo, 2014.

[735] T. Pauporté and D. Lincot, *Advanced Materials for Optics and Electronics*, 1995, **5**, 289–298.

[736] V. Itthibenchapong, R. S. Kokenyesi, A. J. Ritenour, L. N. Zakharov, S. W. Boettcher, J. F. Wager and D. A. Keszler, *Journal of Materials Chemistry C*, 2013, **1**, 657–662.

[737] J. Marzik, A. Hsieh, K. Dwight and A. Wold, *Journal of Solid State Chemistry*, 1983, **49**, 43–50.

[738] T. Hindia and Y. A. Valov, *physica status solidi (a)*, 1975, **30**, K41–K43.

[739] B. E. Waters, 2012.

[740] K. Chen, *Ph.D. thesis*, Queen Mary University of London, 2016.

[741] A. Suzumura, M. Watanabe, N. Nagasako and R. Asahi, *Journal of Electronic Materials*, 2014, **43**, 2356–2361.

[742] Y. Goto, Y. Sakai, Y. Kamihara and M. Matoba, *Journal of the Physical Society of Japan*, 2015, **84**, 044706.

[743] W. Scott and J. Kench, *Materials Research Bulletin*, 1973, **8**, 1257–1267.

[744] C.-H. Chang, C.-L. Chen, W.-T. Chiu and Y.-Y. Chen, *Materials Letters*, 2017, **186**, 227–230.

[745] D. Li, R. Li, X.-Y. Qin, C.-J. Song, H.-X. Xin, L. Wang, J. Zhang, G.-l. Guo, T.-H. Zou, Y.-F. Liu *et al.*, *Dalton Transactions*, 2014, **43**, 1888–1896.

[746] X. Li, D. Li, H. Xin, J. Zhang, C. Song and X. Qin, *Journal of Alloys and Compounds*, 2013, **561**, 105–108.

[747] H. Nakanishi, S. Endo and T. Irie, *Japanese Journal of Applied Physics*, 1969, **8**, 443.

[748] T.-R. Wei, H. Wang, Z. M. Gibbs, C.-F. Wu, G. J. Snyder and J.-F. Li, *Journal of Materials Chemistry A*, 2014, **2**, 13527–13533.

[749] C. Yang, F. Huang, L. Wu and K. Xu, *Journal of Physics D: Applied Physics*, 2011, **44**, 295404.

[750] D. Zhang, J. Yang, Q. Jiang, Z. Zhou, X. Li, J. Xin, A. Basit, Y. Ren, X. He, W. Chu *et al.*, *ACS applied materials & interfaces*, 2017, **9**, 28558–28565.

[751] D. Zhao, D. Wu and L. Bo, *Energies*, 2017, **10**, 1524.

[752] E. J. Skoug, J. D. Cain and D. T. Morelli, *Applied Physics Letters*, 2011, **98**, 261911.

[753] A. DIROCHKA, G. Ivanova, L. Kurbatov, E. Sinitsyn, F. Kharakhorin and E. Kholina, *CATHODE LUMINESCENCE OF SEMICONDUCTIVE COMPOUND CU3SBSE4*, 1976.

[754] A. Raymond, J. Robert and C. Bernard, *Journal of Physics C: Solid State Physics*, 1979, **12**, 2289.

[755] P. Hageman, W. Schaff, J. Janinski and Z. Liliental-Weber, *Journal of crystal growth*, 2004, **267**, 123–128.

[756] Y. Arakawa, K. Ueno, A. Kobayashi, J. Ohta and H. Fujioka, *APL Materials*, 2016, **4**, 086103.

[757] D. As, D. Schikora, A. Greiner, M. Lübbers, J. Mimkes and K. Lischka, *Physical Review B*, 1996, **54**, R11118.

[758] Y. Chen, H. Wu, G. Yue, Z. Chen, Z. Zheng, Z. Wu, G. Wang and H. Jiang, *physica status solidi (b)*, 2015, **252**, 1109–1115.

[759] V. Chin, T. Tansley and T. Osotchan, *Journal of Applied Physics*, 1994, **75**, 7365–7372.

[760] R. Crouch, W. Debnam and A. Fripp, *Journal of Materials Science*, 1978, **13**, 2358–2364.

[761] G. Denninger, R. Beerhalter, D. Reiser, K. Maier, J. Schneider, T. Detchprohm and K. Hiramatsu, *Solid state communications*, 1996, **99**, 347–351.

[762] C. Eiting, P. Grudowski and R. Dupuis, *Journal of electronic materials*, 1998, **27**, 206–209.

[763] S. Fischer, C. Wetzel, E. Haller and B. Meyer, *Applied physics letters*, 1995, **67**, 1298–1300.

[764] K. Gillessen, K.-H. Schuller and B. Struck, *Materials Research Bulletin*, 1977, **12**, 955–960.

[765] M. Ilegems and R. Dingle, *Journal of Applied Physics*, 1973, **44**, 4234–4235.

[766] M. Ilegems and H. Montgomery, *Journal of Physics and Chemistry of Solids*, 1973, **34**, 885–895.

[767] J. Kim, A. Frenkel, H. Liu and R. Park, *Applied physics letters*, 1994, **65**, 91–93.

[768] K. Koike, A. Nakamura, M. Sugiyama, Y. Nakano and K. Fujii, *physica status solidi (c)*, 2014, **11**, 821–823.

[769] M. Kumar, T. N. Bhat, B. Roul, M. K. Rajpalke, A. Kalghatgi and S. Krupanidhi, *Materials Research Bulletin*, 2012, **47**, 1306–1309.

[770] H. á. Maruska and J. Tietjen, *Applied Physics Letters*, 1969, **15**, 327–329.

[771] H. Ng, D. Doppalapudi, T. Moustakas, N. Weimann and L. Eastman, *Applied physics letters*, 1998, **73**, 821–823.

[772] A. Usikov, O. Kovalenkov, V. Soukhoveev, V. Ivantsov, A. Syrkin, V. Dmitriev, A. Y. Nikiforov, S. Sundaresan, S. Jeliazkov and A. Davydov, *physica status solidi (c)*, 2008, **5**, 1829–1831.

[773] R. K. Wong, *P-type doping of GaN*, Lawrence berkeley national lab.(lbnl), berkeley, ca (united states) technical report, 2000.

[774] C.-C. Yu, C.-F. Chu, J.-Y. Tsai, C.-F. Lin, W.-H. Lan, C.-I. Chiang and S.-C. Wang, *Japanese Journal of Applied Physics*, 2001, **40**, L417.

[775] G. Irmer, V. Toporov, B. Bairamov and J. Monecke, *physica status solidi (b)*, 1983, **119**, 595–603.

[776] H. Casey Jr, F. Ermanis and K. Wolfstirn, *Journal of Applied Physics*, 1969, **40**, 2945–2958.

[777] W. Kauschke, V. Vorlicek and M. Cardona, *Physical Review B*, 1987, **36**, 9129.

[778] K. Suzuki and N. Miura, *Solid State Communications*, 1976, **18**, 233–236.

[779] R. Baxter, F. Reid and A. Beer, *Physical Review*, 1967, **162**, 718.

[780] R. Wiersma, J. Stotz, O. Pitts, C. Wang, M. Thewalt and S. Watkins, *Journal of electronic materials*, 2001, **30**, 1429–1432.

[781] D. Benyahia, L. Kubiszyn, K. Michalczewski, A. Keblowski, P. Martyniuk, J. Piotrowski and A. Rogalski, *JOURNAL OF SEMICONDUCTOR TECHNOLOGY AND SCIENCE*, 2016, **16**, 695–701.

[782] H. Ehsani, I. Bhat, C. Hitchcock, R. Gutmann, G. Charache and M. Freeman, *Journal of crystal growth*, 1998, **195**, 385–390.

[783] A. Joullie, A. Z. Eddin and B. Girault, *Physical Review B*, 1981, **23**, 928.

[784] K. Longenbach, S. Xin and W. Wang, *Journal of applied physics*, 1991, **69**, 3393–3395.

[785] A. J. Strauss, *Physical Review*, 1961, **121**, 1087.

[786] W. G. Spitzer, F. Trumbore and R. Logan, *Journal of Applied Physics*, 1961, **32**, 1822–1830.

[787] L. Liu, N. Chen, Y. Wang, X. Zhang, Z. Yin, F. Yang and C. Chai, *Solid state communications*, 2006, **137**, 126–128.

[788] S. Prucnal, F. Liu, M. Voelskow, L. Vines, L. Rebohle, D. Lang, Y. Berencén, S. Andric, R. Boettger, M. Helm *et al.*, *Scientific reports*, 2016, **6**, 27643.

[789] R. E. Camacho-Aguilera, Y. Cai, J. T. Bessette, L. C. Kimerling and J. Michel, *Optical Materials Express*, 2012, **2**, 1462–1469.

[790] V. Y. Rud, Y. V. Rud, A. Vaipolin, N. Fernelius *et al.*, *Semiconductors*, 2003, **37**, 1283–1290.

[791] S. Eshraghi, S. Kianian, B. Ostrom, O. Stafsudd and A. Gentile, *physica status solidi (a)*, 1988, **105**, 563–566.

[792] R. S. Becker, G. D. Zhou and J. Elton, *The Journal of Physical Chemistry*, 1986, **90**, 5866–5870.

[793] E. Gorton, Lasers' 85; Proceedings of the Eighth International Conference, 1986, pp. 658–662.

[794] K. Siemsen and H. Riccius, *Physica status solidi (b)*, 1970, **37**, 445–451.

[795] R. Zallen and M. Slade, *Solid State Communications*, 1970, **8**, 1291–1294.

[796] D. Niculescu, N. Nistor, M. Popa, M. Vantza and R. Ionescu, *Journal of Materials Science*, 1970, **5**, 385–388.

[797] S. Mahajan and L. Kimerling, *Concise encyclopedia of semiconducting materials & related technologies*, Elsevier, 2013.

[798] H. Gobrecht, U. Gerhardt, B. Peinemann and A. Tausend, *Journal of Applied Physics*, 1961, **32**, 2246–2250.

[799] A. Manabe and A. Mitsuishi, *Solid State Communications*, 1975, **16**, 743–745.

[800] M. Blue and P. Kruse, *Journal of Physics and Chemistry of Solids*, 1962, **23**, 577–586.

[801] W. Giriat, *British Journal of Applied Physics*, 1964, **15**, 151.

[802] Z. Dziuba and T. Zakrzewski, *physica status solidi (b)*, 1964, **7**, 1019–1025.

[803] Z. Dziuba and K. Szlenk, *Journal of Physics and Chemistry of Solids*, 1984, **45**, 97–103.

[804] G. Pitt and J. Lees, *HIGH TEMP-HIGH PRESSURES*, 1969, **1**, 581–587.

[805] V. Radhakrishnan and P. Sharma, *Physical Review B*, 1981, **23**, 3004.

[806] A. Brown, N. Baril, D. Zuo, L. Almeida, J. Arias and S. Bandara, *Journal of Electronic Materials*, 2017, **46**, 5367–5373.

[807] I. Catalano, A. Cingolani, C. Arnone and S. Riva-Sanseverino, *Solid State Communications*, 1981, **37**, 183–185.

[808] Y. J. Jung, B. H. Kim, H. J. Lee and J. C. Woolley, *Physical Review B*, 1982, **26**, 3151.

[809] S. Kurtz, R. Biefeld and L. Dawson, *Physical Review B*, 1995, **51**, 7310.

[810] A. Lind, T. Martin Jr, V. Sorg, E. Kennon, V. Truong, H. Aldridge, C. Hatem, M. Thompson and K. Jones, *Journal of Applied Physics*, 2016, **119**, 095705.

[811] J. McCarthy, *Solid State Communications*, 1967, **5**, 5–6.

[812] C. Pickering, A. Adams and G. Pitt, *Solid State Communications*, 1975, **16**, 1359–1363.

[813] D. Rode, *Physical Review B*, 1971, **3**, 3287.

[814] L. Marasina, I. Pichugin and M. Tlaczala, *Crystal Research and Technology*, 1977, **12**, 541–545.

[815] V. Cimalla, V. Lebedev, F. M. Morales, M. Niebelschütz, G. Ecke, R. Goldhahn and O. Ambacher, *Materialwissenschaft und Werkstofftechnik*, 2006, **37**, 924–928.

[816] F. Chen, A. Cartwright, H. Lu and W. Schaff, *physica status solidi (a)*, 2005, **202**, 768–772.

[817] T. Hofmann, T. Chavdarov, V. Darakchieva, H. Lu, W. Schaff and M. Schubert, *physica status solidi (c)*, 2006, **3**, 1854–1857.

[818] H. Hovel and J. Cuomo, *Applied Physics Letters*, 1972, **20**, 71–73.

[819] L. Piper, T. Veal, C. McConville, H. Lu and W. Schaff, *Applied physics letters*, 2006, **88**, 252109.

[820] T. Tansley and C. Foley, *Electronics Letters*, 1984, **20**, 1066–1068.

[821] J. Thakur, R. Naik, V. Naik, D. Haddad, G. Auner, H. Lu and W. Schaff, *Journal of applied physics*, 2006, **99**, 023504.

[822] J. Trainor and K. Rose, *Journal of Electronic Materials*, 1974, **3**, 821–828.

[823] A. Yamamoto, T. Shin-ya, T. Sugiura and A. Hashimoto, *Journal of crystal growth*, 1998, **189**, 461–465.

[824] D. Zanato, E. Tiras, N. Balkan, A. Boland-Thoms, J. Wah and G. Hill, *physica status solidi (c)*, 2005, **2**, 3077–3081.

[825] D. Anderson, N. Apsley, P. Davies and P. Giles, *Journal of applied physics*, 1985, **58**, 3059–3067.

[826] B. Tuck and M. Zahari, *Journal of Physics D: Applied Physics*, 1977, **10**, 2473.

[827] J. Betko and K. Merínskỳ, *physica status solidi (a)*, 1993, **135**, year.

[828] W. Dumke, M. Lorenz and G. Pettit, *Physical Review B*, 1970, **1**, 4668.

[829] V. Galavanov and N. Siukaev, *physica status solidi (b)*, 1970, **38**, 523–530.

[830] A. Kadri, K. Zitouni, L. Konczewicz and R. Aulombard, *Physical Review B*, 1987, **35**, 6260.

[831] J. Leloup, H. Djerassi, J. Albany and J. Mullin, *Journal of Applied Physics*, 1978, **49**, 3359–3362.

[832] S. Messenger, R. Walters, M. Xapsos, G. Summers and E. Burke, *IEEE Transactions on Nuclear Science*, 1998, **45**, 2857–2860.

[833] J. Pastrňák, I. Gregora, J. Oswald, Z. Chvoj, L. Pekárek and V. Vorlíček, *physica status solidi (a)*, 1991, **126**, 493–500.

[834] M. Razeghi, P. Maurel, M. Defour, F. Omnes, G. Neu and A. Kozacki, *Applied physics letters*, 1988, **52**, 117–119.

[835] W. Siegel, G. Kühnel, H. Koi and W. Geelach, *physica status solidi (a)*, 1986, **95**, 309–316.

[836] W. Walukiewicz, L. Lagowski, L. Jastrzebski, M. Lichtensteiger and H. C. Gatos, *Journal of Applied Physics*, 1979, **50**, 899–908.

[837] M. Y. Dashevskii, A. Filipchenko and L. Okun, *physica status solidi (a)*, 1971, **5**, 597–600.

[838] A. Filipchenko and L. Bolshakov, *physica status solidi (b)*, 1976, **77**, 53–58.

[839] M. Oszwałldowski and M. Zimpel, *Journal of Physics and Chemistry of Solids*, 1988, **49**, 1179–1185.

[840] E. Burstein, *Physical Review*, 1954, **93**, 632.

[841] K. Chen and J. Furdyna, *Journal of Applied Physics*, 1972, **43**, 1825–1829.

[842] R. Cunningham and J. Gruber, *Journal of Applied Physics*, 1970, **41**, 1804–1809.

[843] R. Enck, A. Saleh and H. Fan, *Physical Review*, 1969, **182**, 790.

[844] A. Filipchenko, R. Piotrzkowski and S. Porowski, *physica status solidi (b)*, 1969, **31**, K103–K105.

[845] A. Filipchenko and D. Nasledov, *physica status solidi (a)*, 1975, **27**, 11–26.

[846] D. Gaskill, G. Stauf and N. Bottka, *Applied physics letters*, 1991, **58**, 1905–1907.

[847] H. Hrostowski, F. Morin, T. Geballe and G. Wheatley, *Physical Review*, 1955, **100**, 1672.

[848] E. Litwin-Staszewska, W. Szymańska and R. Piotrzkowski, *physica status solidi (b)*, 1981, **106**, 551–559.

[849] H. Mattausch and D. Aspnes, *Physical Review B*, 1981, **23**, 1896.

[850] B. McCombe, *Physical Review*, 1969, **181**, 1206.

[851] E. Putley, *Proceedings of the Physical Society*, 1959, **73**, 280.

[852] E. Putley, *Journal of Physics and Chemistry of Solids*, 1961, **22**, 241–247.

[853] R. Sladek, *Physical Review*, 1960, **120**, 1589.

[854] Z. Li, H. Bender, M. Malfait, V. Moshchalkov, G. Borghs and W. V. Roy, *physica status solidi (a)*, 2007, **204**, 152–158.

[855] R. Bekimbetov, A. Vaipolin, N. Konstantinova, L. Kradinova, G. Medvedkin, V. Prochukhan, Y. V. Rud and M. Tairov, *Crystal Research and Technology*, 1987, **22**, K238–K240.

[856] C. Jacoboni, C. Canali, G. Ottaviani and A. A. Quaranta, *Solid-State Electronics*, 1977, **20**, 77–89.

[857] I. Kirnas, P. Kurilo, P. Litovchenko, V. Lutsyak and V. Nitsovich, *physica status solidi (a)*, 1974, **23**, year.

[858] W. Nelson, F. Halden and A. Rosengreen, *Journal of Applied Physics*, 1966, **37**, 333–336.

[859] S. Asada, T. Okuda, T. Kimoto and J. Suda, *Applied Physics Express*, 2016, **9**, 041301.

[860] D. Barrett and R. Campbell, *Journal of Applied Physics*, 1967, **38**, 53–55.

[861] E. Biedermann, *Solid State Communications*, 1965, **3**, 343–346.

[862] W. Choyke and G. Pensl, *Mrs Bulletin*, 1997, **22**, 25–29.

[863] M. Ikeda, H. Matsunami and T. Tanaka, *Physical Review B*, 1980, **22**, 2842.

[864] K. Narita, Y. Hijikata, H. Yaguchi, S. Yoshida and S. Nakashima, *Japanese journal of applied physics*, 2004, **43**, 5151.

[865] S. Nishino, J. A. Powell and H. A. Will, *Applied Physics Letters*, 1983, **42**, 460–462.

[866] G. Pensl and W. Choyke, in *Wide-Band-Gap Semiconductors*, Elsevier, 1993, pp. 264–283.

[867] G. Rutsch, R. Devaty, W. Choyke, D. Langer and L. Rowland, *Journal of applied physics*, 1998, **84**, 2062–2064.

[868] K. Sasaki, E. Sakuma, S. Misawa, S. Yoshida and S. Gonda, *Applied physics letters*, 1984, **45**, 72–73.

[869] M. Schadt, G. Pensl, R. Devaty, W. Choyke, R. Stein and D. Stephani, *Applied physics letters*, 1994, **65**, 3120–3122.

[870] P. Staikov, D. Baum, J. Lin and H. Jiang, *Solid state communications*, 1994, **89**, 995–998.

[871] A. Suzuki, A. Uemoto, M. Shigeta, K. Furukawa and S. Nakajima, *Applied physics letters*, 1986, **49**, 450–452.

[872] H. Van Daal, W. Knippenberg and J. Wasscher, *Journal of Physics and Chemistry of Solids*, 1963, **24**, 109–127.

[873] R. Weingärtner, P. Wellmann, M. Bickermann, D. Hofmann, T. Straubinger and A. Winnacker, *Applied physics letters*, 2002, **80**, 70–72.

[874] X. Weng and H. Cui, *Journal of Physics: Condensed Matter*, 1997, **9**, 7089.

[875] M. B. Wijesundara and R. G. Azevedo, in *Silicon carbide microsystems for harsh environments*, Springer, 2011, pp. 33–95.

[876] M. Yamanaka, H. Daimon, E. Sakuma, S. Misawa and S. Yoshida, *Journal of applied physics*, 1987, **61**, 599–603.

[877] J. Zhang, R. T. Howe and R. Maboudian, *Journal of The Electrochemical Society*, 2006, **153**, G548–G551.

[878] M. Yamanaka, H. Daimon, E. Sakuma, S. Misawa, K. Endo and S. Yoshida, *Japanese journal of applied physics*, 1987, **26**, L533.

[879] O. Tufte and A. Ewald, *Physical Review*, 1961, **122**, 1431.

[880] R. J. Wagner and A. Ewald, *Journal of Physics and Chemistry of Solids*, 1971, **32**, 697–707.

[881] E. Kohnke and A. Ewald, *Physical Review*, 1956, **102**, 1481.

[882] B. Mercey, D. Chippaux, J. Vizot and A. Deschanvres, *Journal of Physics and Chemistry of Solids*, 1986, **47**, 37–43.

[883] L. Koroleva, V. Y. Pavlov and Zashchirinskiĭ.

[884] F. Scholl and E. Cory, *Materials Research Bulletin*, 1974, **9**, 1511–1515.

[885] S. Shah and J. Greene, *Materials Letters*, 1983, **2**, 115–118.

[886] S. Shah and J. Greene, *Journal of crystal growth*, 1984, **68**, 537–544.

[887] G. Solomon, M. Timmons and J. Posthill, *Journal of Applied Physics*, 1989, **65**, 1952–1956.

[888] J. Dyck, J. Colvin, P. Quayle, T. Peshek and K. Kash, *Journal of Electronic Materials*, 2016, **45**, 2920–2925.

[889] W. L. Larson, H. P. Maruska and D. A. Stevenson, *Journal of The Electrochemical Society*, 1974, **121**, 1673–1674.

[890] V. Grigoreva, V. Prochukhan, Y. V. Rud and A. Yakovenko, *physica status solidi (a)*, 1973, **17**, year.

[891] I. Bertoti and K. Somogyi, *physica status solidi (a)*, 1971, **6**, 439–443.

[892] V. Brudnyi, D. Budnitskii, M. Krivov, R. Masagutova, V. Prochukhan and Y. V. Rud, *physica status solidi (a)*, 1978, **50**, 379–384.

[893] H. Hobgood, T. Henningsen, R. Thomas, R. Hopkins, M. Ohmer, W. Mitchel, D. Fischer, S. Hegde and F. Hopkins, *Journal of applied physics*, 1993, **73**, 4030–4037.

[894] K. Somogyi and I. Bertoti, *Japanese Journal of Applied Physics*, 1972, **11**, 103.

[895] E. Gombia, N. Romeo, G. Sberveglieri and C. Paorici, *physica status solidi (a)*, 1976, **34**, 651–655.

[896] O. Vigil, O. Calzadilla, D. Seuret, J. Vidal and F. Leccabue, *Solar energy materials*, 1984, **10**, 139–143.

[897] A. Abdullayev, T. Kerimova, M. Kyazumov and A. S. Khidirov, *Thin Solid Films*, 1990, **190**, 309–315.

[898] E. Nowak, H. Neumann, B. Schumann and B. Steiner, *physica status solidi (a)*, 1992, **133**, year.

[899] D. Dhruv and B. Patel, *Significance*, 2015, **3**, year.

[900] A. K. Das, P. Misra, R. Ajimsha, D. Phase and L. Kukreja.

[901] D. C. Look, D. Reynolds, C. Litton, R. Jones, D. Eason and G. Cantwell, *Applied physics letters*, 2002, **81**, 1830–1832.

[902] M. Brett and R. Parsons, *Solid state communications*, 1985, **54**, 603–606.

[903] S. Chatman, L. Emberley and K. M. Poduska, *ACS applied materials & interfaces*, 2009, **1**, 2348–2352.

[904] M. Gacic, G. Jakob, C. Herbort, H. Adrian, T. Tietze, S. Brück and E. Goering, *Physical Review B*, 2007, **75**, 205206.

[905] R. R. Gade, *Ph.D. thesis*, Youngstown State University, 2015.

[906] W. Göpel and U. Lampe, *Physical Review B*, 1980, **22**, 6447.

[907] K. Hagemark and L. Chacka, *Journal of Solid State Chemistry*, 1975, **15**, 261–270.

[908] J. Hu and R. G. Gordon, *Journal of Applied Physics*, 1992, **71**, 880–890.

[909] U. Ilyas, R. S. Rawat, T. Tan, P. Lee, R. Chen, H. Sun, L. Fengji and S. Zhang, *Journal of Applied Physics*, 2011, **110**, 093522.

[910] M. Jakani, G. Campet, J. Claverie, D. Fichou, J. Pouliquen and J. Kossanyi, *Journal of Solid State Chemistry*, 1985, **56**, 269–277.

[911] A. Janotti and C. G. Van de Walle, *Reports on progress in physics*, 2009, **72**, 126501.

[912] Y. S. Jung, O. V. Kononenko and W.-K. Choi, *Solid state communications*, 2006, **137**, 474–477.

[913] J. W. Kim, H. S. Kang, J. H. Kim, S. Y. Lee, J.-K. Lee and M. Nastasi, *Journal of applied physics*, 2006, **100**, 033701.

[914] P. Li and K. Hagemark, *Journal of Solid State Chemistry*, 1975, **12**, 371–375.

[915] X. Li, S. Asher, B. Keyes, H. Moutinho, J. Luther and T. Coutts, Photovoltaic Specialists Conference, 2005. Conference Record of the Thirty-first IEEE, 2005, pp. 152–154.

[916] Y. Liu, Y. Li and H. Zeng, *Journal of Nanomaterials*, 2013, **2013**, year.

[917] D. C. Look, J. W. Hemsky and J. Sizelove, *Physical review letters*, 1999, **82**, 2552.

[918] B.-K. Na, M. A. Vannice and A. B. Walters, *Physical Review B*, 1992, **46**, 12266.

[919] D. P. Norton, Y. Heo, M. Ivill, K. Ip, S. Pearton, M. F. Chisholm and T. Steiner, *Materials today*, 2004, **7**, 34–40.

[920] D. C. Reynolds, D. C. Look and B. Jogai, *Solid State Communications*, 1996, **99**, 873–875.

[921] A. Sedky, M. Abu-Abdeen and A. A. Almulhem, *Physica B: Condensed Matter*, 2007, **388**, 266–273.

[922] B. E. Sernelius, K.-F. Berggren, Z.-C. Jin, I. Hamberg and C. Granqvist, *Physical Review B*, 1988, **37**, 10244.

[923] M. Snure and A. Tiwari, *Journal of applied physics*, 2007, **101**, 124912.

[924] E. Klaus, K. Andreas and R. Bernd, *Springer Series in Materials Science, New York*, 2008, **104**, 140.

[925] S. Fujita, H. Mimoto, H. Takebe and T. Noguchi, *Journal of Crystal Growth*, 1979, **47**, 326–334.

[926] R. Mach, P. Flögel, L. Suslina, A. Areshkin, J. Maege and G. Voigt, *physica status solidi (b)*, 1982, **109**, 607–615.

[927] W.-S. Ni and Y.-J. Lin, *Applied Physics A*, 2015, **119**, 1127–1132.

[928] L. Svob, C. Thiandoume, A. Lusson, M. Bouanani, Y. Marfaing and O. Gorochov, *Applied Physics Letters*, 2000, **76**, 1695–1697.

[929] T. Yasuda, B.-P. Zhang and Y. Segawa, *Journal of crystal growth*, 1997, **175**, 583–586.

[930] T. McGill, C. S. Torres and W. Gebhardt, *Growth and Optical Properties of Wide-Gap II–VI Low-Dimensional Semiconductors*, Springer Science & Business Media, 2012, vol. 200.

[931] W. Faschinger, S. Ferreira and H. Sitter, *Applied physics letters*, 1994, **64**, 2682–2684.

[932] N. Teraguchi, S. Hirata, H. Mouri, Y. Tomomura, A. Suzuki and H. Takiguchi, *Journal of crystal growth*, 1995, **150**, 803–806.

[933] K. Agarwal, B. Daniel, T. Hofmann, M. Schubert, C. Klingshirn and M. Hetterich, *physica status solidi (b)*, 2006, **243**, 914–918.

[934] A. Avdonin, G. Ivanova, D. Nedeoglo, N. Nedeoglo and V. Sirkeli, *Physica B: Condensed Matter*, 2005, **365**, 217–224.

[935] M. Aven, D. Marple and B. Segall, *Journal of Applied Physics*, 1961, **32**, 2261–2265.

[936] J. Qiu, H. Cheng, J. DePuydt and M. Haase, *Journal of crystal growth*, 1993, **127**, 279–286.

[937] K. Shahzad, D. J. Olego and D. A. Cammack, *Physical Review B*, 1989, **39**, 13016.

[938] M. Aven and B. Segall, *Physical Review*, 1963, **130**, 81.

[939] F. Rong and G. Watkins, *Physical review letters*, 1986, **56**, 2310.

[940] D. Chippaux, B. Mercey and A. Deschanvres, *Journal of Physics and Chemistry of Solids*, 1987, **48**, 447–457.

[941] Y.-C. Wen and B. Parkinson, *The Journal of Physical Chemistry B*, 1997, **101**, 2659–2662.

[942] G. Averkieva, V. Prochukhan, Y. V. Rud and M. Tashtanova, *physica status solidi (a)*, 1973, **17**, K153–K156.

[943] L. I. Koroleva and Zashchirinskiĭ.

[944] W. Siegel, E. Ziegler and G. Kühnel, *physica status solidi (a)*, 1973, **15**, 521–524.

[945] E. Alekperova, Y. A. Valov, N. Goryunova, S. Ryvkin and G. Shpenkov, *physica status solidi (b)*, 1969, **32**, 49–54.

[946] E. Ziegler, W. Siegel and G. Kuehnel, *physica status solidi (a)*, 1973, **18**, 483–487.

[947] I. Gorban, G. Grishchenko, A. Sakalas and I. Tychina, *physica status solidi (a)*, 1976, **35**, 571–574.

[948] A. Bychkov, N. Goryunova, F. Kesamanly, V. Mityurev, Y. Rud and S. Slobodchikov, *Ukranian Journal of Physics*, 1965, **10**, 872.

[949] W. Siegel and E. Ziegler, *physica status solidi (a)*, 1974, **21**, 639–647.

[950] W. Siegel, A. Heinrich and E. Ziegler, *physica status solidi (a)*, 1976, **35**, 269–279.

[951] W. Siegel, G. Kühnel, E. Ziegler, P. Kirsten and H. Schneider, *Kristall und Technik*, 1980, **15**, 947–954.

[952] A. Springthorpe and R. Monk, *physica status solidi (a)*, 1970, **1**, K9–K12.

[953] E. Ziegler, W. Siegel, G. Kühnel and E. Buhrig, *physica status solidi (a)*, 1978, **48**, K63–K65.

[954] F. Kesamanly, D. Nasledov and Y. V. Rud, *physica status solidi (b)*, 1965, **8**, year.

[955] Y. Agatsuma, J. T. Asubar, Y. Jinbo and N. Uchitomi, *Physics Procedia*, 2010, **3**, 1341–1344.

[956] I. Bertoti, in *Growth of Crystals*, Springer, 1984, pp. 174–180.

[957] V. Brudnyi, S. Borisenko and A. Potapov, *physica status solidi (a)*, 1990, **118**, 505–511.

[958] T. Kato, T. Uchiyama, H. Toyota and N. Uchitomi, *physica status solidi (c)*, 2015, **12**, 512–515.

[959] K. Masumoto and S. Isomura, *Journal of Physics and Chemistry of Solids*, 1965, **26**, 163–171.

[960] N. Feldberg, J. Aldous, W. Linhart, L. Phillips, K. Durose, P. Stampe, R. Kennedy, D. Scanlon, G. Vardar, R. Field III *et al.*, *Applied Physics Letters*, 2013, **103**, 042109.

[961] F. Deng, H. Cao, L. Liang, J. Li, J. Gao, H. Zhang, R. Qin and C. Liu, *Optics letters*, 2015, **40**, 1282–1285.

[962] A. N. Fioretti, A. Zakutayev, H. Moutinho, C. Melamed, J. D. Perkins, A. G. Norman, M. Al-Jassim, E. S. Toberer and A. C. Tamboli, *Journal of Materials Chemistry C*, 2015, **3**, 11017–11028.

[963] A. N. Fioretti, E. S. Toberer, A. Zakutayev and A. C. Tamboli, *arXiv preprint arXiv:1506.07789*, 2015.

[964] A. N. Fioretti, A. Stokes, M. R. Young, B. Gorman, E. S. Toberer, A. C. Tamboli and A. Zakutayev, *Advanced Electronic Materials*, 2017, **3**, 1600544.

[965] L. Lahourcade, N. C. Coronel, K. T. Delaney, S. K. Shukla, N. A. Spaldin and H. A. Atwater, *Advanced Materials*, 2013, **25**, 2562–2566.

[966] R. Qin, H. Cao, L. Liang, Y. Xie, F. Zhuge, H. Zhang, J. Gao, K. Javaid, C. Liu and W. Sun, *Applied Physics Letters*, 2016, **108**, 142104.

[967] T. D. Veal, N. Feldberg, N. F. Quackenbush, W. M. Linhart, D. O. Scanlon, L. F. Piper and S. M. Durbin, *Advanced Energy Materials*, 2015, **5**, 1501462.

[968] A. Vaipolin, N. Goryunova, L. Kleshchinskii, G. Loshakova and E. Osmanov, *physica status solidi (b)*, 1968, **29**, 435–442.

[969] M. Ryan, M. W. Peterson, D. Williamson, J. S. Frey, G. E. Maciel and B. Parkinson, *Journal of Materials Research*, 1987, **2**, 528–537.

[970] P. Ajmera, H. Shin and B. Zamanian, *Solar cells*, 1987, **21**, 291–299.

[971] H. Shin and P. Ajmera, *Materials Letters*, 1989, **8**, 464–467.

[972] W. Scott, *Journal of Applied Physics*, 1973, **44**, 5165–5166.

[973] L. Kradinova and T. Voronina, *physica status solidi (b)*, 1969, **32**, K173–K174.

[974] H. Ogawa and M. Nishio, *Journal of applied physics*, 1988, **64**, 6750–6753.

[975] M. Abazari, F. R. Ahmad, K. C. Raghavan, J. R. Cournoyer, J.-H. Her, R. Davis, J. Chera, V. Smentkowski and B. A. Korevaar, *MRS Proceedings*, 2013, **1538**, 383–389.

[976] A. G. Fischer, J. N. Carides and J. Dresner, *Solid State Communications*, 1964, **2**, 157–159.

[977] M. Grün, A. Haury, J. Cibert and A. Wasiela, *Journal of applied physics*, 1996, **79**, 7386–7388.

[978] Y. Hishida, H. Ishii, T. Toda and T. Niina, *Journal of Crystal Growth*, 1989, **95**, 517–521.

[979] N. Magnea and J. Pautrat, *Solid State Communications*, 1980, **34**, 261–263.

[980] M. Nishio, Y. Nakamura and H. Ogawa, *Japanese Journal of Applied Physics*, 1983, **22**, 1101.

[981] H. Ogawa, G. S. Irfan, H. Nakayama, M. Nishio and A. Yoshida, *Japanese journal of applied physics*, 1994, **33**, L980.

[982] H. Pelletier, B. Theys, A. Lusson, J. Chevallier and N. Magnéa, *Journal of crystal growth*, 1998, **184**, 419–424.

[983] H. Ruda, *Journal of Physics D: Applied Physics*, 1991, **24**, 1158.

[984] J. Scott and R. Hollis, *Solid State Communications*, 1976, **20**, 1125–1128.

[985] S. Sakakibara, N. Amano, K. Ishino, A. Ishida and H. Fujiyasu, *Japanese journal of applied physics*, 1993, **32**, 4703.

[986] F. Smith, *Solid State Communications*, 1971, **9**, 957–960.

[987] H. Tubota, *Japanese Journal of Applied Physics*, 1963, **2**, 259.

[988] D. Verity, F. Bryant, C. Scott and D. Shaw, *Solid state communications*, 1983, **46**, 795–798.

[989] S. P. Ong, W. D. Richards, A. Jain, G. Hautier, M. Kocher, S. Cholia, D. Gunter, V. L. Chevrier, K. A. Persson and G. Ceder, *Comput. Mater. Sci.*, 2013, **68**, 314–319.

[990] W. Tang, E. Sanville and G. Henkelman, *Journal of Physics: Condensed Matter*, 2009, **21**, 084204.

[991] E. Sanville, S. D. Kenny, R. Smith and G. Henkelman, *Journal of computational chemistry*, 2007, **28**, 899–908.

[992] G. Henkelman, A. Arnaldsson and H. Jónsson, *Computational Materials Science*, 2006, **36**, 354–360.

[993] M. Yu and D. R. Trinkle, *The Journal of chemical physics*, 2011, **134**, 064111.

[994] J. Goss, P. Briddon, M. Rayson, S. Sque and R. Jones, *Physical Review B*, 2005, **72**, 035214.

[995] W. Walukiewicz, *Mater. Res. Soc. Symp. Proc.*, 1993, **300**, year.

[996] R. Longini and R. Greene, *Phys. Rev.*, 1956, **102**, 992.

[997] W. Li, Y. Wu, S. Lin, Z. Chen, J. Li, X. Zhang, L. Zheng and Y. Pei, *ACS Energy Lett.*, 2017, **2**, 2349–2355.

[998] M. Zhou, Z. M. Gibbs, H. Wang, Y. Han, C. Xin, L. Li and G. J. Snyder, *Phys. Chem. Chem. Phys.*, 2014, **16**, 20741–20748.

[999] R. Moshwan, L. Yang, J. Zou and Z.-G. Chen, *Adv. Funct. Mater.*, 2017, **27**, 1703278.

[1000] T.-R. Wei, Z. Li, F.-H. Sun, Y. Pan, C.-F. Wu, M. U. Farooq, H. Tang, F. Li, B. Li, J.-F. Li *et al.*, *Sci. Rep.*, 2017, **7**, 43262.